Acoustical Physics, Vol. 47, No. 6, 2001, pp. 633–639. Translated from Akusticheskiĭ Zhurnal, Vol. 47, No. 6, 2001, pp. 725–731.

Study of the Second Harmonics in Nonlinear Scattering of Interacting Acoustic Waves by a Rigid Cylinder

I. B. Abbasov

Taganrog State Radio Engineering University, Nekrasovskiĭ per. 44, Taganrog, 347928 Russia

e-mail: ig@egf.tsure.ru

Received February 17, 2000

Abstract—The field formed by the second harmonics in the case of the nonlinear scattering of interacting plane acoustic waves by a rigid cylinder is considered. The method of successive approximations is used to obtain the solutions to the inhomogeneous wave equation in the first and second approximations. Asymptotic expressions are derived for the components of the total acoustic pressure of the second harmonics, and the scattering diagrams for these components are presented. *© 2001 MAIK "Nauka/Interperiodica".*

The problem of nonlinear scattering of acoustic waves by bodies of regular geometric shape is a reference problem in the theory of nonlinear interaction of sound waves. This problem was studied in [1, 2]. The use of parametric radiators in studying the scattering of sound by discrete inhomogeneities of the water medium at the difference frequency was considered in [3]. The field of the second harmonic in the case of scattering of focused ultrasound by a straight edge was studied both theoretically and experimentally in [4]. The problem on the nonlinear scattering of interacting plane acoustic waves by spherical bodies was considered in [5, 6]. The secondary field of the difference-frequency wave caused by the nonlinear scattering of interacting acoustic waves by a cylinder was studied in [7]. The field of the second harmonics of the initial waves is of special interest, because it covers the geometric scattering region and can supplement the information obtained from a received signal.

This paper presents a study of the field of the second harmonics formed in the case of the scattering of interacting plane acoustic waves by a rigid cylinder. Let us consider the propagation of high-frequency plane waves in a homogeneous medium and assume that their velocity potentials are

$$\psi_{ni} = \psi_{n0}\exp[i(\omega_n t + k_n r\cos\varphi)],$$

where ψ_{n0} is the amplitude of the velocity potential function; $n = 1$ and 2 for the waves with the frequencies ω_1 and ω_2, respectively; k_n is the wave number; and $\varphi = \pi$ corresponds to the propagation direction of the incident wave.

The geometry of the problem is presented in Fig. 1. The axis of the cylinder of infinite length coincides with the z axis of the cylindrical coordinate system. Plane waves are incident on the cylinder normally to the z axis. The scattering of the plane waves by the cylinder gives rise to scattered cylindrical waves with the velocity potential

$$\psi_{ns} = \psi_{n0}\exp(i\omega_n t)\sum_{m=0}^{\infty} A_m^{(n)}\cos(m\varphi + \alpha_m)H_m^{(2)}(k_n r),$$

where $H_m^{(2)}(k_n r)$ is the mth-order Hankel cylindrical function of the second kind and $A_m^{(n)}$ is determined by the boundary conditions; in our case, the cylinder is perfectly rigid and satisfies the Neumann boundary conditions

$$A_m^{(n)} = -\varepsilon_m i^{-m}\frac{J_m'(k_n a)}{H_m^{(2)'}(k_n a)}, \quad \alpha_m = 0,$$

where $J_m(k_n a)$ is the mth-order Bessel cylindrical function and a is the cylinder radius.

To proceed with the transformations, we expand the plane waves in cylindrical functions [8]:

$$\psi_{ni} = \psi_{n0}\exp[i(\omega_n t + k_n r\cos\varphi)]$$

$$= \psi_{n0}\exp(i\omega_n t)\sum_{l=0}^{\infty}\varepsilon_l i^l J_l(k_n r)\cos l\varphi,$$

where l is the number of cylindrical functions and

$$\varepsilon_l = \begin{cases} 1, & l = 0 \\ 2, & l = 1, 2, 3, \ldots. \end{cases}$$

Then, the velocity potential function of the total primary acoustic field ψ_n will have the form

$$\psi_n = \psi_{ni} + \psi_{ns} = \psi_{n0}\exp(i\omega_n t)$$

$$\times\left[\sum_{l=0}^{\infty}\varepsilon_l i^l J_l(k_n r)\cos l\varphi + \sum_{m=0}^{\infty} A_m^{(n)}\cos m\varphi H_m^{(2)}(k_n r)\right]. \quad (1)$$

1063-7710/01/4706-0633$21.00

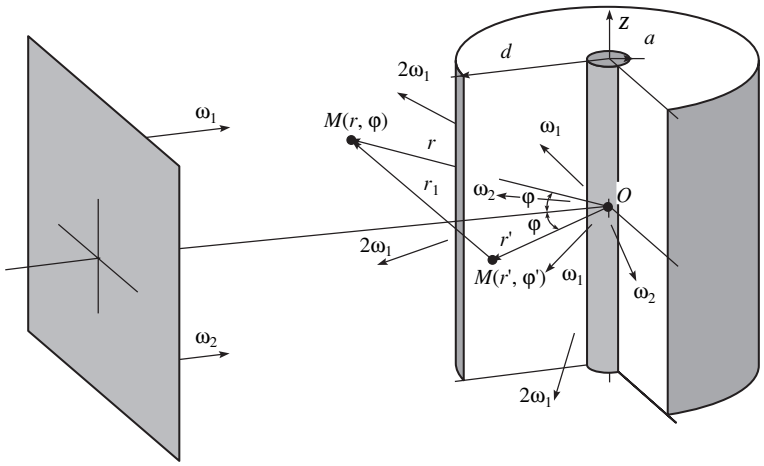

Fig. 1. Geometry of the problem.

To solve the problem on the interaction of the primary high-frequency waves, Eq. (1) is represented with a complex conjugate part [9]:

$$\bar{\psi}_n = \psi_{n0}\left[\sum_{l=0}^{\infty}\varepsilon_l J_l(k_n r)\cos l\varphi\exp[i(\omega_n t + l\pi/2)]\right.$$

$$\left. + \sum_{m=0}^{\infty} A_m^{(n)} D_m^{(n)}\cos m\varphi\exp[i(\omega_n t - \delta_m^{(n)} - \pi/2)]\right] + (\text{c.c.}),$$

where $D_m^{(n)}$ and $\delta_m^{(n)}$ are the magnitude and phase of the Hankel cylindrical function $H_m^{(2)}(k_n r) = -iD_m^{(n)}\exp(-i\delta_m^{(n)})$.

The total primary field of acoustic pressure will then consist of the fields with two frequencies ω_1 and ω_2:

$$p^{(1)} = p_1^{(1)} + p_2^{(1)}$$

$$= \left\{ i\omega_1\rho_0\psi_{10}\left[\sum_{l=0}^{\infty} B_{1l}^{(1)}\exp[i(\omega_1 t + l\pi/2)]\right.\right.$$

$$\left.\left. + \sum_{m=0}^{\infty} B_{2m}^{(1)}\exp[i(\omega_1 t - \delta_m^{(1)} - \pi/2)]\right] + (\text{c.c.})\right\} \quad (2)$$

$$+ \left\{ i\omega_2\rho_0\psi_{20}\left[\sum_{l=0}^{\infty} B_{1l}^{(2)}\exp[i(\omega_2 t + l\pi/2)]\right.\right.$$

$$\left.\left. + \sum_{m=0}^{\infty} B_{2m}^{(2)}\exp[i(\omega_2 t - \delta_m^{(2)} - \pi/2)]\right] + (\text{c.c.})\right\},$$

where $B_{1l}^{(n)} = \varepsilon_l J_l(k_n r)\cos l\varphi$ and $B_{2m}^{(n)} = A_m^{(n)} D_m^{(n)}\cos m\varphi$.

This scattering problem can be solved using the inhomogeneous wave equation that describes the nonlinear processes in the primary field [10]:

$$\Delta p^{(2)} - \frac{1}{c_0^2}\frac{\partial^2 p^{(2)}}{\partial t^2} = -Q = -\frac{\varepsilon}{c_0^4\rho_0}\frac{\partial^2 p^{(1)^2}}{\partial t^2}, \quad (3)$$

where Q is the volume density of the sources of secondary waves, c_0 is the sound velocity in the medium, ε is the quadratic nonlinearity parameter, ρ_0 is the density of the unperturbed medium, and $p^{(1)}$ and $p^{(2)}$ are the total acoustic pressures of the primary and secondary fields.

This wave equation can be solved by the method of successive approximations. In the first approximation, the solution is represented by expression (2) for the acoustic pressure of the primary field $p^{(1)}$. In the case of the determination of the solution in the second approximation $p^{(2)}$, the right-hand side of Eq. (3) will consist of four frequency components: $2\omega_1$, $2\omega_2$, $\omega_1 + \omega_2$, and $\omega_2 - \omega_1 = \Omega$.

For the second harmonic $2\omega_1$ of the pumping wave ω_1, the expression for the volume density of the sources of secondary waves has the form

$$Q_{2\omega} = K_{2\omega}\left[\sum_{l=0}^{\infty}\sum_{m=0}^{\infty} B_{1l}^{(1)} B_{1m}^{(1)}\cos(2\omega_1 t + (l+m)\pi/2)\right.$$

$$+ \sum_{l=0}^{\infty}\sum_{m=0}^{\infty} B_{1l}^{(1)} B_{2m}^{(1)}\cos(2\omega_1 t + l\pi/2 - \delta_m^{(1)} - \pi/2) \quad (4)$$

$$\left. + \sum_{m=0}^{\infty}\sum_{l=0}^{\infty} B_{2m}^{(1)} B_{2l}^{(1)}\cos(2\omega_1 t - \delta_m^{(1)} - \delta_l^{(1)} - \pi)\right],$$

where $K_{2\omega} = 2\varepsilon\omega_1^2\rho_0\psi_{10}^2/c_0^4$.

To solve the inhomogeneous wave equation (3) with the right-hand side given by Eq. (4) in the second approximation, it is convenient to seek the solution in the complex form [10]

$$p_{2\omega}^{(2)} = \frac{1}{2}P_{2\omega}^{(2)}\exp[i(2\omega_1 t + \delta)] + (\text{c.c.}). \quad (5)$$

With the use of Eq. (5), the inhomogeneous wave equation (3) is reduced to the inhomogeneous Helmholtz equation

$$\Delta P_{2\omega}^{(2)} + k_{2\omega}^2 P_{2\omega}^{(2)} = -q_{2\omega}(r, \varphi), \quad (6)$$

where

$$q_{2\omega}(r, \varphi) = K_{2\omega}\Bigg[\sum_{l=0}^{\infty}\sum_{m=0}^{\infty} B_{1l}^{(1)}B_{1m}^{(1)}\exp[i(l+m)\pi/2] + \sum_{l=0}^{\infty}\sum_{m=0}^{\infty} B_{1l}^{(1)}B_{2m}^{(1)}\exp[i(l\pi/2 - \delta_m^{(1)} - \pi/2)] + \sum_{m=0}^{\infty}\sum_{l=0}^{\infty} B_{2m}^{(1)}B_{2l}^{(1)}\exp[i(\delta_m^{(1)} + \delta_l^{(1)} + \pi)]\Bigg]$$

and $k_{2\omega} = 2k_1$ is the wave number of the second harmonic $2\omega_1$. Here and below, the time factor $\exp(i2\omega_1 t)$ is omitted.

The solution to the inhomogeneous Helmholtz equation (6) has the form of a volume integral of the product of the Green function by the density of the secondary wave sources [10, 11]:

$$P_{2\omega}^{(2)}(r, \varphi) = \frac{1}{4\pi}\int_V q_{2\omega}(r', \varphi')G(r_1)r'd\varphi'dz'dr', \quad (7)$$

where $G(r_1) = \exp(-ik_{2\omega}r_1)/r_1$ is the Green function.

In the far zone $r' \ll r$, the Green function is determined by the asymptotic expression

$$G(r_1) \approx \exp[-ik_{2\omega}(r - r'\cos(\varphi - \varphi'))]/r,$$

where r is the distance to the observation point $M(r, \varphi, z)$, r', φ', and z' are the coordinates of the current point $M'(r', \varphi', z')$ of the volume; and r_1 is the distance between the current point of the volume $M'(r', \varphi', z')$ and the observation point $M(r, \varphi, z)$ (Fig. 1).

The integration in Eq. (7) is performed over the volume V occupied by the secondary wave sources. In the cylindrical coordinates, this volume is bounded by the relations $a \le r' \le d$, $0 \le \varphi' \le \pi$, and $-z_\lambda \le z' \le z_\lambda$ ($z_\lambda \gg \lambda$, λ is the initial high-frequency wavelength) and has the form of a cylindrical layer of the medium surrounding the scatterer and having the inner radius a (the cylinder radius) and the outer radius d (Fig. 1). The distance d is the length of the region of nonlinear interaction between the initial high-frequency waves, and beyond this distance d, the initial waves are assumed to completely attenuate.

The problem is considered in the high-frequency limit, and, hence, after the integration with respect to the coordinates φ' and z' with allowance for the asymptotic expansions of the Bessel function [12, 13], Eq. (7) takes the form

$$P_{2\omega}^{(2)}(r, \varphi) = P_{2\omega\,\mathrm{I}}^{(2)}(r, \varphi) + P_{2\omega\,\mathrm{II}}^{(2)}(r, \varphi) + P_{2\omega\,\mathrm{III}}^{(2)}(r, \varphi)$$

$$= C_{2\omega}(1 + i\sin\varphi)\int_a^d\Bigg[\sum_{l=0}^{\infty}\sum_{m=0}^{\infty}\varepsilon_l J_l(k_1 r')\cos l\varphi\varepsilon_m \times J_m(k_1 r')\cos m\varphi\exp[i(l+m)\pi/2] + \sum_{l=0}^{\infty}\sum_{m=0}^{\infty}\varepsilon_l J_l(k_1 r')\cos l\varphi A_m^{(1)}D_m^{(1)}\cos m\varphi \times \exp[i(l\pi/2 - \delta_m^{(1)} - \pi/2)] + \sum_{m=0}^{\infty}\sum_{l=0}^{\infty}A_m^{(1)}D_m^{(1)} \times \cos m\varphi A_l^{(1)}D_l^{(1)}\cos l\varphi\exp[i(\delta_m^{(1)} + \delta_l^{(1)} + \pi)]\Bigg] \times \cos k_{2\omega}r'\sqrt{r'}dr', \quad (8)$$

where $C_{2\omega} = -\exp(-ik_{2\omega}r)K_{2\omega}/\sqrt{2\pi k_{2\omega}}r$.

As one can see from expression (8) for the total acoustic pressure of the second harmonic $P_{2\omega}^{(2)}$, it consists of three spatial components. It should be noted that the expression for the acoustic pressure of the difference-frequency wave consists of four spatial components [7], and, therefore, for the second harmonic, the contribution of each spatial component is considerably increased. The first component $P_{2\omega\,\mathrm{I}}^{(2)}$ of Eq. (8) corresponds to the part of the acoustic pressure of the second harmonic that is formed in the cylindrical layer of the nonlinear interaction region by the incident high-frequency plane wave ω_1. The second component $P_{2\omega\,\mathrm{II}}^{(2)}$ describes the interaction of the incident plane wave ω_1 with the scattered cylindrical wave ω_1. The third component $P_{2\omega\,\mathrm{III}}^{(2)}$ corresponds to the self-action of the scattered cylindrical wave ω_1. It should be noted that the nonlinear interaction occurs between the waves with both identical and different wave front configurations.

To obtain the final expression for the acoustic pressure of the second harmonic $P_{2\omega}^{(2)}$, we consider the first spatial component $P_{2\omega\,\mathrm{I}}^{(2)}$ of Eq. (8), which characterizes

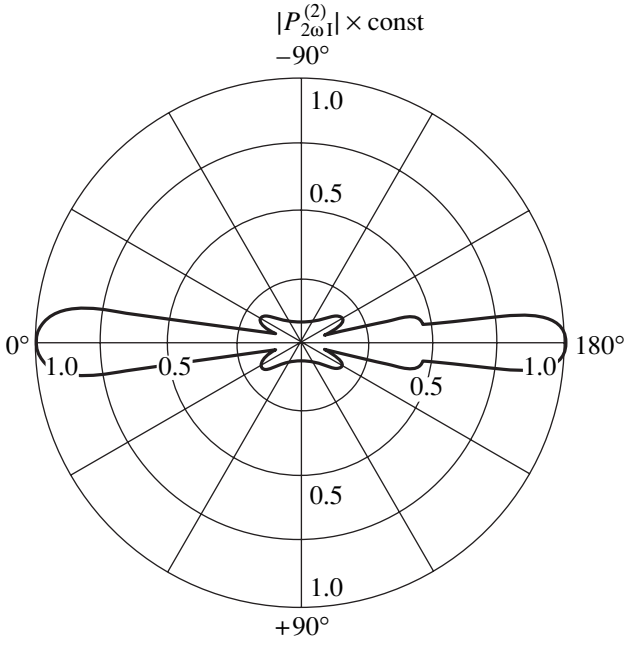

Fig. 2. Scattering diagram of the spatial component $P^{(2)}_{2\omega\,\mathrm{I}}$ of the total acoustic pressure produced by the second harmonic in the case of the scattering by a rigid cylinder for $2f_1 = 1520$ kHz, $k_{2\omega}a = 64$, $d = 0.17$ m, and $a = 0.01$ m ($d = a + 0.5l_D$, $l_D = 0.31$ m is the quasi-diffraction distance of the scatterer, and the values of the second harmonic are selected from the set of initial frequencies given in [7]).

the nonlinear self-action of the incident high-frequency plane wave:

$$P^{(2)}_{2\omega\,\mathrm{I}}(r, \varphi) = C_{2\omega}(1 + i\sin\varphi) \times \int_a^d \sum_{l=0}^{\infty}\sum_{m=0}^{\infty} \varepsilon_l J_l(k_1 r')\cos l\varphi\, \varepsilon_m J_m(k_1 r')\cos m\varphi \times \exp[i(l+m)\pi/2]\cos k_{2\omega} r' \sqrt{r'}\, dr'. \quad (9)$$

Taking into account the expansion of the plane wave in cylindrical functions [9] and performing some trigonometric transformations [14], we represent Eq. (9) in the form

$$P^{(2)}_{2\omega\,\mathrm{I}}(r, \varphi) = \frac{C_{2\omega}(1 + i\sin\varphi)}{2} \times \left[\int_a^d \exp[ik_{2\omega} r'(\cos\varphi + 1)]\sqrt{r'}\, dr' + \int_a^d \exp[ik_{2\omega} r'(\cos\varphi - 1)]\sqrt{r'}\, dr'\right].$$

After the final integration in Eq. (9), the component $P^{(2)}_{2\omega\,\mathrm{I}}$ takes the form

$$P^{(2)}_{2\omega\mathrm{I}}(r, \varphi) = [P^{(2)}_{1\,1} + P^{(2)}_{1\,2}], \quad (10)$$

where

$$P^{(2)}_{1\,1} = \frac{C_{2\omega}(1 + i\sin\varphi)}{2ik_{2\omega}(\cos\varphi + 1)} \times [\exp[ik_{2\omega}(\cos\varphi + 1)d] - \exp[ik_{2\omega}(\cos\varphi + 1)a]],$$

$$P^{(2)}_{1\,2} = \frac{C_{2\omega}(1 + i\sin\varphi)}{2ik_{2\omega}(\cos\varphi - 1)} \times [\exp[ik_{2\omega}(\cos\varphi - 1)d] - \exp[ik_{2\omega}(\cos\varphi - 1)a]].$$

From Eq. (10), it follows that the scattering diagram of the first component $P^{(2)}_{2\omega\,\mathrm{I}}$ of the total acoustic pressure produced by the second harmonic of the incident wave is determined by the behavior of the functions $1/(\cos\varphi \pm 1)$. The scattering diagram of the component $P^{(2)}_{2\omega\,\mathrm{I}}$ is shown in Fig. 2. It characterizes the geometric scattering, since the scattering of the second harmonics is of purely geometric character $k_{2\omega}a \gg 1$. This diagram is symmetric with respect to the angle $\varphi = \pi/2$ and has the major maximums in the directions $\varphi = 0$ and π, which is a result of the effect of the functions $1/(\cos\varphi \pm 1)$.

To test the result obtained for the problem under study, we consider the component $P^{(2)}_{2\omega\,\mathrm{I}}$ in the case when the cylinder radius tends to zero (i.e., the scatterer is absent) and the region of nonlinear interaction is transformed from the cylindrical layer to a full cylinder of radius d:

$$P^{(2)}_{1\,1}\big|_{a=0} \approx \frac{C_{2\omega}(1 + i\sin\varphi)\sqrt{d}}{2ik_{2\omega}(\cos\varphi + 1)} \times \left[\frac{\exp[ik_{2\omega}(\cos\varphi + 1)d]}{\sqrt{d}}\right] = \frac{C_{2\omega}(1 + i\sin\varphi)\sqrt{d}}{2ik_{2\omega}(\cos\varphi + 1)} H_0^{(1)}(k_{2\omega}(\cos\varphi + 1)d), \quad (11)$$

where $H_0^{(1)}(k_{2\omega}(\cos\varphi + 1)d)$ is a zero-order Hankel cylindrical function of the first kind. Expression (11) characterizes a diverging cylindrical wave with some amplitude coefficient that depends on the angle φ [15]. This confirms the physical meaning of this spatial component of the total acoustic pressure.

Now, we consider the second component of the total acoustic pressure of the second harmonic $P^{(2)}_{2\omega\,\mathrm{II}}$, which

characterizes the interaction of the incident plane wave with the scattered cylindrical wave:

$$P^{(2)}_{2\omega\,\mathrm{II}}(r,\varphi) = C_{2\omega}(1+i\sin\varphi) \times \int_a^d \sum_{l=0}^{\infty}\sum_{m=0}^{\infty} \varepsilon_l J_l(k_1 r')\cos l\varphi A^{(1)}_m D^{(1)}_m \cos m\varphi \times \exp[i(l\pi/2-\delta^{(1)}_m-\pi/2)]\cos k_{2\omega} r'\sqrt{r'}\,dr'. \quad (12)$$

After similar transformations with allowance for the asymptotic values of the Hankel functions [8, 14] and after integration, Eq. (12) takes the form

$$P^{(2)}_{2\omega\,\mathrm{II}}(r,\varphi) = [P^{(2)}_{\mathrm{II}\,1} + P^{(2)}_{\mathrm{II}\,2}], \quad (13)$$

where

$$P^{(2)}_{\mathrm{II}\,1} = \frac{C_{2\omega}A^{(1)}_0(1+i\sin\varphi)(\cos\varphi-1)}{\sqrt{8\pi k_1}ik_1\cos\varphi(\cos\varphi+1)} \times [\exp[ik_1(\cos\varphi+1)d]-\exp[ik_1(\cos\varphi+1)a]],$$

$$P^{(2)}_{\mathrm{II}\,2} = \frac{C_{2\omega}A^{(1)}_0(1+i\sin\varphi)(\cos\varphi-1)}{\sqrt{8\pi k_1}ik_1\cos\varphi(\cos\varphi-3)} \times [\exp[ik_1(\cos\varphi-3)d]-\exp[ik_1(\cos\varphi-3)a]].$$

An analysis of Eq. (13) shows that the effect of the function $1/(\cos\varphi+1)$ is dominant for the scattering diagram of the component $P^{(2)}_{2\omega\,\mathrm{II}}$. The scattering diagram is presented in Fig. 3. It has a single major maximum in the direction $\varphi=\pi$ and very small lateral maximums, which are related to the behavior of the function $1/\cos\varphi$. The appearance of the major maximum in the forward direction is caused by the coincidence of the wave fronts of the incident plane wave and the scattered cylindrical wave in this direction.

Now, we consider the third component of the total acoustic pressure of the second harmonic $P^{(2)}_{2\omega\,\mathrm{III}}$. This component characterizes the self-action of the scattered cylindrical wave and has the form

$$P^{(2)}_{2\omega\,\mathrm{III}}(r,\varphi) = C_{2\omega}(1+i\sin\varphi) \times \int_a^d \sum_{m=0}^{\infty}\sum_{l=0}^{\infty} A^{(1)}_m D^{(1)}_m \cos m\varphi A^{(1)}_l D^{(1)}_l \cos l\varphi \times \exp[i(\delta^{(1)}_l+\delta^{(1)}_m+\pi)]\cos k_{2\omega} r'\sqrt{r'}\,dr'. \quad (14)$$

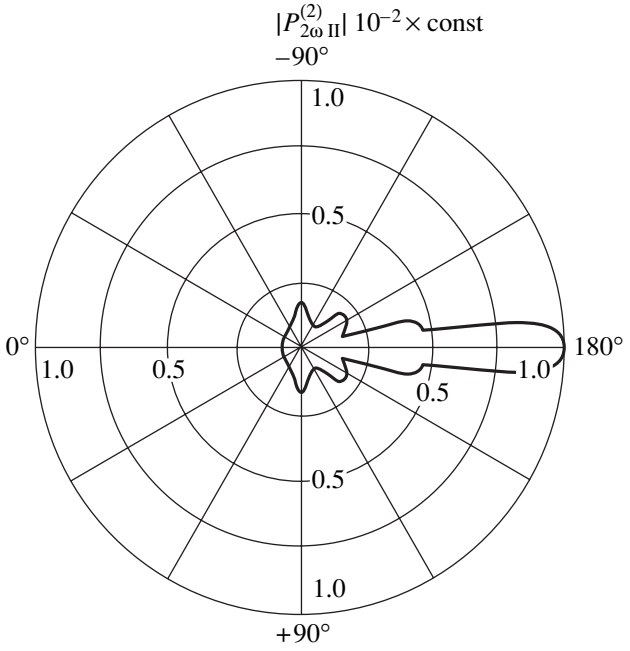

Fig. 3. Scattering diagram of the spatial component $P^{(2)}_{2\omega\,\mathrm{II}}$ of the total acoustic pressure of the second harmonic for $2f_1 = 1520$ kHz, $k_{2\omega}a = 64$, $d = 0.17$ m, and $a = 0.01$ m.

After some transformations and the final integration [14, 16], the expression for the component $P^{(2)}_{2\omega\,\mathrm{III}}$ takes the form

$$P^{(2)}_{2\omega\,\mathrm{II}}(r,\varphi) = \frac{C_{2\omega}A^{(1)^2}_0(1+i\sin\varphi)(\cos\varphi-1)^2}{2\pi k_{2\omega}\cos^2\varphi} \times \left[\left[\sqrt{\frac{\pi}{2ik_{2\omega}}}(erfi(\sqrt{2ik_{2\omega}}d)-erfi(\sqrt{2ik_{2\omega}}a))\right] + 2[\sqrt{d}-\sqrt{a}]\right],$$

where $erfi(x) = \frac{2}{\sqrt{\pi}}\int_0^x \exp(t^2)\,dt$ is the probability integral with complex argument [14].

The scattering diagram of the third component $P^{(2)}_{2\omega\,\mathrm{III}}$ is shown in Fig. 4. Its form is determined by the behavior of the function $1/\cos^2\varphi$, which results in the appearance of the major maxim in the directions $\varphi = \pm\varphi/2$ without any additional levels.

Figure 5 presents the scattering diagrams of the total acoustic pressure of the second harmonic $P^{(2)}_{2\omega}$. From these diagrams, one can see that they have major maximums in the directions $\varphi = 0, \pm\pi/2$, and π, which cor-

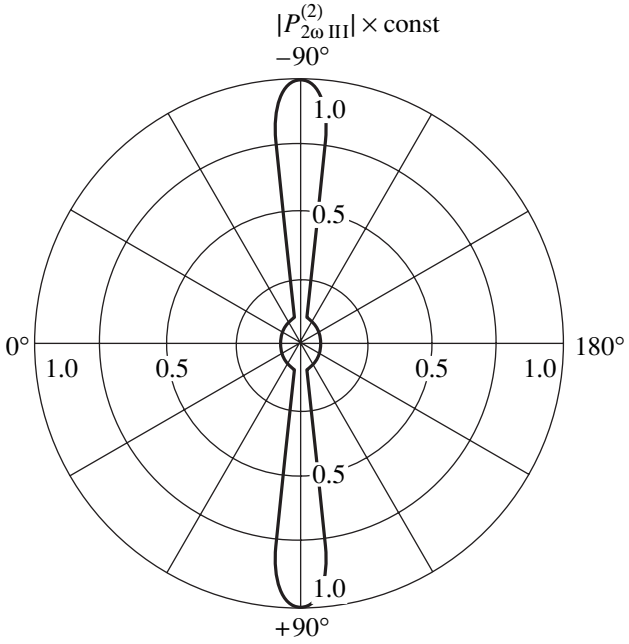

Fig. 4. Scattering diagram of the spatial component $P^{(2)}_{2\omega\,\mathrm{III}}$ of the total acoustic pressure of the second harmonic for $2f_1$ = 1520 kHz, $k_{2\omega}a$ = 64, d = 0.17 m, and a = 0.01 m.

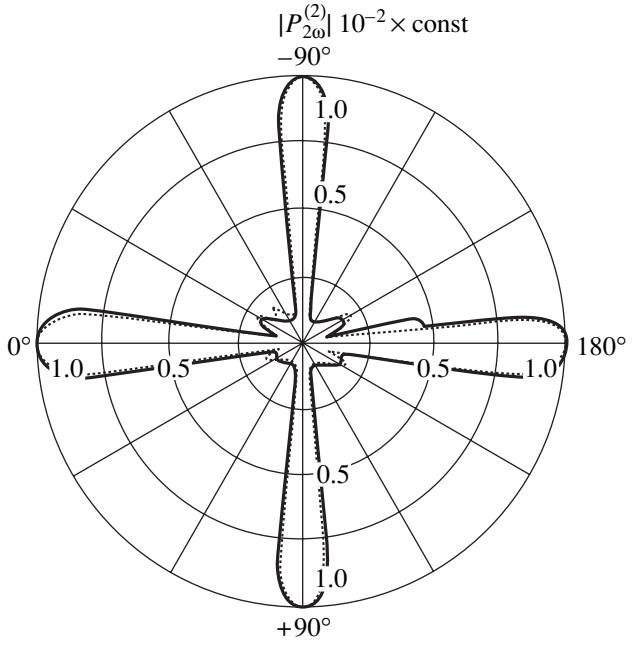

Fig. 5. Scattering diagrams of the total acoustic pressure of the second harmonic $P^{(2)}_{2\omega}$ in the case of scattering by a rigid cylinder for $2f_1$ = (*1*) 1520 and (*2*) 1952 kHz, $k_{2\omega}a$ = (*1*) 64 and (*2*) 82, a = 0.01 m, and d = (*1*, —) 0.17, (*1*, •••) 3.21, (*2*, —) 0.2, and (*2*, •••) 4.1 m.

respond to the directions of the minimal phase differences between the nonlinearly interacting initial high-frequency waves. An increase in the wave size of the cylindrical scatterer leads to insignificant changes in the scattering diagram because of the geometric character of the scattering process. An increase in the width of the cylindrical volume around the scatterer leads to a narrowing of the major maximums, which is characteristic of parametric antennas, because the dimensions of the reradiating volume become increased.

It should be noted that, because of the different spatial configurations of the wave fronts of the initial interacting waves, the contributions of individual spatial components to the total scattering field become unequal. Therefore, the effect of the spatial component $P^{(2)}_{2\omega\,\mathrm{II}}$ on the total acoustic pressure field proves to be insignificant, since the interaction is of a counter character.

On the whole, one can conclude that the theoretical model under consideration provides a sufficiently detailed description of the physical processes that accompany the scattering of nonlinearly interacting plane acoustic waves by a rigid cylinder.

ACKNOWLEDGMENTS

I am grateful to N.P. Zagraĭ for supervising this study.

REFERENCES

1. J. C. Piquette and A. L. van Buren, J. Acoust. Soc. Am. **76**, 880 (1984).
2. L. M. Lyamshev and P. V. Sakov, Akust. Zh. **38**, 100 (1992) [Sov. Phys. Acoust. **38**, 51 (1992)].
3. P. A. Chinnery, V. E. Humphrey, and J. Zhang, J. Acoust. Soc. Am. **101**, 2571 (1997).
4. S. Shigemi and K. Jung-Soon, Jpn. J. Appl. Phys., Part 1 **38** (5B), 3085 (1999).
5. I. B. Abbasov and N. P. Zagraĭ, Akust. Zh. **40**, 535 (1994) [Acoust. Phys. **40**, 473 (1994)].
6. I. B. Abbasov and N. P. Zagrai, J. Sound Vibr. **216**, 194 (1998).
7. I. B. Abbasov and N. P. Zagraĭ, Akust. Zh. **45**, 590 (1999) [Acoust. Phys. **45**, 523 (1999)].
8. L. F. Lependin, *Acoustics* (Vysshaya Shkola, Moscow, 1978).
9. L. K. Zarembo and V. I. Timoshenko, *Nonlinear Acoustics* (Mosk. Gos. Univ., Moscow, 1984).
10. B. K. Novikov, O. V. Rudenko, and V. I. Timoshenko, *Nonlinear Underwater Acoustics* (Sudostroenie, Lenin-

grad, 1981; Acoustical Society of America, New York, 1987).

11. L. W. Dean, J. Acoust. Soc. Am. **34**, 1039 (1962).
12. *Handbook of Mathematical Functions*, Ed. by M. Abramowitz and I. A. Stegun (Dover, New York, 1971; Nauka, Moscow, 1979).
13. E. Skudrzyk, *The Foundations of Acoustics. Basic Mathematics and Basic Acoustics* (Springer, New York, 1971; Mir, Moscow, 1976), Vol. 2.
14. A. P. Prudnikov, Yu. A. Brychkov, and O. I. Marichev, *Integrals and Series. Elementary Functions* (Nauka, Moscow, 1981).
15. E. P. Shenderov, *Wave Problems in Hydroacoustics* (Sudostroenie, Leningrad, 1972).
16. H. B. Dwight, *Tables of Integrals and Other Mathematical Data*, 4th ed. (Macmillan, London, 1961; Nauka, Moscow, 1983).

Translated by E. Golyamina

Acoustical Physics, Vol. 47, No. 6, 2001, pp. 640–643. Translated from Akusticheskiĭ Zhurnal, Vol. 47, No. 6, 2001, pp. 732–735.

Application of a Mobile Seismoacoustic System for Studying Geological Structure and Prospecting for Inhomogeneities to a Depth of 100 m

V. S. Averbakh, V. V. Artel'nyĭ, B. N. Bogolyubov, D. V. Dolinin, Yu. M. Zaslavskiĭ, A. P. Maryshev, Yu. K. Postoenko, and V. I. Talanov

Institute of Applied Physics, Russian Academy of Sciences, ul. Ul'yanova 46, Nizhni Novgorod, 603155 Russia

e-mail: zaslav@hydro.appl.sci-nnov.ru

Received October 2, 2000

Abstract—The results of a practical evaluation of a mobile seismoacoustic system intended for the search for underground engineering structures and their imaging are presented. The system was designed at the Institute of Applied Physics of the Russian Academy of Sciences and consists of an electrodynamic radiator of seismoacoustic waves that operates in the frequency range 200–800 Hz, an array of receivers, and a computer-based control unit. The signal is controlled digitally, which allows the system to store up to 10^3 realizations. The signal is received by high-sensitivity seismic sensors, amplified by low-noise amplifiers, supplied to a 16-channel A/D converter, and displayed on the computer monitor. The system was used in a field experiment to determine the location of an antilandslide drainage adit. © *2001 MAIK "Nauka/Interperiodica"*.

This paper presents the results of the field experiments carried out to evaluate the 3D imaging of underground engineering structures by using a special-purpose mobile high-frequency seismoacoustic system designed and manufactured at the Institute of Applied Physics of the Russian Academy of Sciences in 1999 and intended for active sounding under the ground surface. Seismic monitoring and imaging of inhomogeneities in the uppermost subsurface layers of the ground is quite an urgent problem, which was addressed repeatedly using various approaches and physical fields [1]. The most burning problem is that of imaging for the depths from a few meters to several tens of meters. At these depths, the medium is characterized by a high friability, instability, and even strong variability of its structure. These factors, together with the high content of underground water at these depths, determine the most unfavorable propagation conditions due to high coefficients of attenuation of elastic seismoacoustic fields. Therefore, in solving routine problems of geophysical prospecting, the presence of such regions is taken into account by introducing the corresponding corrections in the calculations. At greater depths, the structure of the ground medium in the direction of the horizontal coordinates is characterized by a much smaller variability and, as a consequence, the developed geophysical methods and the facilities available in practice make it possible, as a rule, to trace only smooth changes in the subsurface structure. The imaging of local inhomogeneities located in the upper part of the profile is currently carried out in rare cases by conventional methods of surveying with the use of miniature explosion sources and with seismic braids repeatedly repositioned on the ground surface. The repeated repositioning makes it possible to provide the incoherent storage of signals with the use of explosion sources.

In our case, the sounding of an antilandslide drainage adit located in the ground thickness was carried out by using a special-purpose mobile high-frequency seismic system generating a coherent seismoacoustic illuminating field. The high stability of the generated seismic field allows one to use all the advantages of modern means and methods of signal processing in application to signals scattered by inhomogeneities. Among the most efficient methods is the method of focusing the fields received by one- and two-dimensional arrays, which makes it possible to obtain high-resolution images of a given volume of the ground medium potentially containing a local inhomogeneity.

The field experiment was carried out in a bank region near the Volga slope, where the ground surface makes an angle of 30° with the horizontal and the soil has the tendency to landslide. As a consequence, in the lower part of the slope, in the built-up area, drainage adits are present. The length of an adit is several hun-

1063-7710/01/4706-0640$21.00

dred meters, and its cross section has the form of a trapezoid slightly narrowed at the top with a height of 1.8 m and a lower base width of 1.2 m. The interior of the adit is faced with concrete tiles. Thus, the problem of the seismic imaging of the adit is additionally complicated by the character of the geological structure in the experimental area. It should be noted that seismoacoustic monitoring of regions including landslide hazard zones is a complicated technical problem, and many attempts were made to solve it by using pulsed sounding techniques [2–5].

The receiving–transmitting part of the system was installed above the entrance to the adit (see the schematic view of the experiment in Fig. 1). The vertical distance from the nearest point of the linear chain of the receiving antenna to the level of the adit ceiling was 3.5 m. The antenna array consisted of an eight-channel chain of geophones–accelerometers. The output of the preamplifier of every geophone was connected to the corresponding input of an eight-channel A/D converter. The receiving aperture was synthesized by the four successive lengthwise displacements of the eight-channel antenna, i.e., it consisted of 32 points of measurement. The realization of such an antenna consisting of 32 points of measurement with a step of 0.5 m was possible only due to the high coherence of the generated field. The reconstructed projection of the line of adit on the inclined ground surface passed through the geometric center of the synthesized aperture. The signal source was a vibrator with a vertical polarization of a variable force action. The source was installed at a leveled horizontal site (0.3×0.3 m). The site was 1 m away from the line of the receiving antenna and displaced from the aperture center by 2 m to the left. The source excited signals of a complex form in the frequency range 100–1000 Hz with an adjustable force, the maximal value of which was 250 N.

The recording and controlling instruments connected with the receivers and the source by cables was installed in a vehicle located near the entrance to the adit. The dynamic range of measurement, i.e., the difference in the levels of the maximal linear signal and the electron noise relative to the input of the amplifier, was 100 dB. The recorded signals were stored by a PC-Note Book (Pentium 150).

Below, we consider only the results of sounding by pulsed tone signals, although the control equipment and the electromechanical unit make it possible to generate signals of various forms. In the described experiment, as the driving signals, we used short sequences consisting of three periods of the carrier frequency equal to 300 Hz. The quality of the reproduction of these signals by the mechanical unit was monitored by an accelerometer mounted vertically on the operating plate of the source, and this plate was in contact with the ground. The signal from this accelerometer was transmitted by an auxiliary channel and was also stored in the computer memory.

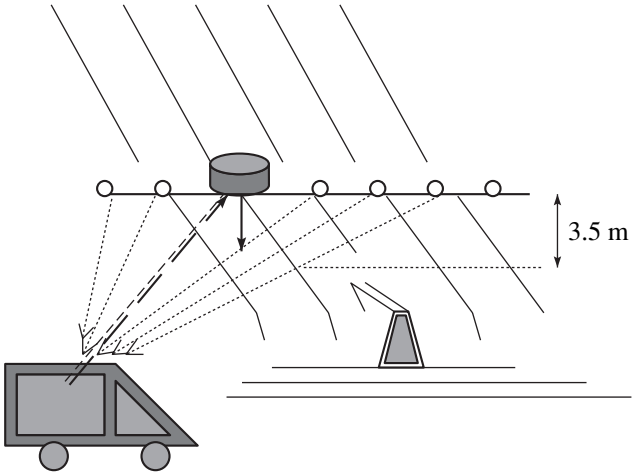

Fig. 1. Position of the receiving–transmitting system in the experiment on seismoacoustic sounding of an adit in the region of the Volga slope.

The experiments were preceded by preliminary measurements aimed at evaluating the attenuation of the desired signal along the path of the primary beam to determine the necessary amplification of the input channel. These measurements showed that, at a frequency of about 300 Hz and at a distance of 4 m, the primary beam attenuated in level by 50 dB. Such a strong decrease in level due to the high dissipative loss is evidence of the friability of the soil in the landslide zone, which is confirmed below by the low values of the propagation velocities of the corresponding seismoacoustic waves [2, 5].

Figure 2 shows the general pattern of the wave field recorded by the antenna array. This pattern reveals the presence of weakly pronounced (against the noise background) equiphase axes corresponding to the arrival of some regularly excited surface waves at the receiver chain. Initially, these are the waves propagating through the air (with a velocity of 340 m/s), which are recorded by the four or five geophones nearest to the source. Then, it is possible to distinguish two more equiphase axes corresponding to "pure" seismic waves: the Rayleigh wave (with a velocity of 200 m/s) and the wave refracted by a deeper boundary (with a velocity of 500 m/s), which are recorded by the sensors lying at the points away from the aperture center. Due to the attenuation, the level of signals received by the sensors away from the aperture center is much lower than the level of signals received at the center. As a result, the actual aperture decreases to 16 m,

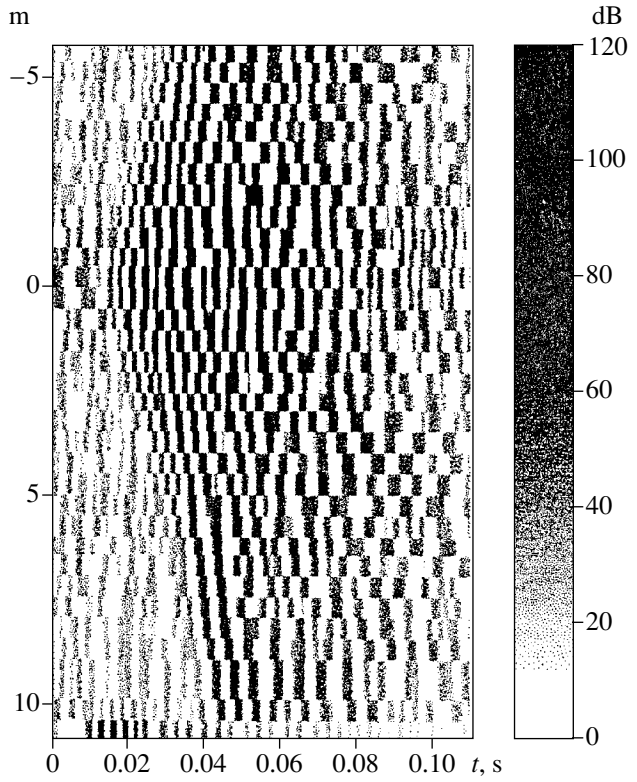

Fig. 2. Wave field recorded by a linear antenna array in the sounding area.

eight meters on both sides of the center of the antenna. It should be noted that the irregularities of the microprofile of the surface and the variability of the elastic parameters, i.e., the fluctuations of the acoustic characteristics at various points of the ground medium near the surface, are quite considerable. As a result, in the wave field presented in Fig. 2 with a rather chaotic form, it is difficult to detect any regular distinctions between the upper and lower parts of the pattern, although it was known beforehand that, in the region of the left wing of the array (the lower half of the figure), an artificial inhomogeneity would be present.

By using the value of the propagation velocity of the signal 200 m/s, we performed the procedure of focusing at the region of the medium under the antenna at a depth of about 20 m. The picture obtained in this case is presented in Fig. 3, which shows the "image" of a portion of a depth profile near the vertical cross section of the adit. In Fig. 3a, the picture of the inhomogeneity distribution corresponds to the focusing of pulsed tone signals in the frequency band with a central frequency of 300 Hz, and in Fig. 3b, with a central frequency of 400 Hz. Figure 3c displays the result of the multiplication of the two aforementioned focusings. The last procedure makes it possible to sharpen the outline of the inhomogeneity, although within the area of focusing it is easy to see that, in addition to the main spot corresponding to the location of the adit, some side spots are observed because of the interference of the incident wave field and the wave field scattered by the obstacle.

Thus, on the basis of the experiments on seismic sounding by a mobile receiving–transmitting system, it is possible to conclude that the imaging of local inhomogeneities at high frequencies of the seismic survey range can be realized in practice. The created system accomplishes all stages of sounding, including the algorithmic procedures of processing the recorded signal and displaying the results in the form of a

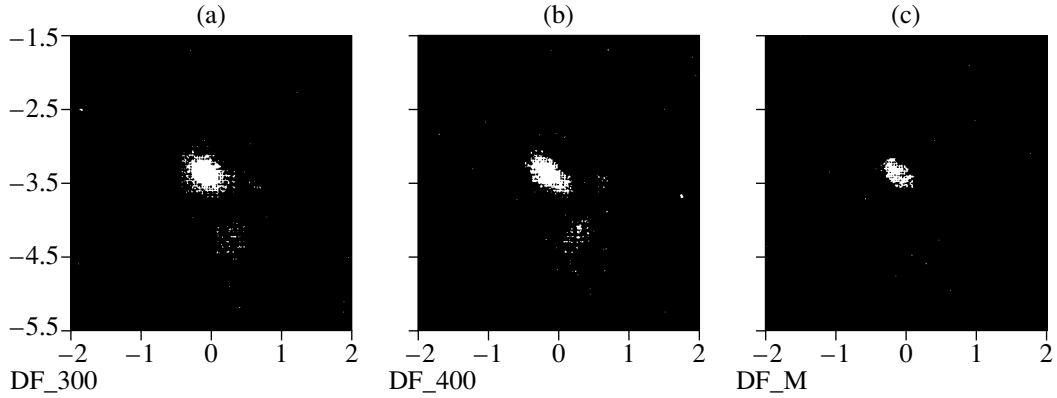

Fig. 3. Picture representing the distribution of the inhomogeneity (the vertical profile); the picture is obtained by focusing at the adit region: at a frequency of (a) 300 and (b) 400 Hz and (c) the product of the above two focusings.

brightness picture corresponding to the spatial distribution of the physical parameters of the ground medium. In the future, we plan to modify the system so as to enhance the efficiency of its application.

ACKNOWLEDGMENTS

This work was supported by the Ministry of Science and Technologies of the Russian Federation (Contract no. 4 of March 14, 1997), by the Russian Foundation for Basic Research (grant no. 96-15-96592 in Support of the Leading Scientific Schools and grant no. 99-02-16957), and by the Integration Program.

REFERENCES

1. V. D. Lomtadze, *Engineering Geology. Engineering Geodynamics* (Nedra, Leningrad, 1977).
2. N. N. Goryainov, A. N. Bogolyubov, N. M. Varlamov, *et al*., *Study of Landslides by Geophysical Methods* (Nedra, Moscow, 1987).
3. G. S. Baker, C. Schmeisner, and W. Don Steeples, Geophys. Res. Lett. **26**, 279 (1999).
4. R. D. Miller, W. Don Steeples, and M. Brannan, Geophysics **54**, 1528 (1989).
5. N. N. Goryainov and F. M. Lyakhovitskiĭ, *Seismic Methods in Engineering Geology* (Nedra, Moscow, 1979).

Translated by A. Svechnikov

Acoustical Physics, Vol. 47, No. 6, 2001, pp. 644–648. Translated from Akusticheskiĭ Zhurnal, Vol. 47, No. 6, 2001, pp. 736–740.

Effect of the Dissipation, Dispersion, and Diffraction on the Amplitude and the Transverse Stability of Solitons

A. G. Bagdoev and A. V. Shekoyan

Institute of Mechanics, National Academy of Sciences of Armenia, pr. Marshala Bagramyana 24b, Yerevan, 375019 Armenia

e-mail: mechins@sci.am

Received November 26, 1999

Abstract—The transverse stability and the amplitude variations of soliton-like wave motions in the presence of nonlinearity, dispersion, diffraction, and dissipation in the medium are studied. The wave process is described by a quintic nonlinear evolution equation. It is demonstrated that the stability of the solution does not depend on the dissipation when the dissipation, diffraction, and dispersion are of the same order of magnitude. It depends on the sign of the ratio of the diffraction and dispersion coefficients. When the sign is positive, the soliton is stable. This result coincides with the stability condition for a nonlinear modulation wave. For the case of strong dissipation, an expression describing the soliton amplitude is obtained and the dissipation is shown to have no effect on the soliton stability. *© 2001 MAIK "Nauka/Interperiodica".*

Several papers [1–4] studying waves in the media, where nonlinearity, dispersion, diffraction, and dissipation exist simultaneously, appeared in the recent years. Examples of such media are soil, an absorbing medium with cavities, a composite with piezoelectric properties, a conducting nonsymmetric liquid with gas bubbles, etc. A nonlinear evolution equation of the following form is used to describe the waves studied in these papers:

$$\frac{\partial^2 u}{\partial x \partial \tau} + \frac{1}{2} L \Delta_\perp u = p \frac{\partial}{\partial \tau}\left(u \frac{\partial u}{\partial \tau}\right) + D \frac{\partial^3 u}{\partial \tau^3} - E \frac{\partial^4 u}{\partial \tau^4} + N \frac{\partial^5 u}{\partial \tau^5}, \quad (1)$$

where $\Delta_\perp$ is the Laplacian with respect to the y and z coordinates; $\tau = x c_n^{-1} - t$, c_n is the linear normal velocity of the wave; u is the perturbed particle velocity normal to the wave; x is the Cartesian coordinate along which the wave propagates; and L, p, E, D, and N are the diffraction, nonlinear, dispersion, and dissipation coefficients, respectively.

A soliton solution was obtained in our previous papers [2, 5], and Karpman and Maslov [6] obtained the solution to the one-dimensional Korteveg-de-Vries–Burgers equation. In the book [7], the Korteveg-de-Vries equation with the right-hand side proportional to u is solved. The absorption is artificially taken into account in this way. A question about the stability of the soliton solutions to transverse perturbations was formulated for the first time by Kadomtsev and Petviashvili [8]. This problem was also solved by Zakharov [9] using the method of an inverse problem. In the book [7] cited above, a general approach was developed for solving the problem of the transverse stability of solitons, and this approach was applied to the Kadomtsev–Petviashvili equation.

Below, we consider the transverse stability of solitons for the complex dissipation laws given by Eq. (1).

Let us first discuss the problem of the stability of soliton solutions to Eq. (1) on the assumption that the diffraction and dissipative terms are small and are of the same order of magnitude. Following [7], we introduce the notation

$$v = pu(6E)^{-1}, \quad L(2E)^{-1} = 3\beta^2\sigma, \quad \sigma = \pm 1,$$
$$x = E^{-1}t, \quad T = \beta t, \quad \frac{\partial \theta}{\partial \tau} = 1, \quad \frac{\partial \theta}{\partial t} = -4\eta^2, \quad (2)$$
$$DE^{-1} = \beta^2\kappa, \quad NE^{-1} = \beta^2\xi,$$

where β is a constant small parameter characterizing the deviation of the solution to a three-dimensional dissipative evolution equation from a one-dimensional nondissipative solution to the corresponding equation; T is the slowly varying time; $4\eta^2$ is the propagation velocity of a soliton; and, in this case, $2\eta^2$ is its amplitude, as it will be demonstrated below. Using Eqs. (2), Eq. (1) in the unknowns θ, T, y, and z can be represented in the form

$$\frac{\partial}{\partial \theta}\left(-4\eta^2 \frac{\partial v}{\partial \theta} + 6v \frac{\partial v}{\partial \theta} + \frac{\partial^3 v}{\partial \theta^3}\right) = -\beta \frac{\partial^2 v}{\partial T \partial \theta} - 3\beta^2 \sigma \Delta_\perp v + \kappa \beta^2 \frac{\partial^3 v}{\partial \theta^3} + \beta^2 \xi \frac{\partial^5 v}{\partial \theta^5}. \quad (3)$$

1063-7710/01/4706-0644$21.00

We try a solution to Eq. (3) in the form

$$v = v_0 + \beta v_1 + \beta^2 v_2 + \ldots. \quad (4)$$

Substituting Eq. (4) into Eq. (3) in the zeroth order, we obtain

$$L_0(v_0) = -4\eta^2\frac{\partial v_0}{\partial\theta} + 6v_0\frac{\partial v_0}{\partial\theta} + \frac{\partial^3 v_0}{\partial\theta^3} = 0. \quad (5)$$

Equation (5) has the soliton solution of the following type [7]:

$$v_0 = 2\eta^2\operatorname{sech}^2\eta\theta_2, \quad \theta_2 = \theta - \theta_0(T, y, z), \quad (6)$$

where θ_0 is a certain additional phase that characterizes small transverse and dissipative perturbations and is to be determined. One can easily see that, in the case of the selected orders of Eqs. (2), we can assume η to be constant [7, 8].

From Eq. (3), in the orders of β and β^2, we obtain

$$L(v_n) \equiv -4\eta^2\frac{\partial v_n}{\partial\theta} + 6\frac{\partial}{\partial\theta}(v_0 v_n) + \frac{\partial^3 v_n}{\partial\theta^3} = F_n, \quad (7)$$

$$(n = 1, 2).$$

By virtue of Eq. (6), we can write the expressions for F_1 and F_2:

$$F_1 = -\frac{\partial v_0}{\partial T} = \frac{\partial v_0}{\partial\theta}\frac{\partial\theta}{\partial T}, \quad (8)$$

$$F_2 = -\frac{\partial v_1}{\partial T} + 3\sigma\int_{\infty}^{\theta}\Delta_\perp v_0 d\theta' + \kappa\frac{\partial^2 v_0}{\partial\theta^2} + \xi\frac{\partial^4 v_0}{\partial\theta^4} - 6v_1\frac{\partial v_1}{\partial\theta}. \quad (9)$$

We introduce the operator L^* conjugate to L and assume that $L^*(v_0) = -L_0(v_0) = 0$. It is possible to demonstrate that the expression $v_0 L(v_n) - v_n L^*(v_0)$ is the derivative with respect to θ of a certain function containing the products of v_0, v_n, and their derivatives [7]. Then, assuming that v_n are finite at infinity, we obtain the following conditions:

$$\int_{-\infty}^{+\infty} v_0 F_1 d\theta = 0, \quad (10)$$

$$\int_{-\infty}^{+\infty} v_0 F_2 d\theta = 0. \quad (11)$$

As shown in [7], a solution to Eq. (7) at $n = 1$ has the form

$$v_1 = (2\eta^2)^{-1}\frac{\partial\theta_0}{\partial T}\left(2v_0 + \theta_2\frac{\partial v_0}{\partial\theta}\right). \quad (12)$$

Taking into account that only even functions of θ_2 contribute to Eq. (11), because

$$\frac{\partial v_0}{\partial y} = -\frac{\partial v_0}{\partial\theta}\frac{\partial\theta}{\partial y}, \quad \frac{\partial v_0}{\partial z} = -\frac{\partial v_0}{\partial\theta}\frac{\partial\theta_0}{\partial z},$$

we can substitute in Eq. (9)

$$\Delta_\perp v_0 \approx -\frac{\partial v_0}{\partial\theta}\Delta_\perp\theta_0.$$

Then, after partial integration, the condition given by Eq. (11) yields

$$\frac{\partial^2\theta_0}{\partial T^2} - 16\sigma\eta^2\Delta_\perp\theta_0 + \Lambda = 0, \quad (13)$$

where

$$\Lambda = 16\kappa\eta^2(3f_0)^{-1}f_1 - 16\xi\eta^2(3f_0)^{-1}f_2,$$

$$f_0 = \int_{-\infty}^{+\infty} v_0^2 d\theta, \quad f_1 = \int_{-\infty}^{+\infty}\left(\frac{\partial v_0}{\partial\theta}\right)^2 d\theta, \quad f_2 = \int_{-\infty}^{+\infty}\left(\frac{\partial^2 v_0}{\partial\theta^2}\right)^2 d\theta.$$

Taking into account Eq. (6) for f_0, f_1, and f_2, we obtain

$$f_0 = \frac{16}{3}\eta^3, \quad f_1 = \frac{64}{15}\eta^5, \quad f_2 = \frac{256}{21}\eta^7. \quad (14)$$

Using the expression

$$\theta_0 = \theta_1 + \Lambda(64\sigma\eta^2)^{-1}(y^2 + z^2),$$

we represent Eq. (13) in the form

$$\frac{\partial^2\theta_1}{\partial T^2} - 16\sigma\eta^2\Delta_\perp\theta_1 = 0. \quad (15)$$

Since θ_0–θ_1 does not depend on time T, it does not affect the stability. Dependence of θ_0 on the transverse coordinates leads to only a phase shift for both Eq. (6) and Eq. (12). From Eq. (15), one can judge the soliton stability. At $\sigma = 1$, this equation is of a hyperbolic type and θ_1 is finite, which corresponds to a stable soliton, i.e., to a small initial perturbation of the zeroth solution causes a small variation of the solution at a given moment. At $\sigma = -1$, Eq. (15) is of elliptical type, i.e., when $T \longrightarrow \infty$, we have $\theta_1 \longrightarrow \infty$, and the soliton solution [Eqs. (6) and (12)] is unstable. A stability condition follows from Eqs. (2):

$$L_1/E > 0. \quad (16)$$

The physical meaning of Eq. (16) is that the transverse stability of a soliton in the presence of dissipation is determined by the sign of the ratio of the coefficients of diffraction L_1 and dispersion E. It also follows from inequality (16) that, in the presence of the orders given by Eq. (2), the dissipation does not affect the transverse stability of a soliton. It is interesting to note that Eq. (16) coincides with the stability condition for modulation waves [3] in the adiabatic approximation.

In the case of a conducting liquid with gas bubbles in a magnetic field that is close in its direction to the wave normal, condition (16) has the form [3]

$$c_n^2 - a_1^2 > 0, \tag{17}$$

where a_1 is the Alfven velocity.

Now, let us consider the absorption that is assumed to be strong compared to diffraction. The two last equalities in Eqs. (2) for this absorption have the form

$$DE^{-1} = \beta\kappa, \quad NE^{-1} = \beta\xi. \tag{18}$$

In this case, Eq. (3) takes the form

$$\begin{aligned}&\frac{\partial}{\partial\theta}\left(-4\eta^2\frac{\partial v}{\partial\theta} + 6v\frac{\partial v}{\partial\theta} + \frac{\partial^3 v}{\partial\theta^3}\right)\\ &= -\beta\frac{\partial^2 v}{\partial T\partial\theta} - 3\beta^2\sigma\Delta_\perp v + \beta\kappa\frac{\partial^3 v}{\partial\theta^3} + \beta\xi\frac{\partial^5 v}{\partial\theta^5}.\end{aligned} \tag{19}$$

Equations (4)–(6) stay valid, while in Eq. (7), we have to assume that

$$F_1 = -\frac{\partial v_0}{\partial T} + \kappa\frac{\partial^2 v_0}{\partial\theta^2} + \xi\frac{\partial^4 v_0}{\partial\theta^4}, \tag{20}$$

$$\begin{aligned}F_2 = &-6v_1\frac{\partial v_1}{\partial\theta} - \frac{\partial v_1}{\partial T} - 3\sigma\int_{\infty}^{\theta}\Delta_\perp v_0 d\theta'\\ &+ \kappa\frac{\partial^2 v_1}{\partial\theta^2} + \xi\frac{\partial^4 v_1}{\partial\theta^4}.\end{aligned} \tag{21}$$

By virtue of the new orders of dissipation [Eqs. (18)], we consider $\eta = \eta(T)$ as a variable. Then, taking into account Eqs. (6), we obtain

$$\frac{\partial v_0}{\partial T} = -\frac{\partial\theta_0}{\partial T}\frac{\partial v_0}{\partial\theta} + \frac{1}{\eta}\frac{\partial\eta}{\partial T}\left(2v_0 + \theta_2\frac{\partial v_0}{\partial\theta}\right). \tag{22}$$

Taking into account Eqs. (20), (22), and (14), from Eq. (10), we derive the following equation for η:

$$-\frac{3}{2\eta}\frac{\partial\eta}{\partial T} - \frac{4\kappa}{5}\eta^2 + \frac{16\xi}{7}\eta^4 = 0. \tag{23}$$

In the case of a conducting but nonmicropolar liquid with gas bubbles, we have $\xi = 0$. Then, from Eq. (23), we obtain the solution

$$\eta = \eta(0)\left[1 + \frac{16}{15}\kappa T\eta^2(0)\right]^{-1/2}. \tag{24}$$

Expression (24) was obtained using a different technique by Karpman and Maslov [6]. Since, by virtue of Eqs. (2), $\kappa T > 0$ for the media under consideration, the soliton amplitude decreases in space, in the course of the soliton propagation, according to the law given by Eq. (24).

In a general case when $\xi \neq 0$, a solution to Eq. (23) has the form

$$\begin{aligned}&\frac{20\xi}{7\kappa}\ln\frac{\eta^2}{\eta^2(0)} - \eta^{-2} + \eta^{-2}(0)\\ &-\frac{20\xi}{7\kappa}\ln\left(\eta^2 - \frac{7\kappa}{20\xi}\right)\left[\eta^2(0) - \frac{7\kappa}{20\xi}\right]^{-1} = -\frac{16}{15}\kappa T.\end{aligned} \tag{25}$$

This equation can be solved numerically. However, one can see already from Eq. (23) that, when $\xi\eta^2 < 7\kappa/20$, an attenuation of η takes place; i.e., for $T \longrightarrow \infty$, we have $\eta \longrightarrow 0$. At the same time, an approximate solution of Eq. (25) for small ξ/η shows that, for sufficiently large values of $\eta(0)$ and finite values of T, an increase in the soliton amplitude is possible.

We try the solution to Eq. (7) at $n = 1$ in the form

$$v_1 = v_2 + q, \tag{26}$$

where v_2 is the solution to Eq. (7) for $n = 1$, when only the first terms are taken on the right-hand side of Eq. (20) and in Eqs. (22). In this case, v_2 has the form of Eq. (12). The quantity q is a solution to the equation

$$L(q) = \kappa\frac{\partial^2 v_0}{\partial\theta^2} + \xi\frac{\partial^4 v_0}{\partial\theta^4} + \mu\left(2v_0 + \theta_2\frac{\partial v_0}{\partial\theta}\right). \tag{27}$$

The operator $L(q)$ is given by the left-hand side of Eq. (7) at $n = 1$ by the substitution of q for v_1. The quantity μ can be obtained from Eqs. (22) and (23) and is expressed as

$$\mu = \frac{2}{3}\left(\frac{4}{5}\eta^2\kappa - \frac{16}{7}\xi\eta^4\right).$$

To determine the contribution of v_2 to Eqs. (11) and (21) according to the fact that a nonzero contribution to Eq. (11) is made by only the even terms of $\partial v_2/\partial T$, we obtain

$$\begin{aligned}&\int_{-\infty}^{+\infty}\frac{\partial v_2}{\partial T}v_0 d\theta\\ &= \frac{3}{16\eta^2}\frac{\partial^2\theta_0}{\partial T^2}f_0 + \frac{1}{3\eta^2}\frac{\partial\theta_0}{\partial T}\left(\frac{\eta\chi}{5} - \frac{4}{7}\xi\eta^4\right)f_3,\end{aligned} \tag{28}$$

where

$$f_3 = \int_{-\infty}^{+\infty}\theta_2^2\left(\frac{\partial v_0}{\partial\theta}\right)^2 d\theta.$$

Following [7], we introduce $y_1 = \tanh\eta\theta_2$. Then, from Eq. (27), we obtain the following equation for q:

$$\frac{d^2q}{dy^2}(1-y^2) - 2y\frac{dq}{dy} + \left(12 - \frac{4}{1-y^2}\right)q = 16\xi\eta^3 y(1-y^2)(2-3y^2) - 4\eta\kappa y + \frac{\mu}{2}\ln\frac{1+y}{1-y} + 2\mu(y-1)[\eta(1-y^2)]^{-1}. \quad (29)$$

The solution to Eq. (29) for the case $\xi = 0$, which is true for a wide class of media (e.g., a conducting symmetric mixture), has the form

$$q = \frac{4}{15}\eta\kappa y(y^2-1)\left\{\frac{2}{y} + \ln\left[|y|^{-1}\frac{(1-y)^2}{1+y}\right] + (1+y)^{-1}\right\} + \frac{2}{15}(1-y^2)\eta\kappa y\left(y^{-1}\ln\frac{1+y}{1-y} - \frac{1}{4}\ln^2\frac{1+y}{1-y} - \ln\frac{y^2}{1-y^2}\right). \quad (30)$$

The contribution of q to Eqs. (11) and (21) gives

$$\int_{-\infty}^{+\infty}\frac{\partial q}{\partial T}v_0 d\theta_2 = -4\eta^2\frac{\partial\theta_0}{\partial T}\int_{-1}^{+1} qy\,dy + \frac{3}{16}\kappa^2 q_2. \quad (31)$$

Now, the equation for θ_0 takes the form

$$\frac{\partial^2\theta_0}{\partial T} - 16\eta^2\sigma\Delta_\perp\theta_0 + \chi\frac{\partial\theta_0}{\partial T} - \kappa^2 f_0^{-1}q_2\eta^2 = 0. \quad (32)$$

The expression for q_2 is not given here because of its awkwardness, especially as this quantity does not affect the stability, because it does not depend on θ_2. This fact was revealed in the derivation of Eqs. (15) and (13).

The quantity χ in Eq. (32) has the form

$$\chi = \frac{76}{45}\eta^2\kappa + \frac{14}{15}\eta^2\kappa\int_{-1}^{+1}(1-y^2)y^2\ln^2\frac{1+y}{1-y}dy + \frac{144}{15}\eta^2\kappa P,$$

$$P = \int_0^1(1-y^2)\left(1-\frac{y}{2}\ln\frac{1+y}{1-y}\right)y \times\left[(1-y^2)\left(\ln\frac{1+y}{1-y} - \frac{y}{4}\ln^2[(1+y)(1-y)^{-1}]\right) - 2y\right]dy. \quad (33)$$

The integral P has a numerical value of –0.33. However, the term added to Eq. (33) on this account is smaller than $\frac{76}{45}\kappa\eta^2$, and, as one can see from Eq. (33), the condition $\chi\kappa^{-1} > 0$ still holds.

As in the derivation of Eq. (15), we assume that

$$\theta_0 = \theta_1 - (y^2+z^2)q_2\kappa^2(64\sigma f_0)^{-1}.$$

We obtain the following relation for θ_1:

$$\frac{\partial^2\theta_1}{\partial T^2} - 16\eta^2\sigma\Delta_\perp\theta_1 + \chi\frac{\partial\theta_1}{\partial T} = 0. \quad (34)$$

At $\sigma = -1$, Eq. (34) is of elliptical type, which leads to the instability of the solution at constant η [12].

Let us show that this is also true for η determined by Eq. (24).

We recast Eq. (34) using the substitution

$$\theta_1 = A(T)\exp[i(k_1y + k_2z)],$$

where $k_1^2 + k_2^2 = k^2$. In this case, Eq. (34) is reduced to the equation

$$\frac{d^2A}{dX_1^2} + \frac{a}{X_1}\frac{dA}{dX_1} + \frac{b}{X_1A} = 0, \quad (35)$$

where $a = \frac{15}{16}\mu$, $b = \frac{225}{16}\chi^2\sigma\eta^{-2}(0)$, $X_1 = 1 + \frac{16}{15}\chi T\eta^2(0)$, and

$$\mu = \frac{76}{45} + \frac{14}{15}\int_{-1}^{+1}(1-y^2)y^2\ln[(1+y)(1-y)^{-1}]dy - \frac{1.44}{3}. \quad (36)$$

Since $\beta > 0$ and $D > 0$, we have $\kappa E > 0$ also for large values of x; moreover, $x > 0$ and $TE^{-1} > 0$ by virtue of Eqs. (2). Therefore, we obtain $X_1 > 0$, and it is large.

A solution to the equation for $b > 0$ has the form [13]

$$A = X_1^{(1-a)/2}Z_\nu[2(bX_1)^{1/2}], \quad (37)$$

where Z_ν is the Bessel function and $\nu = |1-a|$.

The asymptotics of Eq. (37) at $X_1 \longrightarrow \infty$ with $b > 0$ is as follows [14]:

$$A \sim X_1^{(1-2a)/4}. \quad (38)$$

Thus, for $b > 0$ or $\sigma = 1$ and $a > 1/2$, when $X_1 \longrightarrow \infty$, we have $A \longrightarrow 0$, and the solution is stable. It is possible to demonstrate that, according to Eq. (36), we have $a > 1/2$ and, therefore, at $\sigma = 1$ a dissipative soliton is stable. A nondissipative soliton at $\sigma = 1$ is also stable. Therefore, the dissipation does not affect the transverse stability.

In the case of $b < 0$ or $\sigma = -1$, one can see from Eq. (37) that

$$A \sim X_1^{(1-2a)/4}\exp[2(-bX_1)^{1/2}], \quad (39)$$

i.e., $A \longrightarrow \infty$ when $X_1 \longrightarrow \infty$, and a dissipative soliton is unstable, as well as a non-dissipative soliton.

It is necessary to note that condition (16) obtained in this way from the condition $\sigma = 1$ agrees well with the

condition of the transverse stability of modulation waves [3, 10, 11]. The solutions in this paper also agree with the results by Averkiou and Hamilton [15].

Thus, we arrive at the conclusion that the dissipation does not affect the transverse stability of the soliton determined by the solution of the quintic evolution equations of the type of Eqs. (1) or (2) in the case of both weak dissipation (when dissipation and diffraction are of the same order of magnitude) and strong dissipation. The stability depends on the sign of the ratio of the diffraction and dispersion coefficients, a soliton being stable in the case of the positive sign. This result coincides with the condition of the modulation stability of nonlinear waves.

Above, we derived the expressions for the soliton amplitude and the solution to the soliton-type equations, including the first-order ones. The soliton amplitude proves to be weakly attenuating with time, and its variations do not affect the transverse stability of the soliton.

The term quadratic in the transverse coordinates that is present in the additional phase does not affect the transverse stability and leads only to a phase shift in the first- and second-order solutions.

ACKNOWLEDGMENTS

We are grateful to the reviewer for valuable advice and also to Prof. S.G. Saakyan for useful discussions.

REFERENCES

1. A. G. Bagdoev and A. V. Shekoyan, Int. J. Non-Linear Mech. **32** (2), 385 (1997).
2. A. G. Bagdoev and A. V. Shekoyan, Akust. Zh. **45**, 149 (1999) [Acoust. Phys. **45**, 119 (1999)].
3. A. G. Bagdoev and L. G. Petrosyan, Izv. Akad. Nauk Arm. SSR, Mekh. **36** (5), 3 (1983).
4. A. G. Bagdoev and A. V. Shekoyan, Izv. Nats. Akad. Nauk Arm., Mekh. **48** (1), 64 (1995).
5. A. V. Shekoyan, Izv. Nats. Akad. Nauk Arm., Fiz. **33** (4), 187 (1998).
6. V. I. Karpman and E. M. Maslov, Zh. Éksp. Teor. Fiz. **75** (2), 504 (1978) [Sov. Phys. JETP **48**, 252 (1978)].
7. M. Ablowitz and H. Segur, *Solitons and the Inverse Scattering Transform* (SIAM, Philadelphia, Penn., 1981; Mir, Moscow, 1987).
8. B. B. Kadomtsev and V. I. Petviashvili, Dokl. Akad. Nauk SSSR **192** (4), 753 (1970) [Sov. Phys. Dokl. **15**, 539 (1970)].
9. V. E. Zakharov, Pis'ma Zh. Éksp. Teor. Fiz. **22** (7), 364 (1975) [JETP Lett. **22**, 172 (1975)].
10. A. V. Shekoyan, Izv. Akad. Nauk Arm. SSR, Ser. Fiz. (1988).
11. A. G. Bagdoev and A. V. Shekoyan, Phys. Status Solidi A **89**, 499 (1985).
12. D. B. Whitham, Proc. R. Soc., Ser. A: Math. Phys. Sc. **299**, No. 1456, (1967) [in *Nonlinear Theory of Wave Propagation* (Mir, Moscow, 1979)].
13. E. Kamke, *Gewöhnliche Differentialgleichungen* (Academie, Leipzig, 1959; Nauka, Moscow, 1976).
14. I. S. Gradshteĭn and I. M. Ryzhik, *Table of Integrals, Series, and Products* (Nauka, Moscow, 1971; Academic, New York, 1980).
15. M. A. Averkiou and M. F. Hamilton, J. Acoust. Soc. Am. **102**, 2539 (1997).

Translated by M. Lyamshev

Acoustical Physics, Vol. 47, No. 6, 2001, pp. 649–653. Translated from Akusticheskiĭ Zhurnal, Vol. 47, No. 6, 2001, pp. 741–745.

Utilization of Double Scanning in Ultrasonic Testing to Improve the Quality of the Scatterer Images

E. G. Bazulin

Russian Scientific Centre Kurchatov Institute, OOO Nauchno-Proizvodstvennyĭ Tsentr Echo+, pl. Kurchatova 1, Moscow, 123182 Russia

e-mail: echo.ndt@g23.relcom.ru

Received December 18, 2000

Abstract—Derivation of a formula for double scanning, when a radiator and a receiver move independently along parallel straight lines, is presented. Advantages of this technique are discussed in comparison with the method of projection in the spectral space, which is also used for a coherent reconstruction of a scatterer image. The efficiency of the double scanning technique in suppressing the phantom images produced by transformed and rescattered pulses is demonstrated in a numerical experiment. © *2001 MAIK "Nauka/Interperiodica".*

Methods of ultrasonic flaw detection are widely used in various industries for nondestructive testing of equipment. The major shortcomings of the conventional methods of ultrasonic flaw detection are a low precision of the determination of defect size and the problem of defect classification. Moreover, a conventional testing does not guarantee the detection of the most dangerous defects like cracks because of the complex character of ultrasonic diffraction by them. This results in unjustified strict standards of testing that are adopted in various fields. Meanwhile, just the correct information on the type of a defect and its size and position determines the possibility of operation and the service life of an object under test. To obtain high-resolution images of scatterers, various systems incorporating a coherent processing of the measured echo-signals are used in industry. For example, the Avgur 4.2 system is used in Russia to test welds of pipelines at nuclear power stations [1], and the Masera system by the Technoatom company and the μ+ system by the Sonomatic company are used for testing critical parts abroad. Rather simple algorithms based on the solution of an inverse scalar problem of scattering in the Born approximation are used in such industrial systems to obtain the images of scatterers [2, 3]. The SAFT technique [4, 5] and the method of projection in the spectral space [6–8] are examples of such algorithms. The practical realization of the latter method is especially efficient owing to the high rate of image generation from a set of echo-signals measured in a combined mode, when both radiation and reception of ultrasonic pulses is performed by a single transducer.

The other side of the simplicity of the algorithms used is the fact that sometimes the images of scatterers have insufficiently high quality. The level of phantom images formed by rescattered pulses and pulses resulting from the transformation of the wave types in the process of scattering by inhomogeneities is sufficiently high. Moreover, it is not always possible to unambiguously determine the scatterer shape, since the image of only the part of its boundary is reconstructed that reflects the pulses detected later in the reception region. A separate scheme of echo-signal detection, when the radiator is stationary and the detector moves, is used to obtain additional information on the shape of a scatterer [3]. In another case, the radiator and the detector move synchronously along a receiving aperture [9]. In the first case, it is necessary for an emitted wave to be plane in order to reconstruct the scatterer images correctly. Unfortunately, this condition cannot be satisfied in the practice of ultrasonic testing. In the second case, the data processing is conducted not in the spectral space using the fast Fourier transform [4], but directly, and, therefore, it is rather time consuming. We also note that the increase in the signal-to-noise ratio achieved with the use of a coherent system of the Avgur 4.2 type for ultrasonic testing of austenitic materials is not large enough [10].

A scheme of ultrasonic testing and processing of measured echo-signals was proposed [11] with a radiator and a receiver moving independently along parallel straight lines; in this case, it is not necessary that the radiated field be a plane-wave one. If the lines of motion of the radiator and receiver are located on the same side of the region where the scatterers are located (Fig. 1), a reflection scheme is realized that is characteristic of ultrasonic testing. If they are positioned on different sides (the dashed line in Fig. 1), a transmission scheme is realized that is characteristic of tomography. Such a mode of echo-signal detection that is equivalent to multiply repeated measurements in the separate scheme we will call the mode of double scanning. Its application can improve the quality of the reconstructed image on account of a decrease in the amplitude of the

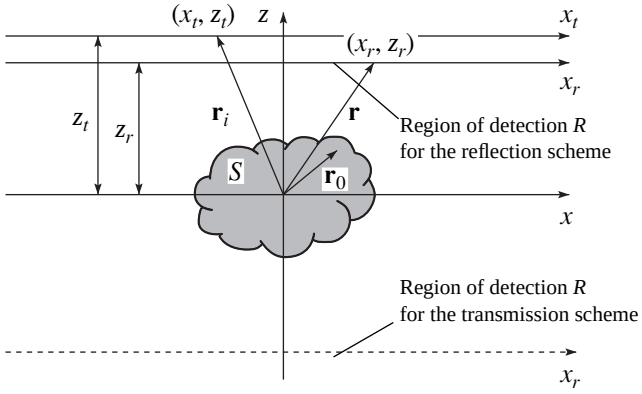

Fig. 1. Scheme of the experiment in the double scanning mode: measurement of the scattered field by using a radiator and a receiver moving along a line independently of each other.

phantom images produced by transformed and rescattered pulses, because their coherent accumulation does not occur in contrast to the singly reflected pulses [3]. It is possible to additionally increase the signal-to-noise ratio in materials with a well-defined structure, where the principal background noise is produced just by the rescattered pulses. From the algorithmic point of view, this approach is very convenient for a computer realization, because it ideally suits the principles of spectral projection and the technique of the fast Fourier transform and does not need plane incident waves. Considerable excessive information and an increase in the time of echo-signal detection can be considered disadvantages of the double scanning technique.

Further, we will discuss the derivation of a formula for double scanning, when a radiator and a receiver move independently along parallel straight lines. Let us consider its advantages and disadvantages in comparison with the technique of projection in the spectral space that is also used in the case of coherent reconstruction of scatterer images. The efficiency of the application of the double scanning technique for the suppression of the phantom images caused by the transformed and rescattered pulses is demonstrated numerically.

As is well known, the solution of the problem of diffraction tomography in the Born approximation in the case of the radiation at a single frequency $k_0 = \frac{2\pi}{\lambda_0}$, where λ_0 is the wavelength at the frequency f_0 in a medium with the sound velocity c, is reduced to the solution of the following equation:

$$\Psi_S(\mathbf{r}) = \iint_S \xi(\mathbf{r}_0)\Psi_i(\mathbf{r}_0)g(\mathbf{r}/\mathbf{r}_0)\mathbf{r}_0 d\mathbf{r}_0,$$

where $\Psi_S(\mathbf{r})$ is the scattered field, $\Psi_i(\mathbf{r})$ is the irradiation field, $g(\mathbf{r}/\mathbf{r}_0)$ is the Green function, $\xi(\mathbf{r}_0)$ is the function characterizing the refractive inhomogeneity of the medium, and S is the region of scatterers.

Let us consider a particular two-dimensional case when the line x_t (the line of radiator motion) is at the distance z_t from the origin of an absolute coordinate system and the line x_r (the line of receiver motion) is at the distance z_r from the center of the absolute coordinate system, xz (Fig. 1). The scattered field is described in the Born approximation by the expression

$$\Psi_S(\mathbf{r}) = \frac{i}{4}\iint_S \xi(\mathbf{r}_0)\Psi_i(\mathbf{r}_0)H_0(k_0|\mathbf{r} - \mathbf{r}_0|)d\mathbf{r}_0,$$

where $H_0(k_0|\mathbf{r} - \mathbf{r}_0|)$ is the zero-order Hankel function. Let $\Psi_S(\mathbf{r}; x_t, z_t)$ be the scattered field and $\Psi_i(\mathbf{r}_0; x_t, z_t)$ be the irradiation field at the point $\mathbf{r}_0 = (x, z) \in S$ at the moment when the radiator is located at the point (x_t, z_t). At $x_t = 0$, the incident field $\Psi_i(\mathbf{r}_t; 0, z_t)$ on the radiation line can be represented in the form

$$\Psi_i(\mathbf{r}_t; 0, z_t) = \frac{1}{2\pi}\int_{-\infty}^{\infty} A_t(k_x; 0, z_t)\exp(i\mathbf{k}\mathbf{r}_t)dk_x,$$

where $\mathbf{k} = (k_x, k_z)$, $k_z = \sqrt{k_0^2 - k_x^2}$ is the wave vector, and $A_t(k_x; 0, z_t)$ is the function representing the complex amplitude of the angular spectrum of the incident field. This function is the Fourier transform of the incident field on the line z_t:

$$A_t(k_x; 0, z_t) = \frac{1}{2\pi}\int_{-\infty}^{\infty} \Psi_i(x; 0, z_t)\exp(-ik_x x)dx.$$

If the radiator is positioned at another point x_t of the radiation line z_t, the angular spectrum of the incident field $\Psi_i(x; x_t, z_t)$ has the form

$$A_t(k_x; x_t, z_t) = \frac{1}{2\pi}\int_{-\infty}^{\infty} \Psi_i(x; x_t, z_t)\exp(-ik_x x)dx.$$

From the equality $\Psi_i(z; x_t, z_t) = \Psi_i(x - x_t; 0, z_t)$, it follows that

$$A_t(k_x; x_t, z_t) = A_t(k_x; 0, z_t)\exp(-ik_x x_t).$$

The field from the radiation line can be recalculated to the origin of the xz absolute coordinate system, which allows us to write down the last formula in the form

$$A_t(k_x; x_t, z_t) = A_t(k_x; 0, z_t)\exp(-ik_x x_t + i\sqrt{k_0^2 - k_x^2}z_t).$$

Using it, we can represent the incident field $\Psi_i(\mathbf{r}_0; x_t)$ in the form

$$\Psi_i(\mathbf{r}_0; x_t, z_t) = \frac{1}{2\pi}\int_{-\infty}^{\infty} A_t(k_x)$$

$$\times \exp(i\sqrt{k_0^2 - k_x^2}z_t)\exp(-ik_x x_t)\exp(i\mathbf{k}\mathbf{r}_0)dk_x,$$

where $A_t(k_x) \equiv A_t(k_x; 0, z_t)$.

The Green function for a free space at $|\mathbf{r}| > |\mathbf{r}_0|$ can be expanded in plane waves

$$H_0(k_0|\mathbf{r}-\mathbf{r}_0|) = \frac{1}{2\pi}\int_{-\infty}^{\infty}\frac{\exp(i\mathbf{\Lambda}(\mathbf{r}-\mathbf{r}_0))}{\beta}d\alpha,$$

where $\mathbf{\Lambda}$ is the wave vector of the scattered field, $\mathbf{\Lambda} = (\alpha, \beta)$, $\beta = \sqrt{k_0^2-\alpha^2}$, and $\Psi_S(x_r, z_r; x_t)$. Let the scattered field be

$$\Psi_S(x_r, z_r; x_t) = \frac{i}{4(2\pi)^2}\iint_S\int_{-\infty}^{\infty}\int_{-\infty}^{\infty}\xi(\mathbf{r}_0)A_t(k_x)$$
$$\times\exp(i\sqrt{k_0^2-k_x^2}z_t)\exp(-ik_x x_t)\exp(i\mathbf{k}\mathbf{r}_0)$$
$$\times\frac{\exp(i\mathbf{\Lambda}(\mathbf{r}-\mathbf{r}_0))}{\sqrt{k_0^2-\alpha^2}}dk_x d\alpha d\mathbf{r}_0,$$

where $\mathbf{r}_0 = (x, z) \in S$ is a point belonging to the scatterer region and $\mathbf{r} = (x_r, z_r) \in R$ is a point belonging to the detection region of the scattered field. Ignoring the constant factor, after the transformation of the integrand, we obtain the following expression for calculating the incident field on the detection line:

$$\Psi_S(x_r, x_t)$$
$$= \int_{-\infty}^{\infty}\int_{-\infty}^{\infty}A_t(k_x)\frac{\exp(i\sqrt{k_0^2-k_x^2}z_t + i\sqrt{k_0^2-\alpha^2}z_r)}{\sqrt{k_0^2-\alpha^2}}$$
$$\times\left\{\iint_S\xi(\mathbf{r}_0)\exp(i(\mathbf{k}-\mathbf{\Lambda})\mathbf{r}_0)d\mathbf{r}_0\right\}$$
$$\times\exp(-ik_x x_t + i\alpha x_r)dk_x d\alpha.$$

Thus, we obtained a basic expression that provides an opportunity to determine the relation through the spectral space between the measured field $\Psi_S(x_r, x_t)$ and the function $\xi(\mathbf{r}_0)$ characterizing the scatterers. If we perform its two-dimensional Fourier transformation with respect to x_r and x_t, we obtain the expression

$$\tilde{\Psi}_S(\alpha, k_x) = A_t(k_x)\frac{\exp(i\sqrt{k_0^2-k_x^2}z_t + i\sqrt{k_0^2-\alpha^2}z_r)}{\sqrt{k_0^2-\alpha^2}}$$
$$\times\left\{\iint_S\xi(\mathbf{r}_0)\exp(i(\mathbf{k}-\mathbf{\Lambda})\mathbf{r}_0)d\mathbf{r}_0\right\},$$

where

$$\tilde{\Psi}_S(\alpha, k_x) = \int_{-\infty}^{\infty}\int_{-\infty}^{\infty}\Psi_S(x_r, -x_t)\exp(-ik_x x_t - i\alpha x_r)dx_r dx_t.$$

Thus, the algorithm for generating the scatterer images consists of the following steps.

(1) The scattered field $\Psi_S(x_r, x_t)$ is measured in the double scanning mode.

(2) Then, its two-dimensional spectrum $\tilde{\Psi}_S(\alpha, k_x)$ is determined.

(3) After that, the function $\tilde{\Psi}_S(\alpha, k_x)$ is divided by $A_t(k_x)\dfrac{\exp(i\sqrt{k_0^2-k_x^2}z_t + i\sqrt{k_0^2-\alpha^2}z_r)}{\sqrt{k_0^2-\alpha^2}}$ for correcting the phase relationships. It should be noted that the function $A_t(k_x)$ is identical to a reference hologram. The technique of application and measurement of this hologram is considered in [12]. If one does not intend to additionallly increase the resolution, it is possible to assume that $A_t(k_x) = 1$. A characteristic case in the practice of ultrasonic nondestructive testing is when the radiation line and the detection line of the scattered field coincide, i.e., $x_r = x_t = d$.

(4) The projection in the spectral space is obtained in the same way as in the scheme with a fixed detection line of the scattered field and a plane sound wave insonifying the scattering region at various angles. The gray areas in Figs. 2 and 3 indicate the regions of the spectral space, the information on which can be obtained using ideal point transducers operating by the transmission and reflection schemes (Figs. 2 and 3, respectively). One can see that the utilization of even a single irradiation frequency provides an opportunity to obtain the information on the spectrum of the function $\xi(\mathbf{r}_0)$ in a rather wide region and, therefore, to obtain an image of a rather high quality. The application of a multifrequency version of the double scanning technique provides an opportunity to considerably extend the range of spatial frequencies, where the spectrum of the function $\xi(\mathbf{r}_0)$ is known, and to increase the quality of the reconstructed images of scatterers.

A numerical experiment and the reconstruction of defect images in the double scanning mode was conducted using the software of a coherent ultrasonic defectoscope of the Avgur 4.2 series developed and manufactured by the Echo+ Research and Production Center. Four point scatterers with the coordinates (–4; 0), (0; 0), (3; 0), and (5; 0) mm in an absolute coordinate system were used as a model. The detection and radiation lines coincided and were located at a distance of 15 mm from the origin of the absolute coordinate system, i.e., the reflection scheme of detection was considered. The fourfold rescattering and wave transformation at the point scatterers were taken into account in calculating the echo-signals. To make the situation approach reality, it was assumed that the opening half-angle of a direct transducer was 40°, its resonance frequency was 2.5 MHz, and the pulse length was equal to 1 μs. It was assumed that the transducer emitted a transverse wave. The spatial aperture, along which the transducer moved, started from the point –25.6 mm and consisted of 256 samples with the interval 0.2 mm; the time

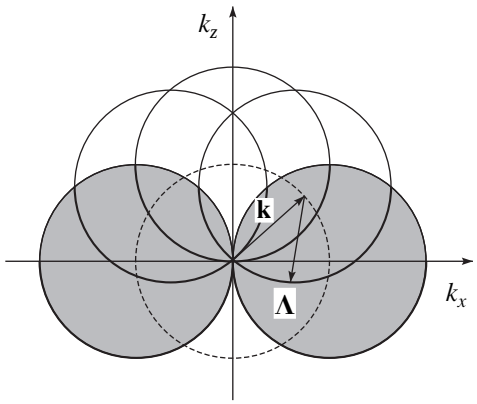

Fig. 2. Data structure in the spectral space for the transmission scheme in the double scanning mode.

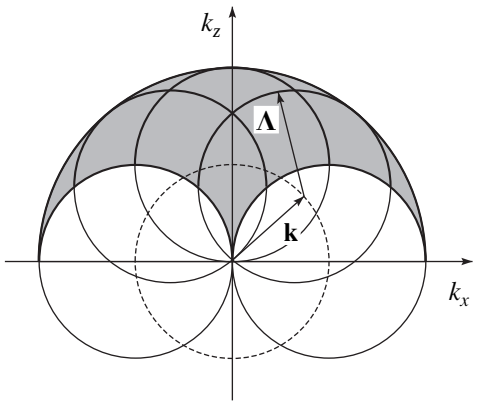

Fig. 3. Data structure in the spectral space for the reflection scheme in the double scanning mode.

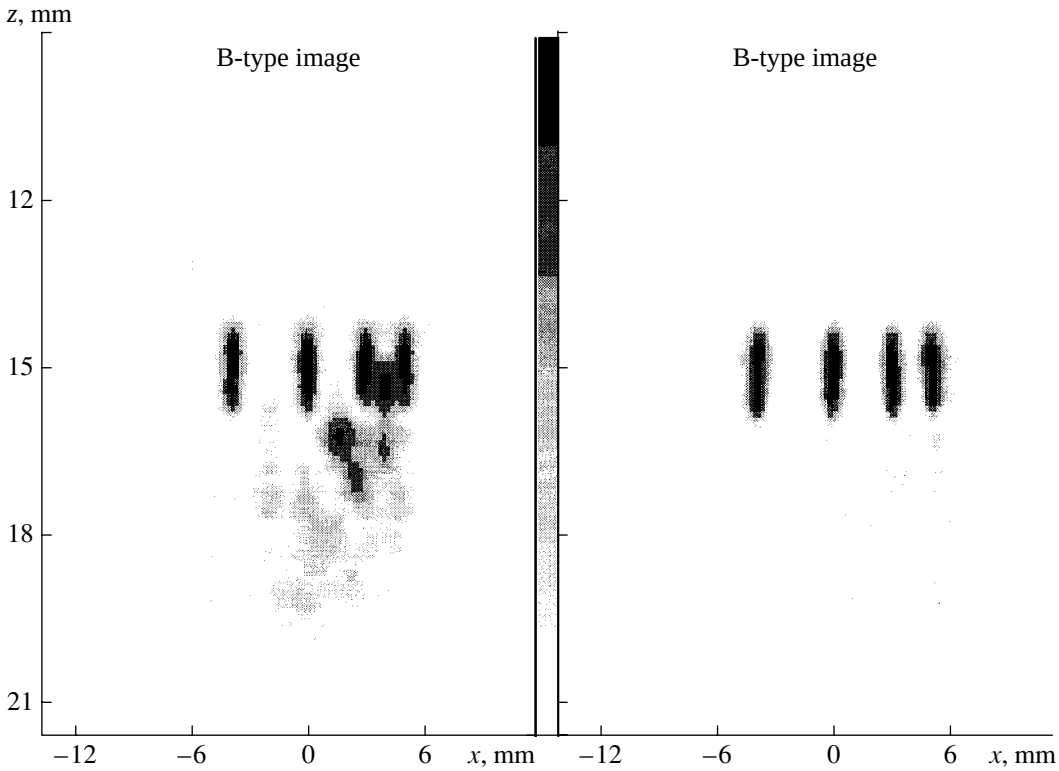

Fig. 4. Images of four point scatterers: the method of projection in the spectral space (left) and the double scanning technique (right). Fourfold rescattering and wave transformation at the point scatterers were taken into account in the calculations.

aperture started from 6 μs and contained 256 samples measured at 0.05 μs intervals. The transducer coordinates changed 64 times at a step of 0.4 mm, starting from the point 12.8 mm.

An image obtained by the method of projection in the spectral space with the use of echo-signals measured in a combined mode is shown in the left part of Fig. 4. Phantom flashes with the amplitude reaching 100% of the amplitude of the direct scatterer images can be seen clearly together with the direct images of the four point scatterers. An image obtained using the echo-signals measured in the double scanning mode is given in the right part of Fig. 4. One can see that the phantom flashes produced by the echo-signals that were transformed and rescattered by the point inhomogeneities decreased in amplitude. This result can be explained by the fact that the double scanning technique has a very important feature. Despite the fact that this technique of generating the scatterer images is based on the Born approximation, which does not take into account multiple rescattering, the phantom flashes

formed by the rescattered echo-signals are present in the reconstructed image. This follows from the property that measurements in the double scanning mode are equivalent to a multiple repetition of the detection of the scattered field in a separate mode, and the combined processing of their data leads to the situation when the flashes corresponding to singly reflected echo-pulses are added in phase and their amplitude increases by a factor of N_{trm}, where $N_{trm} = 64$ is the number of the radiator positions. The phantom images generated by transformed and rescattered echo-signals are not in phase, and their combined amplitude increases by a factor of $\sqrt{N_{trm}} = 8$ [3].

Thus, we considered the possibility of using the double scanning technique for improving the quality of the scatterer images in ultrasonic flaw detection. By a numerical experiment, it was demonstrated that, in the reconstruction of the scatterer images, the phantom flashes produced by the echo-signals transformed and rescattered by inhomogeneities are considerably reduced in amplitude. This property of the double scanning technique can be useful for the practice of ultrasonic testing in the analysis of coherent images of defects.

REFERENCES

1. V. G. Badalyan, A. Kh. Vopilkin, V. V. Grebennikov, *et al.*, in *XV Russian Scientific and Technical Conference on Nondestructive Control and Diagnostics* (Moscow, 1999).
2. V. A. Burov, A. A. Goryunov, A. V. Saskovets, and T. A. Tikhonova, Akust. Zh. **32**, 433 (1986) [Sov. Phys. Acoust. **32**, 273 (1986)].
3. A. A. Goryunov and A. V. Saskovets, *Inverse Problems of Scattering in Acoustics* (Mosk. Gos. Univ., Moscow, 1989).
4. T. E. Hall, S. R. Doctor, L. D. Reid, *et al.*, Acoust. Imaging **15**, 253 (1987).
5. A. Erhard, B. Lucht, E. Schulz, *et al.*, J. Nondestr. Test. Ultrason. **5** (9) (2000).
6. K. Mayer, R. Markelein, K. J. Langenberg, and T. Kreutter, Ultrasonics **28**, 241 (1990).
7. V. G. Badalyan and E. G. Bazulin, Akust. Zh. **34**, 222 (1988) [Sov. Phys. Acoust. **34**, 132 (1988)].
8. F. Takahashi, Y. Nagashima, I. Tanaka, *et al.*, in *First International Conference on NDE in Relation to Structural Integrity for Nuclear and Pressurised Components* (Amsterdam, Netherlands, 1998).
9. M. V. Grigor'ev, V. V. Grebennikov, and A. K. Gurvich, Defektoskopiya, No. 1, 8 (1978).
10. V. G. Badalyan, A. Kh. Vopilkin, V. V. Grebennikov, and D. V. Grebennikov, Kontrol Diagnost., No. 9(27), 29 (2000).
11. D. Nahamoto, B. X. Pan, and A. S. Kak, IEEE Trans. Sonics Ultrason. **SU-31**, 218 (1984).
12. V. G. Badalyan and E. G. Bazulin, Defektoskopiya, No. 11, 76 (1987).

Translated by M. Lyamshev

Acoustical Physics, Vol. 47, No. 6, 2001, pp. 654–658. Translated from Akusticheskiĭ Zhurnal, Vol. 47, No. 6, 2001, pp. 746–750.

Excitation of a Tube Wave in a Borehole by an External Isotropic Point Source

P. M. Bokov and A. M. Ionov

Moscow State Engineering Physics Institute (Technical University), Kashirskoe sh. 31, Moscow, 115409 Russia

e-mail: aionov@hotmail.com

Received October 24, 2000

Abstract—The excitation of a tube wave in an infinite fluid-filled borehole by an external isotropic point source is considered. The solution to the problem is obtained in the form of a double integral with respect to the ray parameter (slowness) and frequency. The integral with respect to the slowness is transformed to a contour integral in the complex slowness plane and then reduced to the integral over the edges of the cut of the vertical slowness function and the semiresidues at the poles. An asymptotic expression for the wave field in the borehole is obtained with allowance for the radiation condition at infinity. It is shown that, when a longitudinal spherical wave is incident on the borehole, only one low-frequency Stoneley wave is excited and not two, as was assumed earlier [1]. © *2001 MAIK "Nauka/Interperiodica".*

The dynamic and kinematic characteristics of tube waves in a borehole provide information on the properties of the geological formations surrounding the borehole. The tube wave field carries information on all exchange waves that appear at the borehole interfaces. There exist a great number of publications concerned with the theory of the tube wave propagation in fluid-filled boreholes [2–7]. In particular, some of them [2, 3] consider the modeling of tube waves in relation to the borehole and cross-well sounding. Recently, much attention has been given to the propagation of tube waves in the boreholes embedded in anisotropic geological formations [5, 6] and in irregular boreholes [4].

If a borehole is driven by external seismic sources, the tube waves caused by the incident bulk and guided waves and the borehole eigenmodes (the so-called Stoneley waves) are excited in the borehole fluid. In the limit of a long-wave excitation of the fluid by an external source, only the lowest mode can be excited [7]. In Russian literature, this mode is referred to as the "hydrowave" [8].

The problem on the excitation of tube waves in an infinite fluid-filled borehole by an external isotropic point source was first solved in [1]. It was shown that, in contrast to the incidence of a plane longitudinal wave, a spherical *P*-wave propagating in the surrounding medium generates not only a tube *P*-wave in the borehole, but also two Stoneley waves travelling along the borehole in opposite directions. However, the expression obtained in [1] for the Stoneley wave field does not satisfy the radiation condition at infinity, because one of the poles makes a parasitic contribution to the solution. The goal of this paper is to remedy this flaw. As will be shown below, a longitudinal spherical wave incident on the borehole generates a single Stoneley wave rather than two Stoneley waves.

In the long-wave approximation (which means that the wavelength of the seismic field far exceeds the borehole diameter), the equation describing the Stoneley wave excitation and propagation in a borehole driven by an external seismic source has the form [7, 9]

$$\frac{\partial^2 P}{\partial z^2} - \frac{1}{c_{tw}^2}\frac{\partial^2 P}{\partial t^2} = \frac{2\rho_f}{E}\frac{\partial^2 \sigma_{eff}^{ext}}{\partial t^2}, \tag{1}$$

where c_{tw} is the low-frequency limit of the Stoneley wave velocity at the interface between the fluid and the surrounding formation, ρ_f is the density of the borehole fluid, E is the Young modulus of the surrounding elastic medium, and σ_{eff}^{ext} is the effective stress caused by the isotropic point source.

To solve Eq. (1), we perform the Fourier transformation with respect to time t and to the vertical coordinate z. As a result, we obtain a formal solution for the Fourier-transform of the pressure

$$\bar{P}(r, k, \omega) = \frac{2\rho_f}{E}\frac{\omega^2 \sigma_{eff}^{ext}(r, k, \omega)}{k^2 - \omega^2/c_{tw}^2}. \tag{2}$$

The effective stress σ_{eff}^{ext} produced by the seismic isotropic point source characterized by the source function $\Psi_s(t)$ at the borehole axis can be represented as the Sommerfeld expansion in cylindrical waves [10]

$$\sigma_{eff}^{ext}(r, z, \omega) = i\omega^3 \Psi_s(\omega) E \times \int_0^\infty \frac{p\,dp}{\zeta}\left[p^2 + \frac{1}{2\beta^2} - \frac{1}{\alpha^2}\right] J_0(\omega p r)\exp(i\omega\zeta|z|), \tag{3}$$

where the integration variable p can be considered as the slowness parameter [11]; $\zeta = \sqrt{1/\alpha^2 - p^2}$, $J_0(x)$ is the zero-order Bessel function; and α and β are the velocities of the transverse and longitudinal waves in the surrounding elastic medium, respectively.

Performing the Fourier transformation with respect to the vertical coordinate z in Eq. (3), we obtain the following expression for $\bar{\sigma}_{eff}^{ext}(r, k, \omega)$:

$$\sigma_{eff}^{ext}(r, k, \omega) = 2\omega^4\Psi_s(\omega)E\int_0^\infty \frac{pdp}{k^2 - \omega^2\zeta^2}\left[p^2 + \frac{1}{2\beta^2} - \frac{1}{\alpha^2}\right]J_0(\omega pr). \quad (4)$$

Substituting Eq. (4) into solution (2), we obtain the pressure field excited by an isotropic point source in the fluid-filled borehole in the form of a double integral:

$$\bar{P}(r, z, \omega) = \frac{2}{\pi}\rho_f\omega^6\Psi_s(\omega)\int_{-\infty}^{+\infty}\frac{\exp(ikz)dk}{(k^2 - \omega^2/c_{tw}^2)(k^2 - \omega^2\zeta^2)} \times \int_0^\infty pdp\left[p^2 + \frac{1}{2\beta^2} - \frac{1}{\alpha^2}\right]J_0(\omega pr). \quad (5)$$

Note that solution (5) is an even function of the vertical coordinate z, which follows from the symmetry of the problem. At this step, solution (5) is formal, because the rules of bypassing the poles are not yet determined.

We will use the residue theorem to calculate the integral in Eq. (5) with respect to the variable k,

$$I = \int_{-\infty}^{+\infty}\frac{\exp(ikz)dk}{(k^2 - \omega^2/c_{tw}^2)(k^2 - \omega^2\zeta^2)}.$$

To move the poles away from the real axis, we apply the limiting absorption principle [12]. As can be easily seen, for $\omega > 0$, this principle moves the poles $k_1 = +\omega\zeta$ and $k_2 = +\omega/c_{tw}$ to the upper half-plane $\mathrm{Im}k > 0$. Simultaneously, the poles $k_3 = -\omega\zeta$ and $k_4 = -\omega/c_{tw}$ are shifted to the lower half-plane $\mathrm{Im}k < 0$ for $\omega > 0$. Closing the integration contour in the upper half-plane $\mathrm{Im}k > 0$ for $z > 0$ and the lower half-plane $\mathrm{Im}k < 0$ for $z < 0$, we obtain the following result for the integral I:

$$I = \frac{i\pi}{\omega^3}\frac{1}{1/c_{tw}^2 - \zeta^2} \times \{c_{tw}\exp(i\omega|z|/c_{tw}) - \zeta^{-1}\exp(i\omega\zeta|z|)\}. \quad (6)$$

Figure 1 shows the integration contour and the pole positions for $z < 0$. Using the relationships $J_0(x) = \frac{1}{2}[H_0^{(1)}(x) + H_0^{(2)}(x)]$ and $H_0^{(2)}(-x) = -H_0^{(1)}(x)$, where $H_0^{(1,2)}(x)$ are the zero-order Hankel functions of the first and second kinds, we represent the desired solution

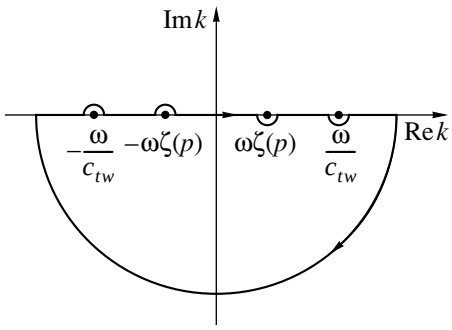

Fig. 1. Integration contour in the complex plane of the variable k and the rule of bypassing the poles for $z < 0$.

in the form of an integral with respect to the slowness p over the whole real axis:

$$\bar{P}(r, z, \omega) = i\omega^3\rho_f\Psi_s(\omega)\int_{-\infty}^{\infty}\frac{pdp}{1/c_{tw}^2 - \zeta^2}\left(p^2 + \frac{1}{2\beta^2} - \frac{1}{\alpha^2}\right) \times \{c_{tw}\exp(i\omega|z|/c_{tw}) - \zeta^{-1}\exp(i\omega\zeta|z|)\}H_0^{(1)}(\omega pr) = I_1 + I_2. \quad (7)$$

One can see that solution (7) consists of two terms. The first term I_1 allows an exact calculation in the complex plane p by using the residue theorem. Taking into account the asymptotic behavior of the Hankel function for large arguments $H_0^{(1)}(w) \longrightarrow \sqrt{2/\pi w}\exp(iw - i\pi/4)$, we close the integration contour in the upper half-plane $\mathrm{Im}p > 0$, where the integrand decreases according to an exponential law: $\exp(i\omega pr) = \exp(i\omega r(\mathrm{Re}p + i\mathrm{Im}p)) \sim \exp(-\omega r\mathrm{Im}p)$. In this case, the first integral is reduced to the residue at the pole $p_1 = +i\sqrt{c_{tw}^2 - \alpha^{-2}}$. As a result, we obtain

$$\bar{P}^{\mathrm{Res}}(r, z, \omega) = 2i\omega^3\Psi_s(\omega)\rho_f c_{tw} \times \left(\frac{1}{2\beta^2} - \frac{1}{\alpha^2}\right)K_0(\omega\sqrt{c_{tw}^{-2} - \alpha^{-2}}r)\exp(i\omega|z|/c_{tw}), \quad (8)$$

where the expression $H_0^{(1)}(ix) = 2(\pi i)K_0(x)$ is used and $K_0(x)$ is the zero-order Macdonald function.

The rearrangement of the second term I_2 in Eq. (7) appears somewhat more complicated. In this case, to perform the rearrangement in the complex plane of the integration variable p, it is necessary for the integrand to simultaneously satisfy two conditions: $\mathrm{Im}p > 0$ (the upper half-plane) and $\mathrm{Im}\zeta > 0$ (the proper cut in the complex plane p). The cut should be as follows. According to the limiting absorption principle, in the expression $\zeta = \sqrt{\alpha^{-2} - p^2}$, we must replace $1/\alpha$ by $1/\alpha + i\varepsilon$ ($\varepsilon > 0$). Then, we obtain

$$(\mathrm{Re}\zeta + i\mathrm{Im}\zeta)^2 = (\alpha^{-1} + i\varepsilon)^2(\mathrm{Re}p + i\mathrm{Im}p)^2. \quad (9)$$

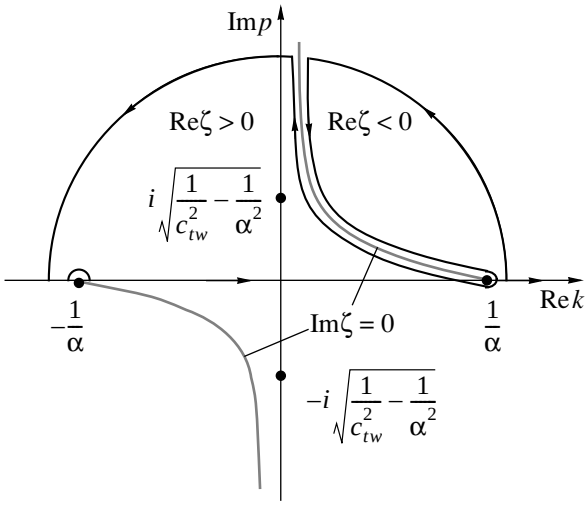

Fig. 2. Integration contour in the complex plane of the slowness (ray) parameter p and the positions of the poles and cuts.

Separating Eq. (9) into the real and imaginary parts, we arrive at the system of equations

$$\begin{cases} (\mathrm{Re}\zeta)^2 - (\mathrm{Im}\zeta)^2 = \alpha^{-2} - \varepsilon^2 - (\mathrm{Re}p)^2 + (\mathrm{Im}p)^2 \\ \mathrm{Re}\zeta\mathrm{Im}\zeta = \varepsilon/\alpha - \mathrm{Re}p\mathrm{Im}p. \end{cases} \quad (10)$$

Since the cut is determined by the condition $\mathrm{Im}\zeta = 0$, the second equation of system (10) determines a hyperbola for the cut in the complex plane p:

$$\mathrm{Re}p\mathrm{Im}p = \varepsilon/\alpha. \quad (11)$$

Note that, for $\varepsilon \longrightarrow 0$, the cut consists of the positive imaginary half-axis $\mathrm{Im}p > 0$ ($\mathrm{Re}p = 0$) and the segment of the real axis $0 < \mathrm{Re}p < 1/\alpha$ ($\mathrm{Im}p = 0$). Additionally, we note that the passage from the upper edge of the cut to the lower edge is accompanied by a jump in the function $\mathrm{Re}\zeta(p)$. Thus, the integration path of the second term I_2 along the whole real axis can be transformed to the integration contour in the complex plane of the variable p shown in Fig. 2. It consists of the real axis, the upper and lower edges of the cut, and the semicircle of an infinite radius in the upper half-plane. Inside this contour, the integrand is an analytical function of the complex variable p everywhere excluding the simple pole at the point $p_1 = +i\sqrt{c_{tw}^{-2} - \alpha^{-2}}$.

Taking this fact into account, we use the analytical function theorem to represent the integral over the closed contour shown in Fig. 2 in the form

$$I_2 + \int_{cut} dp\ldots + \int_{\cap} dp\ldots = 2\pi i\mathrm{Res}(p_1 = i\sqrt{c_{tw}^{-2} - \alpha^{-2}}), \quad (12)$$

where $\int_{cut} dp\ldots$ is the integral along the cut edges, $\int_{\cap} dp\ldots$ is the integral along the semicircle of an infinite radius in the upper half-plane, and $\mathrm{Res}(p_1 = i\sqrt{c_{tw}^{-2} - \alpha^{-2}})$ is the residue of the integrand at the simple pole p_1 located in the upper half-plane. To avoid misunderstanding in what follows, we emphasize that the integrand in the contour integrals appearing in Eq. (12) is determined solely by the second term in Eq. (7). Taking into account the fact that $\int_{\cap} dp\ldots = 0$ and

$$2\pi i\mathrm{Res}(p_1) = -2i\omega^3\Psi_s(\omega)\rho_f c_{tw}\left(\frac{1}{2\beta^2} - \frac{1}{\alpha^2}\right)K_0 \times (\omega\sqrt{c_{tw}^{-2} - \alpha^{-2}}r)\exp(i\omega|z|/c_{tw}) = \bar{P}^{\mathrm{Res}}(r, z, \omega) = -I_1,$$

we obtain that solution (7) is representable as the integral over the cut

$$\bar{P}(r, z, \omega) = I^{(tot)} = I_1 + I_2 = -\int_{cut} dp\ldots. \quad (13)$$

To rearrange the integral over the cut, we replace the integration variable p with ζ. Taking into consideration that $pdp = -\zeta d\zeta$, we obtain

$$\bar{P}(r, z, \omega) = -i\omega^3\Psi_s(\omega)\rho_f \times \int_{-\infty}^{+\infty} \frac{d\zeta}{c_{tw}^{-2} - \zeta^2}\left(\frac{1}{2\beta^2} - \zeta^2\right)H_0^{(1)}(\omega\sqrt{1/\alpha^2 - \zeta^2}r)\exp(i\omega\zeta|z|). \quad (14)$$

One can easily see that the integrand in Eq. (14) contains poles on the integration path. Representing the denominator of the integrand in the form

$$\frac{1}{1/c_{tw}^2 - \zeta^2} = \frac{c_{tw}}{2}\left(\frac{1}{\zeta + 1/c_{tw}} - \frac{1}{\zeta - 1/c_{tw}}\right),$$

applying the limiting absorption principle, and using the Sokhotsky formulas [12]

$$\frac{1}{\zeta + 1/c_{tw}} \longrightarrow \frac{1}{\zeta + 1/c_{tw} + i\varepsilon} \longrightarrow \mathrm{v.p.}\frac{1}{\zeta + 1/c_{tw}} - i\pi\delta(\zeta + 1/c_{tw});$$

$$\frac{1}{\zeta - 1/c_{tw}} \longrightarrow \frac{1}{\zeta - 1/c_{tw} - i\varepsilon} \longrightarrow \mathrm{v.p.}\frac{1}{\zeta - 1/c_{tw}} + i\pi\delta(\zeta - 1/c_{tw});$$

where the notation v.p. means the Cauchy principal value and $\delta(x)$ is the delta-function, we obtain (after simple rearrangements) the representation of the

desired solution as the sum of an integral principal value and a pole contribution:

$$\bar{P}(r, z, \omega) = -i\omega^3\Psi_s(\omega)\rho_f \text{v.p.}\int_{-\infty}^{+\infty}\frac{d\zeta}{c_{tw}^{-2}-\zeta^2}\left(\frac{1}{2\beta^2}-\zeta^2\right)$$
$$\times H_0^{(1)}(\omega\sqrt{1/\alpha^2-\zeta^2}r)\exp(i\omega\zeta|z|)$$
$$+ i\omega^3\Psi_s(\omega)\rho_f c_{tw}\left(\frac{1}{2\beta^2}-\frac{1}{c_{tw}^2}\right) \quad (15)$$
$$\times K_0(\omega\sqrt{c_{tw}^{-2}-\alpha^{-2}}r)[\exp(i\omega z/c_{tw})+\exp(-i\omega z/c_{tw})].$$

As can be easily seen from Eq. (15), the principal value of the integral includes pole singularities. This integral cannot be calculated exactly; however, it allows an asymptotic evaluation using appropriate methods [13]. As will be shown in what follows, the asymptotic expression for this integral consists of the contributions formed near the poles and at the stationary point. The pole singularities produce additional contributions to the Stoneley wave field, while the stationary point contributes to the tube *P*-wave generated by the external dynamic field incident on the borehole.

The field of the tube *P*-wave can be found by an asymptotic calculation of the first term in Eq. (15) according to the method of stationary phase. Taking into account the asymptotic behavior of the Hankel function for large arguments, we obtain the following expression for the phase of the integrand:

$$\vartheta(\zeta) = i\omega(\zeta|z| + \sqrt{1/\alpha^2-\zeta^2}r). \quad (16)$$

The stationary point is the point where the first derivative of phase (16) vanishes, and it is equal to

$$\zeta_0(|z|/R) = \frac{1}{\alpha}\frac{|z|}{R} = \frac{\cos\gamma}{\alpha},$$

where $R=\sqrt{r^2+z^2}$ and $\cos\gamma=|z|/R$. Taking into account the fact that $\vartheta(\zeta_0)=i\omega R/\alpha$ and $\vartheta''(\zeta_0)=-i\omega\alpha R^3/r^2$, we obtain the following asymptotic expression for the field induced in the fluid-filled borehole by a longitudinal wave [1]:

$$\bar{P}^P(r, z, \omega) \approx -2i\omega^3\Psi_s(\omega)\rho_f$$
$$\times\frac{\exp(i\omega R/\alpha - i\pi/4)}{\sqrt{2\pi\omega r}}\frac{(1/2\beta^2-\zeta_0^2)}{(1/c_{tw}^2-\zeta_0^2)\sqrt{1/\alpha^2-\zeta_0^2}}$$
$$\times\int_{-\infty}^{+\infty}d\zeta\exp\left(-\frac{i\omega\alpha R^3}{2r^2}(\zeta-\zeta_0)^2\right)\longrightarrow -\omega^2\Psi_s(\omega)\rho_f \quad (17)$$
$$\times\frac{(1/\beta^2-2\cos^2\gamma/\alpha^2)\exp(i\omega R/\alpha)}{(1/c_{tw}^2-\cos^2\gamma/\alpha^2)}\frac{\exp(i\omega R/\alpha)}{R}.$$

We now turn to the asymptotic calculation of the contributions at the poles $\zeta=\pm 1/c_{tw}$ in the integral term of Eq. (15). Decomposing the denominator of the integrand into simple fractions and taking into account the relationship between the Hankel and Macdonald functions, we obtain the following expression after the corresponding substitutions $\zeta \pm 1/c_{tw} \longrightarrow x$ in integrals:

$$\text{v.p.}\int_{-\infty}^{+\infty}\frac{d\zeta}{c_{tw}^{-2}-\zeta^2}\left(\frac{1}{2\beta^2}-\zeta^2\right)H_0^{(1)}(\omega\sqrt{1/\alpha^2-\zeta^2}r)$$
$$\times\exp(i\omega\zeta|z|) = -\frac{ic_{tw}}{\pi}\left\{\text{v.p.}\int_{-\infty}^{+\infty}\frac{dx}{x}\left[\frac{1}{2\beta^2}-\left(x-\frac{1}{c_{tw}}\right)^2\right]\right.$$
$$\times K_0(\omega r\sqrt{(x-1/c_{tw})^2-1/\alpha^2}) \quad (18)$$
$$\times\exp(i\omega x|z|-i\omega|z|/c_{tw})$$
$$-\text{v.p.}\int_{-\infty}^{+\infty}\frac{dx}{x}\left[\frac{1}{2\beta^2}-\left(x+\frac{1}{c_{tw}}\right)^2\right]$$
$$\left.\times K_0(\omega r\sqrt{(x+1/c_{tw})^2-1/\alpha^2})\exp(i\omega x|z|-i\omega|z|/c_{tw})\right\}.$$

To determine the asymptotic contributions of the points near $x=0$ to integrals (18), we factor out of the integral sign the slowly varying functions. Since we have

$$\int_{-\infty}^{+\infty}\frac{dx}{x}\exp(i\gamma x) = i\pi\,\text{sgn}(\gamma),$$

where γ is the real parameter, we obtain the following asymptotic estimator for the pole contributions to the integral under consideration:

$$I_{pol}\longrightarrow i\omega^3\Psi_s(\omega)\rho_f c_{tw}\left(\frac{1}{2\beta^2}-\frac{1}{c_{tw}^2}\right)K_0 \quad (19)$$
$$\times(\omega\sqrt{c_{tw}^{-2}-\alpha^{-2}}r)[\exp(-i\omega|z|/c_{tw})-\exp(i\omega|z|/c_{tw})].$$

Combining results (19) and (17) and substituting them in Eq. (15) as an asymptotic estimator of the principal value of the integral, we obtain the final result for the tube wave field generated in a fluid-filled borehole by the isotropic point source:

$$\bar{P}(r, z, \omega) = -\omega^2\Psi_s(\omega)\rho_f\frac{(1/\beta^2-2\cos^2\gamma/\alpha^2)}{1/c_{tw}^2-\cos^2\gamma/\alpha^2}$$
$$\times\frac{\exp(i\omega R/\alpha)}{R}+2i\omega^3\Psi_s(\omega)\rho_f c_{tw}\left(\frac{1}{2\beta^2}-\frac{1}{c_{tw}^2}\right) \quad (20)$$
$$\times K_0(\omega\sqrt{c_{tw}^{-2}-\alpha^{-2}}r)\exp(i\omega|z|/c_{tw}).$$

The first term in Eq. (20) describes the tube *P*-wave, and the second term describes the Stoneley wave. This asymptotic estimator is applicable when the *P*-wave and the Stoneley wave are separated in space. In contrast to the result obtained earlier [1], which contained two Stoneley waves and violated the radiation condi-

tion, the result obtained above shows that only one Stoneley wave exists in the borehole, and it travels along the borehole in the upward and downward directions from the region where it is generated by the external action. Unlike the solution obtained in [1], solution (20) satisfies the radiation condition at infinity. Additionally, we note that asymptotic estimator (20) obtained for the field in the borehole can be derived immediately from representation (7).

Thus, in this paper, using the method of integral transformations, we solved the problem on the tube waves excited in a fluid-filled borehole by an external isotropic source. The integral with respect to the slowness (ray) parameter was transformed to a contour integral in the complex plane and then reduced to an integral over the edges of the cut of the vertical slowness function and the semi-residues at the poles.

The representation obtained for the solution to the problem under consideration allows an asymptotic solution in the form of the tube *P*-wave and the Stoneley wave traveling along the borehole in the upward and downward directions. This solution is shown to satisfy the radiation condition at infinity (the Sommerfeld condition), in contrast to the solution obtained in [1]. From the solution obtained above, it follows that only one Stoneley wave is generated and not two Stoneley waves.

The procedure developed in this paper for calculating the tube waves in a borehole appears quite useful in analyzing the dynamic field of pressure in a borehole driven by more complex external sources and, in particular, by a point force. In this case, the wave field in the borehole becomes much more complex, especially if the velocity of the shear waves in the formation is smaller than the low-frequency Stoneley wave velocity.

REFERENCES

1. A. M. Ionov and G. A. Maksimov, Akust. Zh. **45**, 354 (1999) [Acoust. Phys. **45**, 311 (1999)].
2. R. T. Coates, Geophys. Prospect. **46**, 153 (1998).
3. A. L. Kurkjian, R. T. Coates, J. E. White, and H. Schmidt, Geophysics **59**, 1053 (1994).
4. K. Tezuka, C. H. Cheng, and X. M. Tang, Geophysics **62**, 1047 (1997).
5. W. Dong and M. N. Toksöz, Geophysics **60**, 29 (1995).
6. W. Dong and M. N. Toksöz, Geophysics **60**, 748 (1995).
7. J. E. White, *Underground Sound. Application of Seismic Waves* (Elsevier, Amsterdam, 1983; Nedra, Moscow, 1986).
8. A. S. Ibatov and P. V. Krauklis, in *Problems of the Dynamic Theory of Seismic Wave Propagation* (Moscow, 1982), Issue 22, pp. 221–226.
9. A. M. Ionov, Fiz. Zemli, Nos. 7–8, 152 (1994).
10. A. M. Ionov and G. A. Maximov, Geophys. J. Int. **124** (3), 888 (1996).
11. K. Aki and P. G. Richards, *Quantitative Seismology: Theory and Methods* (Freeman, San Francisco, 1980; Mir, Moscow, 1983).
12. V. S. Vladimirov, *Equations of Mathematical Physics*, 4th ed. (Nauka, Moscow, 1981; Dekker, New York, 1971).
13. M. V. Fedoryuk, *Asymptotics: Integrals and Series* (Nauka, Moscow, 1987).

Translated by A. Vinogradov

Acoustical Physics, Vol. 47, No. 6, 2001, pp. 659–664. Translated from Akusticheskiĭ Zhurnal, Vol. 47, No. 6, 2001, pp. 751–756.

Relationship between the Amplitude and Phase of a Signal Scattered by a Point-Like Acoustic Inhomogeneity

V. A. Burov and S. A. Morozov

Moscow State University, Vorob'evy gory, Moscow, 119899 Russia

e-mail: burov@phys.msu.su

Received February 21, 2001

Abstract—Wave scattering by a point-like inhomogeneity, i.e., a strong inhomogeneity with infinitesimal dimensions, is described. This type of inhomogeneity model is used in investigating the point-spread functions of different algorithms and systems. Two approaches are used to derive the rigorous relationship between the amplitude and phase of a signal scattered by a point-like acoustic inhomogeneity. The first approach is based on a Marchenko-type equation. The second approach uses the scattering by a scatterer whose size decreases simultaneously with an increase in its contrast. It is shown that the retarded and advanced waves are scattered differently despite the relationship between the phases of the corresponding scattered waves. © *2001 MAIK "Nauka/Interperiodica".*

The concept of an infinitesimal but rather strong inhomogeneity is a natural and convenient idealization the use of which provides information on the point-spread functions of various algorithms and systems intended for reconstructing the internal structure of objects. However, closer consideration of this concept shows that it requires certain refinement and caution in its use.

It appears that the amplitude and phase of the secondary source formed by such a concentrated inhomogeneity cannot be chosen arbitrarily: the factor that we introduce in what follows to characterize the secondary source has a finite magnitude, and its phase uniquely determines its amplitude. Two approaches can be used to deduce this inference.

The first, more formal approach is related to the Marchenko-type relationship that governs the Green function for an inhomogeneous medium. The derivation of this relationship is fairly short, and we present it here following Budreck and Rose [1].

We assume that a finite region R containing an inhomogeneity of the phase velocity $c(\mathbf{r})$,

$$c(\mathbf{r}) = \begin{cases} c(\mathbf{r}), & \mathbf{r} \in R \\ c_0, & \mathbf{r} \notin R, \end{cases}$$

appears in a homogeneous infinite medium characterized by constant values of velocity and density. Closed smooth contours (surfaces, in the three-dimensional case) filled with sources and receivers enclose the scatterer, as is shown in the figure. For the sake of definiteness, we assume that the contour of receivers Ω_y is totally inside the region V_z bounded by the contour of sources Ω_z and outside the region R containing the inhomogeneity. (If Ω_y is outside V_z, the reasoning remains similar, though the final relationship has a somewhat different form. The only important point is that the region R lies inside the regions bounded by the contours Ω_z and Ω_y.)

For an inhomogeneous medium, we introduce a retarded Green function G^+ that satisfies the Sommerfeld radiation condition and an advanced Green function G^- that does not satisfy this condition. These functions satisfy the Helmholtz equations

$$\Delta_{\mathbf{r}} G^+(\omega, \mathbf{r}, \mathbf{y}) + \frac{\omega^2}{c^2(\mathbf{r})} G^+(\omega, \mathbf{r}, \mathbf{y}) = \delta(\mathbf{r} - \mathbf{y}), \quad \mathbf{y} \in \Omega_y, \tag{1}$$

$$\Delta_{\mathbf{r}} G^-(\omega, \mathbf{r}, \mathbf{x}) + \frac{\omega^2}{c^2(\mathbf{r})} G^-(\omega, \mathbf{r}, \mathbf{x}) = \delta(\mathbf{r} - \mathbf{x}), \quad \mathbf{x} \in R. \tag{2}$$

The difference between Eq. (1) multiplied by $G^-(\omega, \mathbf{r}, \mathbf{x})$ and Eq. (2) multiplied by $G^+(\omega, \mathbf{r}, \mathbf{y})$ does not involve

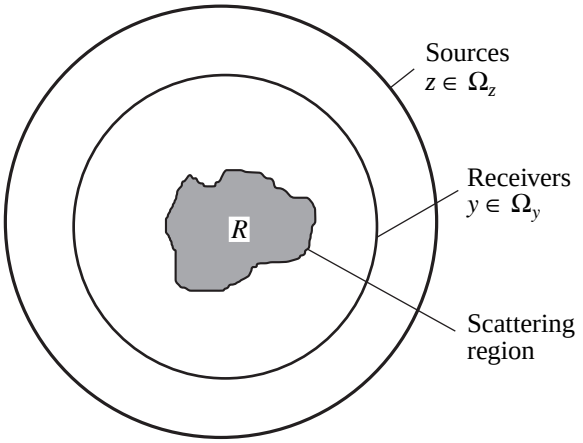

Geometry of the problem for the derivation of the Marchenko-type equation.

1063-7710/01/4706-0659$21.00 © 2001 MAIK "Nauka/Interperiodica"

the sound velocity $c(\mathbf{r})$. If we integrate the difference relationship with respect to $d\mathbf{r}$ over the region V_z and use the Gauss theorem to transform the integral over the region V_z to an integral along the contour Ω_z, we obtain a Marchenko-type equation

$$G^-(\omega, \mathbf{y}, \mathbf{x}) - G^+(\omega, \mathbf{x}, \mathbf{y}) = \oint_{\Omega_z} d\sigma_z \left\{ \frac{\partial G^+(\omega, \mathbf{z}, \mathbf{y})}{\partial n_z} G^-(\omega, \mathbf{z}, \mathbf{x}) - G^+(\omega, \mathbf{z}, \mathbf{y}) \frac{\partial G^-(\omega, \mathbf{z}, \mathbf{x})}{\partial n_z} \right\}. \quad (3)$$

Here, $\frac{\partial G(\omega, \mathbf{z}, \cdot)}{\partial n_z}$ is the derivative along the external normal $\mathbf{n}_z$ to the contour Ω_z at a point $\mathbf{z} \in \Omega_z$, and $d\sigma_z$ is the element of the contour Ω_z.

Equation (3) holds in both two- and three-dimensional cases. It gives an integral relationship between the unknown fields $G^\pm$, which are generated at an arbitrary point $\mathbf{x} \in R$ by point sources located in the inhomogeneous medium, and the scattered fields $G^+(\omega, \mathbf{z}, \mathbf{y})$, which can be obtained by measuring the field of the point sources located on the contour Ω_z by the point receivers located on the contour Ω_y. If we replace the functions $G^+(\omega, \mathbf{r}, \mathbf{y})$ and $G^-(\omega, \mathbf{r}, \mathbf{x})$ appearing in Eqs. (1) and (2) by $G^-(\omega, \mathbf{r}, \mathbf{y})$ and $G^+(\omega, \mathbf{r}, \mathbf{x})$, respectively, we obtain another similar equation for G^+ and G^-:

$$G^+(\omega, \mathbf{y}, \mathbf{x}) - G^-(\omega, \mathbf{x}, \mathbf{y}) = \oint_{\Omega_z} d\sigma_z \left\{ \frac{\partial G^-(\omega, \mathbf{z}, \mathbf{y})}{\partial n_z} G^+(\omega, \mathbf{z}, \mathbf{x}) - G^-(\omega, \mathbf{z}, \mathbf{y}) \frac{\partial G^+(\omega, \mathbf{z}, \mathbf{x})}{\partial n_z} \right\}. \quad (4)$$

According to the reciprocity theorem, $G^\pm(\omega, \mathbf{y}, \mathbf{x}) = G^\pm(\omega, \mathbf{x}, \mathbf{y})$.

Now, we assume that the inhomogeneity is composed of a sole point-like scatterer located at the point $\mathbf{x}_0 \in R$. Then, the total fields $G^\pm$ satisfy the Lippman–Schwinger equation

$$G^\pm(\omega, \mathbf{y}, \mathbf{x}) = G_0^\pm(\omega, \mathbf{y}, \mathbf{x}) + \int_R G_0^\pm(\omega, \mathbf{y}, \mathbf{r}) \varepsilon(\mathbf{r}) G^\pm(\omega, \mathbf{r}, \mathbf{x}) d\mathbf{r}, \quad (5)$$

where $G_0^\pm$ is the Green function of a homogeneous space and $\varepsilon(\mathbf{r}) \equiv \frac{\omega^2}{c_0^2} - \frac{\omega^2}{c^2(\mathbf{r})}$ is the scatterer function. On the other hand, for the point scatterer that is assumed to scatter as a monopole, one can try to represent the secondary sources generated in the scatterer region by the incident fields $G_0^\pm$ in the following form:

$$\varepsilon(\mathbf{r}) G^\pm(\omega, \mathbf{r}, \mathbf{x}) = \beta^\pm \delta(\mathbf{r} - \mathbf{x}_0) G_0^\pm(\omega, \mathbf{r}, \mathbf{x}). \quad (6)$$

Indeed, the delta-function on the right-hand side of Eq. (6) takes into account the point-like nature of the scatterer, the functions $G_0^\pm$ represent the monopole behavior of the scattered field, and the effective factors $\beta^\pm$ describe the wave rescattering that occurs in the region occupied by the point-like scatterer. These factors, which hereafter will be called the rescattering factors, will be shown to be complex quantities. They determine the amplitude and phase of the field scattered by the inhomogeneity $G_{sc}^\pm(\omega, \mathbf{y}, \mathbf{x}) \equiv G^\pm(\omega, \mathbf{y}, \mathbf{x}) - G_0^\pm(\omega, \mathbf{y}, \mathbf{x})$.

In view of Eq. (6), the limiting solution to Eq. (5) takes the form

$$G^\pm(\omega, \mathbf{y}, \mathbf{x}) = G_0^\pm(\omega, \mathbf{y}, \mathbf{x}) + G_0^\pm(\omega, \mathbf{y}, \mathbf{x}_0) \beta^\pm G_0^\pm(\omega, \mathbf{x}_0, \mathbf{x}). \quad (7)$$

Physically, Eq. (7) means that the scattering component $G_{sc}^\pm$ of the corresponding Green function is the wave arriving at the observation point $\mathbf{y}$ from the secondary point source generated by the field $G_0^\pm(\omega, \mathbf{x}_0, \mathbf{x})$ incident on the point scatterer. The rescattering coefficients β^+ and β^- must not coincide, because the secondary source has internal degrees of freedom due to the rescattering processes in a certain limiting sense.

Now, we find the relationship between β^+ and β^-. If the absorption is absent in both the background medium and the scattering region, the functions $G^\pm(\omega, \mathbf{y}, \mathbf{x})$ are complex conjugated. Then, from Eq. (6) it follows that the rescattering coefficients β^+ and β^- are also complex conjugate: $\beta^- = (\beta^+)^*$.

The substitution of the Green functions in the form of Eq. (7) into Eq. (4) yields the relationship

$$G_0^+(\omega, \mathbf{y}, \mathbf{x}_0) \beta^+ G_0^+(\omega, \mathbf{x}_0, \mathbf{x}) - G_0^-(\omega, \mathbf{y}, \mathbf{x}_0) \beta^- G_0^-(\omega, \mathbf{x}_0, \mathbf{x}) = \oint_{\Omega_z} d\sigma_z \left\{ \frac{\partial G_0^-(\omega, \mathbf{z}, \mathbf{x}_0)}{\partial n_z} G_0^+(\omega, \mathbf{z}, \mathbf{x}) - G_0^-(\omega, \mathbf{z}, \mathbf{x}_0) \frac{\partial G_0^+(\omega, \mathbf{z}, \mathbf{x})}{\partial n_z} \right\} \beta^- G_0^-(\omega, \mathbf{x}_0, \mathbf{y}) + \oint_{\Omega_z} d\sigma_z \left\{ \frac{\partial G_0^-(\omega, \mathbf{z}, \mathbf{y})}{\partial n_z} G_0^+(\omega, \mathbf{z}, \mathbf{x}_0) \right. \quad (8)$$

$$- G_0^-(\omega, \mathbf{z}, \mathbf{y})\frac{\partial G_0^+(\omega, \mathbf{z}, \mathbf{x}_0)}{\partial n_z}\Bigg\}\beta^+ G_0^+(\omega, \mathbf{x}_0, \mathbf{x})$$

$$+ \oint_{\Omega_z} d\sigma_z \Bigg\{\frac{\partial G_0^-(\omega, \mathbf{z}, \mathbf{x}_0)}{\partial n_z} G_0^+(\omega, \mathbf{z}, \mathbf{x}_0)$$

$$- G_0^-(\omega, \mathbf{z}, \mathbf{x}_0)\frac{\partial G_0^+(\omega, \mathbf{z}, \mathbf{x}_0)}{\partial n_z}\Bigg\}$$

$$\times \beta^+ G_0^+(\omega, \mathbf{x}_0, \mathbf{x})\beta^- G_0^-(\omega, \mathbf{x}_0, \mathbf{y}).$$

Deriving relationship (8), we took into account the fact that the Green functions of the homogeneous space $G_0^\pm$ satisfy an equation similar to Eq. (4); we also factored out the functions independent of the integration variable from under the integrals. On the right-hand side of Eq. (8), the first two integral terms coincide with the right-hand sides of Eqs. (3) and (4) for the Green functions $G_0^\pm(\omega, \mathbf{x}, \mathbf{x}_0)$ and $G_0^\pm(\omega, \mathbf{y}, \mathbf{x}_0)$, respectively,

$$G_0^+(\omega, \mathbf{x}, \mathbf{x}_0) - G_0^-(\omega, \mathbf{x}, \mathbf{x}_0)$$

$$= \oint_{\Omega_z} d\sigma_z \Bigg\{\frac{\partial G_0^-(\omega, \mathbf{z}, \mathbf{x}_0)}{\partial n_z} G_0^+(\omega, \mathbf{z}, \mathbf{x})$$

$$- G_0^-(\omega, \mathbf{z}, \mathbf{x}_0)\frac{\partial G_0^+(\omega, \mathbf{z}, \mathbf{x})}{\partial n_z}\Bigg\}$$

and

$$G_0^+(\omega, \mathbf{y}, \mathbf{x}_0) - G_0^-(\omega, \mathbf{y}, \mathbf{x}_0)$$

$$= \oint_{\Omega_z} d\sigma_z \Bigg\{\frac{\partial G_0^-(\omega, \mathbf{z}, \mathbf{y})}{\partial n_z} G_0^+(\omega, \mathbf{z}, \mathbf{x}_0)$$

$$- G_0^-(\omega, \mathbf{z}, \mathbf{y})\frac{\partial G_0^+(\omega, \mathbf{z}, \mathbf{x}_0)}{\partial n_z}\Bigg\}.$$

The integral in the third term is independent of the integration contour; it is determined by the dimension of the problem and can be directly calculated

$$\oint_{\Omega_z} d\sigma_z \Bigg\{\frac{\partial G_0^-(\omega, \mathbf{z}, \mathbf{x}_0)}{\partial n_z} G_0^+(\omega, \mathbf{z}, \mathbf{x}_0)$$

$$- G_0^-(\omega, \mathbf{z}, \mathbf{x}_0)\frac{\partial G_0^+(\omega, \mathbf{z}, \mathbf{x}_0)}{\partial n_z}\Bigg\} = \text{const}_{\text{dim}},$$

where the subscript dim denotes the dimension of the problem; $\text{const}_{\text{dim}=2} = \frac{i}{2}$ and $\text{const}_{\text{dim}=3} = +\frac{ik_0}{2\pi}$ [the time dependence is $\exp(i\omega t)$]. Therefore, Eq. (8) takes the form

$$G_0^+(\omega, \mathbf{y}, \mathbf{x}_0)\beta^+ G_0^+(\omega, \mathbf{x}_0, \mathbf{x})$$

$$- G_0^-(\omega, \mathbf{y}, \mathbf{x}_0)\beta^- G_0^-(\omega, \mathbf{x}_0, \mathbf{x})$$

$$= [G_0^+(\omega, \mathbf{x}, \mathbf{x}_0) - G_0^-(\omega, \mathbf{x}, \mathbf{x}_0)]\beta^- G_0^-(\omega, \mathbf{x}_0, \mathbf{y})$$

$$+ [G_0^+(\omega, \mathbf{y}, \mathbf{x}_0) - G_0^-(\omega, \mathbf{y}, \mathbf{x}_0)]\beta^+ G_0^+(\omega, \mathbf{x}_0, \mathbf{x})$$

$$+ \text{const}_{\text{dim}}\beta^+ G_0^+(\omega, \mathbf{x}_0, \mathbf{x})\beta^- G_0^-(\omega, \mathbf{x}_0, \mathbf{y}).$$

Collecting similar terms and eliminating the common factor $G_0^+(\omega, \mathbf{x}_0, \mathbf{x})G_0^-(\omega, \mathbf{x}_0, \mathbf{y})$, we obtain that the rescattering factors $\beta^\pm$ must satisfy the relationship

$$\begin{aligned}\frac{1}{\beta^-} - \frac{1}{\beta^+} &= \frac{i}{2} \text{ in the two-dimensional case,}\\ \frac{1}{\beta^-} - \frac{1}{\beta^+} &= +\frac{ik_0}{2\pi} \text{ in the three-dimensional case.}\end{aligned} \tag{9}$$

For the sake of definiteness and simplicity of expressions appearing in the second approach described below, we will only consider the two-dimensional case. The fact that the rescattering factors are complex conjugate makes it possible to seek these factors in the form

$$\beta^\pm = \beta e^{\pm i\psi}, \text{ where } \beta = |\beta^+| = |\beta^-|.$$

Then, Eq. (9) yields the relationship $\beta = 4\sin(\psi)$ that has two families of solutions

$$\psi = \begin{cases}\arcsin\left(\frac{\beta}{4}\right) + 2\pi k \\ \qquad\qquad (k \text{ is an integral}) \\ \pi - \arcsin\left(\frac{\beta}{4}\right) + 2\pi k.\end{cases} \tag{10}$$

Because the phase ψ is a real quantity, the amplitude β varies from 0 to 4 and the phase lies in the segments $\psi \in \left[2\pi k;\ 2\pi k + \frac{\pi}{2}\right]$ in the first case and $\psi \in \left[2\pi k + \frac{\pi}{2};\ 2\pi k + \pi\right]$ in the second case.

The rigorous relationship between the phase and the amplitude of the scattered wave and the limitation on the maximal possible amplitude were obtained above from Eqs. (3) and (4). They can also be derived using another, more physical approach, in which one analyzes the scattering by a scatterer whose size decreases simultaneously with an increase in its contrast. However, this passage to the limit is not trivial, because its result depends on a number of additional accompanying assumptions. Thus, to find the field scattered by a

point-like inhomogeneity, one should perform the passage to the limit in the expression for the Green function of a space containing a scatterer of a finite size under the condition that its maximal dimension tends to zero. In the two-dimensional case, such an inhomogeneity can be represented by a cylindrical inhomogeneity, in which the sound velocity differs from that of the background space:

$$c(\mathbf{r}) = \begin{cases} c_1, & r < R_1 \\ c_0, & r > R_1, \end{cases} \qquad r \equiv |\mathbf{r}|,$$

where c_1 and c_0 are the sound velocities inside and outside the inhomogeneity, respectively, and R_1 is the radius of the cylinder. In this case, the Green function satisfies the equations [2] (in what follows, we omit the frequency ω in the function arguments for brevity):

$$\begin{cases} \Delta G(\mathbf{r}, \mathbf{y}) + k_1^2 G(\mathbf{r}, \mathbf{y}) = \delta(\mathbf{r} - \mathbf{y}) \quad \text{for} \quad r < R_1 \\ \Delta G(\mathbf{r}, \mathbf{y}) + k_0^2 G(\mathbf{r}, \mathbf{y}) = \delta(\mathbf{r} - \mathbf{y}) \quad \text{for} \quad r > R_1. \end{cases} \tag{11}$$

The solution of system (11) with the boundary conditions (the continuity of the field and its normal derivative at the boundary)

$$\begin{cases} G(\omega, \mathbf{r}, \mathbf{y})|_{r \to R_1 - 0} = G(\omega, \mathbf{r}, \mathbf{y})|_{r \to R_1 + 0} \\ \left.\dfrac{\partial G(\omega, \mathbf{r}, \mathbf{y})}{\partial n_r}\right|_{r \to R_1 - 0} = \left.\dfrac{\partial G(\omega, \mathbf{r}, \mathbf{y})}{\partial n_r}\right|_{r \to R_1 + 0}, \end{cases}$$

and with the Sommerfeld radiation condition is representable as a sum of angular harmonics [2] (the expression below is given in the polar reference system $\mathbf{r} = \{r, \varphi\}$, $\mathbf{y} = \{y, \varphi_y\}$; the time dependence is given by the factor $\sim\exp(i\omega t)$; and the point source is assumed to be at the point $\mathbf{y} = \{y, \varphi_y = 0\}$, where $y > r > R_1$):

$$G^+(r, \varphi; y, \varphi_y = 0) = \frac{i}{4} \sum_{n=-\infty}^{\infty} e^{in\varphi} H_n^{(2)}(k_0 y)[J_n(k_0 r) - H_n^{(2)}(k_0 r)\beta_n^+], \tag{12}$$

where

$$\beta_n^+ = \frac{k_1 J_n'(k_1 R_1) J_n(k_0 R_1) - k_0 J_n(k_1 R_1) J_n'(k_0 R_1)}{k_1 J_n'(k_1 R_1) H_n^{(2)}(k_0 R_1) - k_0 J_n(k_1 R_1)[H_n^{(2)}(k_0 R_1)]'}.$$

Here, the functions J_n and $H_n^{(2)}$ are the Bessel and Hankel functions of order n, and the prime denotes the derivative with respect to the whole argument. The known representation of the Green function of the homogeneous space in the form of a series in angular harmonics for $y > r$ and $\varphi_y = 0$ [3],

$$G_0^+(r, \varphi; y, \varphi_y = 0) \equiv \frac{i}{4} H_0^{(2)}(k_0|\mathbf{r} - \mathbf{y}|) = \frac{i}{4} \sum_{n=-\infty}^{\infty} e^{in\varphi} H_n^{(2)}(k_0 y) J_n(k_0 r),$$

allows one to separate from Eq. (12) the scattered component of the Green function $G_{sc}^+ \equiv G^+ - G_0^+$:

$$\begin{cases} G_{sc}^+(r, \varphi; y, \varphi_y = 0) = -\dfrac{i}{4} \displaystyle\sum_{n=-\infty}^{\infty} e^{in\varphi} H_n^{(2)}(k_0 y) H_n^{(2)}(k_0 r) \beta_n^+ = \sum_{n=-\infty}^{\infty} e^{in\varphi} \frac{i}{4} H_n^{(2)}(k_0 y) \frac{i}{4} H_n^{(2)}(k_0 r) \tilde{\beta}_n^+ \\ \tilde{\beta}_n^+ \equiv 4i\beta_n^+ = 4i \dfrac{k_1 J_n'(k_1 R_1) J_n(k_0 R_1) - k_0 J_n(k_1 R_1) J_n'(k_0 R_1)}{k_1 J_n'(k_1 R_1) H_n^{(2)}(k_0 R_1) - k_0 J_n(k_1 R_1)[H_n^{(2)}(k_0 R_1)]'}. \end{cases} \tag{13}$$

A similar expression holds for the advanced Green function (the function $G_{sc}^- \equiv G^- - G_0^-$ is complex conjugate to function G_{sc}^+):

$$\begin{cases} G_{sc}^-(r, \varphi; y, \varphi_y = 0) = \displaystyle\sum_{n=-\infty}^{\infty} e^{in\varphi} \left(-\frac{i}{4}\right) H_n^{(1)}(k_0 y) \left(-\frac{i}{4}\right) H_n^{(1)}(k_0 r) \tilde{\beta}_n^- \\ \tilde{\beta}_n^- \equiv -4i\beta_n^- = -4i \dfrac{k_1 J_n'(k_1 R_1) J_n(k_0 R_1) - k_0 J_n(k_1 R_1) J_n'(k_0 R_1)}{k_1 J_n'(k_1 R_1) H_n^{(1)}(k_0 R_1) - k_0 J_n(k_1 R_1)[H_n^{(1)}(k_0 R_1)]'}. \end{cases} \tag{14}$$

In the approximation of a monopole scattering (this approximation is valid due to the cylindrical symmetry of the scatterer), the asymptotic behavior of the functions $G_{sc}^{\pm}$ for $R_1 \longrightarrow 0$ is governed exclusively by the zero-order angular harmonic $n = 0$. For example,

$$G_{sc}^{+}(r, \varphi; y\varphi_y = 0)\big|_{R_1 \to 0} \cong \frac{i}{4}H_0^{(2)}(k_0 y)\frac{i}{4}H_0^{(2)}(k_0 r)\tilde{\beta}_0^{+} \equiv G_0^{+}(\mathbf{y}, 0)\tilde{\beta}_0^{+}G_0^{+}(0, \mathbf{r}). \quad (15)$$

This expression is similar to the above Eq. (7) for $\mathbf{x}_0 = 0$ and $\mathbf{x} = \mathbf{r}$.

One can assume that not only the cylinder radius R_1 varies under the passage to the limit, but the wavenumber k_1 as well. The behavior of the wavenumber k_1 at $R_1 \longrightarrow 0$ depends on the internal structure of the point-like scatterer and, in turn, governs the scattering characteristics of the scatterer. Since the arguments of the cylindrical functions in Eqs. (13) and (14) for the factors $\tilde{\beta}_0^{\pm}$ are k_0R_1 ($k_0R_1 \longrightarrow 0$ for $R_1 \longrightarrow 0$) and k_1R_1, one can obtain different limiting values for $\tilde{\beta}_0^{\pm}$, depending on the asymptotic behavior of the quantity k_1R_1 at $R_1 \longrightarrow 0$, which hampers the analysis of the properties of the point-like scatterer. However, we can achieve our goal without such an analysis. Indeed, since the considered cylindrical scatterer is lossless, the retarded and advanced Green functions are complex conjugate, as was assumed earlier,

$$G^{-} = (G^{+})^* \Rightarrow G_{sc}^{-}(G_{sc}^{+})^*.$$

As a consequence, the factors $\tilde{\beta}_0^{-}$ and $\tilde{\beta}_0^{+}$ are complex conjugate as well, which also follows from Eqs. (13) and (14):

$$\boxed{\tilde{\beta}_0^{-} = (\tilde{\beta}_0^{+})^*}. \quad (16)$$

To obtain the second relationship between $\tilde{\beta}_0^{-}$ and $\tilde{\beta}_0^{+}$, it is convenient to consider the inverse quantities

$$\begin{cases} \dfrac{1}{\tilde{\beta}_0^{+}} = \dfrac{1}{4i}\dfrac{k_1J_0'(k_1R_1)H_0^{(2)}(k_0R_1) - k_0J_0(k_1R_1)[H_0^{(2)}(k_0R_1)]'}{k_1J_0'(k_1R_1)J_0(k_0R_1) - k_0J_0(k_1R_1)J_0'(k_0R_1)} \\ = -\dfrac{1}{4}\dfrac{k_1J_0'(k_1R_1)N_0(k_0R_1) - k_0J_0(k_1R_1)N_0'(k_0R_1)}{k_1J_0'(k_1R_1)J_0(k_0R_1) - k_0J_0(k_1R_1)J_0'(k_0R_1)} + \dfrac{1}{4i} \\ \dfrac{1}{\tilde{\beta}_0^{-}} = -\dfrac{1}{4}\dfrac{k_1J_0'(k_1R_1)N_0(k_0R_1) - k_0J_0(k_1R_1)N_0'(k_0R_1)}{k_1J_0'(k_1R_1)J_0(k_0R_1) - k_0J_0(k_1R_1)J_0'(k_0R_1)} - \dfrac{1}{4i}. \end{cases}$$

The difference of $\frac{1}{\tilde{\beta}_0^{-}}$ and $\frac{1}{\tilde{\beta}_0^{+}}$ is independent of R_1:

$$\boxed{\frac{1}{\tilde{\beta}_0^{-}} - \frac{1}{\tilde{\beta}_0^{+}} = \frac{i}{2}}. \quad (17)$$

Relationship (17) is similar to the above Eq. (9).

Using Eqs. (16) and (17), we can find the relationship between the magnitude and the argument of the complex factors $\tilde{\beta}_0^{\pm}$ in the second approach. From Eq. (16) it follows that

$$\tilde{\beta}_0^{\pm} = \tilde{\beta}\exp(\pm i\psi), \quad (18)$$

where $\tilde{\beta} \equiv |\tilde{\beta}_0^{+}| = |\tilde{\beta}_0^{-}|$ and ψ is the argument.

Substituting Eq. (18) into Eq. (17),

$$\frac{1}{\tilde{\beta}}[\exp(+i\psi) - \exp(-i\psi)] = \frac{i}{2}$$

$$\Rightarrow \tilde{\beta} = 4\frac{\exp(+i\psi) - \exp(-i\psi)}{2i}$$

we obtain the relationship

$$\boxed{\tilde{\beta} = 4\sin(\psi)} \quad (19)$$

that corresponds to Eq. (10) presented above. Relationship (19) means that the phase ψ uniquely determines the magnitude $\tilde{\beta}$. As for the reciprocal relationship considering the phase ψ as a function of β, it appears to be two-valued. For this reason, the magnitude of the rescattering factor increases as the phase ψ increases from 0 to $\frac{\pi}{2}$ and decreases with a further increase in ψ. Therefore, Eq. (19) limits the resulting efficiency of rescattering inside the point-like scatterer; namely, the magnitude of the rescattering factor $\tilde{\beta}$ is limited and cannot exceed four in the two-dimensional case.

It should be noted that, in solving an auxiliary problem of a plane wave incident on a thin but high-contrast layer, Rudenko *et al.* [4] also found a rigorous relationship between the amplitude and phase of the response (i.e., the reflected and transmitted waves) whose values were governed by two parameters of the passage to the limit: the layer thickness and the layer contrast relative

to the background medium. A rigorous relationship between the amplitude and phase of the response is also characteristic of nonlinear processes.

The result obtained above can be interpreted in physical terms. The complex conjugation property of the rescattering factors $\tilde{\beta}_0^{\pm}$ means that the multiple scattering processes occurring inside a point-like scatterer appear to be different for the retarded and advanced fields. In the case of a retarded field, the phase of the scattered wave field increases (in comparison with the phase of this field at the instant of its origination) in each scattering event because of the time delays due to the wave "propagation" in the scatterer after rescattering. At the same time, the phase of the scattered field lags behind the phase of the incident field at a fixed observation point. By contrast, for an advanced field, the "propagation" of the scattered waves inside the point-like scatterer results in a decrease in the phase of the scattered field in comparison with the phase of this field at the instant of its origination. As a result, the phase of the scattered field gets advanced relative to the phase of the incident field (because G^- is a complex conjugate to G^+). In the time domain, this effect manifests itself as a time delay for the incident field and a time advance for the scattered field.

ACKNOWLEDGMENTS

We are grateful to O.V. Rudenko for useful advice and discussions.

This work was supported by the Russian Foundation for Basic Research, project nos. 01-02-16282 and 00-15-96530.

REFERENCES

1. D. Budreck and J. H. Rose, Inverse Probl. **6**, 331 (1990).
2. V. M. Babich, M. B. Kapilevich, S. G. Mikhlin, *et al.*, *Linear Equations of Mathematical Physics*, Ed. by S. G. Mikhlin (Nauka, Moscow, 1964).
3. G. Korn and T. Korn, *Mathematical Handbook for Scientists and Engineers*, 2nd ed. (McGraw-Hill, New York, 1968; Nauka, Moscow, 1970).
4. O. V. Rudenko, L. E. Sobisevich, A. L. Sobisevich, and C. M. Hedberg, Dokl. Akad. Nauk **374** (2), 194 (2000) [Dokl. Phys. **45** (9), 485 (2000)].

Translated by A. Vinogradov.

Acoustical Physics, Vol. 47, No. 6, 2001, pp. 665–670. Translated from Akusticheskiĭ Zhurnal, Vol. 47, No. 6, 2001, pp. 757–762.

Reconstruction of the Dynamic Contact Stresses in an Elastic Layer from the Displacements of Its Free Surface

A. O. Vatul'yan*, V. M. Dragilev, and L. L. Dragileva*****

** Department of Mechanics and Mathematics, Rostov State University, ul. Zorge 5, Rostov-on-Don, 344090 Russia*

e-mail: vatulyan@mail.tp.ru

*** Research Institute of Physics, Rostov State University, ul. Stachki 194, Rostov-on-Don, 344090 Russia*

e-mail: vdragil@uic.rnd.runnet.ru

**** Department of Mathemetics, Rostov State Pedagogical University, ul. Bol'shaya Sadovaya 33, Rostov-on-Don, 344082 Russia*

e-mail: grekov@edu.donpac.ru

Received November 20, 2000

Abstract—An inverse problem on the reconstruction of the wave field of contact stresses produced by an external load in an elastic layer from the displacements of its free surface is considered for the model of forced steady-state vibrations in the approximation of plane deformations. The solution is constructed using two approaches: (1) a reduction of the problem to the Fredholm integral equation of the first kind with the use of the Tikhonov regularization and (2) an expansion of the solution in a discrete set of waves. It is shown that both approaches are approximately equivalent in the model under consideration. Possibilities for an adequate reconstruction of the source field from far-zone measurements of a finite number of propagating wave modes are analyzed. *© 2001 MAIK "Nauka/Interperiodica".*

Inverse problems of restoring the stressed deformed state of a medium from incomplete data specified at the boundaries form a relatively new field of the theory of elasticity [1–7]. The interest in these problems is related to their practical applications in such fields as structural intensimetry, vibration stability of structures, and flaw detection. The boundary-value inverse problems of the theory of elasticity are ill-posed problems in the sense of Tikhonov [8, 9], which links them to inverse problems in other fields of science and engineering [10].

The boundary-value problem on the reconstruction of a time-harmonic acoustic field in a linear elastic medium was first considered in [4, 5]. The problem statement assumes that vibrations of the medium are caused by external contact stresses, and the wave pattern is to be reconstructed from the displacement amplitudes measured at the free surface area accessible for observation. The approach developed in [4, 5] for the wave field reconstruction is based on the expansion of the field in a discrete set of solutions; in this case, the order of the reduced system of equations is the regularization parameter, which is characteristic of the method of singular expansions [11]. The problem allows another approach [1, 2, 7], according to which it is reduced to the Fredholm integral equation of the first kind whose solution can be found using the Tikhonov regularization [8, 9].

The geometry of the particular model considered in detail in [4, 5] allowed one to abstract from external contact loads and to expand the solution in normal waves. Unlike the cited papers [4, 5], this paper deals with the reconstruction of the field in the region of the surface contact. The goal of this paper is to test both discrete expansion [4, 5] and Tikhonov regularization methods with the use of model examples and to compare their potentialities.

Consider an elastic layer occupying the region $[-\infty < x < \infty, 0 \le y \le h]$ and assume that it performes forced steady-state vibrations under a plane deformation. We assume that the lower boundary of the layer ($y = 0$) is fixed and the upper boundary ($y = h$) is loaded by an external force $\exp(-i\omega t)q(x)$ distributed over the segment $x \in [X_1, X_2]$. The dynamics of the layer is governed by the Lamé equations [12]. The basic parameters of the model are the Poisson ratio ν and the dimensionless frequency $\kappa = \omega h\sqrt{\rho/(\lambda + 2\mu)}$, where ρ is the density and λ and μ are the Lamé coefficients. In what follows, we use the layer thickness h as the length unit. In all examples, we use $\nu = 0.3$.

Let us formulate the problem on determining the load $q(x)$ from the normal displacements of the free surface of the layer $u_y(x, h) \equiv u(x)$, where the function $u(x)$ is specified within the interval $x \in [X_3, X_4]$ not intersecting with the interval $[X_1, X_2]$. The function $q(x)$ is

related to $u(x)$ by the Fredholm integral equation of the first kind with a smooth kernel:

$$\int_{X_1}^{X_2} k(x-x')q(x')dx' = u(x), \quad x \in [X_3, X_4], \qquad (1)$$

where $k(x-x')$ is the corresponding component of the Green matrix [13]. Using the Fourier representation, we have

$$k(\zeta) = \frac{1}{2\pi}\int_{\sigma} K(p)e^{ip\zeta}dp, \qquad (2)$$

where $\zeta = x - x'$, and σ is the integration contour passing along the real axis and bypassing the poles according the rules following from the limiting absorption principle [13]. The Fourier transform $K(p)$, whose explicit expression is given in monograph [13], is an even meromorphic function (real for real p). Real poles corresponding to continuous homogeneous waves appear for frequencies exceeding the critical frequency; their number increases with frequency but remains finite [13].

Consider the solution in the far-zone approximation. For nonresonance frequencies, all real poles of the function $K(p)$ are simple poles; hence, the asymptotic estimator

$$\begin{cases} k(\zeta) = k_\infty(\zeta) + O[\exp(-c|\zeta|)] & (3a) \\ k_\infty(\zeta) = i\sum_{m=1}^{M} (\pm R_m)\exp(\pm ip_m|\zeta|) & (3b) \end{cases}$$

is appropriate for the far zone (i.e., for $|\zeta| \longrightarrow \infty$). In Eqs. (3a) and (3b), R_m is the residue of the function $K(p)$ at the mth positive pole p_m, the lower (minus) signs are used for waves with the negative group velocity, and $c > 0$ is the distance from the real axis p to the nearest complex pole. Note that the main term (3b) of asymptotic expression (3) exactly describes the imaginary part of kernel (2).

We simulated the load reconstruction using mainly two frequencies, $\kappa = 3$ and 6, for which $M = 3$ and 6 homogeneous modes exist, respectively (the group velocities of all modes are positive). The corresponding wave numbers lie in the interval $1.6 < p_m < 6$ for $\kappa = 3$ and in the interval $2.7 < p_m < 12$ for $\kappa = 6$. The numerical comparison of the kernel $k(\zeta)$, Eq. (2), with its degenerate finite-dimension component (3b) showed that the relative contribution of the residual term of asymptotics (3a) is less than a few fractions of percent and rapidly decreases with increasing $|\zeta| \gtrsim 2$ for both frequencies (the calculated complex poles give $c \approx 3.8$ for both frequencies). In the examples below, the segments $[X_1, X_2]$ and $[X_3, X_4]$ are chosen so as to satisfy the inequality $|\zeta| \geq 5$, which made it possible to replace the kernel by its finite-dimension part (3b). This substitution is justified both technically and physically, because the exponentially small inhomogeneous modes responsible for the residual term in Eq. (3a) are indistinguishable against the background of random errors. In similar examples with shorter distances $|\zeta| \sim 1$–2, we directly checked that the load reconstruction gives identical results for both exact kernel (2) and approximate kernel (3b).

In view of the kernel smoothness, the integral operator of Eq. (1) is completely continuous. This means that the inverse operator is unbounded, so that the operator equation requires some regularization [8]. The finite-difference regularization schemes for such equations are developed exhaustively in the Tikhonov method [9]. We used the standard version of this algorithm with the first-order stabilizer. In the calculations, we specified the displacement function by a discrete set of values $\{u_j = u(x_j), j = 1, \ldots, J\}$ corresponding to the points x_j chosen in the interval $[X_3, X_4]$. The initial parameters of our algorithm include the initial data array $\{x_j, u_j\}$, the regularization parameter α [8], and the discrete parameter J', the latter being the number of nodes of the finite-difference grid in the interval $[X_1, X_2]$. The solution is constructed as an array of J' values of the function $q(x)$ for equidistant points of the segment.

The most natural implementation of the method of discrete expansions in the discussed model is as follows. Let $\{f_n(x), n = 1, 2, \ldots\}$ be a complete orthonormal set of functions in the space $L_2[X_1, X_2]$ and let $q_N(x)$ be an approximation of the desired solution $q(x)$ with the segment of its generalized Fourier series:

$$q_N(x) = \sum_{n=1}^{N} a_n f_n(x). \qquad (4)$$

Substituting formally Eq. (4) into Eq. (1), we obtain the operator equation $A\mathbf{a} = \mathbf{u}$, where $\mathbf{a} = \{a_n\}$, $\mathbf{u} = \{u_j\}$, and $A = \{A_{jn}\}$ is the rectangular matrix with the elements

$$A_{jn} = \int_{X_1}^{X_2} k(x_j - x')f_n(x')dx'$$

$$(n = 1, \ldots, N;\ j = 1, \ldots, J).$$

In accordance with the concept of the method [4, 5], coefficients a_n are to be found from the condition that the mismatch functional is minimal, i.e., from the self-conjugated equation

$$B\mathbf{a} = \mathbf{v}, \qquad (5)$$

where $B = A^*A$, $\mathbf{v} = A^*\mathbf{u}$, and A^* is the Hermitian conjugated matrix. The optimal value of the parameter N must fit the initial data errors (the corresponding procedures are discussed in what follows); the limit $N = \infty$ corresponds to the exact right-hand side of Eq. (1). The fact that this algorithm is the Tikhonov regularization algorithm [8] is established in the projection method [10].

We used the Legendre polynomials orthonormalized on the segment $[X_1, X_2]$ as the basis functions $f_n(x)$.

To simplify the correlation of the results, we specified real-valued model loads $q(x)$. For this reason, we replaced Eq. (1) with its real-valued analog with the kernel $\mathrm{Re}\{\theta k_\infty(\zeta)\}$ and the right-hand side $\mathrm{Re}\{\theta u(x)\}$, where $\theta = \exp(-i\omega t)$ is the given phase factor. Equation (5) was modified in a similar manner. This modification means that we *a priori* considered the load as a real-valued function (thus approximately doubling the efficiency of the algorithms).

Now, we discuss the results of our simulations. In the calculations, we used two types of model loads $q(x)$: (I) a combination of sine-like and step functions specified within the segment $[X_1, X_2] = [0, 1]$ and (II) the function $q(x) = 1/\sqrt{1 - x^2}$ specified within the segment $[X_1, X_2] = [-0.99, 0.99]$. The latter models the action of a rectangular punch in the static approximation [14]. We formed the arrays of initial data on the basis of the numerical solution of the direct problem with a specific load $q(x)$ by adding the thus obtained u_j with the random error whose relative values were uniformly distributed in a given interval $[-\Delta, \Delta]$. As is customary, the numerical solution of the inverse problem was then correlated with the initial model function $q(x)$. Figures 1–3 shows typical examples of such a correlation. The solid lines correspond to the model functions, the circles correspond to the solutions by the Tikhonov method, and the dashed lines correspond to the solutions by the method of discrete expansions. All curves were calculated for the frequency $\kappa = 6$ and are stable relative to the choice of the phase ωt. These results were obtained for random errors of about a percent, which corresponds to the usual accuracy of modern measurement techniques [4].

For the above examples, we used 12 observation points x_j uniformly spaced in the interval $[X_3, X_4] = [6, 12]$. The particular arrangement of these points and their exact number J are inessential. It is only desirable that the condition $J \geq 2M$ holds; otherwise, one can partially lose the useful information ($2M$ is the number of real-valued parameters corresponding to M complex amplitudes of inhomogeneous modes). If the initial data consist of the complex amplitudes u_j (rather than of real-valued quantities $\mathrm{Re}\{\theta u_j\}$, as in the model examples), the condition for J takes on the form $J \geq M$.

In the calculations by the Tikhonov method, we used the parameter $J' = 30$ (increasing the parameter by a factor of 3 changed nothing in the calculated results). The ways of determining the parameter α are described in [8, 9, 15].

In the simulations, we smoothly increased the parameter Δ (appropriately fitting the regularization parameters α and N) to determine roughly (on the order of magnitude) the upper boundary of the parameter Δ, beginning from which the quality of the reconstructed pattern was drastically degraded (the average relative error measured about 100%, the extremums of the model function cease to be distinguishable, false extrema appear, and so on). For all our examples, this upper limit was approximately the same for both algorithms, i.e., for the method of discrete expansions and the Thikhonov method. Indeed, for the model function of type I with two extremums (Fig. 1), the above upper limit can be estimated as $\Delta = 0.005$ and 0.05 for the frequencies $\kappa = 3$ and 6, respectively. For the function of type I with four extremums and for the function of type II at the frequency $\kappa = 6$, these limits are close to $\Delta = 0.02$ and 0.005 (the corresponding curves are shown in Figs. 2 and 3). To sum up these simulations, we deduce that both algorithms are of approximately identical efficiency.

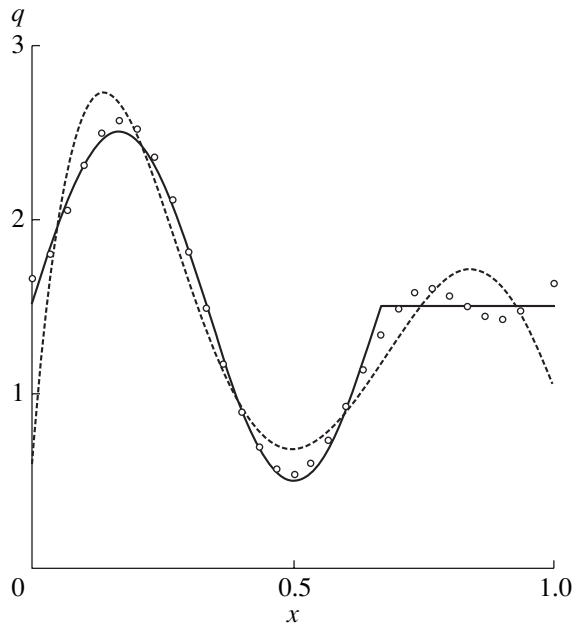

Fig. 1. Reconstruction of a load of type I for $\Delta = 0.02$; $N = 7$, and $\alpha = 10^{-7}$.

It is noteworthy that the random error smallness by itself does not assure an adequate reconstruction. There are additional factors that govern the reconstruction quality, namely, the number of homogeneous modes M and the configuration of the contact stress field, which must be relatively simple (this simplicity meaning will be given later). The following example is a good illustration of this fact. At the frequency $\kappa = 3$, for which only three modes exist, both algorithms reconstruct with confidence the model load function of type I with two extremums (Fig. 1) with random errors up to $\Delta \approx 0.005$. At the same time, both algorithms fail to reconstruct a similar curve with four extremums (Fig. 2) even at $\Delta = 0$ (they approximate the desired function by the curves that do not reproduce the positions of the extremums). However, the algorithms reconstruct this function at the frequency $\kappa = 6$, for which the number of modes is greater by a factor of two (see Fig. 2). The explanation consists in the fact that kernel (3) is degenerate in the far zone.

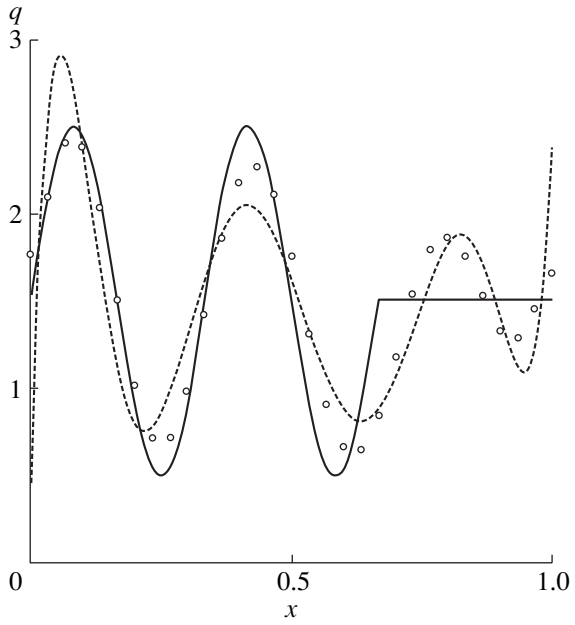

Fig. 2. Reconstruction of a load of type I for $\Delta = 0.02$, $N = 7$, and $\alpha = 10^{-9}$.

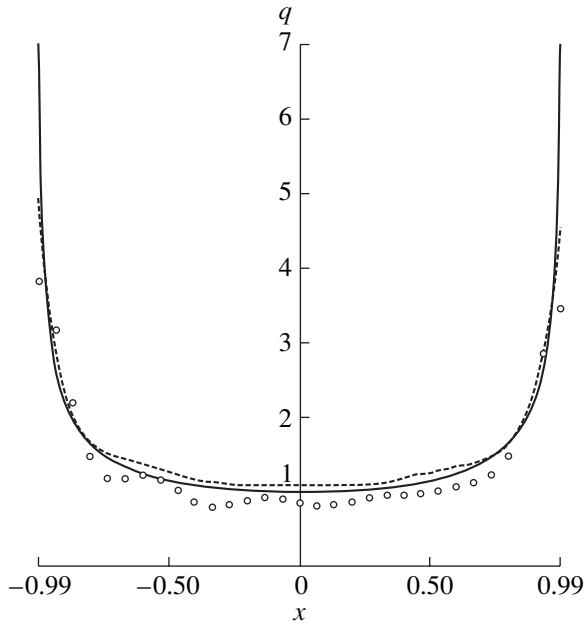

Fig. 3. Reconstruction of a load of type II for $\Delta = 0.005$, $N = 9$, and $\alpha = 10^{-9}$.

Special care must be given to the choice of the parameter N in the method of discrete expansions. The reason is that, for $\Delta \gtrsim 10^{-2}$, the optimal values of N are usually small, about 5–10 (see [4, 5] for comparison). As a result, even small deviations [say, by $\pm(1–2)$] of the parameter N from its optimal value can appreciably decrease the reconstruction quality (note that the instability of the results drastically increases when the value of N is too high).

To estimate the greatest admissible value of the parameter N, one should proceed from the result sensitivity to random errors. Let $\mathbf{u}$ and $\mathbf{u} + \delta\mathbf{u}$ be two vectors of the initial data obtained in independent measurements. We will use the following notation: $\mathbf{a}$ and $\mathbf{a} + \delta\mathbf{a}$ for the corresponding vectors of the solution of problem (5) for certain N, $\mathbf{u}' = A\mathbf{a}$ for the approximate direct problem solution reconstructed from the solution of the inverse problem, $\sigma_1 > \sigma_2 > \ldots > \sigma_N > 0$ for the singular values [4, 11] of the matrix B, $C_N = \sigma_1/\sigma_N$ for the conditionality number of this matrix, and $S_N = \sigma_1^{-1} + \ldots + \sigma_N^{-1}$. Using the singular expansion formalism [4, 11], one can easily prove the inequality $\|\delta\mathbf{a}\| \le S_N\|\delta\mathbf{u}\|$, or, what is the same,

$$\Delta_a \le S_N \Delta_u \|\mathbf{u}\|/\|\mathbf{a}\|, \tag{6a}$$

where $\Delta_a = \|\delta\mathbf{a}\|/\|\mathbf{a}\|$, $\Delta_u = \|\delta\mathbf{u}\|/\|\mathbf{u}\|$, and the norms are calculated in the Euclidean spaces R^N and R^J. In view of the orthonormality of the set $\{f_n\}$ in Eq. (4), Δ_a is the characteristic error of the solution $q_N(x)$ (the quantity of our interest), and the quantity Δ_u can be identified with the average error of the initial data Δ. From the singular expansion for $\mathbf{a}$, we have $\|\mathbf{a}\| \ge \sigma_1^{-1}\|\mathbf{u}\|$. Since the sequence of singular values decreases rapidly according to the quasi-exponential law [4], we can set $S_N \approx \sigma_N^{-1}$; in addition, we can use $\|\mathbf{u}'\| \approx \|\mathbf{u}\|$. Substituting these results in inequality (6a), we obtain a restriction on the order of magnitude:

$$\Delta_a \lesssim C_N \Delta_u. \tag{6b}$$

The right-hand sides of inequalities (6) give too high an estimator for Δ_a. As long as these sides are below unity, the error Δ_a still appears reasonable. From these considerations, two interchangeable criteria follow for determining the optimal N from the given error $\Delta_u = \Delta$. Namely, the optimum is the maximal value of N for which (A) the right-hand side of inequality (6a) or (B) the right-hand side of inequality (6b) is less than unity. Criterion (A) based on the accuracy loss S_N ensures that the statistical scatter of the results is below 100%. The more convenient criterion (B) was stated earlier [4] from empirical considerations. Using a large number of simulated examples, we checked that, despite the nonstrict character of the estimator, both criteria usually give identical (or differing by unity) values for N, and these values coincide with the optimal values obtained from the condition of the best correspondence between the model function and the reconstruction. Such efficiency of the criteria follows from the fact that singular values strongly depend on their order number (Fig. 4).

As was mentioned above, the features of the kernel in the far zone impose specific restrictions on the reconstruction. The essence of these restrictions can be easily clarified using the discrete approach. For this purpose,

we consider complex-valued loads; in the version with *a priory* real-valued functions $q(x)$, all subsequent relationships hold with the number of modes M being replaced by the corresponding number of the real-valued parameters $2M$. In the far zone approximation, i.e., in the problem with a degenerate kernel, Eq. (3b), admissible values of the regularization parameter N are limited from above by the dimension of the vector **u**-space, which coincides with the number of homogeneous modes M (for $N > M$, higher singular values of the matrix B appear to be zero, and the solution becomes unstable). Let $N[q]$ be the characteristic minimal number of terms in the Fourier expansion (4) that is required for an acceptable approximation of the given function $q(x)$ in accordance with the norm $C[X_1, X_2]$. In this case, a successful reconstruction assumes that the condition

$$N[q] \le M \tag{7}$$

must hold. In the limit $\Delta \longrightarrow 0$, the necessary condition (7) of the reconstruction becomes, in a certain sense, the sufficient condition as well. Indeed, in the class of functions $q(x)$ representable by finite Fourier series (4) with $N \le M$, the solution to the inverse problem with kernel (3b) is unique and stable to disturbances in the initial data **u**. In the case of loads given in the general form, the contributions of higher terms of the Fourier series (with $n > M$) can be considered as small disturbances under condition (7), which ensures the reconstruction of the lower terms of the series by the method given in [4, 5]. Hence, condition (7) is the desired estimation criterion that determines the possibility of an adequate reconstruction for moderate errors Δ. According to inequality (7), a decrease in the number of homogeneous modes M narrows the class of admissible functions $q(x)$ rather than deteriorates the general quality of the reconstructed patterns. Precisely this effect was observed in the above simulations.

Since $N[q]$ is only an order-of-magnitude estimator, it can be treated as a characteristic intrinsic in the function $q(x)$, which only weakly depends on the choice of the basis functions in Eq. (4). Therefore, it is not surprising that criterion (7) appears to be empirically justified not only in the discrete approach, but also in the Tichonov method in which the basis is not fixed. Considering condition (7), it is pertinent to additionally emphasize that, in the far zone approximation, the limit $\Delta \longrightarrow 0$ corresponds physically to a small, but finite measurement error that exceeds the contribution of inhomogeneous waves.

Thus, in this paper, we investigated the reconstruction of the dynamic contact stresses acting on an elastic layer in the context of the general problem of the field reconstruction [4, 5]. The reconstruction can be performed by both the method of discrete expansions [4, 5] and the method of an integral operator equation with the Tikhonov regularization. The efficiency of both approaches appeared to be approximately equal, which indicates that it is close to the fundamentally attainable one.

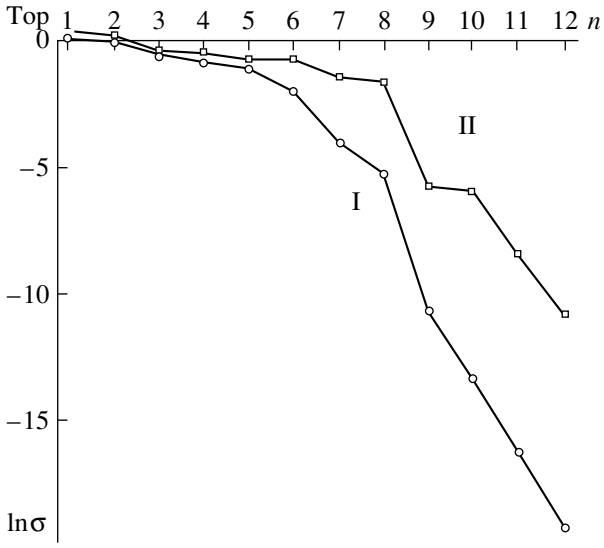

Fig. 4. Singular values in the examples with loads of types I and II (curves I and II, respectively) for $\kappa = 6$ and $N = 12$. The difference between the curves is determined by the different regions of the load application. For $N < 12$, the results only slightly differ from those represented by curves I and II, because the lower singular values only slightly depend on the dimension N.

A disadvantage of the discrete approach is its low stability to variations in the order N of the reduced system of equations. As was shown, this difficulty is not insuperable. Discussing this point, we mathematically explained the origin of the empirical estimator [4] for the optimal values of the parameter N, determined an alternative estimator, and showed that both estimators are quite practicable.

A reconstruction of the contact load appears to be possible even when the measurements are carried out in the far zone and the experimental information is scarce because of the low number of modes existing in this zone. In this case, the degeneracy of the kernel in the integral Fredholm equation imposes natural restrictions on the reconstruction of the stress field: the configuration of the field must *a priori* be sufficiently simple. For simple fields satisfying condition (7), we predict a stable reconstruction with the reproduction of the spatial features of the wave pattern, provided that the measurement errors are not too large.

ACKNOWLEDGMENTS

This work was supported in part by the Russian Foundation for Basic Research, project nos. 00-01-00545 and 00-15-96087.

REFERENCES

1. A. V. Fomin and A. K. Preĭss, Mashinovedenie, No. 1, 79 (1982).
2. A. V. Fomin, Mashinovedenie, No. 4, 67 (1982).

3. A. K. Preĭss, Mashinovedenie, No. 2, 77 (1984).
4. Yu. I. Bobrovnitskiĭ, Akust. Zh. **40**, 367 (1994) [Acoust. Phys. **40**, 331 (1994)].
5. Yu. I. Bobrovnitskiĭ, M. P. Korotkov, A. A. Kochkin, and T. M. Tomilina, Dokl. Akad. Nauk **359** (2), 190 (1998) [Dokl. Phys. **43**, 177 (1998)].
6. S. E. S. Karlsson, J. Sound Vibr. **196**, 59 (1996).
7. A. O. Vatul'yan and A. N. Solov'ev, Akust. Zh. **46**, 451 (2000) [Acoust. Phys. **46**, 385 (2000)].
8. A. N. Tikhonov and V. Ya. Arsenin, *Methods of Solving Ill-Posed Problems* (Nauka, Moscow, 1986).
9. A. N. Tikhonov, A. V. Goncharskiĭ, V. V. Stepanov, and A. G. Yagola, *Numerical Methods for Solving Ill-Posed Problems* (Nauka, Moscow, 1990).
10. A. M. Denisov, *Introduction to the Theory of Inverse Problems* (Mosk. Gos. Univ., Moscow, 1994).
11. S. K. Godunov, A. G. Antonov, O. P. Kirilyuk, and V. I. Kostin, *Guaranteed Accuracy of Solving Sets of Linear Equations in Euclidean Spaces* (Nauka, Novosibirsk, 1998).
12. L. I. Sedov, *A Course in Continuum Mechanics*, 2nd ed. (Nauka, Moscow, 1973; Wolters-Noordhoff, Groningen, 1971), Vol. 1.
13. I. I. Vorovich and V. A. Babeshko, *Dynamic Mixed Problems of the Theory of Elasticity for Nonclassical Regions* (Nauka, Moscow, 1979).
14. I. I. Vorovich, V. M. Aleksandrov, and V. A. Babeshko, *Nonclassical Mixed Problems of the Theory of Elasticity* (Nauka, Moscow, 1974).
15. N. N. Kalitkin, *Numerical Methods* (Nauka, Moscow, 1978).

Translated by A. Vinogradov

Acoustical Physics, Vol. 47, No. 6, 2001, pp. 671–676. Translated from Akusticheskiĭ Zhurnal, Vol. 47, No. 6, 2001, pp. 763–768.

Calculation of the Velocity of Sound in Rubber Containing Cylindrical Voids with Allowance for Dynamic Correction

V. E. Glazanov and A. V. Mikhaĭlov

Morfizpribor Central Research Institute, Chkalovskiĭ pr. 46, St. Petersburg, 197376 Russia

e-mail: eugenia@dg3409.spb.edu

Received December 19, 2000

Abstract—The problem of the velocity of sound in a medium containing cylindrical voids is solved with the use of the theory describing coupled vibrations of a tube of finite height, which serves as a model of the medium. The expression for the velocity of sound is derived with allowance for the dynamic correction similar to the Rayleigh correction for an infinitely long rod. Good agreement is obtained between the calculations (by the formulas derived for the velocity) and the experimental characteristics of the reflection and transmission coefficients of multilayer samples made of rubber with cylindrical voids, which were measured in the Low-Frequency Acoustic Pipe system in the frequency range 100–5000 Hz under hydrostatic pressures up to 30 kg/cm^2. © *2001 MAIK "Nauka/Interperiodica".*

Artificial voided media are used in underwater acoustics for making sound-insulating and sound-absorbing coatings and screens [1–4]. For example, layers made of rubber with cylindrical voids, first described by Tyutekin [5], have found wide application. Theoretical methods for calculating the acoustic and elastic parameters of the aforementioned media are considered in many publications, the most comprehensive reviews of which can be found in [3, 6]. In this paper, we propose and justify a method for calculating the velocity of sound in a layer of rubber with cylindrical voids with allowance made for dynamic correction. It is well known that the static approximation used for calculating the velocity of sound in a medium with cylindrical voids is valid for frequencies well below the resonance of the tube with a radially fixed outer surface, which serves as a model of the medium under consideration (below, we will call it "the tube" for brevity). Therefore, at higher frequencies, it is necessary to introduce a correction that is similar to the Rayleigh dynamic correction for infinitely long solid rods [7] or tubes [6]. As noted in [7], the method of coupled vibrations developed in [8] yields a result that is closer to reality than the result obtained with the Rayleigh correction. Hence, we calculate the velocity of sound in rubber with cylindrical voids by taking into account the dynamic correction and using the results obtained in [8]. To justify the proposed method, we first consider a thin cylindrical shell of radius a and height h with its lateral surface and ends being free from stress. The equation describing the vibrations of this shell [9] can be represented in the form

$$F^4 - F^2\frac{1}{1-\nu^2}[(nf_z)^2 + f_r^2] + (nf_z)^2 f_r^2\frac{1}{1-\nu^2} = 0, \quad (1)$$

where

$$f_r = \sqrt{\frac{E}{\rho}}\frac{1}{2\pi a} \quad (2)$$

is the radial natural frequency of the shell vibrating at the zeroth mode;

$$nf_z = \frac{n}{2h}\sqrt{\frac{E}{\rho}} \quad (n = 1, 2, 3\ldots) \quad (3)$$

is the axial natural frequency of the shell vibrations along the z axis; F is the natural frequency of the combined radial and axial vibrations of the shell; and E, ν, and ρ are the Young modulus, the Poisson ratio, and the density of the shell material.

Following the approach used in [8], we calculate the velocity with allowance for the dynamic correction on the basis of the theory of natural vibrations in a system with two degrees of freedom. The most complete and mathematically correct description of this theory can be found in [10]. Expressing the equations of motion of the system through the Lagrange equations for each of the two coordinates, we obtain

$$(f_1^2 - F^2)(f_2^2 - F^2) = (pf_1f_2 - qF^2)^2. \quad (4)$$

Here, q is the inertial coupling coefficient and p is the elastic coupling coefficient.

The roots of Eq. (4), F_1 and F_2, are always real, and the partial frequencies f_1 and f_2 lie between F_1 and F_2. This means that, in the presence of coupling, the highest natural frequency of the system lies above the higher natural partial frequency and the lowest natural frequency is below the lower partial one; i.e., the pres-

ence of the coupling between the vibrations of two isolated systems leads to an increase in the higher partial frequency and a decrease in the lower one. If we choose two oscillatory systems with widely separated natural frequencies, the inertial coupling will predominate, and the elastic coupling can be neglected. (We note that in [8] this statement is proved only experimentally.) In this case, $p = 0$, and the coupling coefficient q, which is to be determined for a specific oscillatory system, is a finite quantity.

Following [8, 10], we apply the theory of coupled vibrations to the calculation of the natural frequencies of a thin cylindrical shell of finite height. To use Eq. (4), it is necessary to understand what are the frequencies f_1 and f_2 in the case of the shell vibrations. If the shell is very long or has a very small diameter, we have $f_2 \gg f_1$, and, for vibrations propagating along the shell axis, Eq. (3) must be used. If the shell length is small compared to the shell diameter and, in the axial direction, the shell degenerates into a thin ring, we have $f_1 \gg f_2$; in this case, for the frequency of natural vibrations, we must use Eq. (2). Therefore, if in Eq. (4), we replace the frequencies f_1 and f_2 by the determining frequencies given by Eqs. (3) and (2), i.e., $f_1 = nf_z$ and $f_2 = f_r$, and assume that $p = 0$, we obtain the solution for the natural frequency of the first series of vibrations in the form of the expression

$$F_1^2 = f_r^2 \frac{\left(\frac{nf_z}{f_r}\right)^2 + 1 - \sqrt{\left[\left(\frac{nf_z}{f_r}\right)^2 - 1\right]^2 + 4q^2\left(\frac{nf_z}{f_r}\right)^2}}{2(1-q^2)}. \quad (5)$$

Below, this expression will be used for calculating the velocity in the tube. From Eq. (4), it follows that

(a) at $z = 0$, i.e., for a very short tube ($f_z \approx \infty$), we have

$$F_1 = f_r, \quad (6)$$

which is the natural frequency of radial vibrations of a thin ring;

(b) at $z \approx \infty$ ($f_z = 0$), we have

$$F_2 = \frac{f_r}{\sqrt{1-q^2}}, \quad (7)$$

which is the natural frequency of radial vibrations of an infinitely long shell;

(c) at the resonance between the axial and radial vibrations, when $nf_z = f_r$, we obtain the so-called dead zone [8]: no tensile vibrations can be excited in the shell at a given radius and elastic waves cannot propagate along the tube axis in this case.

From Eqs. (6) and (7), we determine the coupling coefficient

$$q = \sqrt{1 - \frac{F_1^2}{F_2^2}}. \quad (8)$$

Hence, the coupling coefficient can be calculated from the radial natural frequency of a thin ring $F_1 = f_r$ and the radial frequency of an infinitely long tube

$$F_2 = \frac{1}{2\pi a}\sqrt{\frac{E}{\rho(1-\nu^2)}}. \quad (9)$$

Substituting Eqs. (6), (7) and (9) in Eq. (8) and taking into account Eq. (2), we obtain

$$q = \sqrt{1 - \frac{1}{(2\pi a)^2}\frac{E}{\rho}\frac{(2\pi a)^2\rho(1-\nu^2)}{E}} = \sqrt{1-(1-\nu^2)} = \nu. \quad (10)$$

Thus, the coupling coefficient for the axial and radial vibrations of a thin cylindrical shell with stress-free lateral surfaces proves to be equal to the Poisson ratio ν. Substituting $q = \nu$ in Eq. (4) and correlating it with Eq. (1), one can easily show that these equations fully coincide. This allows one to use the theory of coupled vibrations in other cases and, specifically, in the problem on the vibrations of a tube with a radially fixed outer surface, which is (as noted above) a model of a medium with cylindrical voids.

The velocity of the elastic wave propagation in the tube is analogous to the velocity in a rod with the Rayleigh dynamic correction, and it can be determined from the relation

$$h = n\frac{\Lambda_F}{2} = n\frac{c}{2F_{tu}} \quad (n = 1, 2, 3\ldots), \quad (11)$$

which yields

$$c = \frac{2hF_{tu}}{n}, \quad (12)$$

where Λ_F is the wavelength in the tube at the natural frequency of the tube with allowance for its axial and radial vibrations F_{tu}, and h is the tube height. The value of F_{tu} can be determined from Eq. (5) (by setting $F_1 = F_{tu}$), if the coupling coefficient q is known. The resonance frequencies of a thin ($h = 0$) and an infinitely long ($h = \infty$) tube of radius a with the radially fixed outer surface of radius b are determined by the expressions [11]

$$\omega_0^2 = (2\pi F_1)^2 = \frac{4E}{\rho_0(1-\nu^2)a^2}\frac{(1+\nu)\varepsilon^2 + (1-\nu)}{L}; \quad (13)$$

$$\omega_\infty^2 = (2\pi F_2)^2 = \frac{4E}{\rho_0(1+\nu)(1-2\nu)a^2}\frac{1-2\nu+\varepsilon^2}{L}, \quad (14)$$

where

$$L = \varepsilon^2 - 3 - \frac{2\ln\varepsilon^2}{(1-\varepsilon^2)} \tag{15}$$

and $\varepsilon^2 = \left(\frac{a}{b}\right)^2$ is the perforation coefficient. Knowing these two frequencies, we obtain

$$\left(\frac{F_1}{F_2}\right)^2 = \frac{(1+\nu)\varepsilon^2 + (1-\nu)}{1-2\nu+\varepsilon^2}\frac{(1-2\nu)}{(1-\nu)}. \tag{16}$$

For rubber (for $\nu \longrightarrow 0.5$), from Eq. (16) it follows that $\frac{F_1}{F_2} \longrightarrow 0$. Then, according to Eq. (8), the coupling coefficient between the longitudinal and radial vibrations of a rubber tube of arbitrary height with a radially fixed outer surface is $q = 1$.

To calculate the velocity by Eq. (12) with allowance for Eq. (5), we introduce the notation

$$\frac{nf_z}{f_r} = \frac{nc_{\text{ef}}}{2h}\frac{2\pi a}{c_t(k_t a)_0} = \frac{c_{\text{ef}}}{c_t}\frac{s}{(k_t a)_0} = \frac{1}{Y}, \tag{17}$$

where $s = \frac{n\pi a}{h}$ is a dimensionless parameter; c_{ef} is the effective velocity in the tube, as calculated in the static approximation; c_t is the velocity of shear waves in the basic rubber material; $k_t = \frac{\omega}{c_t}$ is the wave number for shear waves; and $(k_t a)_0$ is the resonance wave radius of the tube of an infinitely small height.

Setting

$$\frac{F_{\text{tu}}}{f_r} = \frac{\frac{2\pi F_{\text{tu}} a}{c_t}}{\frac{2\pi f_r a}{c_t}} = \frac{k_t a}{(k_t a)_0} = Q \tag{18}$$

and taking into account Eqs. (12), (17), and (18), we obtain

$$\begin{gathered} F_{\text{tu}} = f_r Q; \quad f_z = \frac{c_{\text{ef}}}{2h}; \\ \frac{c}{c_{\text{ef}}} = \frac{2hF_{\text{tu}}}{n}\frac{1}{2hf_z} = \frac{F_{\text{tu}}}{nf_z} = \frac{f_r}{nf_z} = YQ. \end{gathered} \tag{19}$$

Then, from Eqs. (5) and (19), we obtain the expression for the velocity c:

$$\frac{c}{c_{\text{ef}}} = \sqrt{\frac{1-Q^2}{1-Q^2(1-q^2)}}. \tag{20}$$

Since, for the rubber tube in the case under study, the coupling coefficient is $q = 1$, Eq. (20) takes the form

$$\frac{c}{c_{\text{ef}}} = \sqrt{1-Q^2}. \tag{21}$$

From Eq. (18), it follows that, to determine Q, it is necessary to know $(k_t a)_0$. The values of the resonance wave radii for a tube of arbitrary height, which were calculated in [3] with allowance for Eqs. (13) and (14), can be represented in the form:

(a) for a tube with "sliding" (not radially fixed) ends,

$$(k_t a)^2 = 12\left(\frac{b}{h}\right)^2 \frac{1+3\varepsilon^2}{1+\frac{3}{2}\left(\frac{b}{h}\right)^2 L}; \tag{22}$$

(b) for a tube with radially fixed ends,

$$(k_t a)^2 = 10\left(\frac{b}{h}\right)^2 \frac{1+3\varepsilon^2+\frac{5}{4}\varepsilon^2\left(\frac{b}{h}\right)^2 L}{1+\frac{5}{4}\left(\frac{b}{h}\right)^2 L}. \tag{23}$$

For $h \longrightarrow 0$, we have

$$(k_t a)_0^2 = \frac{8(1+3\varepsilon^2)}{L}; \tag{24}$$

$$(k_t a)_0^2 \longrightarrow \infty, \tag{25}$$

where L is determined from Eq. (15).

As was shown in [3], for tubes with $\frac{h}{b} \geq 1$, the difference between the propagation velocities of elastic waves in the static approximation in the cases of free and fixed ends is insignificant. Therefore, in calculating the dynamic correction, we will use Eq. (24). However, we note that, since the compression diagrams for tubes with free and fixed ends are noticeably different, the dependence of the tube parameters on the hydrostatic pressure will be calculated below on the basis of the theory of large deformations for tubes with radially fixed ends [3].

Since, as the tube is compressed, its radius a varies, and, hence, the perforation coefficient ε^2 also varies, we introduce the dependence on the pressure P (the index p) in Eqs. (18) and (24) and represent them in the form

$$Q^2 = \frac{(k_t a^{(p)})^2}{[(k_t a)_0^2]^{(p)}}, \tag{26}$$

$$[(k_t a)_0^2]^{(p)} = \frac{8(1+3\varepsilon_p^2)}{\varepsilon_p^2 - 3 - \frac{2\ln\varepsilon_p^2}{1-\varepsilon_p^2}}, \tag{27}$$

where

$$\varepsilon_p^2 = \frac{\varepsilon^2 - \delta}{1-\delta}, \tag{28}$$

$$(k_t a^{(p)}) = \frac{2\pi f}{c_t} b\sqrt{\varepsilon_p^2}, \tag{29}$$

and δ is the relative deformation of the tube along its axis.

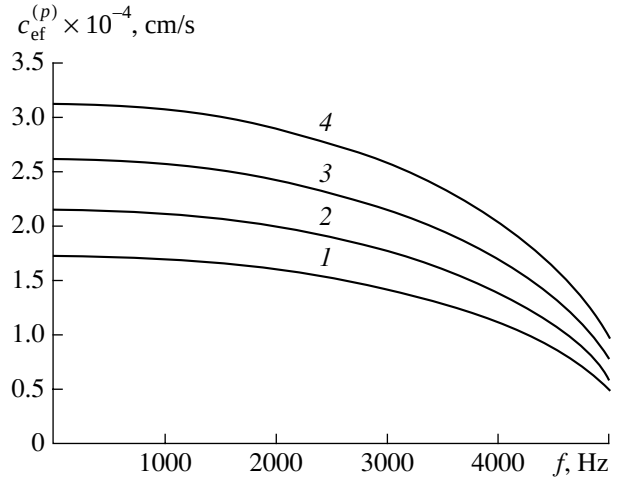

Fig. 1. Frequency dependence of the velocity of sound in rubber with cylindrical voids under different hydrostatic pressures: P = (*1*) 10, (*2*) 20, (*3*) 30, and (*4*) 40 kg/cm^2.

Substituting Eq. (28) in Eqs. (27) and (29), Eqs. (27) and (29) in Eq. (26), and then the resulting expressions in Eqs. (18) and (21), we can calculate the velocity in rubber with cylindrical voids with allowance for the dynamic correction at a given pressure P. Taking into account Eqs. (18) and (26), we represent Eq. (21) in the form

$$\frac{c}{c_{ef}^{(p)}} = \sqrt{1 - \frac{(k_t a^{(p)})^2}{[(k_t a)_0^2]^{(p)}}}. \quad (30)$$

We note that the curve given by Eq. (30) has the form of part of a circle. At low frequencies $\left(\frac{k_t a^{(p)}}{(k_t a)_0^{(p)}} \longrightarrow 0\right)$, the velocity in the tube is determined by the static approximation $\left(\frac{c}{c_{ef}^{(p)}} \cong 1\right)$. As the frequency increases, $\frac{c}{c_{ef}^{(p)}}$ decreases and, when $\frac{k_t a^{(p)}}{(k_t a)_0^{(p)}} \longrightarrow 1$, we have $\frac{c}{c_{ef}^{(p)}} \longrightarrow 0$. Thus, Eq. (30) is valid only for $\frac{k_t a^{(p)}}{(k_t a)_0^{(p)}} < 1$. When $\frac{k_t a^{(p)}}{(k_t a)_0^{(p)}} \geq 1$, no wave propagation occurs in a tube of finite height because of the presence of a "dead zone" (see above), unlike the case of infinitely long tubes [2, 6] when the velocity becomes equal to the Rayleigh wave velocity.

To calculate the velocity in a tube with radially fixed ends under large static deformations in the static approximation, it is necessary to use the following refined formulas from [3]:

$$\frac{c_{ef}^{(p)}}{c_t} = \sqrt{\frac{1-\varepsilon^2}{1-\varepsilon_p^2}\left\{1 + \frac{4}{3}\left[\frac{\partial^2 G}{\partial \delta^2}(1 + GN) + N\left(\frac{\partial G}{\partial \delta}\right)^2\right]\right\}}, \quad (31)$$

where the terms $\partial G/\partial\delta$ and $\partial^2 G/\partial\delta^2$ are determined by the expressions

$$\frac{\partial G}{\partial \delta} = \frac{\frac{3}{4}}{(1-\delta^2)\left(1 - \frac{4}{5}\frac{1-\varepsilon^2}{\varepsilon^2}G\right)};$$

$$N = 2\left[\frac{2}{5}\frac{1+\varepsilon^2}{\varepsilon^2} + \left(\frac{b}{h}\right)^2\left(\varepsilon^2 - 3 - \frac{2\ln\varepsilon^2}{1-\varepsilon^2}\right)\right];$$

$$\frac{\partial^2 G}{\partial \delta^2} = 2(1-\delta)^2\frac{\partial G}{\partial \delta}\left[(1-\delta) + \frac{8}{15}\frac{1-\varepsilon^2}{\varepsilon^2}\left(\frac{\partial G}{\partial \delta}\right)^2\right].$$

Let us compare our theoretical results with experimental data. At the Andreev Acoustics Institute, measurements of the reflection and transmission coefficients were performed for rubber samples with cylindrical voids under different hydrostatic pressures by using the Low-Frequency Acoustic Pipe system [12, 13]. (The measurements were performed by A.E. Vovk, T.B. Golikova, and T.B. Gromova.) Samples nos. 1 and 2 made of rubber with cylindrical voids were studied. The samples had a diameter of 150 mm. Sample no. 1 consisted of three layers of voided rubber with the thickness of each layer h = 1.35 cm and with titanium interlayers vulcanized to rubber between them and titanium straps covering the outer surfaces of the sample. The thickness of the interlayers was Δ_1 = 0.1 cm, and the strap thickness was Δ_2 = 0.4 cm. The diameter of the channel was $2a$ = 1 cm, the outer radius of the tube was b = 0.85 cm, the perforation coefficient of the rubber with cylindrical voids was ε^2 = 0.35, and the relative height of the rubber tube was $\frac{h}{b}$ = 1.6. The static shear modulus of the basic rubber material was μ_{st} = (13–15) kg/cm^2, and the shear wave velocity was $c_t \cong 0.5 \times 10^4$ cm/s. The total thickness of sample no. 1 was $H_1 \cong 5$ cm. Sample no. 2 consisted of two samples no. 1, and its thickness was $H_2 = 2H_1 \cong 10$ cm.

Figure 1 presents the frequency dependences of the velocity $c_{ef}^{(p)}$ calculated from Eq. (30) with allowance for Eq. (31) for the rubber structure under study with the parameters specified above. One can see that, in the frequency range up to 5000 Hz, the velocity curves do not intersect the frequency axis; i.e., in the frequency range under study, the elastic waves can propagate along the tube axis. Figures 2 and 3 present the characteristics of the absolute values of the reflection and transmission factors, r and t, calculated by the theory of multilayer systems [14]. In the computational program,

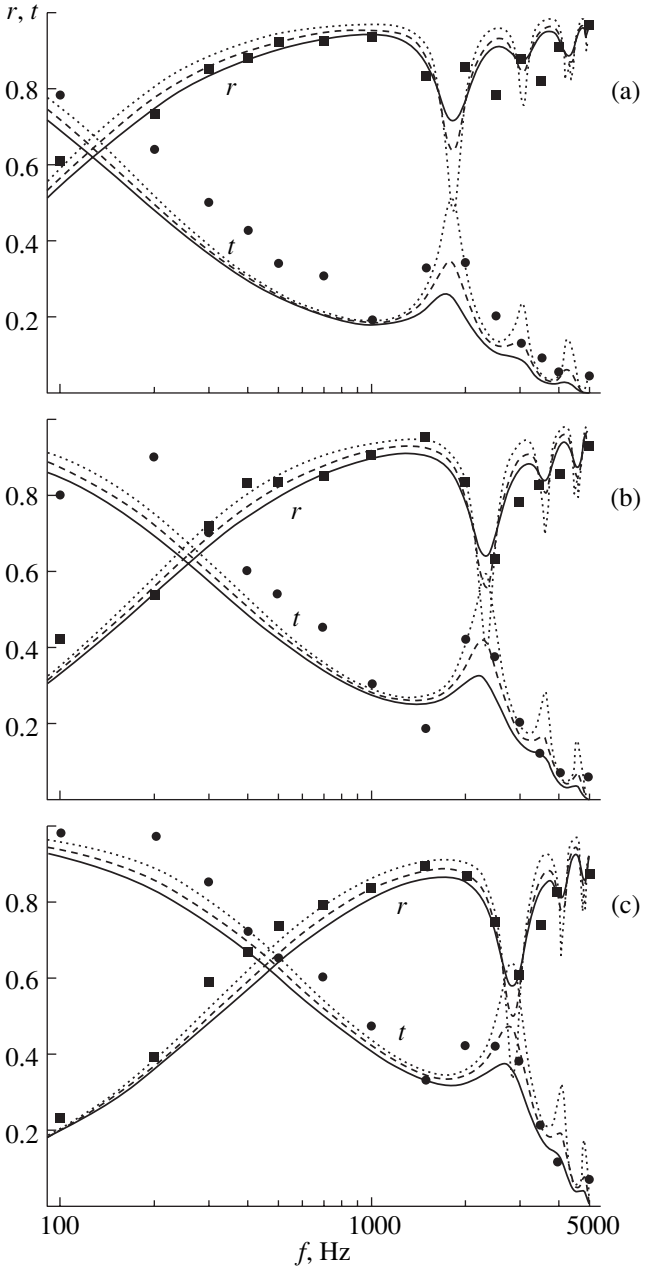

Fig. 2. Frequency dependences of the absolute values of the reflection coefficient r and the transmission coefficient t measured for a three-layer sample made of rubber with cylindrical voids (sample no. 1) under pressures P = (a) 10, (b) 20, and (c) 30 kg/cm^2 and the corresponding calculated characteristics for η_c = (⋯) 0.05, (---) 0.1, and (—) 0.15.

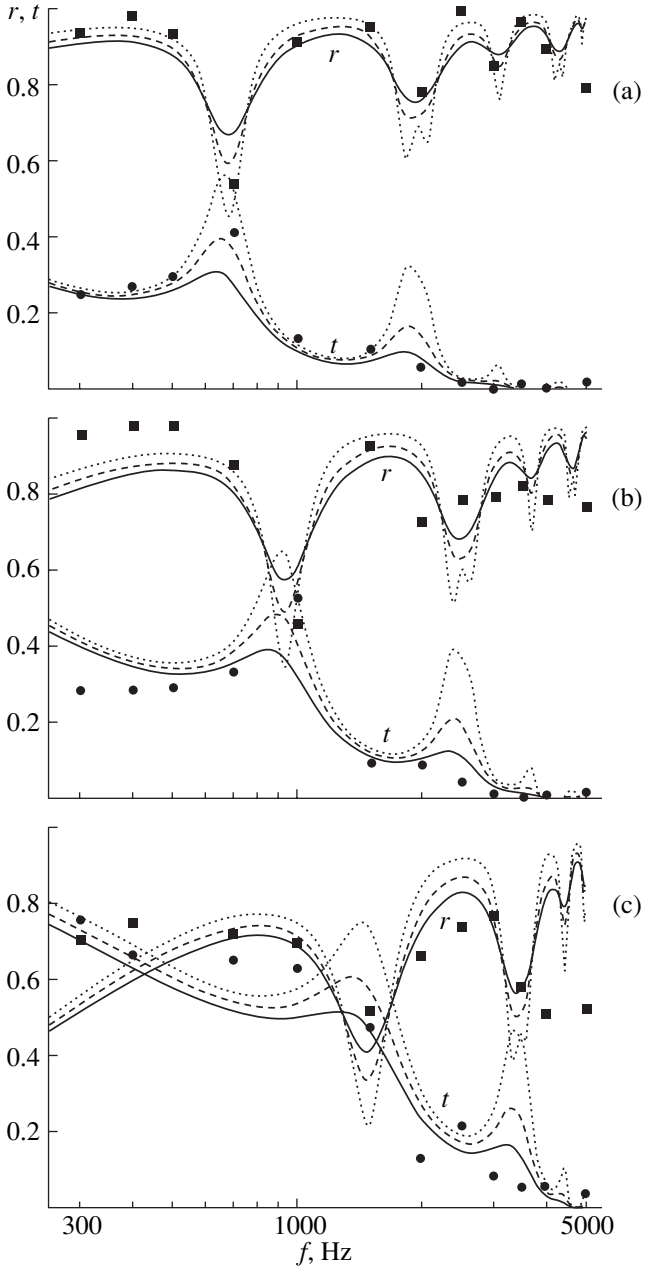

Fig. 3. Frequency dependences of the absolute values of the reflection coefficient r and the transmission coefficient t measured for a six-layer sample made of rubber with cylindrical voids (sample no. 2) under pressures P = (a) 10, (b) 20, and (c) 40 kg/cm^2 and the corresponding calculated characteristics (the notation for the curves is the same as in Fig. 2).

the multilayer system was represented as a cascade connection of quadripoles. The loss coefficients were taken to be η_c = 0.05, 0.1, and 0.15, because η_c could depend on frequency. The experimental values of r and t are represented by dots (squares for the reflection coefficient and circles for the transmission coefficients). The measurements were performed for the hydrostatic pressures P = 10, 20, 30, and 40 kg/cm^2 in the frequency range from 100 (or 300) to 5000 Hz. The water in the experiment was at room temperature. For the pressures P = 10, 20, and 30 kg/cm^2, the calculations agree well with the experimental data. At low frequencies, the curves calculated for the loss coefficient η_c = 0.05 show the best agreement with the measured

characteristics, whereas, at frequencies above 1000 Hz, a better agreement is observed for $\eta_c = (0.1–0.15)$. We note that, since the measurements of η_c for monolithic rubber by the known techniques (specifically, using instrument 3930 by the Bruel and Kjer company for measuring the complex Young modulus [15]) can be performed only for frequencies $f < 500–600$ Hz, the results obtained provide an indirect estimate of the loss coefficient η_c at frequencies above 1000 Hz. At the pressure $P = 40$ kg/cm^2, the difference between the calculations and the experiment proves to be large. Presumably, this can be explained by the effect of the deformations caused by the three-dimensional compression of the voided rubber sample placed in the measuring pipe, because these deformations are not described by the theory [3] of large static deformations of the tube.

Thus, the proposed model, which is developed for the determination of the velocity in a medium containing cylindrical voids with allowance for the dynamic correction on the basis of the previously developed theory [3] of large deformations of the medium under consideration, is experimentally justified. This follows from the fair agreement between the characteristics calculated (using the above-derived formulas for the velocity) for the reflection and transmission coefficients of multilayer samples made of rubber with cylindrical voids and the corresponding experimental data obtained from the measurements in the Low-Frequency Acoustic Pipe in the frequency range 100–5000 Hz under hydrostatic pressures up to 30 kg/cm^2.

REFERENCES

1. *Technical Aspects of Sound*, Vol. 2: *Ultrasonic Range Underwater Acoustics*, Ed. by E. G. Richardson (Elsevier, Amsterdam; Voenizdat, Moscow, 1962).
2. A. E. Vovk, Candidate's Dissertation in Physics and Mathematics (Acoustics Inst., USSR Acad. Sci., Moscow, 1967).
3. V. E. Glazanov, *Screening of Hydroacoustic Antennas* (Sudostroenie, Leningrad, 1986).
4. H. Ko Sung, J. Acoust. Soc. Am. **101**, 3306 (1997).
5. V. V. Tyutekin, Akust. Zh. **2**, 291 (1956) [Sov. Phys. Acoust. **2**, 307 (1956)].
6. V. T. Lyapunov, É. É. Lavendel, and S. A. Shlyapochnikov, *Rubber Vibration Insulators* (Sudostroenie, Leningrad, 1988).
7. H. Kolsky, *Stress Waves in Solids* (Dover, New York, 1963; Inostrannaya Literatura, Moscow, 1965).
8. E. Gibe and E. Blechschmidt, Ann. Phys., No. 8, 417 (1933).
9. A. E. H. Love, *A Treatise on the Mathematical Theory of Elasticity*, 4th ed. (Cambridge Univ. Press, Cambridge, 1927; ONTI, Moscow, 1935).
10. S. P. Strelkov, *Introduction to the Oscillation Theory* (Gos. Izd. Tekh. Teor. Lit., Moscow–Leningrad, 1951).
11. V. E. Glazanov, *Some Problems of Sound Propagation in Elastic Media* (TRTI, Taganrog, 1973).
12. A. V. Vovk, S. P. Klimov, and V. V. Tyutekin, Izmer. Tekh., No. 7, 76 (1975).
13. A. V. Vovk, S. P. Klimov, and V. V. Tyutekin, in *IX All-Union Acoustic Conference* (Acoustics Inst., USSR Acad. Sci., Moscow, 1977), 01VB-5, p. 53.
14. L. M. Brekhovskikh, *Waves in Layered Media*, 2nd ed. (Nauka, Moscow, 1973; Academic, New York, 1980).
15. *Catalog of Devices for Analyzing Sound and Vibration and for Data Processing* (Bruel and Kjer, Denmark, 1978–1981).

Translated by E. Golyamina

Acoustical Physics, Vol. 47, No. 6, 2001, pp. 677–681. Translated from Akusticheskiĭ Zhurnal, Vol. 47, No. 6, 2001, pp. 769–774.

Correlation Properties of the Backscattered Field in a Nonstationary Statistical Problem

O. É. Gulin*, ** and I. O. Yaroshchuk**

** Harbin Engineering University, Harbin, 150001 P. R. China*

*** Pacific Institute of Oceanology, Far East Division, Russian Academy of Sciences, Baltiĭskaya ul. 43, Vladivostok, 690041 Russia*

e-mail: yaroshchuk@mailcity.com

Received December 21, 2000

Abstract—The statistical problem of the scattering of wideband pulses by a random layered medium at normal incidence is considered in the framework of the wave approach in the space–time domain. Simulated correlation functions and power spectral densities of the backscattered field are presented. They extend the earlier findings concerning the backscattered field formation and also confirm and refine a number of conclusions drawn earlier from the behavior of the field's statistical moments. The simulation technique is free from approximations commonly used in the statistical analysis of the propagation problems and can be used to study the statistical properties of the scattered field in a wide range of time intervals, as well as to find the limits of applicability of the approximate methods. © *2001 MAIK "Nauka/Interperiodica".*

Our earlier papers [1–3] addressed the problem of the pulse and signal scattering from a randomly layered medium at normal incidence in the framework of the classical wave approach in the space–time domain. The time behavior of the statistical moments of the backscattered field was studied for the sound velocity fluctuations described by the Markovian process. The stochastic modeling relied on the exact numerical scheme that was based on a combination of analytical and numerical techniques developed earlier for deterministic problems [4]. It should be noted that, although a sufficiently large number of studies are devoted to pulse propagation in inhomogeneous media, the number of papers that address this problem in the framework of the statistical wave theory is not very large. Among these, studies [5–7] are most close to our approach in the initial statement of the problem and in the purpose. In these papers, certain analytical results were obtained for the scattering of smooth pulses: the asymptotic decay behavior of the average intensity, the time evolution of the initial wave form, the probability distribution of the backscattered field, etc. However, studies [5, 6] are mostly mathematical and contain a large number of overlapping assumptions, which make it difficult to understand the final results and limits of their applicability. These circumstances are primarily associated with efforts to convert the results of the approximate analysis of the scattering processes in the frequency domain to the time domain with the help of the Fourier transform. Undoubtedly, of great interest is paper [7], which, in particular, derives the main results obtained in [5, 6] from the asymptotic analysis using a physically clear and elegant approach—an analytical extension of the solution to the steady-state problem with respect to the absorption parameter. Our approach to the problem employs a rigorous simulation technique and removes the limitations imposed on the characteristics of the incident pulses and on the statistical properties of the fluctuating medium. However, the key feature is that this approach is capable of studying the process in arbitrary time domains. In particular, it can derive the transient behavior of the statistical characteristics of the backscattered field, whereas the studies mentioned above describe the processes that evolve mostly in far time regions, in which asymptotic calculations are valid. This paper presents the simulated correlation functions and spectral densities of the backscattered field for two important cases of wideband pulses incident on a random medium: the θ pulse (a constant-amplitude pulse of an infinite duration) and the δ pulse (an infinitely short pulse). It is questionable whether the approximate analysis methods developed in [5–7] can be applied to these pulses.

As previously [1–3], we consider the boundary-value problem of the normal incidence of a pulse $\varphi(|z - L| + c_2 t$ on a randomly layered medium, which occupies part of the uniform space $L_0 < z < L$:

$$\begin{cases} \left(\frac{\partial^2}{\partial z^2} - \frac{1}{c^2(z)}\frac{\partial^2}{\partial t^2}\right)U(z,t) = 0 & (1) \\ \left(\frac{\partial}{\partial z} + \frac{1}{c_2}\frac{\partial}{\partial t}\right)U(z,t)\Big|_{z=L} = \frac{2}{c_2}\frac{\partial}{\partial t}\varphi(t) & (2a) \\ \left(\frac{\partial}{\partial z} - \frac{1}{c_1}\frac{\partial}{\partial t}\right)U(z,t)\Big|_{z=L_0} = 0. & (2b) \end{cases}$$

We assume that the pulse arrives from the right-hand homogeneous semi-infinite space, where $c(z) = c_2$, at the interface $z = L$ at the instant $t = +0$. At times $t > 0$, the fluctuating medium creates the backscattered field $r(|z - L| - c_2 t)$ in this semi-infinite space so that $r(t) = U(L, t) - \varphi(t)$. The subject of inquiry is the time behavior of the statistical characteristics of this field.

The behavior of the statistical moments of the backscattered field for incident pulses of various durations was analyzed in [1, 2]. The scattered field was shown to be nonstationary and was described quantitatively. In this paper, we study the correlation functions and the power spectral densities of the random field $r(t)$ and present the results that extend and refine the earlier findings.

Let the fluctuations of the sound velocity profile be described by the zero-mean Gaussian random process $c(z) = c_0(1 + \varepsilon(z))$ with the correlation function $\langle \varepsilon(z)\varepsilon(z')\rangle = \sigma_\varepsilon^2 \exp(-|z - z'|/l)$, where the intensity of the fluctuations is $\sigma_\varepsilon^2 \ll 1$ and the correlation distance l is the smallest spatial scale of the problem. Based on the previous analysis [1–3], we introduce the parameters that relate the random process to a certain reference narrowband signal with the carrier frequency Ω: the diffusion coefficient $D(\Omega)$ for this frequency [7] and the respective diffusion time scale $T = D^{-1}/c_0$. If $c(z)$ is a deterministic function, a solution to the problem given by Eqs. (1) and (2) at $z = L$, i.e., the field $r(t)$, can be written analytically using a piecewise approximation of the profile $c(z)$ in terms of the appropriate functions to any desired degree of precision. This expression was presented in [1–3] and was used for calculating the field for each realization of the random function $\varepsilon(z)$ specified by its ensemble. Let us consider the results of simulations. As previously [2, 3], in the further analysis, we use only the normalized time variables: $\Omega^* = \Omega T$, $\tau = t/T$, $\xi(z) = T^{-1}\int_{L_0}^{z} d\zeta\, c^{-1}(\zeta)$, $h = \xi(L)$, and $R(\tau) = r(t)/T$. In our calculations, we used the following values: $\Omega^* = 100$, $h = 20$ and 40, and $\sigma_\varepsilon^2 = 0.025$. Note that the chosen frequency of the reference harmonic corresponds to a large number of oscillations that occur on the scale of the diffusion coefficient and also to small inhomogeneity fluctuations. The quantity h determines the thickness of the inhomogeneous layer; it equals the average time for the wave to pass through the layer [2]. The above values of h (it must be $h \gg 1$; see, e.g., [7]) refer to the case, in which a monochromatic wave with the frequency Ω is totally reflected by the layer of the fluctuating medium with probability approaching unity.

We considered incident pulses belonging to two limiting cases: a pulse of a very long duration η (the time the pulse acts on the layer interface), in particular, the Heaviside unit step function $\theta(\tau)$, and a very short pulse (a model of the δ pulse). From the viewpoint of specifying the parameters of the problem, the term *short pulse* means that its duration is $\eta \ll 1 < h$ and, in general, η can be comparable with or even less than the time for the leading edge of the pulse to travel a distance equal to the correlation distance of the inhomogeneous medium. Conversely, a pulse of a very long duration means that $\eta > 2h$. These cases basically differ from the situations in which efforts were made earlier to obtain asymptotic results by approximate methods [5–7]. These works assumed the incident pulse to be narrowband and to have a smooth wave form. Importantly, the function that describes the propagation of the step $[\varphi(t) = \theta(t)]$ is the Green function of problem (1), (2). Therefore, it can be used to study the problem with any other $\varphi(t)$. It was shown earlier [2, 3, 8] that the backscattering process is essentially nonstationary and that this nonstationary time interval is considerably long. In particular, for the δ pulse, the transient domain lies in the time interval $0 < \tau < 20$, during which the major part of the energy of the incident pulse is emitted back from the medium. As for the Green function, the region of its pronounced nonstationary behavior expands to $\tau \sim 35$–40. As is known, the correlation function and the power spectral density of the backscattered field for the general nonstationary process can be written, respectively, as

$$\Psi(\tau, \delta) = \langle R(\tau)R(\tau + \delta)\rangle$$

$$= \int_{-\infty}^{\infty} d\omega_1 \int_{-\infty}^{\infty} d\omega_2 \langle \hat{R}(\omega_1)\hat{R}^*(\omega_2)\rangle \exp\{i\omega_1\tau - i\omega_2(\tau + \delta)\},$$

$$S_\omega(\tau) = (2\pi)^{-1}\int d\delta \Psi(\tau, \delta)e^{-i\omega\delta}$$

$$= e^{-i\omega\delta}\int_{-\infty}^{\infty} d\omega_1 \langle \hat{R}(\omega_1)\hat{R}^*(\omega)\rangle \exp\{i\omega_1\tau\}.$$

We consider the power spectral density as a function of time characterized by its instantaneous values. The evolution of $S_\omega(\tau)$ shows the frequency content of the backscattered field at a particular time moment.

In the process of simulations, we averaged the results over an ensemble of $N = 1000$ random field realizations, which is quite sufficient for obtaining reliable statistical results in this problem. The qualitative behavior of the moments of the field $R(\tau)$ is clearly seen even with a considerably smaller number of realizations. Figure 1 shows the correlation coefficient of the backscattered field versus time in the interval $\delta \in [-2, 2]$ for the incident θ pulse. It is seen that, in the region of the nonstationary behavior, not only the amplitude of the correlation function $\Psi(\tau, 0) = \langle R^2(\tau)\rangle$ decreases [3], but also the correlation scale of the backscattered field changes (the relative width of the correlation coefficient gradually grows and its small-scale fluctuations disappear). The increase in the width of the correlation coefficient means that the power spectral density of the process becomes narrower. In fact, with increasing the observation time τ, the high-frequency components dis-

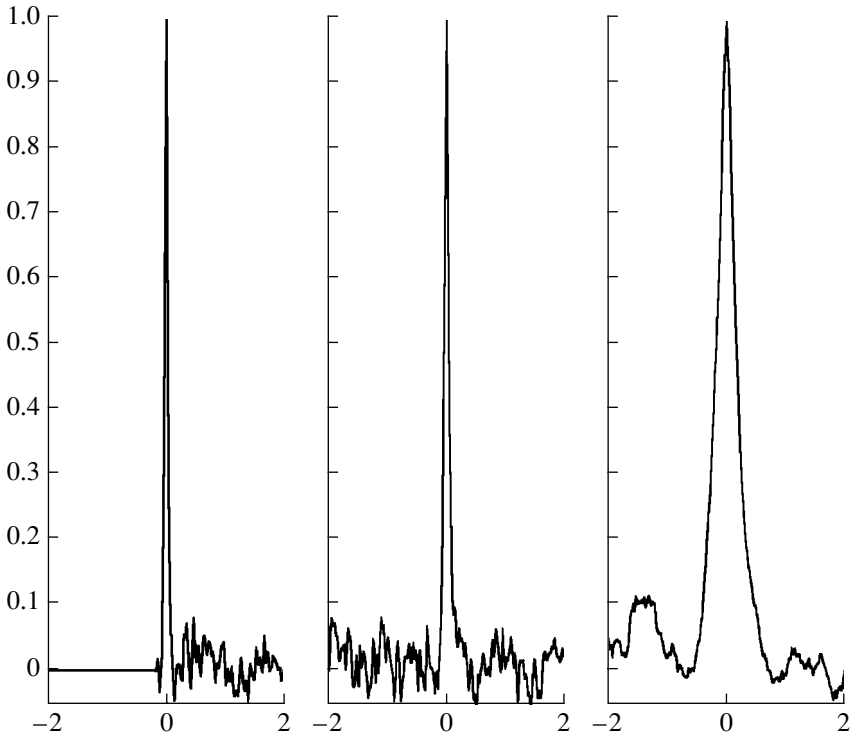

Fig. 1. Correlation coefficient of the backscattered field versus time for the incident θ pulse at the observation times (from left to right) $\tau = 0.2$, 2, and 35.

appear from the power spectrum of the backscattered field and the spectrum gradually moves to the low-frequency region, as shown in Fig. 2. Simultaneously, its amplitude increases near $\omega^* \sim 0$. This behavior validates the qualitative considerations presented in [3]. The low-frequency components of the spectrum form the infinite tail of the θ pulse and penetrate deep into the medium without being scattered. These are the components that cause the second moment of the backscattered field to decay as the power-law function, which was established in [5–7] as the asymptotic limit for the narrowband or video pulses incident on the medium. The power-law field decay in the region of transient processes was also studied in [8], where the law $\sim\tau^{-0.5}$, $\tau \in (20, 40)$, was obtained for the θ pulse. Figures 1 and 2 thus show that the scattering process for the case of the Green function does not become stationary in this problem, and only a certain quasi-stationary mode can be observed within the time interval $\tau \sim (30–40)$, in which $\Psi(\tau, 0) = \langle R^2(\tau)\rangle$ reaches a level of $\cong 0.8 \times 10^{-3}$ [3] and slowly decays further as $\sim\tau^{-0.5}$. It was supposed in [3] that, beginning with these times, the backscattered field can be considered as stationary. The above analysis however shows that this supposition is not completely valid. To a good accuracy, it is valid only for the mean $\langle R(\tau)\rangle$. To illustrate this statement, Figs. 3a and 3b present the functions $\langle R^2(\tau)\rangle$ for very long observation times up to $\tau \sim 80$ [they correspond to the layer dimensions of $(L - L_0) \sim 4000l$] and the monotone curve $\sim\tau^{-0.5}$, which approximates it in terms of the least-squares approach.

Consider the incident pulse in the form of the δ pulse. The correlation functions are similar to those shown in Fig. 4. However, they feature a much smaller relative width, i.e., in this case, the correlation in the backscattered field covers much shorter times and only very weakly tends to grow with τ. The power spectrum of the process at different observation times is shown in Fig. 4. Its specific feature is that the high-frequency components decrease with time. In this case, the amplitude of the low-frequency components ($\omega^* \sim 0$) is very small, which indicates that they carry a small portion of the backscattered energy. The frequency spectrum of the δ pulse is uniform. Therefore, the backscattered field is to a greater degree (than for the θ pulse) determined by high frequencies, which are scattered by the medium. The same behavior as for the θ pulse is observed: the high-frequency harmonics are intensely emitted back from the medium, carrying away almost all of the energy of the incident δ pulse by the instant of time $\tau \sim 20$.

The results of the statistical simulations presented in this paper describe the time interval of pronounced transient processes in the backscattered field, in which approximate asymptotic formulas [5–7] for the second statistical moment of the field $R(\tau)$ for $\tau \longrightarrow \infty$ fail. We have also noted that these formulas can prove to be of little use for the analysis of such incident pulses as the

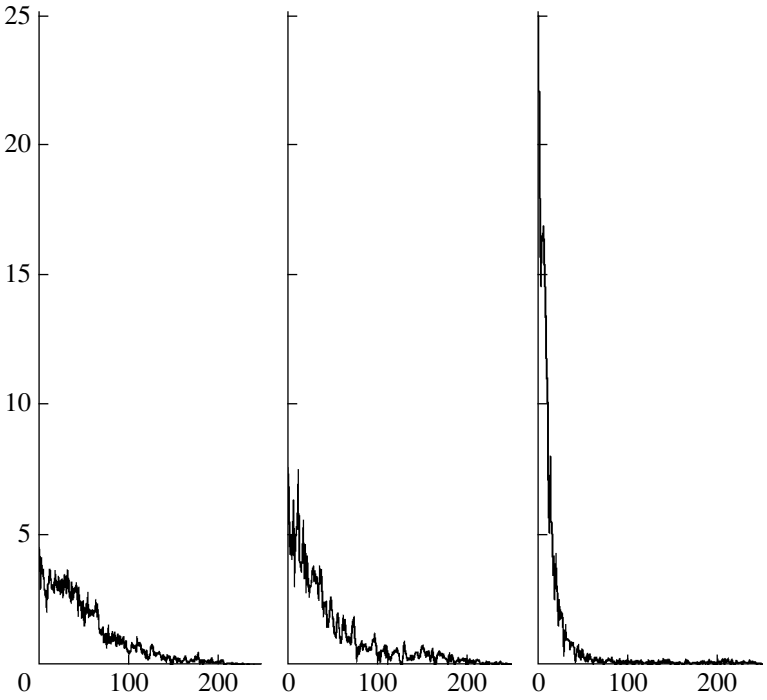

Fig. 2. Power spectra for the correlation coefficients shown in Fig. 1.

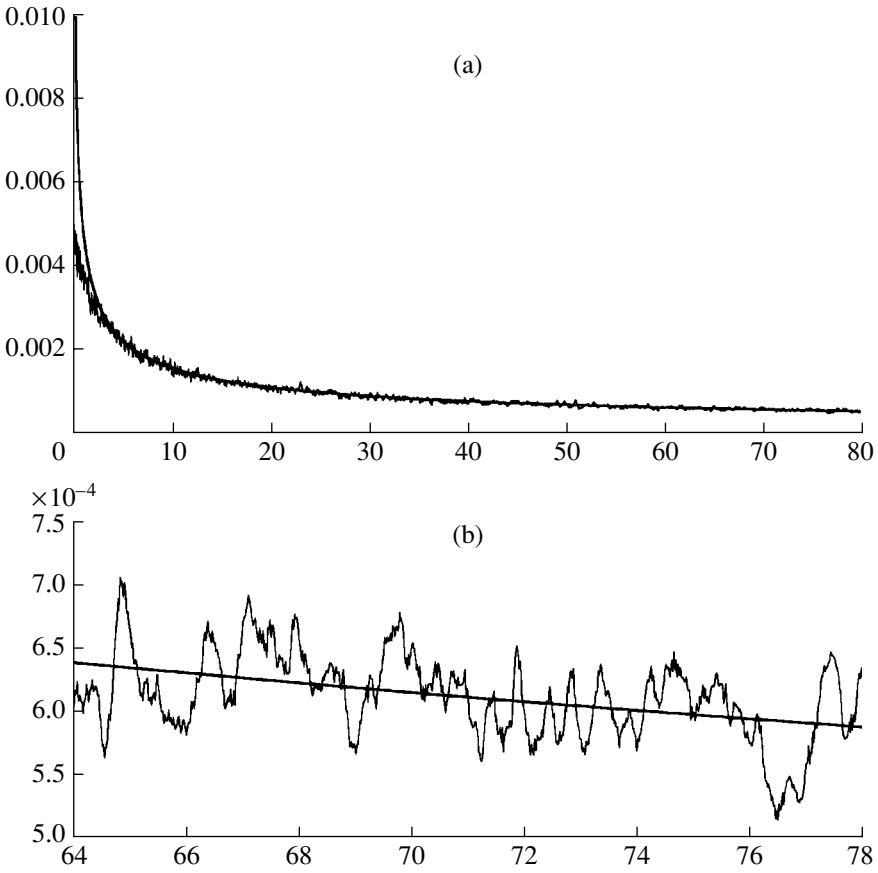

Fig. 3. (a) Function $\langle R^2(\tau)\rangle$ for a very thick layer of the random medium and (b) a scaled-up fragment of the plot at long observation times with the monotone curve $\sim\tau^{-0.5}$ approximating it in terms of the least-squares approach.

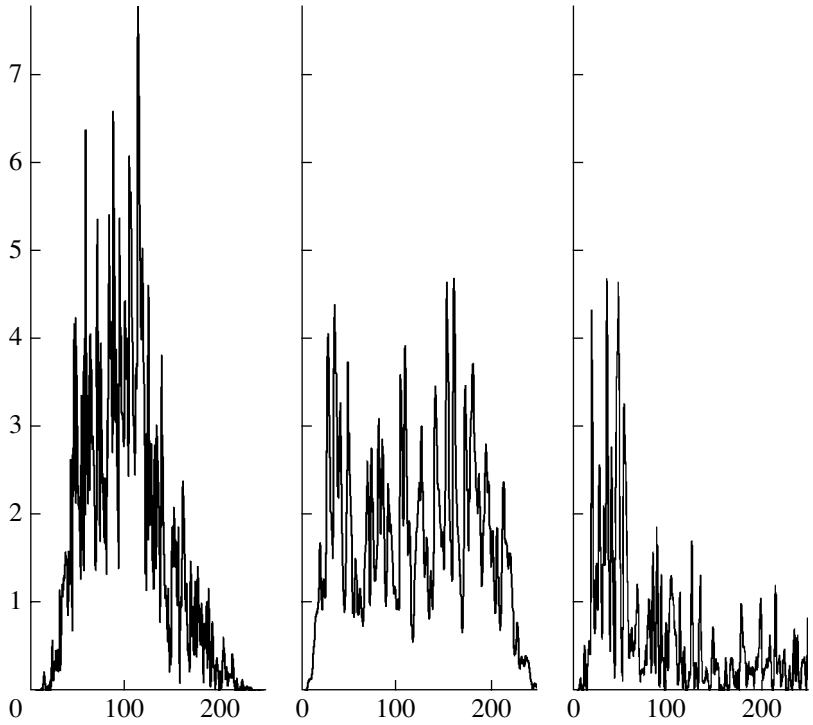

Fig. 4. Power spectra of the backscattered field for the incident δ pulse at the observation times (from left to right) $\tau = 0.2$, 10, and 35.

wideband δ and θ pulses, because they are obtained under the assumption that the pulse incident on the random medium is smooth and bandlimited. These considerations are corroborated by the above-mentioned power-law time behavior of the moments of the backscattered field studied in [8]. Even for sufficiently long observation times τ, exponents of these functions often differ from those predicted by the asymptotic analysis [5–7]. We observed these differences in the function $\langle R^2(\tau)\rangle$ for the δ and θ incident pulses and for a finite rectangular pulse [8]. We have also found that the correlation time of the backscattered field is longer than previously considered, which is particularly pronounced in the case of the Green function. This case is most complex from the viewpoint of simulations. Calculations with the accuracy required for the generalized θ function are only possible due to the numerical scheme based on explicit analytical expressions [2, 3], which describe the solution to the boundary-value problem given by Eqs. (1) and (2).

REFERENCES

1. O. É. Gulin and I. O. Yaroshchuk, in *Acoustics of the Ocean* (GEOS, Moscow, 1998), pp. 243–246.
2. O. É. Gulin and I. O. Yaroshchuk, Izv. Vyssh. Uchebn. Zaved., Radiofiz. **42** (4), 383 (1999).
3. O. É. Gulin and I. O. Yaroshchuk, Akust. Zh. **45**, 781 (1999) [Acoust. Phys. **45**, 704 (1999)].
4. O. É. Gulin and V. V. Temchenko, Zh. Vychisl. Mat. Mat. Fiz. **37** (4), 499 (1997).
5. R. Burridge, G. Papanicolaou, and B. White, SIAM J. Appl. Math. **47** (1), 146 (1987).
6. R. Burridge, G. Papanicolaou, and B. White, SIAM J. Appl. Math. **49** (3), 582 (1989).
7. V. I. Klyatskin and A. I. Saichev, Usp. Fiz. Nauk **162** (3), 161 (1992) [Sov. Phys. Usp. **35**, 231 (1992)].
8. O. E. Gulin and I. O. Yaroshchuk, Proc. Inst. Acoust. (UK) **21**, Part 9, 111 (1999).

Translated by A. Khzmalyan

Acoustical Physics, Vol. 47, No. 6, 2001, pp. 682–687. Translated from Akusticheskiĭ Zhurnal, Vol. 47, No. 6, 2001, pp. 775–780.

Comparative Analysis of the Search Procedures for Surface Acoustic Wave Solutions in Piezoelectric Crystals

M. Yu. Dvoesherstov, V. A. Savin, and V. I. Cherednik

Lobachevskiĭ State University, Nizhni Novgorod, pr. Gagarina 23, Nizhni Novgorod, 603600 Russia

e-mail: sva@rf.unn.runnet.ru

Received November 27, 2000

Abstract—Various search procedures for finding the global extremum of a multivariate target function (TF) necessary for calculating the characteristics of surface acoustic waves (SAW) and leaky surface acoustic waves (LSAW) in crystals are analyzed. The search procedures aimed at determining the optimal orientations for SAW in crystals are considered. A comparative analysis of the promising methods for finding the global extremum of the TF is performed. © *2001 MAIK "Nauka/Interperiodica".*

One of the specific features of the SAW technology is that, prior to designing any SAW device (a generator, delay line, filter, etc.), it is necessary to determine the orientation in the piezocrystal space for the wave propagation with optimal characteristics. The optimal characteristics of SAW and leaky SAW (LSAW) are known to be as follows [1]: thermal stability in a wide range of temperatures (expressed by the temperature coefficient of frequency TCF), a high electromechanical coupling factor K^2, a small angle between the directions of the group and phase velocities pfa, and a small diffraction loss characterized by the anisotropy factor ($\gamma = -1$). In the case of LSAW, it is also necessary to have a low damping factor δ along the direction of wave propagation. It is well known that, to find the wave parameters K^2, pfa, γ, and TCF, one should first determine the phase velocity of the wave V and the damping factor δ.

To determine V and δ, and also the optimal orientation for SAW and LSAW in the piezocrystal space, various search procedures for finding the global extremum of a multidimensional target function (TF) can be used [2–7]. The value of TF depends on the three Euler angles, f1, f2, and f3; [8] describing the crystal cut and the direction of wave propagation; and also on the values of material constants of the piezocrystal. The parameters of the TF are the wave velocity V and the damping factor δ. In its turn, finding the extremum of the TF in terms of the optimal characteristics of SAW and LSAW is a separate complicated computational problem of a multiparameter search for the extremum of the TF [2, 9].

The object of this work is to perform a comparative analysis of several search methods for finding the global extremum of a multivariate function with the aim to solve the above-mentioned problems.

We use the equations describing the propagation of an acoustic wave in a piezocrystal [1]:

$$\begin{aligned} \rho\frac{\partial^2 u_j}{\partial t^2} - C_{ijkl}\frac{\partial^2 u_k}{\partial x_i \partial x_l} - e_{klj}\frac{\partial^2 \varphi}{\partial x_i \partial x_k} &= 0, \\ e_{ikl}\frac{\partial^2 u_k}{\partial x_i \partial x_l} - \varepsilon_{ik}\frac{\partial^2 \varphi}{\partial x_i \partial x_k} &= 0. \end{aligned} \tag{1}$$

Here, C_{ijkl}, e_{ikl}, and ε_{ik} are the material constants of the piezocrystal, u_i are the mechanical displacements, φ is the potential, ρ is the substrate density, t is time, and x_j are the spatial coordinates. The indices are $i, j, k, l = 1, 2, 3$.

To calculate the characteristics of SAW and LSAW propagating at the free surface of a piezocrystal, we should solve the system of equations (1) formulated for an anisotropic piezoelectric medium. If a layer of finite thickness covers the surface of the piezocrystal, a problem of the propagation of SAW in the layer–piezoelectric substrate structure should be solved. In this case, we have two systems of equations (1) relating respectively to the layer material and the substrate material. In both cases, the equations that describe the wave propagation cannot be solved analytically and require the utilization of numerical methods.

Directing the x_1 axis along the wave propagation at the surface (the x_3 axis is normal to the surface), we can write the required solutions for the displacement amplitudes and for the potential in the piezocrystal space as follows:

$$\begin{aligned} u_j &= \alpha_i \exp(jk\beta x_3)\exp\{jk[(1 + i\delta)x_1 - Vt]\}, \\ \varphi &= \alpha_4 \exp(jk\beta x_3)\exp\{jk[(1 + i\delta)x_1 - Vt]\}. \end{aligned} \tag{2}$$

Here, $k = \omega/V$ is the wave number, and ω is the circular frequency. The first exponents in Eqs. (2) describe the decrease in amplitude along the x_3 direction with the

damping factors β determined by their imaginary parts, and α_1 and α_4 are the unknown amplitude factors.

The substitution of Eqs. (2) into Eqs. (1) leads to a system of dispersion equations, which is a homogeneous system of algebraic equations in the unknown variables β for the predetermined values of V and δ. Further, it is necessary to use the boundary conditions at the mechanically and electrically free surface of the crystal [1]: the zero values of the normal components of the stress tensor T_{3i} and the continuity of the normal component of the electric displacement D_3. As a result, we obtain a system of homogeneous complex equations, which has a nontrivial solution only when its determinant, depending on the velocity V and the coefficient δ, is zero:

$$F(V, \delta) = 0. \quad (3)$$

Here, $F(V, \delta)$ is the determinant or the function of the boundary conditions. Generally, $F(V, \delta)$ is a complex function of two real variables, V and δ. According to Eq. (3), the values of V and δ should be found for which both real and imaginary parts of the function $F(V, \delta)$ become zero. The function of the boundary conditions $F(V, \delta)$ is taken as the TF. To solve the Eq. (3), we use a variety of techniques to search for the global extremum of the multivariate target function. We seek the global extremum (the zero minimum) of the TF that is the square of the magnitude of the complex function $F(V, \delta)$. Note that, in the case of the SAW solution ($\delta = 0$), one should minimize the function of one variable $|F(V)|^2$, and in the LSAW case, the function of two variables $|F(V, \delta)|^2$ should be minimized.

The most used search procedures for finding the global extremum of the TF can be classified as follows [5]:

(1) methods of transition from one local minimum to another;

(2) random search methods;

(3) methods based on statistical models of the TF;

(4) covering methods; and

(5) methods of an incomplete directed scanning of the search area.

The main problem in the development of efficient procedures for global search is related to the necessity of assessing a great number of variants. It is generally recognized [5] that none of the search methods possesses such advantages over the other ones to be considered a universal means for solving any problems. Besides, the total number of the TF calculations required to determine the coordinates of the extremum point grows as a power function of the dimensionality of the search area for the majority of the global search procedures.

For the solution of complex optimization problems, such search procedures are required that possess the following set of necessary features:

(1) a high reliability of the extremum search;

(2) the minimal sensitivity to the details of the TF relief, including the ravine situations, the small-slope regions, and the local-extremum regions;

(3) the ability to work in a space of high dimensionality;

(4) the minimal number of adjustable parameters; and

(5) low cost of the search.

This combination of features of the search procedures is contradictory to a considerable extent and, hence, difficult to realize.

The LSAW, contrary to SAW, attenuate along the direction of wave propagation x_1 at the surface ($\delta > 0$). Two types of LSAW are known [9]: the pseudosurface acoustic waves (PSAW) and the high-velocity pseudosurface acoustic waves (HVPSAW). In the SAW and LSAW search area, the TF is almost always a multiextremal function. Furthermore, a complex behavior of the TF for some orientations is attributable to the fact that, for these orientations, the system of dispersion equations becomes ill-conditioned, the corresponding matrix is almost singular, and the problem as a whole becomes ill-posed.

The complications arising in the search for the LSAW solutions in piezocrystals can be illustrated by a specific example. Figures 1 and 2 demonstrate the reliefs of the TF, $F(V, \delta) = 0$, calculated for a $LiNbO_3$ crystal cut with the (0°, –49°, 0°) orientation and covered with an aluminium layer ($h = 0.01\lambda$, where λ is the wavelength) in the velocity V and damping factor δ domain. Figures 1 and 2 relate to the PSAW and to the HVPSAW cases, respectively. It is seen from the figures that the TF reliefs have a rather intricate shape (with many deep and narrow local extremums). This fact limits the possibility of the application of many currently known procedures of global search [5, 6]. The methods of transition from one local minimum to another use in most cases the derivatives of the TF, which is inefficient in the flat-plateau situations. The methods based on statistical models of the TF and the random search methods too strongly depend on the adjustable parameters in the situations with a large number of narrow deep extremums, which makes them inoperative in the absence of *a priori* information on the TF behavior. It only remains to rely on some specific versions of the covering methods and on the methods of an incomplete directed scanning of the search area. In deciding on a particular search procedure, one should also take into account one more specific criterion of efficiency, the computational speed. The search procedures should quickly process their specific information. The high speed requirement for a search procedure is reduced to its software implementation possessing such operating speed that allows the absolutely predominant share of computation time to be allocated to the fulfilment of the model procedure of the user.

Below, we briefly describe three search procedures for finding the global extremum of the TF given

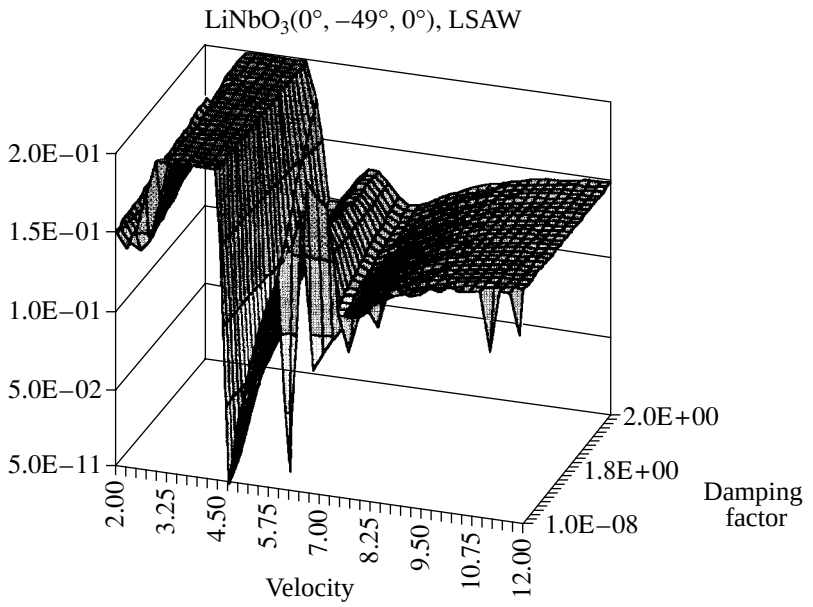

Fig. 1. Relief of the target function $F(V, \delta)$ used in the search for an LSAW solution in a $LiNbO_3$ crystal with the (0°, –49°, 0°) orientation.

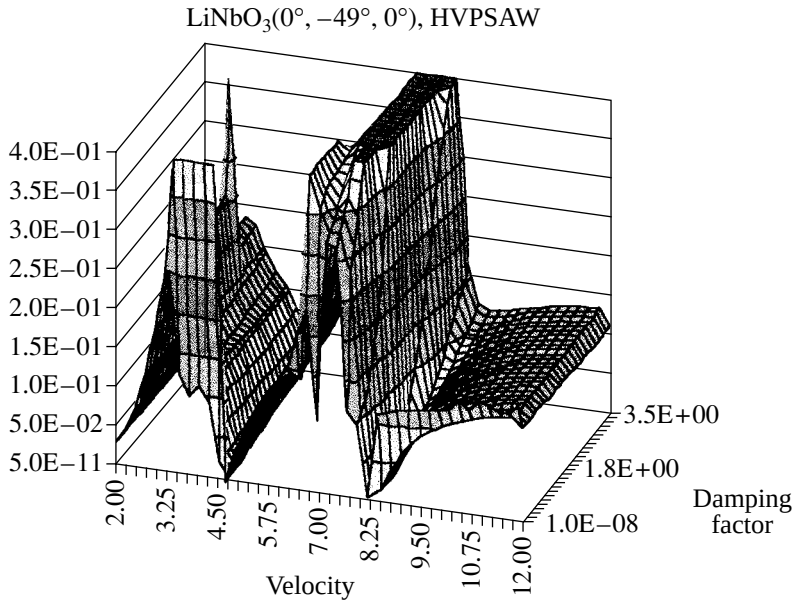

Fig. 2. Relief of the target function $F(V, \delta)$ used in the search for an HVPSAW solution in a $LiNbO_3$ crystal with the (0°, –49°, 0°) orientation.

by Eq. (3) in the calculation of the main characteristics of LSAW.

(1) One of the possible implementations of the covering method is the Hooke–Jeeves Search (HJS) [2–4]. The HJS is a version of the local extremum search by the method of configurations in space. However, this technique can also be adapted for seeking the global extremum of the TF by performing a global exhaustive search over a determinate searching mesh in combination with the local search over the promising points. The local search can be performed by the HJS with the automatic inclusion of the Mudgel procedure in the case of the configuration method failure in ravine situations [4]. The investigated area is covered by a uniform searching mesh. Then, a local search is performed, beginning from an arbitrary point in the area and leading to a local extremum. The values of the TF at the mesh nodes are compared with the values at the

local extremum found. If a point is found that is better than the previous one, the local search is continued from this point on, leading to a new better local extremum, and so on. As a result, after the exhaustive search over the whole mesh is completed, the last of the extremums found will be the global one. A distinctive feature of this procedure is its simplicity, which makes it possible to create a short program implementing this algorithm. In the HJS procedure, the search is performed over a large number of points, but only once and without any additional processing.

(2) Another global-search implementation of the covering method is the Nelder–Meed Search (NMS). This procedure implies the definition of a mesh of starting points followed by the search for a local extremum on the basis of the deformed-polyhedron technique [6]. The local search consists in the determination of the TF values at sampling points belonging to the search area and being the vertices of a polyhedron. The special operations that deform the polyhedron in the space of variables and shift it to the region of the most probable location of an extremum finally result in an exact determination of the coordinates of this extremum. A distinctive feature of the procedure is its low sensitivity to the details of the TF relief: the ravines and the small-slope regions are successfully overcome. The procedure is reliable for the space dimensionality up to ten, the cost of the search being very low. In terms of the global search organization, the competition of starting points is realized.

(3) One of the possible implementations of the method of incomplete directed scanning of the search area is the determinate procedure of seeking the global extremum over the discrete mesh defined by the Grey binary code, the Global Discrete Search (GDS) [7]. A characteristic feature of this procedure is the discretization of variables. In this case, the whole space is covered with the regular mesh whose nodes characterize definite states of the described object. The discretization step in each variable represents the accuracy of the extremum determination. Any discrete state of the object can be unambiguously represented by the binary numbers of the discrete states of each variable, these numbers being recorded in series. In the search procedure under consideration, the state of the object is recorded in terms of the Grey reflexive binary code [7]. Thus, the problem of finding the minimum is reduced to the combinatorial problem of finding a binary word of predetermined length, which satisfies the condition of the minimal value of the TF. The operation of the search procedure consists in the creation of a set of sampling points with an adjustable density of positions relative to the point that is the best at the moment. The specific processing of the information about the values of the TF at the sampling points provides the advance into the region of the most probable location of the global extremum. The advance towards the extremum takes place not along the relief of the TF, but within a cloud that moves with all its points in the direction of the expected position of the extremum. The program implementing this algorithm provides an effective operation in the space of high dimensionality (about ten) and is characterized by a nearly linear growth of the search cost with the number of dimensions of the problem being solved. The only adjustable parameter is the discreteness of the search space.

The comparison of the search procedures for finding the global extremum of the TF was performed by the example of the search of LSAW solutions at the open surface of a $LiNbO_3$ piezocrystal with the (0°, –49°, 0°) orientation. For the LSAW problem, the search for the global minimum was carried out in a two-parameter region formed by the velocity V (km/s) and the damping factor δ (dB/λ, where λ is the wavelength). The coordinates of the initial starting point were chosen at random. The required accuracy of calculating the extremum coordinates corresponded to the accuracy of real data provided by the IBM PC.

In the course of the HJS search procedure for the LSAW problem, after performing 281 calculations of the TF, the parameters $V = 4.7515$ km/s and $\delta = 2.4 \times 10^{-4}$ dB/λ were found with the TF value about 1.2×10^{-18}. For the HVPSAW problem, after performing 4263 calculations of the TF, the parameters $V = 8.314$ km/s and $\delta = 0.531$ dB/λ were found with the TF value of 1.2×10^{-18}. In both cases, the values obtained correspond to the global optimal solutions for the respective types of waves. The considerable search cost in the HJS procedure is explained by the small spacing of the initial searching mesh used for starting the procedure of the local search.

The NMS search procedure was performed with ten starting points. Their coordinates corresponded to a uniform mesh superimposed on the search area. In the course of the LSAW search, a total of 1510 calculations of the TF were made, which corresponds to an average of 151 calculations of the TF at each local descent. All ten descents were completed in the accuracy-tolerable vicinity of the global optimal point with the final values of the TF being of the order of 10^{-17}–10^{-19}. For the HVPSAW problem, 1700 calculations of the TF were made, which corresponds to an average of 170 calculations of the TF at each local descent. As a result, a high probability of hitting the basin of the global extremum was demonstrated: nine out of ten descents were completed in the accuracy-tolerable vicinity of the global optimal point with the final values of the TF being of the order of 10^{-14}–10^{-18}, and only one led to the point of a false local minimum.

In the case of the GDS procedure, the discretization of variables corresponded to the required accuracy of calculating the coordinates of the global extremum. The search was performed with ten starting points, which were generated by the program on the basis of a predetermined initial point and scattered approximately uniformly over the search area. In the course of the LSAW search, a total of 2770 calculations of the TF

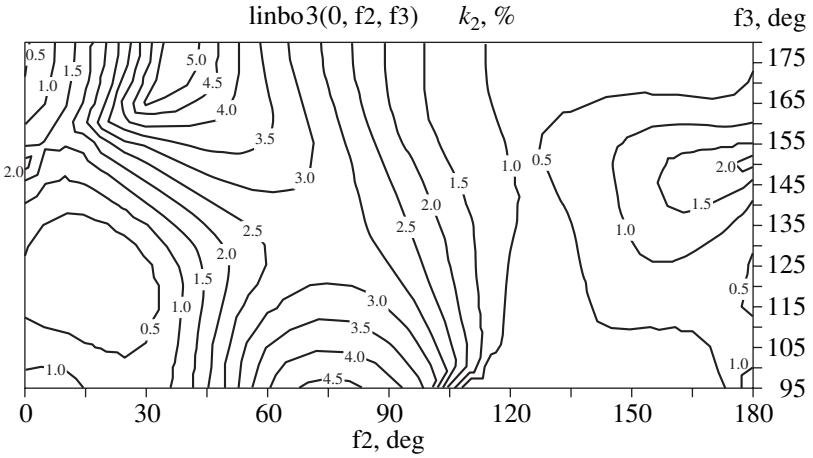

Fig. 3. Lines of equal value for K^2 in the $LiNbO_3$ crystal (f1 = 0°, f2 = 0°–180°, and f3 = 95°–180°).

were made. In this case, the search of one extremum (or the confirmation of one already found) took on average about 214 calculations of the TF, and the check of the width of a newly-found one took about 630 calculations. As a result of the search beginning from all ten starting points, the global extremum was found. In the course of the HVPSAW search, a total of 4915 calculations of the TF were made with the search of an extremum taking on average about 304 calculations of the TF and the check of its width taking about 625 calculations. The search using seven starting points resulted in finding the global extremum with three of them leading to the points of false local minimums. This allows us to assess the reliability of the GDS procedure of seeking the global extremum in the problems under consideration at about 85%, which is a rather high value at a relatively low cost of the search. The results presented above confirmed once more that the GDS search procedure provides a fast advance towards the extremum just after the start from the initial point and a rather slow refinement of its position. The refinement cost can be several times higher than the cost of the approximate determination of the extremum position.

The analysis of the costs of the global search by the procedures chosen for solving the problems of acoustoelectronics confirms their effectiveness in solving practical problems. At the same time, the HJS procedure, which uses a fine mesh of starting points, may well prove to be insufficiently economical for the problems of higher dimensionality. If the search space has four to eight dimensions, the NMS procedure with a sparse mesh of starting points is preferable. Its ability to move towards the extremum with the set of sampling points of a polyhedron appears to be better than any search strategy of the configuration method. In the problems of even higher dimensionality, the GDS procedure proves to be the most effective one. However, by virtue of the discrete nature of the search space, the user has to select this discreteness rather carefully. A too minute representation leads to unjustified search costs, whereas a too rough representation can reduce the reliability of the global search (i.e, increase the probability of missing the extremum).

The search for the spacial orientations corresponding to the optimal value of some parameter of SAW or their linear combination can also be efficiently performed by the above-mentioned procedures of seeking the global extremum of the TF. In this case, the global search should be carried out over all three Euler angles. The TF can be formed as a linear combination of the main parameters of the wave with individual weighting (expert) factors, which provide the variations of individual contributions to the TF. It is hard to expect that there exist orientations for which the values of all SAW parameters become optimal at the same time. It is more realistic to search for the optimal value of the parameter that is most important for a given specific application [2]. It is also possible to search for a compromise between several TF-forming parameters of the wave. An example of the solution of such a problem is the result of the search for the maximal value of the electromechanical coupling factor K^2 for SAW in a $LiNbO_3$ piezoelectric crystal. Using the above-mentioned procedures for the TF extremum search, we calculated the lines of equal value for K^2 in the region of the Euler angles f1 = 0°, f2 = 0°–180°, and f3 = 95°–180°. It is seen from Fig. 3 that, in this case, the region of the maximal value of K^2 (which is within 4–5%) lies in the intervals of the Euler angles f2 = 60°–95°, f3 = 95° and f2 = 30°–45°, f3 = 160°–180°.

The results presented allow us to conclude that the procedures described above are suitable for seeking the SAW and LSAW solutions in piezocrystals. A method for the numerical calculation of the characteristics of SAW and LSAW is proposed on the basis of different search procedures for finding the global extremum of a multivariate function. The procedures for seeking the global extremum of the TF were used for the minimiza-

tion of the function $F(V, \delta)$ of the boundary conditions and for finding the spatial orientations that corresponded to the optimal values of the SAW and LSAW parameters.

The characteristic features of different methods used for seeking the global extremum of the TF were considered. It was shown that none of the search procedures possesses such advantages over the other ones as to be considered the universal means for solving problems. The calculations performed allow us to conclude that, in the search for the LSAW solutions and also for the optimal orientations of SAW in crystals, it is expedient to use a diversity of global-search procedures. In this case, the probability of finding the true solutions will be drastically increased.

A promising idea is to increase the efficiency of solving the search problems by using the dialog mode of interaction with a computer. Then, choosing the optimal search procedures at individual stages of the problem solution and possessing a wide variety of means, one can quickly obtain the required results.

REFERENCES

1. Farnell, J., in *Acoustic Surface Waves*, Ed. by A. A. Oliner (Springer, New York, 1978; Mir, Moscow, 1981).
2. M. Yu. Dvoesherstov, V. I. Cherednick, A. P. Chirimanov, and S. G. Petrov, Proc. SPIE **3900**, 283 (1999).
3. D. J. Wilde, *Optimum Seeking Methods* (Prentice-Hall, Englewood Cliffs, N.J., 1964; Nauka, Moscow, 1967).
4. I. D. Hill, IEEE Trans. Syst. Sci. Cybern. **SSC-S** (1), 2 (1969).
5. A. Zhilinskas, *Global Optimization* (Mokslas, Vilnius, 1986).
6. D. M. Himmelblau, *Applied Nonlinear Programming* (McGraw-Hill, New York, 1972; Mir, Moscow, 1975).
7. A. M. Botenkov, V. A. Vazin, B. S. Voinov, *et al.*, Preprint No. 8711, RTI AN SSSR (Radiotechnical Inst., USSR Academy of Sciences, Moscow, 1988).
8. M. P. Shaskol'skaya, *Acoustic Crystals* (Nauka, Moscow, 1982).
9. M. P. Cunha, in *Proceedings of IEEE Ultrasonics Symposium* (1997), p. 97.

Translated by A. Kruglov

Acoustical Physics, Vol. 47, No. 6, 2001, pp. 688–694. Translated from Akusticheskiĭ Zhurnal, Vol. 47, No. 6, 2001, pp. 781–788.

Acoustic Power Flux in a Waveguide

V. A. Eliseevnin and Yu. I. Tuzhilkin

Andreev Acoustics Institute, Russian Academy of Sciences,
ul. Shvernika 4, Moscow, 117036 Russia

e-mail: bvp@akin.ru

Received June 14, 2000

Abstract—The acoustic power flux that occurs in an ideal waveguide in the presence of two modes propagating in it is considered. Singular points of the saddle and vortex types are found for modes of different numbers. The regions lying near the vortex-type points and characterized by the inverse direction of the power flux (i.e., from the receiver to the source) are determined. When a low-number mode propagates together with a higher-number one, the regions, where the power flux noticeably deviates from the general propagation direction, occupy a considerable part of the longitudinal section area of the waveguide. © *2001 MAIK "Nauka/Interperiodica".*

In the last few decades, the progress in acoustic measurement techniques caused a growing interest in investigating acoustic power fluxes. Measurements are carried out with combined receivers that are able to measure the components of the particle velocity along with the acoustic pressure. The first-in-Russia experiments with receivers measuring the particle velocity were carried out at the Acoustics Department of the Moscow State University [1]. The studies of the energy characteristics of sound fields that were performed prior to the 1990s were described in [2]; more recent investigations are summarized in the dissertation by Gordienko [3]. Foreign investigations are reviewed in [4]. The combined receivers are small in size; this advantageous feature offers a possibility for measuring fields with a complex configuration, such as near fields of large sources [5–9]. In waveguides, the structure of the energy fields is also complex. A possible approach to calculating the energy flux through the waveguide cross section and the total energy per unit length of the waveguide was described in [10]. In [11], it was shown that energy flow lines can form vortexes. The existence of these vortexes is proved experimentally. The behavior of the energy flow lines near singular points, in which the field amplitude or the gradient of the field phase vanish, was studied in [12]. The procedure of finding the positions of the singular points (dislocations) in an ideal waveguide under the assumption that only a small number of modes propagate in it was considered in [17]. It was emphasized that the phase difference of the fields at the points close to a dislocation strongly depends on the waveguide depth, which can vary with rising and falling tides.

However, published works are insufficient to form a complete pattern of an acoustic power flux in a waveguide, while this pattern is of practical interest and is measurable with the combined receivers. The goal of this paper consists in calculating and analyzing this pattern.

A vector field is usually represented as a set of arrows with corresponding lengths and slopes and a set of flow lines. The advantage of this representation is its clarity. We will characterize the field by continuous curves representing the vector components of the power flux and its slope for a set of selected depths. This approach is less obvious, but it describes the field in more detail and corresponds to the customary representations of a scalar field in the form of the horizontal sections.

Primary attention is drawn to the case of a two-mode propagation, because it allows a clear physical interpretation of the results. We start from the basic definitions and evaluations of the positions of singular points. The type of singular points (the vortex or saddle type) is determined according to the indications given in [13]. The size of the regions affected by vortexes essentially depends on the numbers of the propagating modes. For this reason, we consider two cases: low-number modes with close numbers and a pair of modes whose numbers are widely different. In the first case, we use simple mathematics to interpret the results. In the second case, we represent the results in a more obvious form of curves.

Consider a waveguide of depth H with a hard bottom and a soft surface and introduce the reference system with the horizontal and vertical axes R and z and the origin at the bottom. In such a waveguide, the sound field potential ψ for large distances from the source, which is located at the point $(0, Z_0)$, is representable as [14]

$$\Psi = -\frac{V_0}{4\pi} j \frac{2\pi}{H} \sqrt{\frac{2}{\pi R}} \exp\left(-j\frac{\pi}{4}\right) \times \sum_{l=1}^{m} \frac{1}{\sqrt{\xi_l}} \cos(b_l Z_0) \cos(b_1 z) \exp[j(\xi_l R - \omega t)], \quad (1)$$

1063-7710/01/4706-0688$21.00

where V_0 is the source strength, ω is the cyclic frequency of the signal, $\xi_l = \sqrt{k^2 - b_l^2}$ and $b_l = (l - 0.5)\pi/H$ are the horizontal and vertical components of the wave vector of the lth mode, and m is the total number of modes propagating in the waveguide without attenuation.

The sound field p and the particle velocity components V_R and V_z are expressed through the sound potential ψ and the density of the medium ρ according to the following equalities:

$$p = -\rho\frac{\partial\Psi}{\partial t}; \quad V_R = \frac{\partial\Psi}{\partial R}; \quad V_z = \frac{\partial\Psi}{\partial z}. \tag{2}$$

The quantity of our interest is the power flux density vector averaged over the signal period (below, we call it the flux vector for brevity) [2, 13, 15]:

$$\langle\bar{J}\rangle = \frac{1}{2}\mathrm{Re}(p\bar{V}^*).$$

The flux components along the R and z axes are

$$\langle J_R\rangle = \frac{1}{2}\mathrm{Re}(pV_R^*); \quad \langle J_z\rangle = \frac{1}{2}\mathrm{Re}(pV_z^*), \tag{3}$$

and its magnitude and the angle of inclination to the R axis are

$$|\langle\bar{J}\rangle| = \sqrt{\langle J_R\rangle^2 + \langle J_z\rangle^2}, \quad \gamma = \arctan\frac{\langle J_z\rangle}{\langle J_R\rangle}. \tag{4}$$

The sound pressure and the velocity components can be obtained from Eqs. (1) and (2)

$$p = \frac{A}{\sqrt{R}}\sum_{l=1}^{m} u_l\exp[j(\xi_l R - \omega t)];$$

$$V_R = \frac{A}{\rho\omega\sqrt{R}}\sum_{l=1}^{m} v_l\exp[j(\xi_l R - \omega t)]; \tag{5}$$

$$V_z = j\frac{A}{\rho\omega\sqrt{R}}\sum_{l=1}^{m} w_l\exp[j(\xi_l R - \omega t)].$$

Here,

$$u_l = \frac{1}{\sqrt{\xi_l}}\cos(b_l Z_0)\cos(b_l z),$$

$$v_l = \sqrt{\xi_l}\cos(b_l Z_0)\cos(b_l z),$$

$$w_l = \frac{b_l}{\sqrt{\xi_l}}\cos(b_l Z_0)\sin(b_l z),$$

$$A = Q_0\frac{2\sqrt{2\pi}}{H}\exp\left(j\frac{\pi}{4}\right), \quad Q_0 = -j\frac{\rho\omega V_0}{4\pi}.$$

Using these expressions and Eqs. (3), we obtain the components of the power flux in the form

$$\langle J_R\rangle = \frac{B}{R}\sum_{l,q=1}^{m,m} u_l v_q\cos[(\xi_l - \xi_q)R];$$

$$\langle J_z\rangle = \frac{B}{R}\sum_{l,q=1}^{m,m} u_l w_q\sin[(\xi_l - \xi_q)R]; \tag{6}$$

$$B = \frac{\rho\omega V_0^2}{4\pi H^2}.$$

In the general case, the calculations give a complicated pattern for the power flux; however, it becomes much simpler if only a few modes propagate in the waveguide. In particular, for only two modes of numbers l and q propagating in the waveguide, the formulas take on the form

$$\frac{R}{B}\langle J_R\rangle = \cos^2(b_l z) + \cos^2(b_q z) + (2+\alpha)\cos(b_l z)\cos(b_q z)\cos[(\xi_l - \xi_q)R],$$

$$\frac{R}{B}\langle J_z\rangle = \frac{1}{\sqrt{\xi_l\xi_q}}[b_q\cos(b_l z)\sin(b_q z) - b_l\cos(b_q z)\sin(b_l z)]\sin[(\xi_l - \xi_q)R]. \tag{7}$$

$$2 + \alpha = \frac{\xi_l + \xi_q}{\sqrt{\xi_l\xi_q}}.$$

The positions of the singular points are determined from the system of equations $\langle J_R\rangle = \langle J_z\rangle = 0$. From the second equation of Eqs. (7), one can see that these points can be subdivided into two groups. The first group corresponds to the zero sine, and the second group corresponds to the zero value of the expression in the brackets. We begin our analysis with the singular points of the first group. Their horizontal coordinates are determined from the condition

$$(\xi_l - \xi_q)R = n\pi \quad (n = 1, 2\ldots),$$

while the vertical coordinates are obtained from the first equation (7), which, for these horizontal coordinates R, can be rearranged to the form

$$\frac{R}{B}\langle J_R\rangle = [\cos(b_l z) \pm \cos(b_q z)]^2 \pm \alpha\cos(b_l z)\cos(b_q z) = 0. \tag{8}$$

The signs in Eq. (8) correspond to the value of $\cos[(\xi_l - \xi_q)R]$, +1 or –1, at the zero sine. It should be noted that $\alpha \ll 1$ for modes with adjacent numbers. For example, for the third and fourth modes in a waveguide of depth H = 150 m with a signal frequency of 50 Hz, we have $\alpha = 0.2734 \times 10^{-3}$. Using this fact, we first determine the approximate coordinates and then refine them. Setting $\alpha = 0$ and rearranging the sum and the dif-

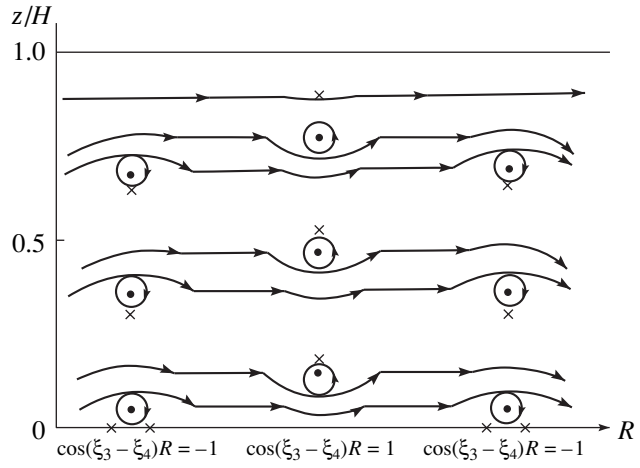

Fig. 1. Positions of the singular points for the third and fourth modes.

ference of cosines in Eq. (8), we obtain for these modes the equations

$$\cos(3\pi z/H)\cos(\pi/2z/H) = 0, \quad (9)$$

$$\sin(3\pi z/H)\sin(\pi/2z/H) = 0. \quad (10)$$

Equations (9) and (10) correspond to the values of $\cos[(\xi_l - \xi_q)R]$ equal plus or minus unity, respectively. From Eq. (9), we obtain $z_1/H = 1/6$, 3/6, 5/6, and 1; from Eq. (10), we have $z_1/H = 0$, 1/3, and 2/3. In reality, $\alpha \neq 0$; as a result, it appears that, at these points, $\langle J_R \rangle < 0$ (i.e., the power flux is directed toward the source). Indeed, if the sign in (8) is the plus, the sum in the brackets is equal to zero, because the cosines are equal in magnitude and have opposite signs. If the sign is the minus, the cosines are equal. In both cases, the second term in Eq. (8) is negative. In particular, $R\langle J_R \rangle/B = -\alpha$ for $z = 0$.

The refined vertical coordinates of the singular points can be obtained by expanding the cosines in series. For the points located near the bottom, $\cos(b_l z) = 1 - 0.5 b_1^2 z^2$. Substituting this expression in Eq. (8) with the minus sign and performing some rearrangements, we obtain $z/H \approx \sqrt[4]{\alpha}/(\pi\sqrt{3})$, which gives $z/H \cong 0.0236$ for the third and fourth modes in the waveguide under consideration. Away from the waveguide boundaries, the singular points form vertical pairs near the heights z_1/H, which were obtained for zero values of α. To estimate the deviation $\pm\Delta z/H$, we use the expansion in the more general form

$$\cos(b_l z) = \cos[b_l(z_1 + \Delta z)]$$

$$= \left[1 - \frac{(b_l \Delta z)^2}{2}\right]\cos(b_l z_1) - b_l \Delta z \sin(b_l z_1).$$

Substituting this expansion in Eq. (8) and taking into account that $\cos(b_3 z_1) = -\cos(b_4 z_1)$ and $\sin(b_3 z_1) = \sin(b_4 z_1)$ for the plus sign and $\cos(b_3 z_1) = \cos(b_4 z_1)$ and $\sin(b_3 z_1) = -\sin(b_4 z_1)$ for the minus sign, we can find the estimator valid for both signs when $z_1 \neq 0$:

$$\frac{\Delta z}{H} \approx \pm\frac{\sqrt{\alpha}}{6\pi\tan(b_3 z_1)}.$$

With this estimator, we obtain the refined values of the vertical coordinates z/H of the singular points belonging to the first group: $z/H = 1/6 \pm 2.35 \times 10^{-4}$, $3/6 \pm 8.77 \times 10^{-4}$, and $5/6 \pm 32.74 \times 10^{-4}$ for $\cos[(\xi_3 - \xi_4)R] = 1$ and $z/H = 236 \times 10^{-4}$, $1/3 \pm 15.19 \times 10^{-4}$, and $2/3 \pm 5.06 \times 10^{-4}$ for $\cos[(\xi_3 - \xi_4)R] = -1$. One can see that the near-bottom points are only slightly above the bottom, and the points in pairs are close to each other. The inversely directed flux occupies the space between these points, so that its total width does not exceed several percent of the waveguide width H.

Consider now the second group of points. Recall that their vertical coordinates make the expression in brackets in the second equation (7) equal to zero. For the third and fourth modes, this condition yields the equation

$$6\sin(\pi z/H) + \sin(6\pi z/H) = 0,$$

which has only two solutions: $z = 0$ and $z = H$. The second solution is of no interest, because the field vanishes at the waveguide surface, and the first solution can be used to determine the horizontal coordinates of the points of the second group. Substituting $z = 0$ in the first equation (7), we obtain

$$R = [2\pi n + \arccos(-2/(2 + \alpha)]/(\xi_3 - \xi_4). \quad (11)$$

Since $\alpha \ll 1$, arccosine in (11) is close to π, in which case $\cos[(\xi_3 - \xi_4)R] \cong -1$.

The deviations $\pm\Delta R$ from the exact values of R corresponding to the exact equality can be found with the use of the identity

$$\arccos(x) = \pi - \arccos(-x).$$

As a result, we obtain

$$\Delta R = \pm\frac{\arccos[2/(2 + \alpha)]}{\xi_3 - \xi_4}$$

$$= \pm\frac{\pi 5.263 \times 10^{-3}}{\pi 2.0997 \times 10^{-3}} = \pm 2.5 \text{ m},$$

which makes only 0.5% of the period (950 m) of the interference structure of the field.

Figure 1 schematically represents the positions of the singular points in the waveguide under consideration for the waveguide part between 7900 and 9400 m. For the sake of obviousness, we distorted the scale in this figure. As follows from the above analysis, the actual distances between the points in pairs are much shorter. Additionally, Fig. 1 shows the types of points: the dots mark the vortex centers and the crosses mark the saddle points. The types of points were determined according to the criteria given in [13]. In addition to the

usual criterion according to which the singular point is a vortex center when $p = 0$ and a saddle point when $|\bar{V}| = 0$, in the cited paper it was shown that the saddle point also appears when the phase difference between p and $\bar{V}$ measures an odd number multiplied by $\pi/2$. This fact follows from the multiplication rule for complex numbers. Indeed, if $\langle J_i \rangle$ is the ith component of the power flux, then we have

$$\langle J_i \rangle \sim \mathrm{Re}(pV_i^*) = p|V_i|\cos[\arg(p) - \arg(V_i)] = p'V_i' + p''V_i'', \quad (12)$$

where the prime and the double prime denote the real and imaginary components of the functions, respectively.

In the case under consideration, when the third and the fourth modes propagate in the waveguide, we have

$$p = B\exp(j\xi_4 R)\left[\frac{1}{\sqrt{\xi_3}}\cos(b_3 z)\exp[j(\xi_3 - \xi_4)R] + \frac{1}{\sqrt{\xi_4}}\cos(b_4 z)\right]\exp(-j\omega t), \quad (13)$$

$$V_R = B\exp(j\xi_4 R)[\sqrt{\xi_3}\cos(b_3 z)\exp[j(\xi_3 - \xi_4)R] + \sqrt{\xi_4}\cos(b_4 z)]\exp(-j\omega t), \quad (14)$$

$$V_z = B\exp\left[j\left(\xi_4 R + \frac{\pi}{2}\right)\right]\left[\frac{b_3}{\sqrt{\xi_3}}\sin(b_3 z) \times \exp[j(\xi_3 - \xi_4)R] + \frac{b_4}{\sqrt{\xi_4}}\sin(b_4 z)\right]\exp(-j\omega t). \quad (15)$$

Substituting the calculated coordinates of the singular points in Eq. (13), one can check that the zero points of the field coincide with the lower points of every pair when $\cos[(\xi_3 - \xi_4)R] = 1$ and with the upper points of every pair when $\cos[(\xi_3 - \xi_4)R] = -1$ (near the bottom, pairs are transformed into triples). Since the power flux between the points is directed toward the source, the first case corresponds to vortexes rotating counterclockwise and the second case corresponds to vortexes rotating clockwise. Other singular points are the saddle points. At these points, $V_R = 0$ and the phase difference between p and V_z is equal to $\pi/2$ for $z \neq 0$ [see Eqs. (13) and (15)]. At $z = 0$, we have $V_z = 0$, because the sines in Eq. (15) are equal to zero, whereas p and V_R are nonzero. Nevertheless, the singular points at the bottom are the saddle points, because the phases of p and V_R differ by $\pi/2$ at these points. This fact can be easily verified by calculating the sum of the products of the real and imaginary parts of functions (13) and (14). This sum is equal to zero, which, according to (12), corresponds to the aforementioned phase difference.

The arrangement of singular points becomes more complex when the mode numbers are widely different. However, in this case, the distances between the points become longer, which makes it possible to represent the calculated results in the graphical form without distorting the scale. As an example, we consider the propagation of the first and the tenth modes in the waveguide under consideration ($H = 150$ m). We again assume that the source is located at the bottom and the signal frequency is 50 Hz. As before, we start with the first group of singular points. Recall that their horizontal coordinates are determined from the condition $\sin[(\xi_1 - \xi_{10})R] = 0$ and the vertical coordinates, from Eq. (8) under the condition that $\cos[(\xi_1 - \xi_{10})R] = \pm 1$. For this pair of modes, $\alpha = 0.3476$ and the period of the interference structure is 43.7 m. Figure 2 shows the left-hand side of Eq. (8) as a function of z for both signs of the cosine. One can see that the direct power flux is periodically replaced by the inverse flux for different depths. Near the bottom, the inverse flux occurs only for the distances corresponding to the negative cosine. The singular points of the first group lie at depths where $\langle J_R \rangle$ vanishes. It should be noted that new branches of the direct flux appear in the upper part of the waveguide. They generate additional points at which $\langle J_R \rangle = 0$.

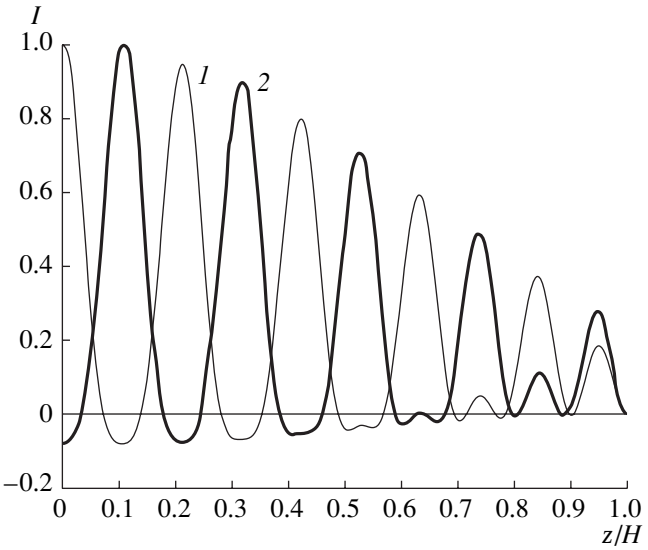

Fig. 2. Flux component $J_R(z)$ for $\cos[(\xi_1 - \xi_2)R]$ equal to (*1*) +1 and (*2*) –1.

The vertical coordinates of the singular points of the second group are determined from the condition that the expression in the brackets in the second equation (7) is equal to zero. This condition is satisfied at the bottom, for eight intermediate depths, and at the waveguide surface (to be more precise, for z/H close to 0, 0.105, 0.211, 0.316, 0.422, 0.530, 0.636, 0.741, 0.850, and 1.0). The horizontal coordinates of these points can be found from the expression following from the first equation (7):

$$\cos[(\xi_1 - \xi_{10})R] = -\frac{\cos^2(b_1 z) + \cos^2(b_{10} z)}{(2 + \alpha)\cos(b_1 z)\cos(b_{10} z)}. \quad (16)$$

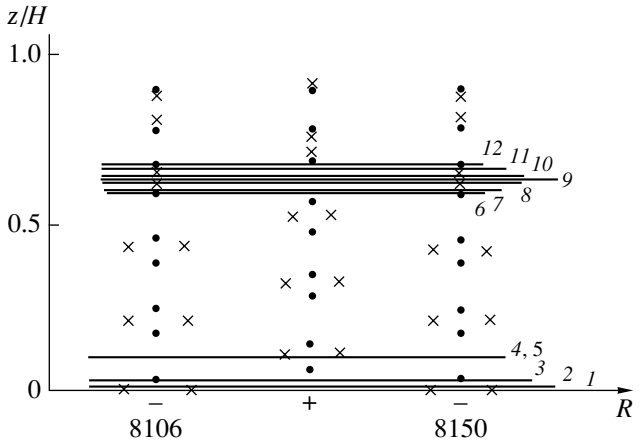

Fig. 3. Positions of the singular points for the first and tenth modes. The horizontal sections are numbered from *1* to *12*.

Substituting the above values of z in Eq. (16), we obtain that, for $\alpha = 0.3476$, solutions exist only for six lower depths, including $z = 0$. For $z/H > 0.53$, the magnitude of the ratio on the right-hand side exceeds unity, and no solutions exist in this case. Figure 3 schematically shows the positions of the singular points of both groups for the case of propagation of the first and tenth modes generated in the waveguide by a near-bottom source. The positions of the singular points of the first group form columns corresponding to $\cos[(\xi_1 - \xi_{10})R] = \pm 1$. The vortex centers predominate among these points, while pairs of saddle points occur in the upper part of the waveguide. They are caused by additional branches of direct fluxes, which were mentioned above in discussing Fig. 2. The singular points of the second group are now located not only at the bottom, but also at five other depths, where they combine with pairs of points of the first group, thus forming quartets of saddles and vortexes. As can be easily seen, in this case, the distances between singular points are comparable with the waveguide depth and with the interference period of the field structure. Therefore, the features in the behavior of the power flux vector cannot be neglected. Below, we consider some of these features in the lower (near-bottom) and upper layers of the waveguide.

Figure 4 shows both components of the power flux (J_R and J_z) and its vertical angle γ as functions of the horizontal coordinate R for z/H in the range from 0 to 0.10558. The range for the horizontal coordinate R is between 8090 and 8165 m, which slightly exceeds the period of the interference structure. The lines, along which the horizontal sections of the vector field are calculated, are given the numbers from *1* to *5* in Fig. 3. Sections *4* and *5* nearly coincide in height and are shown for this reason as a single line. As can be seen from Fig. 4, near the bottom, the horizontal component of the flux J_R periodically changes its sign and becomes negative between the saddle points. Since $J_z = 0$ at the hard bottom, the angle γ can be equal to either 0 or $\pm 180°$, as it is the case in Fig. 4b for the depth $z = 0$. The jump from 180° to –180° is a consequence of the choice of the figure scale and actually means that the vector passes counterclockwise through the direction corresponding to 180°. For a smaller depth $z/H = 0.01$ (line *2*), the segments with the inverse flux ($J_R < 0$) remain almost intact, but J_z vanishes only for individual points. Therefore, the variations become smoother. However, the passage of the angle γ through the direction corresponding to $\gamma = 180°$ again takes place. This passage disappears at the depth of the vortex centers ($z/H = 0.0328$, line *3*). As can be seen from Fig. 4, $J_R = J_z = 0$ at these points, and the angle γ jumps only from 90° to –90°. The physical meaning of such a jump is quite obvious: when the vortex is crossed along the diameter on the left of center, the flux has an upward component, and, when the vortex is crossed on the right of center, the flux has a downward component.

To finish with the near-bottom region, consider the flux at the depth of the saddle points forming a part of the quartets (lines *4*, *5*). Vortexes with their centers above and below the saddle points rotate in the opposite directions: the upper vortexes rotate clockwise, and the lower vortexes, counterclockwise. Inside the quartet, they form an inverse flux well discernible in Fig. 4a. The line separating these vortexes passes at the depth of the saddle points. At this level, we have $J_z = 0$, and the functions J_R calculated slightly above and below this line ($z/H = 0.1055$ and 0.1058) coincide in shape. However, the angle γ passes through the direction corresponding to $\gamma = 180°$ in opposite directions for these depths (see Fig. 4b).

Finally, we consider the behavior of the power flux vector for the depths where the quartets of singular points form vertical columns rather than diamonds. For brevity, we will discuss only the curves for the angle γ. Figure 5 shows the horizontal sections for the angle γ along the lines *6–12* (see Fig. 3). These sections cover the depths z/H ranging from 0.5904 to 0.675. As can be seen from Fig. 3, the depths limiting this range correspond to the vortex centers. A characteristic feature of these centers is the jump of the angle γ from 90° to –90° at the lower depth and the inverse jump at the upper depth, which means that the lower vortex rotates counterclockwise and the upper vortex rotates clockwise (curves *6* and *12*). At the depth between the vortex center and the lower saddle point (curve *7*), the inverse flux occurs and the angle γ jumps from –180° to 180°. Slightly above the lower saddle point, the magnitude of the jump decreases (curve *8*). The depth $z/H = 0.6343$ corresponds to the line separating the system of fluxes. Here, the flux is strictly horizontal (curve *9*). Above this line (curves *10* and *11*), the behavior of the angle γ is similar to that considered earlier, excluding the fact that the functions are of opposite sign. Correlating the curves in Figs. 4 and 5, one can easily see a certain difference in their behavior. In particular, the curves in the

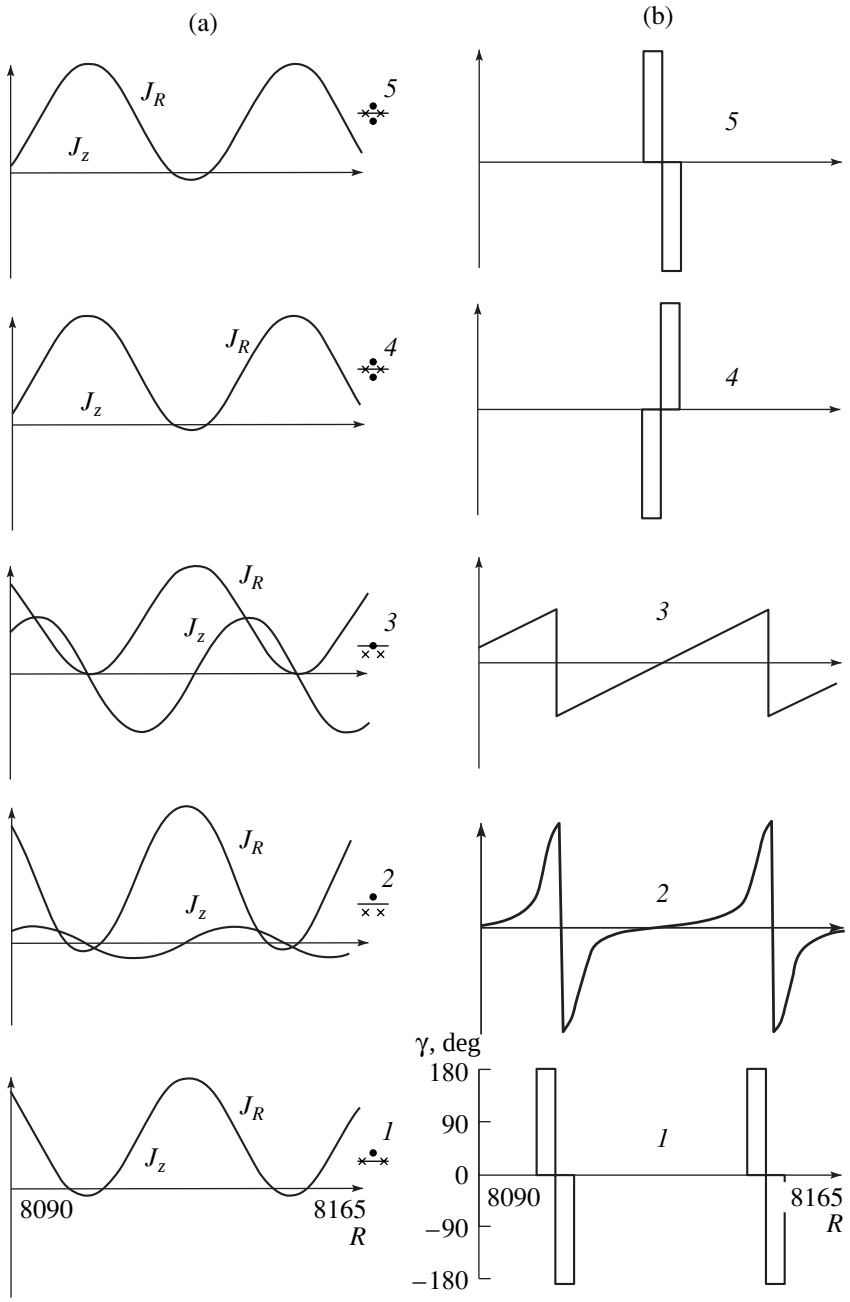

Fig. 4. Curves (a) for J_R and J_z and (b) for γ versus R for sections *1–5*.

form of rectangular pulses are absent in the upper part of the waveguide, because the singular points are arranged in columns rather than in diamonds in this case.

Note that, in some cases, the above set of curves for J_R, J_z and γ can be a more convenient characteristic of the power flux than its usual representation in the form of a family of flow lines. Examples of this representation for quartets of singular points arranged in columns or diamonds can be found in [12].

Thus, the field of the acoustic power flux in a waveguide has a complex structure, which is essentially simplified when only a small number of modes propagate in the waveguide. The power flux forms singular points (saddle points and vortex centers). In the vicinity of vortexes, the flux forms branches whose direction is opposite to the general direction of the power flux. In the case of the propagation of a pair of low-number modes with successive numbers, the scales of the inverse fluxes are small in comparison with the waveguide depth and the period of the interference

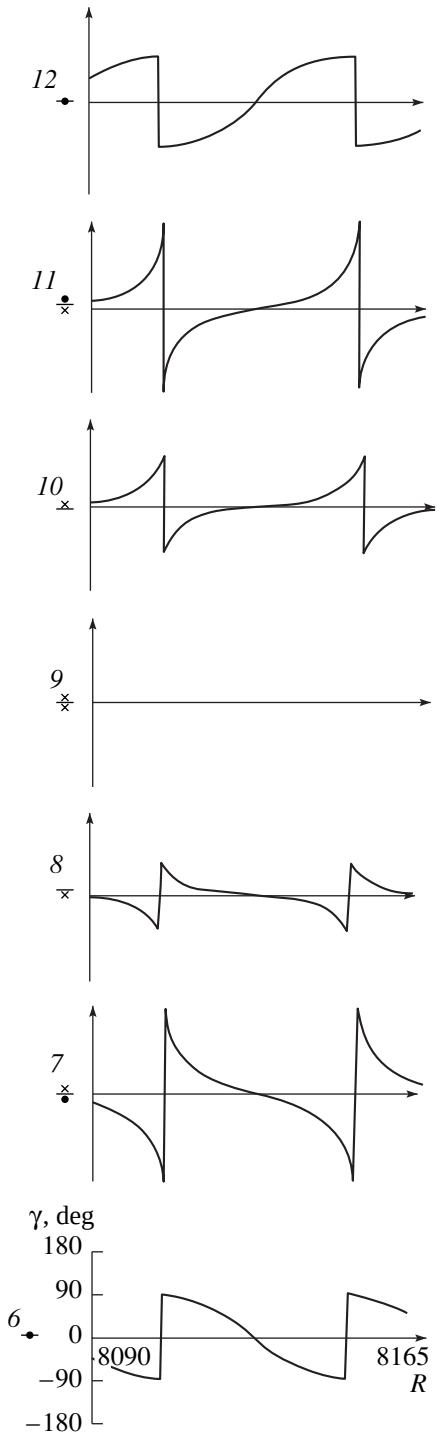

Fig. 5. Curves for γ for sections *6–12*.

structure of the field. The situation is drastically changed when the mode numbers are widely different. The deviations of the flux from the general propagation direction become the rule rather than the exception for this case. The positions of the singular points can be easily calculated for a pair of modes in an ideal waveguide. There are no fundamental limitations that would impede the calculations for more complicated models of the waveguide. For the determination of the power fluxes in practice, one can use a combined receiver that measures both the sound pressure and the components of the particle velocity, or the specialized sensor described in [16]. In the case of multimode propagation, the desired pair of modes can be selected using a vertical chain of combined receivers.

REFERENCES

1. L. N. Zakharov and S. N. Rzhevkin, Akust. Zh. **20**, 393 (1974) [Sov. Phys. Acoust. **20**, 241 (1974)].
2. V. A. Gordienko, V. I. Il'ichev, and L. N. Zakharov, *The Vector-Phase Methods in Acoustics* (Nauka, Moscow, 1989).
3. V. A. Gordienko, Doctoral Dissertation in Physics and Mathematics (Moscow State University, Physical Department, Moscow, 1996).
4. F. Fahy, *Sound Intensity* (Elsevier, London, 1989).
5. R. V. Waterhouse and T. W. Yates, in *2nd International Congress on Acoustic Intensity* (CETIM, Senlis, France, 1985).
6. J. A. Mann III, J. Tichy, and A. J. Romano, J. Acoust. Soc. Am. **82**, 17 (1987).
7. A. N. Zhukov, A. N. Ivannikov, and V. I. Pavlov, Akust. Zh. **36**, 447 (1990) [Sov. Phys. Acoust. **36**, 249 (1990)].
8. G. Schifrer and D. Stanzial, J. Acoust. Soc. Am. **96**, 3645 (1994).
9. E. G. Williams, J. Acoust. Soc. Am. **97**, 121 (1995).
10. V. V. Tyutekin and Yu. I. Bobrovnitskiĭ, Dokl. Akad. Nauk SSSR **4**, 878 (1985) [Sov. Phys. Dokl. **30**, 1043 (1985)].
11. F. J. Fahy, in *2nd International Congress on Acoustic Intensity* (CETIM, Senlis, France, 1985), p. 177.
12. V. A. Zhuravlev, I. K. Kobozev, and Yu. A. Kravtsov, Zh. Éksp. Teor. Fiz. **104**, 3769 (1993) [JETP **77**, 808 (1993)].
13. C. F. Chien and R. V. Waterhouse, J. Acoust. Soc. Am. **101**, 705 (1997).
14. L. M. Brekhovskikh and Yu. P. Lysanov, *Fundamentals of Ocean Acoustics* (Gidrometeoizdat, Leningrad, 1982; Springer, New York, 1991).
15. M. A. Isakovich, *General Acoustics* (Nauka, Moscow, 1973).
16. K. J. Bastyr, G. C. Lauchle, and J. A. McConnell, J. Acoust. Soc. Am. **106**, 3178 (1999).
17. V. A. Zhuravlev, I. K. Kobozev, and Yu. A. Kravtsov, Akust. Zh. **35**, 260 (1989) [Sov. Phys. Acoust. **35**, 156 (1989)].

Translated by A. Vinogradov

Acoustical Physics, Vol. 47, No. 6, 2001, pp. 695–698. Translated from Akusticheskiĭ Zhurnal, Vol. 47, No. 6, 2001, pp. 789–792.

Phase Relations for a Sound Wave at Its Reflection and Transmission through a Plane Layer

V. V. Efimov* and D. I. Sementsov**

** Ul'yanovsk State Technical University, ul. Severnyĭ Venets 32, Ul'yanovsk, 432027 Russia*
e-mail: evv@ulstu.ru
*** Ul'yanovsk State University, ul. L. Tolstogo 42, Ul'yanovsk, 432700 Russia*
e-mail: sdi@sdi.ulsu.ru

Received May 10, 2000

Abstract—A property never considered before in acoustics is established: in the case of a sound wave incidence on a plane layer bordered by two liquid media with identical elastic properties, the phase difference between the reflected and transmitted waves is equal to $\pi/2$ irrespective of the physical constants of the layer and the media contacting it, as well as of the frequency of the incident wave. *© 2001 MAIK "Nauka/Interperiodica".*

Effects that accompany the elastic wave propagation in plane-layered structures always obey certain phase relations at the boundaries of an individual layer for the waves reflected and transmitted through it. The phase relations play an important role in such phenomena as the resonance reflection of a sound wave from a moving layer [1], the interference of counterpropagating waves in a dissipative elastic medium [2–4], and the sound absorption in layered systems [5, 6], as well as in the problems on the waveguide propagation of elastic waves [7]. In this paper, we study the property that consists in the constancy of the phase difference between the reflected and transmitted sound waves at the boundary of a plane layer. In microwave engineering, a similar phenomenon is known: the transmission and reflection coefficients at the terminals of a lossless symmetrical quadripole have a phase difference equal to $\pm\pi/2$ [8]. The analysis of the expressions for the transmission and reflection coefficients of electromagnetic waves in the optical range confirms the validity of the aforementioned relation and other important phase relations connected with it [9]. By virtue of the wave nature of these relations, they should also be valid in acoustics. However, this issue had never been discussed in the literature.

We consider a plane sound wave incident at some angle on a plane layer. We denote the frequency of the wave by ν and the thickness of the layer by d, and we ascribe the indices 1, 2, and 3 to the medium from which the wave arrives, the layer, and the medium into which the wave is transmitted, respectively. All media are assumed to be homogeneous liquids. In this case, the reflection and transmission coefficients r and t, which relate the amplitudes of the reflected and transmitted waves to the amplitude of the incident wave, can be expressed in the form [10]

$$r = \frac{(Z_2 - Z_1)(Z_2 + Z_3)\exp(-2i\varphi) + (Z_1 + Z_2)(Z_3 - Z_2)}{(Z_1 + Z_2)(Z_2 + Z_3)\exp(-2i\varphi) + (Z_2 - Z_1)(Z_3 - Z_2)}, \quad (1)$$

$$t = \frac{4Z_2Z_3}{(Z_2 - Z_1)(Z_3 - Z_2)\exp(i\varphi) + (Z_1 + Z_2)(Z_2 + Z_3)\exp(-i\varphi)}, \quad (2)$$

where $Z_j = \rho_j c_j/\cos\theta_j$ ($j = 1, 2, 3$) are the impedances of the plane wave in the three media, ρ_j and c_j are the densities of the corresponding media and the sound wave velocities in them, and θ_j are the angles made by the direction of the wave propagation in each of the media with the normal to the layer boundaries. The quantity $\varphi = k_2 d\cos\theta_2$ has the meaning of the phase shift of the plane wave at its propagation through the layer, where $k_2 = 2\pi\nu/c_2$ is the wave number in the layer. Then, the changes in the phase of the wave at its reflection from the layer δ_r and at its transmission through the layer δ_t can be represented in the form

$$\delta_r = \arctan\left[\frac{2Z_1Z_2(Z_3^2 - Z_2^2)\cot\varphi}{(Z_2^4 - Z_1^2Z_3^2) + Z_2^2(Z_3^2 - Z_1^2)\cot^2\varphi}\right], \quad (3)$$

$$\delta_t = \arctan\left[\frac{(Z_2^2 + Z_1Z_3)\tan\varphi}{Z_2(Z_1 + Z_3)}\right]. \quad (4)$$

1063-7710/01/4706-0695$21.00 © 2001 MAIK "Nauka/Interperiodica"

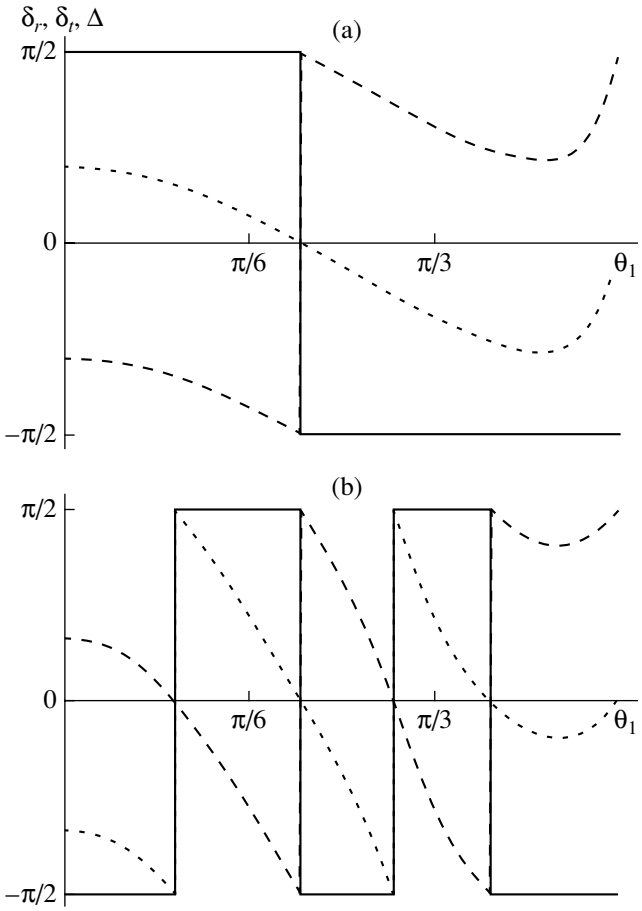

Fig. 1. Phase shifts at reflection δ_r (short dashes) and transmission δ_t (long dashes) and their difference Δ (the solid line) versus the angle of the sound wave incidence on the layer for two values of the layer thickness d = (a) 10 and (b) 30 cm; $c_1 = c_3 = 1482.7$ m/s, $\rho_1 = \rho_3 = 10^3$ kg/m^3, $c_2 = 1165$ m/s, $\rho_2 = 798.3$ kg/m^3, and $\nu = 10$ kHz.

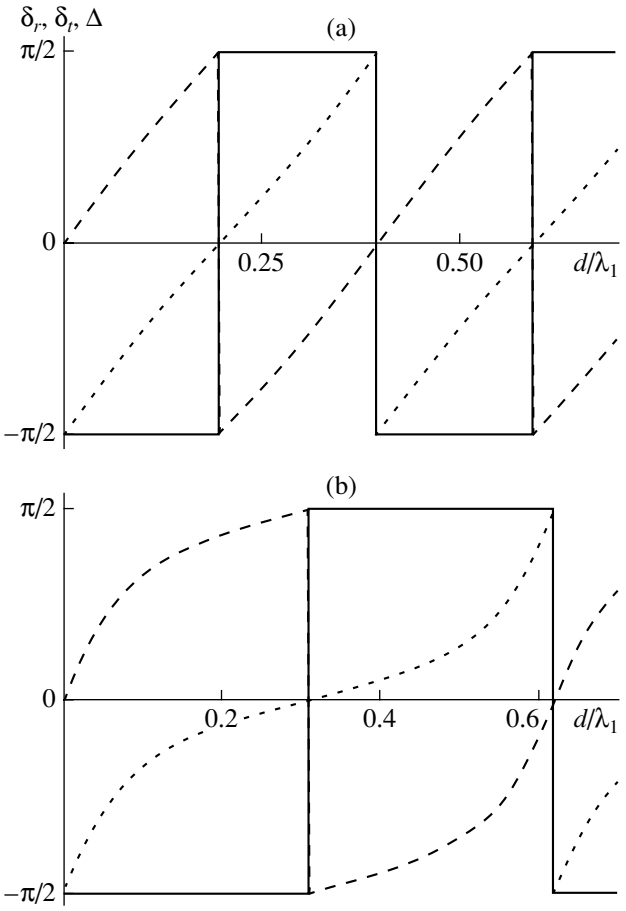

Fig. 2. Phase shifts at reflection δ_r (short dashes) and transmission δ_t (long dashes) and their difference Δ (the solid line) versus the relative layer thickness d/λ_1 for two values of the incidence angle θ_1 = (a) 10° and (b) 80°; $c_1 = c_3 = 1482.7$ m/s, $\rho_1 = \rho_3 = 10^3$ kg/m^3, $c_2 = 1165$ m/s, $\rho_2 = 798.3$ kg/m^3, and $\nu = 10$ kHz.

The analysis of Eqs. (3) and (4) shows that, in the case of a "symmetric" layer, i.e., when the impedances of the media bordering it are equal ($Z_1 = Z_3$), the phase shifts at the reflection and transmission of the wave satisfy a simple relation:

$$\Delta = \delta_r - \delta_t = \pm\frac{\pi}{2}. \qquad (5)$$

This relation is valid regardless of the parameters of the layer and the media surrounding it. In the case $Z_1 \neq Z_3$ or in the case of a layer with absorption, Eq. (5), which determines a kind of phase matching at the reflection and transmission of the plane wave incident on the layer, ceases being valid.

In Figs. 1 and 2 we present the results of a numerical analysis of the relations between the phase shifts of a sound wave at its reflection δ_r (short dashes) and transmission δ_t (long dashes) and their difference Δ (the solid line) for different parameters of the layered structure under consideration and for different angles of incidence of the sound wave.

Figure 1 presents the dependences of the aforementioned quantities on the angle of the sound wave incidence θ_1 on the layer for two values of the layer thickness. The parameters used for the calculations were those of an ethyl alcohol layer in water [11]: $c_1 = c_3 = 1482.7$ m/s, $\rho_1 = \rho_3 = 10^3$ kg/m^3, $c_2 = 1165$ m/s, and $\rho_2 = 798.3$ kg/m^3. From the curves presented in Fig. 1, one can see that relation (5) holds for all angles θ_1. The jumps of the parameter Δ by π are caused by the corresponding changes in the argument of the amplitude reflection or transmission coefficients. The analysis shows that, with an increase in the layer thickness, the number of such jumps within the whole interval of incidence angles ($0 \le \theta_1 < \pi/2$) increases. For the most part, such changes occur in the middle of the interval of θ_1.

The dependences of the phase shifts δ_r and δ_t and the quantity Δ on the relative layer thickness d/λ_1 are shown in Fig. 3 for two values of the incidence angle. Here, $\lambda_1 = c_1/\nu$ is the wavelength of the wave incident on the layer. One can see that the parameter Δ takes only the values $\pm\pi/2$ irrespective of the layer thickness. The calculations show that, as the angle of incidence increases, these dependences become more and more nonlinear in the thickness intervals where they are monotonic.

It should be noted that the curves presented in Fig. 3 exhibit a periodic behavior. The period η of the dependences $\delta_r(d/\lambda_1)$, $\delta_t(d/\lambda_1)$, and $\Delta(d/\lambda_1)$ increases with increasing angle of incidence and with decreasing refraction index of the layer $n = c_1/c_2$ with respect to the surrounding media. This behavior is illustrated in Fig. 3. On a reduced scale, Fig. 3 shows the dependence of the period η on the incidence angle θ_1 for the case $c_1 = c_2 = c_3$ and $\rho_1 = \rho_3 \neq \rho_2$. An analysis shows that the aforementioned dependences are only determined by the relative refractive index of the layer and do not depend on the densities of the three media and on the specific values of the velocity of sound in them.

Figure 4 shows the dependences of the number of jumps N of the parameter Δ on the refraction index of the layer n and on the relative thickness of the layer d/λ_1 for the whole interval of incidence angles. One can see that the number of jumps has a tendency to decrease nonlinearly with increasing refraction index and to increase linearly with increasing normalized thickness of the layer.

It is important to note that the property of a constant phase difference $\Delta = \delta_r - \delta_t$ also holds when the sound wave is incident on an elastic plate placed in a liquid. In this case, the amplitude reflection and transmission coefficients r and t will have the form

$$r = \frac{M(Z_3 - Z_1) + i[(N^2 - M^2)Z_1 - Z_3]}{M(Z_1 + Z_3) + i[(N^2 - M^2)Z_1 + Z_3]}, \qquad (6)$$

$$t = \frac{\rho_1}{\rho_3}\frac{2NZ_3}{M(Z_1 + Z_3) + i[(N^2 - M^2)Z_1 + Z_3]}, \qquad (7)$$

where, in the absence of absorption, M and N are real parameters determined by the impedances of the media, the plate thickness, and the propagation directions and wave numbers of the longitudinal and transverse waves in the plate [10]. When the liquids on the two sides of the plate are described by identical parameters ($Z_1 = Z_3$), the ratio r/t is an imaginary number, which is equivalent to Eq. (5). One can expect that the aforementioned property will also hold for a more general case: the reflection and transmission of a sound wave incident on an arbitrary, but symmetric with respect to the middle plane, stack of lossless elastic layers.

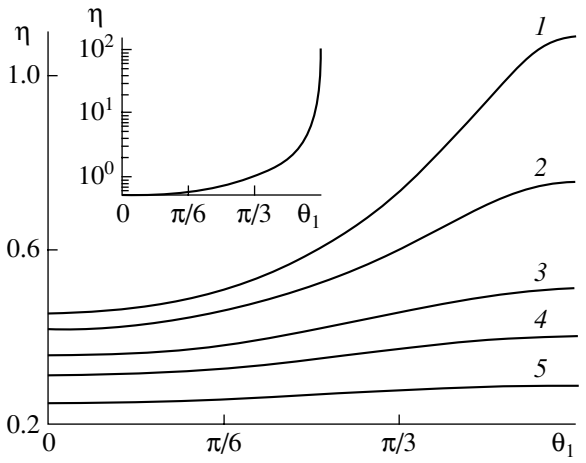

Fig. 3. Dependences of the period of the curves $\delta_r(d/\lambda_1)$, $\delta_t(d/\lambda_1)$, and $\Delta(d/\lambda_1)$ on the angle of the wave incidence θ_1 for different values of the refraction index of the layer: n = (*1*) 1.1, (*2*) 1.2, (*3*) 1.4, (*4*) 1.6, and (*5*) 2.0. The curve shown on the reduced scale corresponds to $n = 1$ and $\rho_1 = \rho_3 \neq \rho_2$.

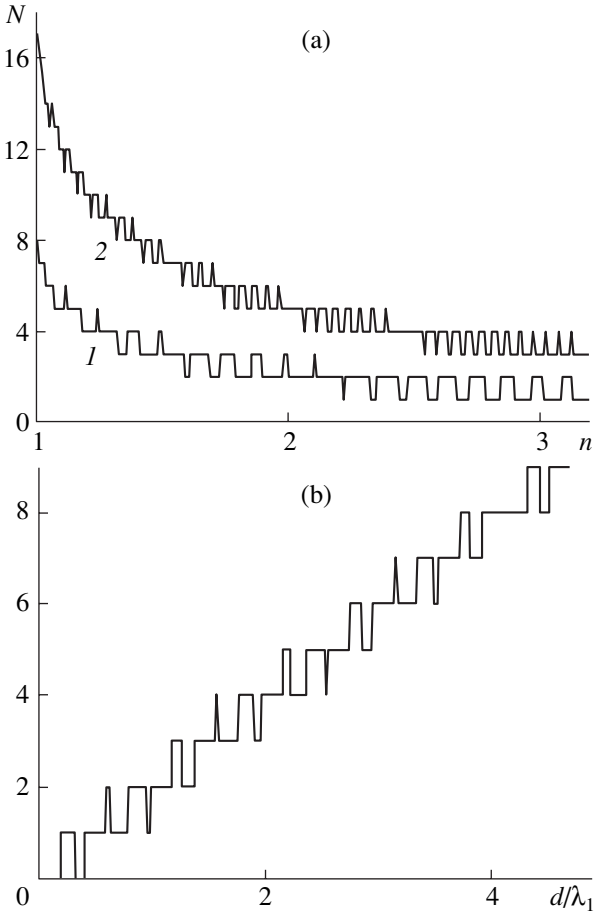

Fig. 4. Number of jumps N of the parameter Δ within the whole interval of incidence angles ($0 \le \theta_1 < \pi/2$) of a wave of frequency ν = 10 kHz (a) versus the refraction index of the layer n for d = (*1*) 30 and (*2*) 70 cm and (b) versus the relative thickness of the layer. The calculations are performed for the parameters: $c_1 = c_3 = 1482.7$ m/s, (a) $\rho_1 = \rho_2 = \rho_3$, (b) $\rho_1 = \rho_3 = 10^3$ kg/m^3, $c_2 = 1165$ m/s, and $\rho_2 = 798.3$ kg/m^3.

In closing, we note that, in our opinion, the property of a constant phase difference Δ is of both fundamental and applied significance, and it can be used in the development of different acoustic devices on the basis of plane-layered structures.

REFERENCES

1. L. M. Lyamshev, Akust. Zh. **28**, 367 (1982) [Sov. Phys. Acoust. **28**, 217 (1982)].
2. Yu. I. Bobrovnitskii, J. Sound Vibr. **152**, 175 (1992).
3. V. V. Efimov and D. I. Sementsov, Akust. Zh. **45**, 565 (1999) [Acoust. Phys. **45**, 504 (1999)].
4. Hsia Shao-Yi and Yang Shiuh-Kuang, Jpn. J. Appl. Phys., Part 1 **38** (5A), 2863 (1999).
5. V. V. Tyutekin, Akust. Zh. **43**, 238 (1997) [Acoust. Phys. **43**, 202 (1997)].
6. T. M. Alibegov and A. E. Vovk, Akust. Zh. **43**, 543 (1997) [Acoust. Phys. **43**, 466 (1997)].
7. N. S. A. Khallaf, L. Parnovski, and D. Vassiliev, J. Fluid Mech. **403**, 251 (2000).
8. G. L. Matthaei, L. Young, and E. M. T. Jones, *Microwave Filters, Impedance-Matching Networks, and Coupling Structures* (McGraw-Hill, New York, 1964; Svyaz', Moscow, 1971), Vol. 1.
9. S. A. Afanas'ev, V. V. Efimov, and D. I. Sementsov, Opt. Spektrosk. **76** (3), 475 (1994) [Opt. Spectrosc. **76**, 425 (1994)].
10. L. M. Brekhovskikh, *Waves in Layered Media*, 2nd ed. (Nauka, Moscow, 1973; Academic, New York, 1960).
11. *Physical Quantities. Handbook*, Ed. by I. S. Grigor'ev and E. Z. Meĭlikhov (Énergoizdat, Moscow, 1991).

Translated by E. Golyamina

Acoustical Physics, Vol. 47, No. 6, 2001, pp. 699–706. Translated from Akusticheskiĭ Zhurnal, Vol. 47, No. 6, 2001, pp. 793–801.

Representation of the Sound Field of a Turbulent Vortex Ring as a Superposition of Quadrupoles

M. Yu. Zaĭtsev, V. F. Kop'ev, and A. N. Kotova

State Research Center Zhukovski Central Aerohydrodynamics Institute, ul. Radio 17, Moscow, 107005 Russia

e-mail: kopiev@mx.iki.rssi.ru

Received September 4, 2000

Abstract—Results of an experimental study of the directivity of noise produced by a turbulent vortex ring ($\mathrm{Re} \approx 10^5$) are presented. The acoustic measurements were performed in an anechoic chamber by a circular array of microphones with its center lying at the symmetry axis of the ring. A method of a synchronous processing of acoustic signals is proposed. This method allows one to separate different quadrupole components in the measured sound field of a turbulent vortex. © *2001 MAIK "Nauka/Interperiodica".*

Microphone arrays and the synchronous multichannel analysis of signals are intensively used for studying different kinds of acoustic noise, including noise of an aerodynamic origin. For example, in [1], jet noise was studied using longitudinal microphone arrays, which made it possible to localize the dipole sources of noise caused by a jet impinging on a thin cylinder. In [2], a combination of polar and azimuthal microphone arrays was used, and these arrays were located in the far field, in the upper hemisphere relative to the nozzle. The technical problems related to the accuracy of this kind of measurement were considered in [3]. The measurement of noise by a circular array with six microphones was proposed in [4] and used in application to jet noise in [5]. This method, which allows one to decompose a flow noise into azimuthal components immediately before averaging over an ensemble of realizations, offered the possibility to separate individual azimuthal components in jet noise. In this paper, we consider in detail this approach in application to the noise produced by the simplest three-dimensional aeroacoustic source represented by a vortex ring.

A vortex ring is a well-known object in aerohydrodynamics [6, 7]. For years, it has been used by researchers as a "reference" object in aeroacoustics, because it combines the possibility of a theoretical description in the framework of the basic equations of continuum mechanics, the simplicity of its construction in laboratory conditions, and the absence of the effect of outer boundaries, which allows one to use it for studying many problems of dynamics and acoustics of vortices in the pure state. The first experimental study of noise produced by a freely moving turbulent vortex ring was described in [8]. It was found that a single vortex ring truly generates sound, and the sound field of the ring is concentrated in a narrow frequency band. Simultaneously, a thorough analysis of the sound signal showed that the radiation produced by even that simple vortex structure is a random process localized in a narrow frequency band.

In [9], in the framework of the Euler equations, a dynamic model of sound radiation by a thin vortex ring was constructed to explain the main experimental characteristics of the observed sound radiation: the presence of a single peak in the radiation spectrum, the values of the frequency and width of the peak, and the nature of the random structure of the signal. It was found that the main features of this radiation can be understood by considering the natural oscillations of the vortex ring. These oscillations are characterized by three integers (l, n, j), which are called the frequency number (all frequencies lie near the crowding points $\frac{\Omega_0 l}{2}$, where Ω_0 is the constant vorticity in the vortex core), the azimuthal number [oscillations with the dependence on the azimuth angle in the form $\exp(in\theta)$], and the radial number (responsible for the inhomogeneous spatial structure of oscillations in the cross-section), respectively. The theory predicts that the sound radiation by a vortex ring is formed by only three families of its natural oscillations, which have the form $\exp(in\theta)$, where $n = 0$, 1, and 2. Moreover, it was found that all eigenfrequencies of effectively radiating modes lie near the common crowding point $\omega = \Omega_0/2$ and, according to the terminology introduced in [9], are called Bessel's ($|j| \geq 1$) or isolated ($j = 0$) modes. These frequencies are determined by the same frequency number $l = 1$ corresponding to the frequency of the crowding point of the radiating modes. In spite of the closeness of frequencies of all radiating modes, the directivity of the radiation is different for each family of oscillations in both the azimuthal and longitudinal directions. In a spherical coordinate system r, θ, χ connected with the vortex ring (Fig. 1), the

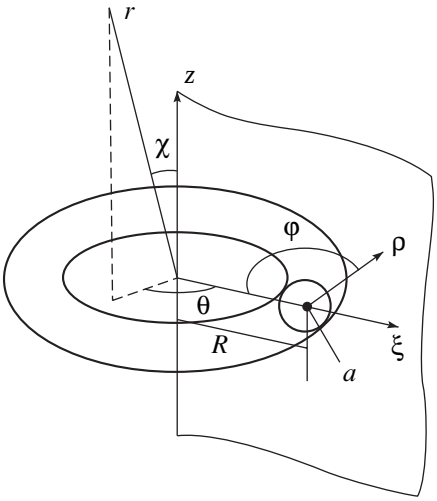

Fig. 1. The coordinate system.

sound field formed by the family of oscillations with $n = 0$ (the axially symmetric modes) has the form

$$p = -\frac{\pi M^2}{2^6\mu}\frac{e^{i\omega_0^{(0)}(t-r/c)}}{r}(3\cos^2\chi - 1). \quad (1)$$

The sound field formed by the family of oscillations with $n = 1$ involves a dependence on the azimuth angle θ and on the longitudinal angle χ in the form $\cos\theta\sin 2\chi$ and is determined by the following two expressions for the isolated ($j = 0$) and Bessel's ($j \geq 1$) modes, respectively:

$$p = \frac{\pi M^2}{2^6\mu}\frac{e^{i\omega_0^{(1)}(t-r/c)}}{r}\cos\theta\sin 2\chi,$$
$$p = \frac{\pi M^2}{5\times 2^6 a_j^{(1)}}\frac{e^{i\omega_j^{(1)}(t-r/c)}}{r}\cos\theta\sin 2\chi. \quad (2)$$

The sound field corresponding to the family of oscillations with $n = 2$ is characterized by the dependence on the azimuth angle θ and the longitudinal angle χ in the form $\cos 2\theta\sin^2\chi$ and is determined by the following expressions for the isolated ($j = 0$) and Bessel's ($j \geq 1$) modes:

$$p = \frac{\pi M^2}{2^7\mu}\frac{e^{i\omega_0^{(2)}(t-r/c)}}{r}\cos 2\theta\sin^2\chi,$$
$$p = \frac{11\pi M^2}{5\times 2^6 a_j^{(2)}}\frac{e^{i\omega_j^{(2)}(t-r/c)}}{r}\cos 2\theta\sin^2\chi. \quad (3)$$

In Eqs. (1)–(3), the oscillation amplitude of the vortex boundary and the liquid density are set equal to unity; $\mu = a/R_0$ is the thinness parameter of the ring, which is determined by the ratio of the radius of the ring cross-section a to the ring radius R_0; M is the Mach number of the flow, which is calculated from the velocity at the boundary of the vortex core $V = \Omega_0 a/2$ and the velocity of sound c; $a_j^{(1,2)}$ are the zeros of the first and second Bessel functions $J_{1,2}(x)$ respectively; and

$$\omega_0^{(0,1,2)} = \frac{\Omega_0}{2}(1 + O(\mu^2))$$

and

$$\omega_j^{(1,2)} = \frac{\Omega_0}{2}(1 + \mu/a_j^{(1,2)} + O(\mu^2))$$

are the frequencies of natural oscillations. We use the dimensionless form [9], in which the pressure is divided by the quantity $V^2/2$. Equations (1)–(3) determine the general form of the radiation dependence on time t and on the azimuth angle θ. Thus, when natural oscillations of the vortex core are excited, the sound radiation of each mode is described by Eqs. (1)–(3). In this case, each mode is characterized by its own directivity in two directions θ and χ.

Now, we consider the total quadrupole sound field P_q that is generated by the vortex ring when all modes are excited. The combination of a great number of close oscillations leads to a total disappearance of the azimuthal inhomogeneity of the sound field (despite the evident dependence of each mode on θ) and to a considerable smoothing of the singularities in the longitudinal direction χ. For definiteness, let us assume that all modes have the same amplitude equal to unity. When combining different harmonics, it is necessary to take into account that each of them has a random orientation with respect to the azimuth angle θ and is shifted in time relative to any other mode by a random phase. This means that the arguments of the trigonometric functions of the azimuth angle θ must be supplemented with a random azimuth phase $\theta_j^{(1,2)}$ (owing to the azimuthal symmetry of the vortex ring, all modes are randomly oriented in the azimuthal direction and their phases should be uniformly distributed within the segment $[0, 2\pi]$), and a random initial phase δ_j must appear in the time dependence. Then, the total quadrupole noise of the vortex ring can be represented in the form

$$P_q = P_0(\cos^2\chi - 1/3) + P_1\cos\theta\sin 2\chi + Q_1\sin\theta\sin 2\chi + P_2\cos 2\theta\sin^2\chi + Q_2\sin 2\theta\sin^2\chi, \quad (4)$$

where P_0, P_1, Q_1, P_2, and Q_2 are random functions of time, which are obtained by combining the exponential functions of time in Eqs. (1)–(3) multiplied by a random amplitude function of the type $\sin\theta_i$ or $\cos\theta_i$. In this case, we have $P_1 \sim \sum_j \cos(\omega_j^{(1)}t + \delta_j)\cos\theta_j^{(1)}$ and $P_2 \sim \sum \cos(\omega_j^{(2)}t + \delta_j)\cos 2\theta_j^{(2)}$. When a great number of harmonics are combined, these functions are random

functions of time. If the amplitudes of harmonics (1)–(3) are unequal, additional factors corresponding to the amplitude of each harmonic should appear in the sums specified above.

Let us calculate the mean value $\overline{P_q^2}$ by using the random character of the time dependence of each of the coefficients P_i and Q_i. Since the signal is a narrow-band one, we perform the averaging over a time interval much greater than $1/\Delta\omega$ (where $\Delta\omega \sim \Omega_0\mu$ is the interval filled with eigenfrequencies near the crowding point $\Omega_0/2$) and, simultaneously, much smaller than the characteristic time of the ring displacement $\frac{2R}{V_0}$. Such an interval can always be selected, because $\frac{2R}{V_0} \sim \frac{\Omega_0}{\mu^2 \ln(\mu)} \gg \Omega_0\mu$. Taking into account that the random phases θ_j, which determine the orientation of each mode relative to the symmetry axis, are uniformly distributed within the segment $[0, 2\pi]$, we easily obtain the relationships

$$\begin{aligned} &\overline{P_1^2} = \overline{Q_1^2} = q_1, \quad \overline{P_2^2} = \overline{Q_2^2} = q_2, \quad \overline{P_0^2} = q_0, \\ &\overline{P_k Q_n} = 0; \quad \overline{P_k P_n} = \overline{Q_k Q_n} = 0, \quad k \neq n, \end{aligned} \tag{5}$$

where the coefficients q_i reflect the contributions of different azimuthal components to the total noise. The equality of the corresponding mean values $\overline{P_1^2} = \overline{Q_1^2}$ and $\overline{P_2^2} = \overline{Q_2^2}$ reflects the aforementioned symmetry property of the vortex ring, i.e., the absence of a selected azimuthal direction. All cross terms disappear after averaging, because each mode radiates independently. As a result, we obtain

$$\overline{P_q^2} = q_0(\cos^2\chi - 1/3)^2 + q_1 \sin^2 2\chi + q_2 \sin^4\chi. \tag{6}$$

The first term in this expression describes the contribution of the axially symmetric modes to the total sound field, the second term describes the contribution of the modes of the type $\exp i\theta$, and the third term corresponds to the modes of the type $\exp 2i\theta$. The relation between the quantities q_0, q_1, and q_2 in the vortex ring is preliminarily unknown and is only associated with the processes of the oscillation instability growth at the nonlinear stage and the establishment of self-sustained oscillations. One can easily see that, independently of this relation, after averaging over t, the radiation ceases to depend on the azimuth angle θ.

The dependence on the longitudinal angle χ is determined by Eq. (6). The contribution of each azimuth component is given by the expressions

$$p_{0q}^2 = \frac{q_0(\cos^2\chi - 1/3)^2}{\overline{P_q^2}}, \quad n = 0,$$

$$p_{1q}^2 = \frac{q_1 \sin^2 2\chi}{\overline{P_q^2}}, \quad n = 1, \tag{7}$$

$$p_{2q}^2 = \frac{q_2 \sin^4\chi}{\overline{P_q^2}}, \quad n = 2.$$

Expression (6) can depend on χ rather weakly. One can easily derive the condition at which the radiation of the vortex ring will be fully isotropic. Changing to multiple angles in Eq. (6) and setting the coefficients of the trigonometric harmonics of χ equal to zero, we obtain $q_1 = q_2 = 1/3q_0$. Thus, when the squared amplitude of noise formed by the first and second azimuthal harmonics makes 1/3 of the contribution of the axially symmetric modes, the radiation is fully isotropic. In this case, the contribution of each of the azimuthal harmonics is nonisotropic and is described by Eqs. (7).

The analysis performed above explains why the sound field generated by turbulence (a turbulent vortex or a turbulent jet) is found to be almost isotropic and the azimuthal components are not revealed in the case of regular measurements. Such a result is related to the averaging of randomly oriented quadrupoles in the azimuthal direction and to the smoothing of the singularities of the fields of individual quadrupoles in the longitudinal direction. Therefore, for the identification of the radiation of individual modes in the experiment, it is necessary to perform the decomposition of noise into azimuthal components before its averaging. This consideration lies at the basis of the experimental study described below.

To measure the directivity in the azimuthal and longitudinal directions, one needs the information on the sound field at the surface surrounding the ring. Taking into account that the ring itself moves along the x axis, it is convenient to use the surface of a cylinder surrounding the trajectory of the moving vortex ring. In this case, it is sufficient to have the information for only one cross-section $x = L_0$ rather than for the whole cylinder surface simultaneously. Then, a change in the angle χ will correspond to a change in the x coordinate of the moving ring; i.e., with increasing x, each azimuthal component will vary according to Eqs. (7) with allowance for the equality $\tan\chi = R/(x - L_0)$, where R is the radius of the cylindrical surface. Thus, if we construct a system capable of measuring individual azimuthal components and place it in a given cross-section $x = L_0$ relative to the trajectory of the ring motion, then, in the course of the vortex motion, the measuring system will provide a record of the variations of the relative contributions of individual components given by Eqs. (7). It was found that such a system can easily be realized using a synchronous analysis of signals taken from only six microphones placed in a circle relative to the trajectory of the ring motion (Fig. 2). However, it is necessary to take into account that the properties of the vortex ring can vary in the course of its motion (e.g., the

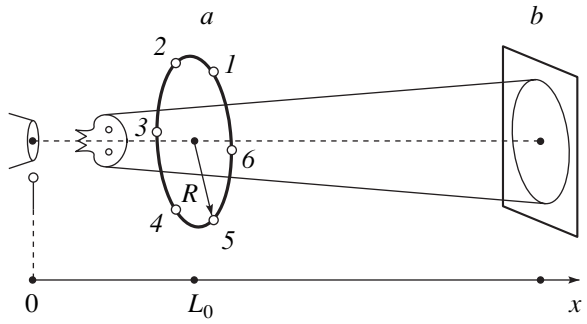

Fig. 2. Schematic representation of the experiment: (*a*) the microphone array and (*b*) the screen with silk threads.

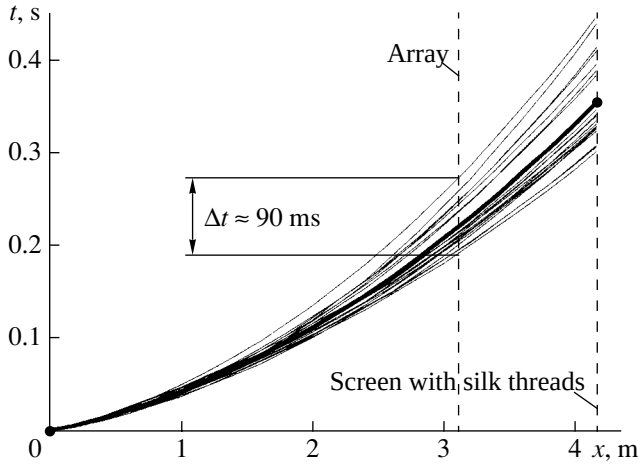

Fig. 3. Dependence of the traveled distance on time for different vortex rings and the mean trajectory (the thick line).

velocity, the geometric dimensions, and the total radiation power). Therefore, the real relative contributions to the radiation of the type of Eqs. (7) will be observed only when the ratio between the amplitudes of the radiating oscillations remains constant.

One more problem is the choice of the averaging interval. On the one hand, it must be sufficiently small for the ring not to be displaced by a considerable distance, and, on the other hand, it must be sufficiently large for the averaging to be possible. To some extent, this contradiction was eliminated, and we managed to obtain the desired directivity of the radiation for individual azimuthal components.

The experimental study of the directivity of noise produced by a freely moving turbulent vortex ring was performed in the anechoic acoustic chamber of the Central Aerohydrodynamics Institute. The dimensions of the chamber were $10 \times 5.5 \times 4.2$ m^3. The acoustic measurements in the far field of the vortex ring were performed by an array of six condenser microphones of the type 4165 by the Bruel and Kjer company (Fig. 2). The microphones were placed in a circle whose radius was $R = 0.4$ m and center lay on the Ox axis ($L_0 = 2.08$ m). The circle plane was perpendicular to the direction of the vortex motion. To visualize the trajectory of the vortex ring, we used a rectangular screen with the dimensions 120×60 cm made of a thin wire with silk threads glued to it. The screen was installed 6 m away from the outlet of the generator nozzle, so that the screen center was at the generator axis. When the vortex ring moved through the screen, the silk threads deviated making the ring position visible, which allowed us to chose for our study those realizations in which the vortex ring was not shifted noticeably from the axis and, hence, moved near the center of the microphone array. At the same time, even a small shift of the ring on the screen, which always takes place, shows which of the microphones is closer to the moving ring. This information proved to be important for the identification of the instant of the vortex passage through the plane of the microphone array (see below).

The signal was obtained by preliminarily recording the acoustic signals by a Sony KS 616 multichannel tape recorder. The total number of realizations recorded in one series of experiments was 40 to 50. In addition to the six acoustic signals, the signal from a microphone installed in the plane of the generator nozzle was recorded simultaneously. This microphone determined the instant of the vortex ring formation, and its signal was used to set the zero time for each realization.

The vortex rings formed in the experiment had a natural scatter in the velocities of their motion, which was related to the somewhat different (uncontrolled) conditions of the rolling-up of the vortex sheet at the instant of its formation. These slight differences lead to an accumulating difference in the travel times of the vortex rings from the instant of their formation to their passage through the screen with silk threads, so that this difference reached 300 to 400 ms (Fig. 3). The trajectory measurement technique used for determining the law of motion $x(t)$ with the help of pressure transducers is described in [4].

To determine the directivity of the sound field produced by the vortex ring, we used the following technique for the experimental data processing [4]. Let us consider the signals $s_p(t)$ of each of the six acoustic microphones. These signals are in fact the measured values of the pressure field $P(\theta, \chi, t)$ for six values of the angle $\theta_p = p\pi/3$, where $p = 1, 2, \ldots, 6$; i.e., $P(\theta_p, \chi, t) = s_p(t)$. We represent the sound field of the vortex ring in the form of a series expansion in azimuthal harmonics:

$$P(\theta, \chi, t) = A_0 + A_1\cos\theta + B_1\sin\theta + A_2\cos 2\theta + B_2\sin 2\theta + \ldots, \quad (8)$$

where the coefficients A_i and B_i are functions of χ and t. The remaining terms of the expansion, which are denoted by the ellipsis, have the multipolarity next after quadrupole and, generally speaking, should be small. Considering Eq. (11) at $\theta = \theta_p$ for each number p as an equation in the unknown amplitudes A_i and B_i with the

known right-hand side $s_p(t)$, we obtain a system of six equations. Owing to the symmetry of the microphone positions, this system can be easily solved for the unknown amplitudes in an explicit form. In fact, because of the symmetry of the choice of θ_p, all combinations of the type of $\sum_1^6 \cos l\theta_p$ and $\sum_1^6 \sin l\theta_p$, where l is a nonzero integer, are equal to zero except for the combination $\sum_1^6 \cos 6n\theta_p = 6$, where n is an integer including zero. Successively multiplying Eq. (8) by $1, \cos\theta_p, \sin\theta_p, \cos 2\theta_p, \sin 2\theta_p$, and $\cos 3\theta_p$ at $\theta = \theta_p$ and summing the result over p from 0 to 6 with allowance for the relations specified above, we obtain six other quantities instead of s_p:

$$
\begin{aligned}
a_0(t) &= \frac{1}{6}\sum_{p=1}^{6} s_p(t) = A_0 + O(A_6, A_{12}, \ldots),\\
a_1(t) &= \frac{1}{3}\left(s_1 + \frac{1}{2}s_2 - \frac{1}{2}s_3 - s_4 - \frac{1}{2}s_5 + \frac{1}{2}s_6\right)\\
&= A_1 + O(A_5, A_{13}, \ldots),\\
b_1(t) &= \frac{1}{\sqrt{3}}\left(\frac{1}{2}s_2 + \frac{1}{2}s_3 - \frac{1}{2}s_5 - \frac{1}{2}s_6\right)\\
&= B_1 + O(B_5, B_{13}, \ldots),\\
a_2(t) &= \frac{1}{3}\left(s_1 - \frac{1}{2}s_2 - \frac{1}{2}s_3 + s_4 - \frac{1}{2}s_5 - \frac{1}{2}s_6\right)\\
&= A_2 + O(A_4, A_{10}, \ldots),\\
b_2(t) &= \frac{1}{\sqrt{3}}\left(\frac{1}{2}s_2 - \frac{1}{2}s_3 + \frac{1}{2}s_5 - \frac{1}{2}s_6\right)\\
&= B_2 + O(B_4, B_{10}, \ldots),\\
a_3(t) &= \frac{1}{6}(s_1 - s_2 + s_3 - s_4 + s_5 - s_6)\\
&= A_3 + O(A_9, A_{15}, \ldots).
\end{aligned}
\qquad (9)
$$

Since, in the far field, the contribution of higher multipole components must be small, the harmonics A_3, B_3, …, which belong to the radiation characterized by a multipolarity higher than quadrupole, must also be small. Therefore, the signals a_i and b_i obtained through the linear combinations of the measured signals s_p are close to the amplitudes of true azimuthal harmonics A_i and B_i. In this case, the real contribution of the octopole component to the measured signal can be easily estimated using the relative value of a_3. One can easily verify that the identity $S^2 = a_0^2 + a_1^2 + b_1^2 + a_2^2 + b_2^2 + a_3^2 = \sum_1^6 s_i^2$ is valid; i.e., the power of the six transformed signals is equal to the power of the six initial signals. Let us introduce the relative contributions of the azimuthal harmonics to the total energy of the sound field: the quantity $p_{0\exp}^2 = a_0^2/S^2$ represents the experimental estimate of the axisymmetric radiation component; the quantity $p_{1\exp}^2 = (a_1^2 + b_1^2)/S^2$ is the estimate of the contribution of the first harmonic; the quantity $p_{2\exp}^2 = (a_2^2 + b_2^2)/S^2$ corresponds to the contribution of the second harmonic; and the quantity $p_{3\exp}^2 = a_3^2/S^2$ corresponds to the contribution of the third harmonic and, in view of the evident condition $a_3^2 = b_3^2$, makes half of this contribution. The estimates $p_{0\exp}^2$, $p_{1\exp}^2$, and $p_{2\exp}^2$ differ from the exact expressions (7) by the presence of higher multipoles in Eqs. (9).

Let us consider a model example. We assume that an ideal harmonic source moves through the microphone array. As the signals $A_i(\chi, t)$ $i = 0, 1, 2$, we take the quadrupole components determined by Eqs. (7), and we replace the sum of higher multipoles $O(A_i, B_i)$ in Eqs. (9) by a constant q, which, generally speaking, is the same for all q_i and b_i. Then, the analogs to the experimental estimates specified above will be the quantities:

$$
\begin{aligned}
p_{0r}^2 &= \frac{q_0(\cos^2\chi - 1/3)^2 + 2q^2}{s^2},\\
p_{1r}^2 &= \frac{q_1\sin^2(2\chi) + 2q^2}{s^2},\\
p_{2r}^2 &= \frac{q_2\sin^4\chi + 2q^2}{s^2}, \quad p_{3r}^2 = \frac{q^2}{s^2},\\
s^2 &= q_0(\cos^2\chi - 1/3)^2 + q_1\sin^2(2\chi) + q_2\sin^4\chi + 7q^2,\\
\tan\chi &= \frac{R}{x(t) - L_0},
\end{aligned}
\qquad (10)
$$

where q_0, q_1, and q_2 are the preset amplitudes of the zeroth, first, and second azimuthal modes; L_0 is the coordinate of the array center; $x(t)$ is the coordinate of the source on a trajectory representing the ring trajectory averaged over many realizations (Fig. 3). The evolution of the relative contributions of multipoles given by Eqs. (10) is presented in Fig. 4 for $q_0 = 0.6$, $q_1 = 0.4$, $q_2 = 0.1$, and $q = 0.07$.

Now, we consider the evolution of the relative contributions of azimuthal harmonics in the experiment, $p_{i\exp}^2$. In comparison with the model example considered above (p_{ir}^2), the situation is more complicated, because the coefficients a_i and b_i in Eqs. (9) contain not only the quadrupole components but also higher multipoles with the same azimuthal dependence. In addition, these functions are random functions of time and are measured with errors. Let us consider a single realization from the instant the vortex ring leaves the

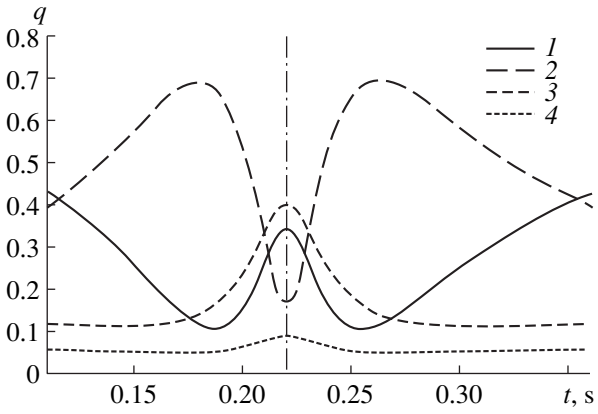

Fig. 4. Contributions of different azimuthal components to the total quadrupole radiation of an ideal vortex ring. A model harmonic source; n = (*1*) 0, (*2*) 1, (*3*) 2, and (*4*) 3.

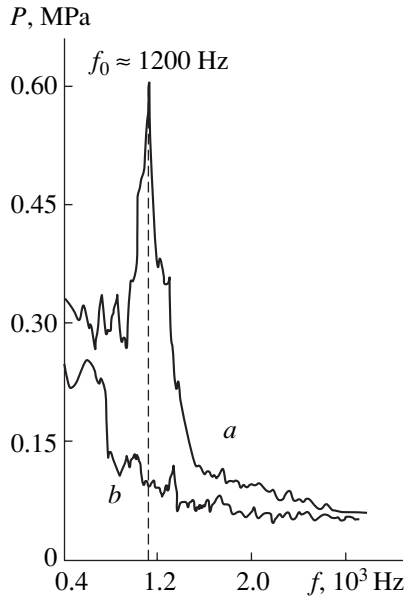

Fig. 5. Average spectrum of sound pressure (*a*) for the vortex ring and (*b*) for the background noise. The delay time relative to the instant of ring initiation is $\tau = 220$ ms.

nozzle to the instant it hits the screen with silk threads. The initial part of the realization (0–110 ms) is unsuitable for analyzing the vortex noise, because the low-frequency noise in the chamber and the structural noise of the experimental setup, which are associated with the condition of the initiation of vortex rings (see [4, 8]), are dominant and considerably exceed the weak noise produced by the ring. The noise of the setup rapidly decreases owing to the use of oscillation-damping means, and the ring noise becomes distinguishable within 110 ms. This noise is localized within the frequency band 800–1500 Hz with a pronounced peak near a frequency of 1200 Hz. The typical form of the spectrum averaged over several realizations obtained 220 ms after the ring initiation is shown in Fig. 5 [8]. The low-frequency noise (0–500 Hz) multiply exceeding the ring noise (by more than 20 dB) cannot be completely damped, and its effect on the measuring system (this noise fills the dynamic range to a considerable extent) inevitably leads to an increase in uncontrolled errors. Thus, for analyzing the vortex noise, we have a realization part approximately 200 ms long (from 110 to 300–400 ms). If we divide it into 30 ms long segments and take the total acoustic power of the process at each segment in the frequency band from 800 to 1500 Hz (most radiation power of the ring is concentrated in this frequency range, see Fig. 5), we obtain six to eight points, which illustrate the variations of the total power of noise S^2 and the contributions of the azimuthal harmonics $p_{i\exp}^2$ in the course of the vortex ring motion. We note that, in the determination of the spectral power, each 30-ms segment of the time realization was multiplied by the smoothing Henning weighting function. An introduction of the overlapping between the adjacent intervals allows one to increase the number of statistically independent spectra, because it partially compensates the property of the Henning weighting window, which considerably reduces the signal near the boundaries of the analysis interval. Thus, to obtain a more detailed picture, one can use the data of the analysis with a 50% overlapping of intervals, which makes it possible to obtain up to 15 points per realization. The typical behavior of the relative contributions in one realization is shown in Fig. 6. Let us estimate the rms error of these measurements. As was noted above, to calculate the evolution of the amplitudes of azimuthal harmonics, we used 30-ms-long time intervals in the frequency band from 800 to 1500 Hz. Within the time of analysis, the ring travels a distance of 25 cm, and the experimental point in Fig. 6 corresponds to the middle of this segment. For the realization length $T \sim 30$ ms, within a bandwidth $\Delta\omega \approx 30$ Hz, the normalized rms error in the spectral power estimate is 100% (this follows from the known condition $\Delta\omega T \sim 1$, see [10, 11]). Since we are interested in the spectrum estimate in a wider frequency band $\Delta\omega_0 \approx 600$ Hz, the error in the estimate of the spectral power of pressure will be $\varepsilon \approx 20\%$.

The main possibility of reducing the error is related to using the averaging over an ensemble of realizations. By accumulating N realizations, it is possible to improve the estimate obtained above by a factor of $\sqrt{N}$. However, in this way, we encounter the following difficulty. Above (Fig. 6), we presented the curves that approximate the law of motion of the vortex ring $x(t)$ for the realizations that were selected for the ensemble used for averaging. One can see that the difference in the instants at which different rings pass through the plane of the microphone array reaches up to 90 ms. This means that, at the instant one ring crosses the array plane, the ring of another realization can be 0.5 m away from this plane, upstream or downstream. Since the

main characteristic features of the desired curves lie near the microphone array plane ($\chi \approx \pi/2$), a conventional averaging leads to a total smearing of the directivity pattern. For an appropriate averaging, it is necessary to be able to determine exactly the instant when the ring crosses the array plane and to use this instant as a reference point.

It was found that this information can be obtained from the analysis of low-frequency acoustic data. The screen with silk threads (Fig. 2) shows which microphone appears to be closest to the moving ring in a given realization. When the readings of any two microphones of the array are subtracted from each other, the low-frequency chamber noise is eliminated. At the same time, each microphone measures the inhomogeneous near field of pressure associated with the flow around the moving ring. This axisymmetric field is not completely compensated by the subtraction of the readings of two microphones, because the ring moves closer to one of them (microphone 1 in our case). The maximal value of the difference is obtained for two opposite microphones (microphone 1 and microphone 4). Figure 7 shows the signals of two microphones positioned symmetrically around the array center. At the instant the ring passes through the array, the difference in the signals exhibits a characteristic peak whose shape corresponds to the pseudosound near field of the ring. The minimum in Δs_{1-4} corresponds to the instant when the ring crosses the plane of the microphone array. Thus, we managed to determine with reasonable accuracy the instants at which the vortex rings passed through the array plane and to perform the averaging over the time intervals equally separated from this instant. The average curves characterizing the directivity of different azimuthal components of the sound field produced by a turbulent vortex ring are shown in Fig. 8; the curves are obtained on the basis of seven selected realizations.

Thus, the radiation of a vortex ring really consists of three different quadrupoles predicted by the theory. It is of interest to compare this result with our previous publication [12] where it was found that, near $t = 245$ ms, the first azimuthal mode dominates. One can easily see that, in this region, the radiation of the zeroth and second modes is small (Fig. 8), and therefore, in [12] it was possible to extract the first mode by a pair-correlation analysis without using the approach described in this paper.

It should be noted that, in the noise of the vortex ring, the zeroth, first, and second azimuthal harmonics dominate, whereas the higher harmonics corresponding to higher-order multipoles have a much lower level. Their total level can be judged from the values of $p_{2\text{exp}}^2$ and $p_{3\text{exp}}^2$ observed away from the array coordinate $x = L_0$. As one would expect, the total noise level is the same (and considerable), although it consists of different azimuthal components $O(A_i, B_i)$ (we note that p_3^2 corresponds to only half of the third harmonic). At the same time, near $x = L_0$, the third harmonic exhibits a noticeable increase, which testifies to the real presence of an octopole component with a level above that of the background in the noise of the vortex ring. Presumably, this result is related to the incomplete fulfillment of the far field condition, which is most strongly violated when the ring travels near the array (by the way, it is precisely the violation of the far field condition that allowed us to perform the averaging of the vortex rings by using the instant of the ring crossing the array plane as the reference point).

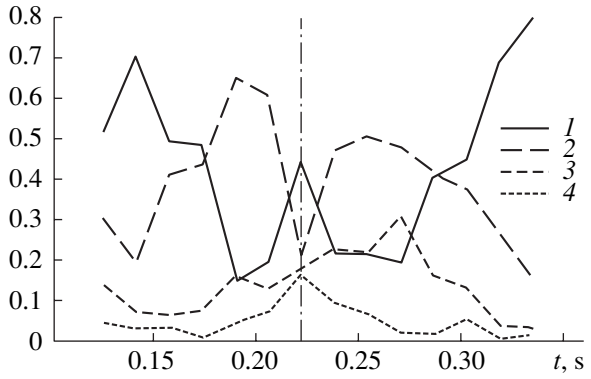

Fig. 6. Contribution of different azimuthal components to the noise of the vortex ring (a single realization) for n = (*1*) 0, (*2*) 1, (*3*) 2, and (*4*) 3.

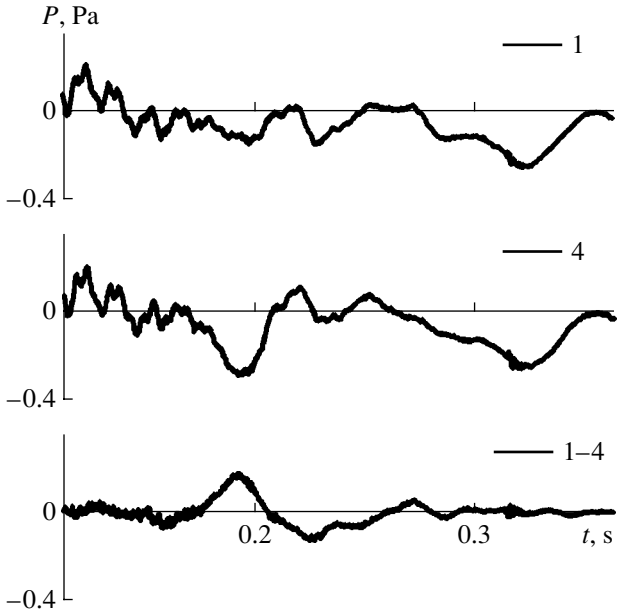

Fig. 7. Nonfiltered sound field measured by the microphones (s_1, s_4) of the array. The field contains the structural noise of the chamber and the pseudosound near field of the vortex ring. The difference in the readings of the opposite microphones is Δs_{1-4}.

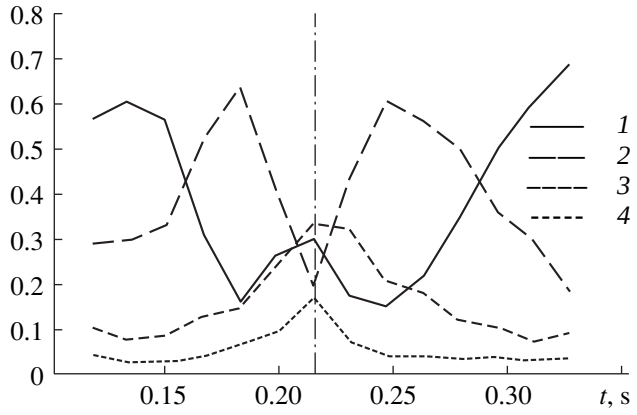

Fig. 8. Average contributions of different azimuthal components to the noise of the vortex ring for n = (*1*) 0, (*2*) 1, (*3*) 2, and (*4*) 3.

The proposed measuring technique allows one to extract individual quadrupole components from the total noise of the vortex ring. As predicted by the theory [9], the noise of a vortex ring consists of three different quadrupoles with close frequencies localized near a single value. The proposed method of analysis, which consists in the separation of azimuthal components before averaging the random signal, seems to be a quite promising method for studying the acoustics of turbulent flows. We also note that, despite the nonstationary character of the average flow (the dimensions and the translational velocity of the ring vary), the dependence of the azimuthal harmonics on the angle χ can be obtained from the analysis of the time evolution of the relative contributions of these harmonics. This indicates that the physical processes leading to the generation of acoustic fluctuations remain invariable in the course of the evolution of the vortex ring; i.e., the relation between the radiating modes is of universal character.

ACKNOWLEDGMENTS

This work was supported by the Russian Foundation for Basic Research, project no. 99-01-00199.

REFERENCES

1. P. Jordan and J. Fitzpatrick, AIAA Pap., No. 2000-1936 (2000).
2. A. Ghosh, J. Bridges, and F. Hussian, Trans. ASME, J. Sound Vib. Acoust. **117**, 172 (1995).
3. S. E. Dosso and B. J. Sotirin, J. Acoust. Soc. Am. **106**, 3445 (1999).
4. V. F. Kopiev, M. Yu. Zaĭtsev, and S. A. Chernyshev, AIAA Pap., No. 98-2371 (1998).
5. V. F. Kopiev, M. Yu. Zaitsev, S. A. Chernyshev, and A. N. Kotova, AIAA Pap., No. 99-1839 (1999).
6. G. K. Batchelor, *An Introduction to Fluid Dynamics* (Cambridge Univ. Press, Cambridge, 1967; Mir, Moscow, 1973).
7. H. Lamb, *Hydrodynamics* (Dover, New York, 1945; Gostekhizdat, Moscow, 1947).
8. M. Yu. Zaĭtsev, V. F. Kop'ev, A. G. Munin, and A. A. Potokin, Dokl. Akad. Nauk SSSR **312** (5), 1080 (1990) [Sov. Phys. Dokl. **35**, 488 (1990)].
9. V. F. Kopiev and S. A. Chernyshev, J. Fluid Mech. **341**, 19 (1997).
10. J. S. Bendat and A. G. Piersol, *Random Data: Analysis and Measurement Procedures* (Wiley, New York, 1986; Mir, Moscow, 1989).
11. S. Minami, T. Utida, S. Kavata, *et al.*, *Experimental Data Processing by a Computer* (Russian translation) (Radio i Svyaz', Moscow, 1999).
12. V. F. Kopiev, S. A. Chernyshev, and M. Yu. Zaitsev, CEAS/AIAA Pap., No. 95-109 (1995).

Translated by E. Golyamina

Acoustical Physics, Vol. 47, No. 6, 2001, pp. 707–713. Translated from Akusticheskiĭ Zhurnal, Vol. 47, No. 6, 2001, pp. 802–808.

Acoustic Field of a Vertical Cylindrical Antenna in an Inhomogeneous Waveguide with an Impedance Lower Boundary

N. V. Zlobina and B. A. Kasatkin

Institute of Marine Technology Problems, Far East Division, Russian Academy of Sciences, ul. Sukhanova 5a, Vladivostok, 690950 Russia

e-mail: kasatkas@marine.febras.ru

Received September 4, 2000

Abstract—An expansion of the field of a vertical antenna located in an inhomogeneous waveguide in terms of the normal waves of a homogeneous reference waveguide is obtained. The frequency dependence of the radiation resistance is analyzed numerically for various antenna depths and sound velocity profiles. Variations in the radiation resistance are correlated with the variations in the sound velocity. *© 2001 MAIK "Nauka/Interperiodica".*

A rather large number of works are devoted to the analysis of acoustic fields of directional antennas operating in waveguides (see, e.g., [1–4]). However, these works provide few (if any) numerical estimates or particular practical recommendations, while the problem itself remains topical. A formalized approach to the analysis of directional antennas operating in the Pekeris waveguide was given in [5]. Particular numerical estimates of the energy and field characteristics of different antennas were obtained in [6].

The purpose of this paper is to generalize the approach proposed in [5] to the more complex case of an inhomogeneous waveguide characterized by a given sound velocity profile $c_1(z)$ and lying on a liquid halfspace. The corresponding boundary-value problem is represented as

$$\begin{gathered}\Delta\varphi + k_1^2(z)\varphi = 0,\\ z = 0, \quad p = 0,\\ z = h, \quad p + Z_{\text{in}}\frac{\partial\varphi}{\partial z} = 0,\end{gathered} \tag{1}$$

$$Z_{\text{in}} = \frac{\rho_2 c_2}{\cos\theta_2} = \frac{\omega\rho_2}{\sqrt{k_2^2 - \xi^2}}, \quad k_2 = \frac{\omega}{c_2}, \quad k_1 = \frac{\omega}{c_1(z)},$$

where Δ is the Laplacian; φ and p are the velocity potential and the pressure in the liquid layer $z \in (0, h)$ characterized by the parameters ρ_1 and $c_1(z)$ and lying on a liquid halfspace with the parameters ρ_2 and c_2 (ρ and c are the density and the sound velocity, respectively); ω is the circular frequency; θ_2 is the angle of refraction; and ξ is the propagation constant.

If the solution to the boundary-value problem given by Eqs. (1) is sought for in the form of a cylindrical wave $\varphi(r, z) = \varphi(z)H_0^{(2)}(\xi r)$, the unknown function of the vertical coordinate $\varphi(z)$ satisfies the equation

$$\frac{\partial^2\varphi(z)}{\partial z^2} + (k_1^2(z) - \xi^2)\varphi(z) = 0. \tag{2}$$

Let us introduce a reference waveguide with a constant sound velocity $\bar{c}_1 = \text{const}$. Then, Eq. (2) can be written in a form convenient for the further application of the perturbation technique:

$$\begin{gathered}\frac{\partial^2\varphi(z)}{\partial z^2} + (\bar{k}_1^2 - \xi^2)\varphi(z) = (\bar{k}_1^2 - k_1^2(z))\varphi(z),\\ \bar{k}_1 = \frac{\omega}{\bar{c}_1}.\end{gathered} \tag{3}$$

Let $\varphi_n^{(0)}(z, \xi_n)$ and ξ_n be the eigenfunctions and the eigenvalues of the propagation constant corresponding to the reference waveguide (the Pekeris waveguide). Then, the left-hand side can be written as the expansion [6]

$$\begin{aligned}f_n(z) &= (\bar{k}_1^2 - k_1^2(z))\varphi_n^{(0)}(z, \xi_n)\\ &= \frac{1}{2}\Biggl\{\sum_{m=1}^{M^-} a_{nm}^-\varphi_m^{(0)}(z, \xi_m^-) + \sum_{m=1}^{M^+} a_{nm}^+\varphi_m^{(0)}(z, \xi_m^+)\\ &\quad + 2\,\text{Re}\sum_{m=1}^{\infty}\tilde{a}_{nm}\varphi_m^{(0)}(z, \tilde{\xi}_m)\Biggr\},\end{aligned} \tag{4}$$

where $a_{nm}^{\pm} = \dfrac{2}{h}\dfrac{(f_n, \varphi_m^{(0)}(\xi_m^{\pm}))_h}{E_m^{\pm}}$, $\tilde{a}_{nm} = \dfrac{2}{h}\dfrac{(f_n, \varphi_m^{(0)}(\tilde{\xi}_m))_h}{\tilde{E}_m}$,

$\xi_n^{\pm}$ are the real propagation constants corresponding to

the transverse wave number $k_{32,n} = \sqrt{k_2^2 - \xi_n^2} = \pm i\alpha_n$ in the lower half-space ($\alpha_n = \sqrt{\xi_n^2 - k_2^2} > 0$), $\tilde{\xi}_n$ are the complex propagation constants corresponding to the normal leaky waves ($\mathrm{Im}\xi_n < 0$, $\mathrm{Re}k_{32,n} > 0$), $\varphi_n^{(0)}(z, \xi_n) = \sin(k_{31,n}z)$,

$$E_m^{\pm} = E_{1m} \mp E_{2m}, \quad E_{1m} = 1 - \frac{\sin(2x_m)}{2x_m},$$

$$E_{2m} = \rho_{12}\frac{\sin^2 x_m}{\alpha_m}, \quad \rho_{12} = \frac{\rho_1}{\rho_2},$$

$$\tilde{E}_m = 1 - \frac{\sin(2x_m)}{2x_m} - i\rho_{12}\frac{\sin^2 x_m}{k_{32,m}h},$$

$$x = k_{31}h, \quad k_{31}^2 = \bar{k}_1^2 - \xi^2,$$

and

$$(f, \varphi)_h = \int_0^h f(z)\varphi(z)dz.$$

In expansion (4), M^- is the number of normal waves with the real propagation constant ξ_n^- ($k_{32,n} = -i\alpha_n$) and M^+ is the number of generalized normal waves with the real propagation constant ξ_n^+ ($k_{32,n} = i\alpha_n$); both these waves are the eigenfunctions of the adjoint operators of problem (1). It is necessary to use the eigenfunctions of both adjoint operators, because only a combination of these functions is a complete orthogonal system of eigenfunctions in the respective regions, the intersection of which is the segment $z \in (0, h)$ [6].

With Eq. (4), a solution to Eq. (3) has the form

$$\varphi_n(z, \xi_n) = \sum_m b_{nm}\varphi_m^{(0)}(z, \xi_m),$$
$$b_{nm} = \delta_{nm} + \frac{a_{nm}}{2(\xi_m^2 - \xi_n^2)}. \tag{5}$$

Here, δ_{nm} is the Kronecker delta; the summation is performed over all the eigenvalues of the propagation constant $\xi_m^{\pm}$, $\tilde{\xi}_m$, and $\tilde{\xi}_m^*$ (the asterisk means complex conjugation); and $b_{nn} = 1 + \beta_{nn}/2$, where $\beta_{nn} = \lim_{m \to n}\left[\frac{a_{nm}}{\xi_m^2 - \xi_n^2}\right]$. Expansion (5) should be supplemented with the definition of the wave number of the reference waveguide

$$(f_n, \varphi_n)_h = 0, \quad \bar{k}_{1n}^2 = \frac{(k_1^2(z), (\varphi_n^{(0)})^2)_h}{(\varphi_n^{(0)}, \varphi_n^{(0)})_h}, \tag{6}$$

which shows that each normal wave is associated with its own reference waveguide with the average sound velocity $\bar{c}_1 = \bar{c}_{1n}$, the dependence of the average velocity on mode index being however sufficiently weak.

Assume that linear transform (5), in which the reference waveguide is defined by Eq. (6) averaged over the set of the normal waves as

$$\langle \bar{k}_{1n}^2 \rangle_n = \bar{k}_1^2 = \frac{1}{h}\int_0^h k_1^2(z)dz, \tag{7}$$

can be taken as an approximate solution to the problem given by Eqs. (3) and (6).

Note that the perturbation technique is often successfully used for solving inhomogeneous and irregular waveguide problems. A list of publications concerned with this issue can be found, for example, in [7]. However, as far as we know, linear transform (5) of the orthogonal bases $\varphi_n(z, \xi_n)$ and $\varphi_n^{(0)}(z, \xi_n)$ in approximation (7) was never used to describe acoustic fields in inhomogeneous waveguides.

Consider a class of profiles $c_1(z)$ described by the bilinear squared refractive index

$$k_1^2(z) = \bar{k}_1^2 n^2(z),$$
$$n^2(z) = \begin{cases} a_1 + b_1 z, & z \in (0, h_0) \\ a_1 + (b_1 + b_2)h_0 - b_2 z, & z \in (h_0, h), \end{cases} \tag{8}$$

where the constants $a_1 > 0$, $b_1 > 0$, and $b_2 > 0$ are determined from the respective function $c_1(z)$

$$c_1(z) = \begin{cases} c_1(0) - g_1 z, & z \in (0, h_0) \\ c_1(0) - (g_1 + g_2)h_0 + g_2 z, & z \in (h_0, h), \end{cases} \tag{9}$$

in which the gradients of the sound velocity $g_1 > 0$ and $g_2 > 0$ are assumed to be given and the transformation formulas are

$$b_1 = \frac{2g_1\bar{c}_1^2}{c_1^3(0)} \approx \frac{2g_1}{c_1(0)}, \quad b_2 = \frac{2g_2\bar{c}_1^2}{c_1^3(0)} \approx \frac{2g_2}{c_1(0)},$$
$$\frac{g_1 h}{c_1(0)} \ll 1, \quad \frac{g_2 h}{c_1(0)} \ll 1,$$
$$a_1 = \left(\frac{\bar{c}_1}{c_1(0)}\right)^2,$$
$$\bar{c}_1 = c_1(0)\left[1 - \frac{g_1 h}{2c_1(0)} + \frac{(g_1 + g_2)h}{2c_1(0)}\left(1 - \frac{h_0}{h}\right)^2\right].$$

Consider boundary-value problem (1) with a solution given by Eqs. (5) and (7) when a source is present

in the form of a vertical cylindrical antenna enclosed in a rigid baffle with the boundary condition

$$r = a,$$
$$v(z) = v_0 F(z), \quad F(z) = \begin{cases} 1, & z \in (z_0 - l, z_0 + l) \\ 0, & z \bar{\in} (z_0 - l, z_0 + 0), \end{cases} \tag{10}$$

on its side surface $r = a$, where v_0 is the normal component of the vibrational particle velocity, a is the radius of the cylinder, and z_0 is the depth of the antenna.

The source function $F(z)$ can be expanded as

$$F(z) = \sum_n a_n \varphi_n(z, \xi_n)$$
$$= \sum_{n,m} a_n b_{nm} \varphi_m^{(0)}(z, \xi_m) = \sum_m a_m^{(0)} \varphi_m^{(0)}(z, \xi_m), \tag{11}$$

where the coefficients $a_m^{(0)}$ of expansion in terms of the eigenfunctions of the reference waveguide are known [6]:

$$a_m^{(0)} = \frac{2l}{h} \frac{\varphi_m^{(0)}(z_0, \xi_m)}{E_m} \Phi_m,$$
$$\Phi_m = \frac{\sin(k_{31,m} l)}{k_{31,m} l} = \frac{\sin(x_m l_1)}{x_m l_1}, \quad l_1 = l/h, \tag{12}$$

and the coefficients a_n are determined by the inverse transform

$$a_n = \sum_m a_m^{(0)} b_{mn}^{-1}, \tag{13}$$

where b_{mn}^{-1} are the elements of the inverse matrix.

With Eqs. (12) and (13), the general solution to the problem given by Eqs. (1) and (10) can be written as

$$\varphi = v_0 \sum_n \frac{a_n \varphi_n(z, \xi_n)}{\xi_n H_1^{(2)}(\xi_n a)} \varepsilon_n H_0^{(2)}(\xi_n r)$$
$$= \varphi^{(0)}(r, z) + \Delta\varphi(r, z), \tag{14}$$

where

$$\varphi^{(0)}(r, z) =$$
$$= \frac{2l v_0}{h} \sum_n \frac{\varphi_n^{(0)}(z_0, \xi_n) \varphi_n^{(0)}(z, \xi_n)}{\xi_n H_1^{(2)}(\xi_n a) E_n} \Phi_n(\xi_n) \varepsilon_n H_0^{(2)}(\xi_n r)$$

is the acoustic field of the directional antenna in the reference waveguide (the Pekeris waveguide),

$$\Delta\varphi = v_0 \frac{2l}{h} (\bar{k}_1 h)^2$$
$$\times \sum_{n, m \neq n} \frac{\varphi_m^{(0)}(z_0, \xi_m) \varphi_n^{(0)}(z, \xi_n) \Phi_m(\xi_m)}{\sqrt{b_{nn} b_{mm}} E_m E_n (\xi_n^2 - \xi_m^2) h^2} \alpha_{nm}(r),$$

$$\alpha_{nm} = \frac{2}{h} ((n^2(z) - 1) \varphi_n^{(0)}, \varphi_m^{(0)})_h \tag{15}$$
$$\times \left[\frac{H_0^{(2)}(\xi_n r) \varepsilon_n}{\xi_n H_1^{(2)}(\xi_n a)} - \frac{H_0^{(2)}(\xi_m r) \varepsilon_m}{\xi_m H_1^{(2)}(\xi_m a)} \right],$$

$$\varepsilon_n = \begin{cases} 1 \text{ for normal waves} \\ \text{with the propagation contants } \xi_n^{\pm} \\ 1 + \dfrac{\tilde{a}_n^*}{\tilde{a}_n} \rho_{12} \dfrac{|\sin x_n|^2}{\alpha_n h E_{1n}} \text{ for leaky normal waves} \\ \text{with the propagation contants } \tilde{\xi}_n, \end{cases}$$

and the summation in Eqs. (14) and (15) is performed over all normal waves with the propagation constants $\xi_n^{\pm}$ and $\tilde{\xi}_n$.

Let us apply solutions (14) and (15) to calculate the radiation resistance of the antenna. According to [6], we have

$$Z_R = \frac{1}{v_0} \int_S p(a, z) dS = \rho_1 \bar{c}_1 S Z_R'$$
$$= \rho_1 c_1(0) S \left(1 + \frac{\Delta c}{c_1(0)}\right) (Z_R'^{(0)} + \Delta Z_R'),$$

where $\Delta c = \bar{c}_1 - c_1(0)$ and $S = 4\pi la$ is the antenna area,

$$Z_R'^{(0)} = \frac{2l}{h} \bar{k}_1 \sum_n \frac{\varphi_n^{(0)^2}(z_0, \xi_n) \Phi_n^2(\xi_n)}{\xi_n E_n H_1^{(2)}(\xi_n a)} i \varepsilon_n H_0^{(2)}(\xi_n a) \tag{16}$$
$$= r_R'^{(0)} + i x_R'^{(0)}$$

is the normalized radiation resistance of the antenna placed into the reference waveguide, and

$$\Delta Z_R' = \frac{4l}{h} (\bar{k}_1 h)^3 \sum_{n, m > n} \frac{\varphi_n^{(0)}(z, \xi_n) \varphi_m^{(0)}(z_0, \xi_m)}{E_m E_n (\xi_n^2 - \xi_m^2) h^2 \sqrt{b_{nn} b_{mm}}} \tag{17}$$
$$\times \Phi_m(\xi_m) \Phi_n(\xi_n) \frac{i \alpha_{nm}(a)}{h}$$

is the change in the normalized radiation resistance due to the inhomogeneity of the waveguide.

The overall change in the normalized radiation resistance consists of two components:

$$\Delta Z_\Sigma' = \Delta Z_1' + \Delta Z_2', \quad \Delta Z_1' = \frac{\Delta c}{c_1(0)} Z_R'^{(0)},$$
$$\Delta Z_2' = \Delta Z_R' = \Delta r_R' + i \Delta x_R',$$

of which the first component $\Delta Z_1'$ is proportional to the total change in the sound velocity $\bar{c}_1$ relative to a certain reference value ($\Delta Z_1 \sim \Delta c$) and the second compo-

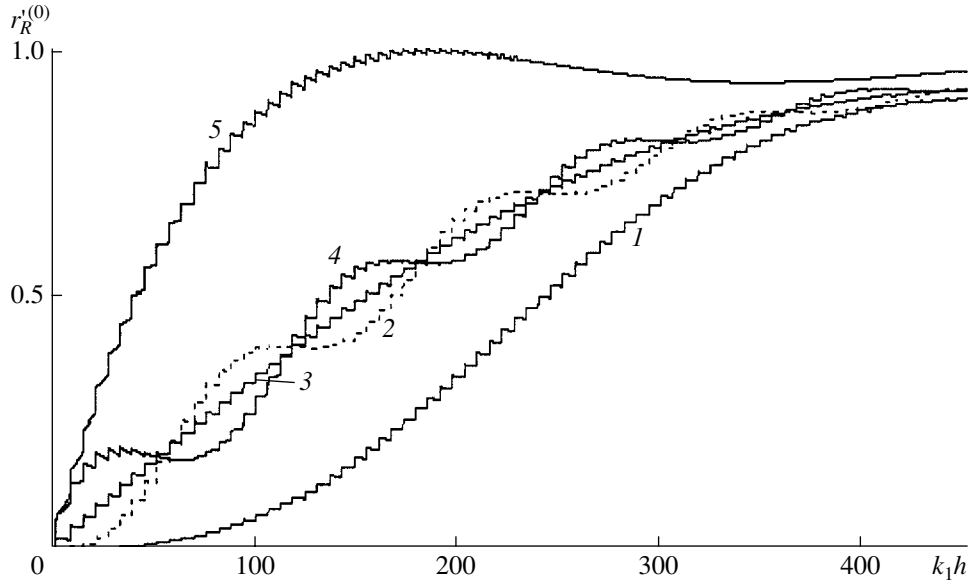

Fig. 1. Real part of the radiation resistance of the antenna $r_R'^{(0)}$ versus frequency for $l/h = 5 \times 10^{-3}$; $l = a$; and z_0/h = (*1*) 0.005, (*2*) 0.05, (*3*) 0.5, (*4*) 0.95, and (*5*) 0.99.

nent $\Delta Z_2' = \Delta Z_R'$ is determined by the local features of the velocity profile and by the antenna depth.

Consider an example of a numerical analysis assuming that $b_1 = b_2 = 10^{-3}$ m^{-1} ($g_1 = g_2 = 0.75$ s^{-1}), $c_{12} = \bar{c}_1/c_2 = 1.5/1.75$, $\rho_{12} = 1/1.6$, and $h = 100$ m, which corresponds to a sandy bottom and to the sound velocity gradient in the near-surface layers in summer.

Figure 1 shows the frequency dependence of the real part of the radiation resistance of the antenna at $l_1 = 5 \times 10^{-3}$ and $a = l$ in the reference waveguide with the antenna depth z_0 as a parameter. Let us consider the specific features of the curves shown in the figure.

In all curves, the small-scale variations in the radiation resistance are associated with the field's mode structure; the medium-scale variations are associated with the interference processes near the closest interface; and the large-scale variations, with the antenna size in terms of the wavelength. For example, for a small antenna ($\bar{k}_1 2l \ll 1$) operating near the free surface ($\bar{k}_1 z_0 \ll 1$), the frequency dependence of the real part of the radiation resistance is similar to that of a dipole antenna ($r_R' \sim \omega^4$). As the antenna moves away from the free surface, the interference maximums corresponding to the condition $2\bar{k}_1 z_0 = (2n + 1)\pi$ ($z_0 = \frac{\lambda_1}{4}(2n + 1)$, where λ_1 is the wavelength) are clearly pronounced. When the antenna approaches the bottom, the medium-scale variations with frequency are determined by the interference processes near this interface and the interference maxima comply with the condition $2\bar{k}_1 (h - z_0) = 2\pi n$, i.e., $(h - z_0) = n\frac{\lambda_1}{2}$.

Figure 2 illustrates the effect of the velocity profile $c(z)$ on the horizontal structure of the acoustic field. The calculations are performed for $z = z_0 = 0.5h$ and $h_0 = 1$, which correspond to a linear sound velocity profile and a negative refraction. The figure presents the normalized sound pressure on the logarithmic scale calculated for the inhomogeneous and reference waveguides

$$A = 20\log\frac{|p(r_1)|}{\rho_1 c_1 v_0},\quad A^{(0)} = 20\log\frac{|p^{(0)}(r_1)|}{\rho_1 c_1 v_0},\quad r_1 = \frac{r}{h}$$

with the averaging window $\Delta r_1 = 1$.

At relatively low frequencies ($k_1h = 100$, curves *1* and *2*), the refraction effects are rather small and the horizontal behavior of the field in the inhomogeneous waveguide, $p(r_1)$, does not significantly differ from that in the reference waveguide, $p^{(0)}(r_1)$. With increasing frequency ($k_1h = 400$, curves *3* and *4*), the directional properties of the transmitter (receiver) and the refraction effects start contributing to the formation of the zone structure of the acoustic field, and the horizontal sections $p(r_1)$ and $p^{(0)}(r_1)$ acquire the corresponding distinctions in their behavior. To make the plots more convenient to perceive, curves *3* and *4* in Fig. 2 are shifted by +10 dB.

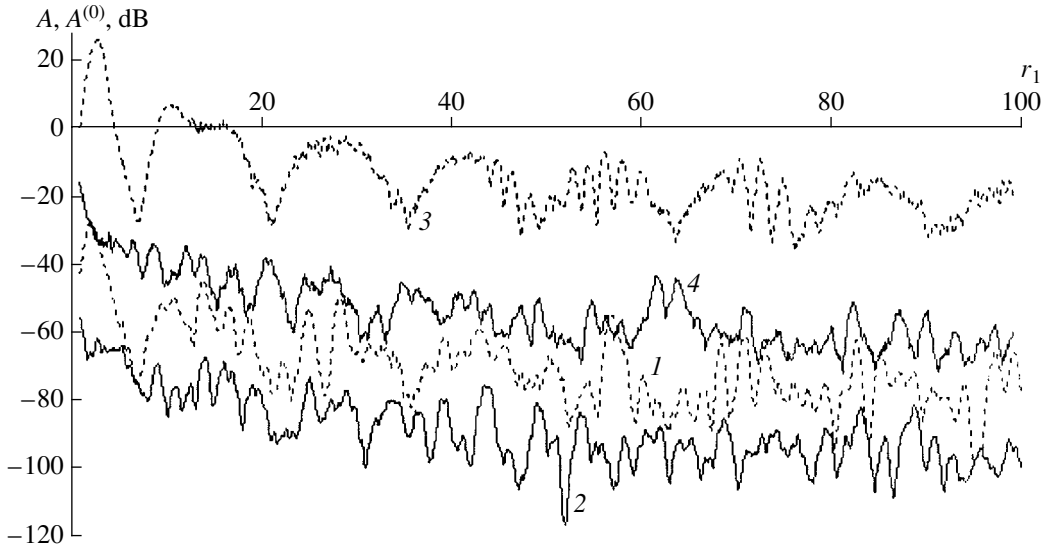

Fig. 2. Horizontal sections of the acoustic field in the inhomogeneous waveguide ($A(r_1)$, curves *1* and *3*) and in the reference waveguide ($A^{(0)}(r_1)$, curves *2* and *4*) for k_1h = (*1*, *2*) 100 and (*3*, *4*) 400.

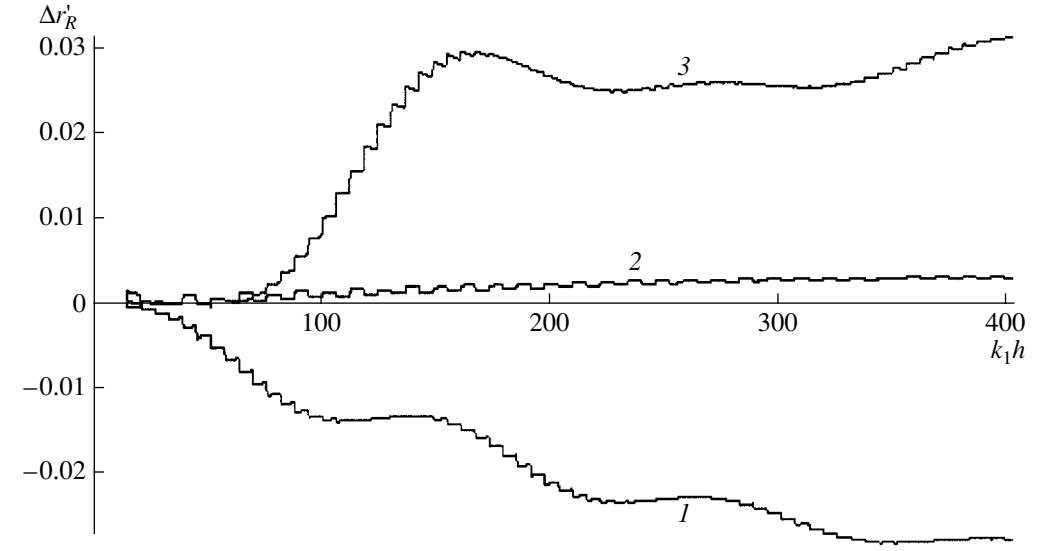

Fig. 3. Real part of the correction $\Delta r'_R$ to the radiation resistance versus frequency for $h_0 = 0$ and z_0/h = (*1*) 0.05, (*2*) 0.5, and (*3*) 0.95.

Figures 3–5 show the real part of the correction $\Delta r'_R$ versus the frequency for various antenna depths and the parameters h_0 of the sound velocity profile.

The main features of this function are as follows. For each sound velocity profile associated with a particular value of the parameter h_0, the frequency behavior of the correction $\Delta r'_R$ is in good agreement with the frequency behavior of $r'^{(0)}_R$, and its sign and the maximal value are determined by the antenna depth. Both quantities $\Delta r'_R$ and $r'^{(0)}_R$ exhibit similar behavior associated with the interference effects due to the interface closest to the antenna.

Another feature of the data we analyze is that the corrections $\Delta r'_R$ corresponding to the velocity profile with $h_0 = 0$ (positive refraction) and 1 (negative refraction) are in antiphase, which can be explained by the corresponding change in the sign of the deviation in the local sound velocity at the antenna depth from the average value [$\Delta r'_R \sim (c_1(z_0) - \bar{c}_1)$].

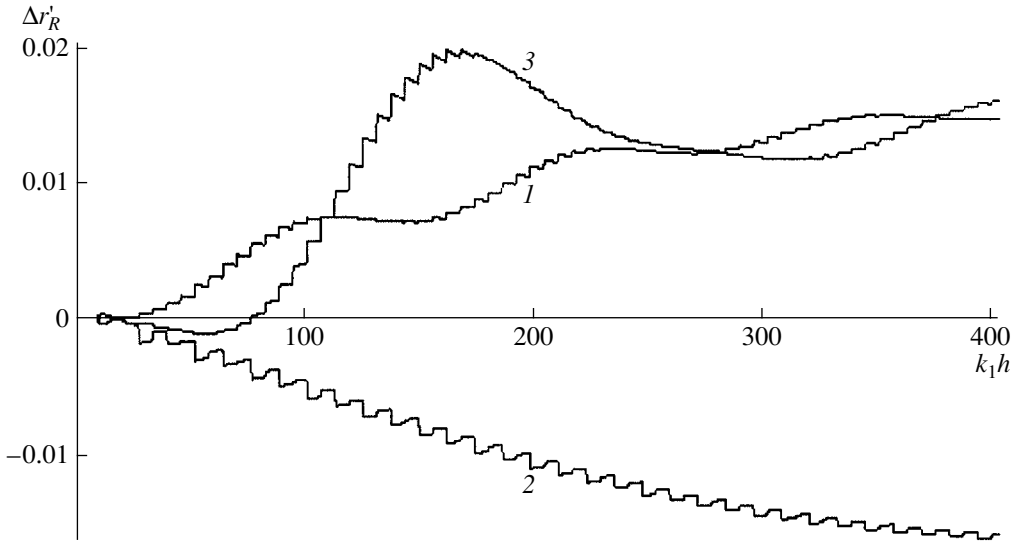

Fig. 4. Real part of the correction $\Delta r'_R$ to the radiation resistance versus frequency for $h_0 = 0.5h$ and z_0/h = (*1*) 0.05, (*2*) 0.5, and (*3*) 0.95.

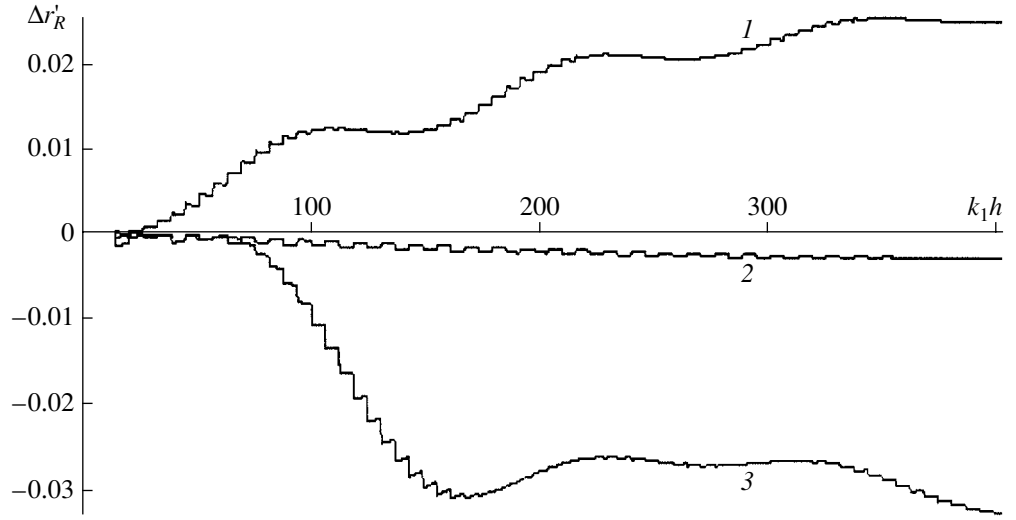

Fig. 5. Real part of the correction $\Delta r'_R$ to the radiation resistance versus frequency for $h_0 = h$ and z_0/h = (*1*) 0.05, (*2*) 0.5, and (*3*) 0.95.

Since both components, $\Delta r'_1$ and $\Delta r'_2$, exhibit a similar frequency dependence and similar features of the interference behavior, the total correction $\Delta r'_\Sigma$ can be analyzed as a function of the parameters h_0 and z_0 at a fixed frequency. Figure 6 illustrates this dependence in the limiting case $k_1h \gg 1$.

It should be noted that, for a near-surface source, the components $\Delta r'_1$ and $\Delta r'_2$ are in antiphase for any h_0 and the total correction is small, whereas, for a near-bottom source, the corrections are combined being in phase. In all cases, the total correction is in good agreement with the variations in the average sound velocity at the source depth.

This fact allows us to use the well-established methods for measuring the radiation resistance and its variations for monitoring the variations in the sound velocity; i.e., the impedance acoustic thermometry method can be realized virtually without any radiation. The absence of both high-intensity low-frequency radiation and long stationary specially equipped acoustic tracks is an important advantage of the impedance acoustic thermometry over the known methods used, for example, in the ATOS project [8, 9]. The operating frequency

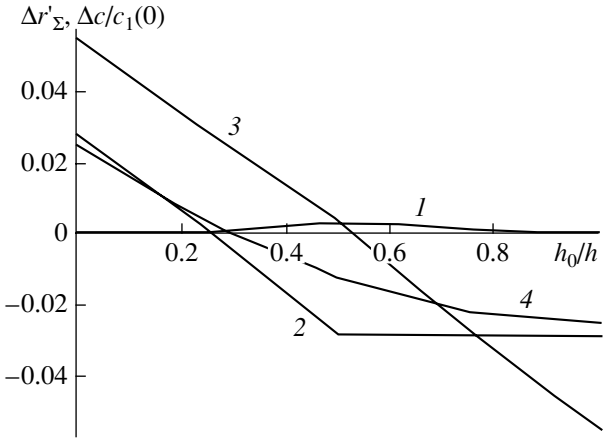

Fig. 6. The quantities (*1–3*) $\Delta r'_\Sigma$ and (*4*) $\Delta c/c_1(0)$ versus the parameter h_0 for z_0/h = (*1*) 0.05, (*2*) 0.5, and (*3*) 0.95.

at which the radiation resistance of such a source and its variation are measured must be sufficiently low in order to increase the efficiency of the spatial averaging of the sound velocity over the waveguide depth, and, at the same time, it must be sufficiently high to reduce the measurement error. The antenna must be placed at a depth where the sound velocity experiences the maximal variation.

REFERENCES

1. V. A. Eliseevnin, Akust. Zh. **27**, 228 (1981) [Sov. Phys. Acoust. **27**, 125 (1981)].
2. B. P. Sharfarets, Akust. Zh. **31**, 119 (1985) [Sov. Phys. Acoust. **31**, 68 (1985)].
3. A. N. Stepanov, Akust. Zh. **45**, 278 (1999) [Acoust. Phys. **45**, 242 (1999)].
4. Yu. A. Kravtsov, E. M. Kuz'min, and V. G. Petnikov, in *Acoustics of the Oceanic Medium* (Nauka, Moscow, 1989), pp. 178–186.
5. N. V. Zlobina, B. A. Kasatkin, and L. G. Statsenko, in *Proceedings of the VIII School–Seminar of Academician L.M. Brekhovskikh "Acoustics of the Ocean"* (GEOS, Moscow, 2000), p. 118.
6. B. A. Kasatkin and L. G. Statsenko, *Energy and Field Characteristics of the Acoustic Antennas in Waveguides* (Dal'nauka, Vladivostok, 2000).
7. B. G. Katsnel'son and V. G. Petnikov, *Acoustics of a Shallow Sea* (Nauka, Moscow, 1997).
8. A. N. Gavrilov, in *Proceedings of the VIII School–Seminar of Academician L.M. Brekhovskikh "Acoustics of the Ocean"* (GEOS, Moscow, 2000), p. 7.
9. P. F. Worcester, B. M. Howe, J. A. Colosi, *et al.*, J. Acoust. Soc. Am. **105**, 3185 (1999).

Translated by A. Khzmalyan

Acoustical Physics, Vol. 47, No. 6, 2001, pp. 714–720. Translated from Akusticheskiĭ Zhurnal, Vol. 47, No. 6, 2001, pp. 809–815.

Analysis of the Natural Vibrations of Circular Piezoceramic Plates with Partial Electrodes

N. F. Ivina

Makarov Pacific Naval Institute, ul. Kamskaya 6, Vladivostok, 690062 Russia

e-mail: helikot@mail.primorye.ru

Received January 20, 2000

Abstract—The finite-element method is used to analyze the thickness-symmetric vibrations of piezoelectric plates with partial electrodes. The spectra of the natural vibrations at resonance and antiresonance, the dynamic electromechanical coupling coefficient, and the vibration modes of these plates are studied for a wide range of geometric dimensions of both the plates and the partial electrodes. The optimal dimensions of the plates and electrodes, which correspond to the maximal values of the coupling coefficient, are determined. The increase in the coupling coefficient due to the utilization of the partial electrodes is considered for piezoelectric plates made of ceramics of various compositions. It is shown that all piezoceramic compositions can be divided into two groups. For the first group, the utilization of the partial electrodes can increase the coupling coefficient of the thickness vibrations by 7–23%, depending on the vibration mode. For the second group of piezoceramics, the coupling coefficient cannot be increased in this way; in other words, complete electrodes are optimal for the thickness vibrations of plates made of piezoceramics that belongs to the second group. © *2001 MAIK "Nauka/Interperiodica".*

Circular piezoceramic plates of commensurable dimensions are widely used in various acoustic devices. The natural vibrations of finite isotropic plates are described in detail in the monograph [1]. Vibrations of circular piezoceramic plates with complete electrodes were investigated experimentally [2, 3] and by the variational [4] and finite-element [5–7] methods.

It is well known from the experiment that the shape of the electrodes of piezoelectric transducers affects their resonance frequencies and the efficiency of excitation of different modes. An approximate mathematical model suitable for describing the radial vibrations of thin disks with axisymmetric partial circular electrodes was developed in [8]. It was shown that the resonance and antiresonance frequencies of the first radial mode increase as the electrode size decreases. It also follows from the presented dependences that the optimal (maximal) value of the dynamic electromechanical coupling coefficient (DCC), which is proportional to the difference between the antiresonance and resonance frequencies [3], is attained for the first mode when the large disk surfaces are not completely covered with electrodes.

A universal method for analyzing commensurable-size piezoelectric transducers, including those with partial electrodes, is the finite-element method [9–15]. Finite-element models were developed [9, 10] for piezoelectric quartz plates with partial electrodes, which are used in energy-trapped electromechanical resonators; shear and torsional modes of vibration were investigated. In [11, 12] the finite-element method was used to calculate the nonuniform electric and acoustic fields in measuring piezoelectric transducers in the two-dimensional (flat) approximation. Thick piezoelectric transducers with unconventionally positioned electrodes were considered.

The purpose of this paper is as follows: the analysis of thickness-symmetric vibrations of circular piezoelectric plates with partial electrodes, the investigation of the natural frequency spectra in the resonance and antiresonance regimes, and the study of the displacement distribution over the radiating surface (the vibrational modes) and the DCC for different geometric dimensions of the plates and partial electrodes. The final objective is the determination of the optimal dimensions of the piezoelectric plates and the electrodes, which correspond to the maximal DCC, and the investigation of the possibilities for increasing the DCC of thickness vibrations of piezoelectric plates for the plates made of piezoceramics of different compositions.

The study is performed by using the finite-element method, which takes into account two components of the displacement and the electric field. This approach makes it possible to study the natural vibrations of circular piezoelectric plates with partial axisymmetric electrodes [6, 7, 16].

Consider a circular piezoelectric plate with the radius a and thickness $2l$. From here on, the plate size will be defined by the ratio l/a. The complete electrodes (Fig. 1a) fully cover the planes $z = l$ and $z = -l$. We study two main variants of the arrangement of axisymmetric partial electrodes. The first is the annular peripheral electrodes leaving the central part (of radius b) of the plate free. The size of the annular electrodes is determined by the ratio b/a, the case $b/a = 0$ corresponding

to the complete electrodes. The second variant is the partial circular electrodes of radius h. Their size is defined by the ratio h/a, and the case $h/a = 1$ corresponds to the complete electrodes.

We assume that the whole surface of the piezoelectric plate is free from mechanical stresses. At the surfaces that are not covered by the electrodes, the normal component of the electric induction is equal to zero; the electrodes are equipotential surfaces. It is shown in [6, 16, 17] that, taking into account the indicated boundary conditions for the resonance (short circuit) and antiresonance (idling) regimes, we obtain the generalized matrix eigenvalue problems of high dimensionality

$$(H_{uu} - (k_t a)^2 c_{44} M)|u_i\rangle = 0, \quad (1)$$

$$(H_{uu} - H_{uv} H_{uv}^T / H_{vv} - (k_t a)^2 c_{44} M)|u_i\rangle = 0, \quad (2)$$

where M is the global dimensionless mass matrix; H_{uu}, H_{uv}, and H_{vv} are the global dimensionless matrices of stiffness, piezoelectric "stiffness," and dielectric "stiffness" with allowance for the boundary conditions at the electrodes and for the condensation (the exclusion of nodal electric potentials outside the electrodes); c_{44} is the element of the dimensionless matrix of elastic constants of piezoceramics; k_t is the wave number of the transverse wave; and $|u_i\rangle$ is the vector of the dimensionless (normalized to a) nodal displacements [6, 16].

The solution of problems (1) and (2) provides the eigenvalues, i.e., the dimensionless resonance and antiresonance frequency parameters $k_t a$, and the eigenvectors, i.e., the dimensionless nodal displacements $|u_i\rangle$. Knowing the eigenvalues and the eigenvectors of problem (1), the DCC (k) can be calculated for each vibrational mode as the ratio of the mutual energy to the geometric mean of the elastic and electric energy [16, 17]

$$k^2 = \frac{k_1^2}{1 + k_1^2}, \quad k_1^2 = \frac{(\langle u_i|H_{uv})^2 H_{vv}^{-1}}{(k_t a)^2 c_{44} \langle u_i|M|u_i\rangle}.$$

In the calculations, the quarter of the axial section of the piezoelectric plate, which lies in the first quadrant at $l/a \in [0.01; 0.5]$, was divided into 48 annular, rectangular in shape, second-order finite elements. Depending on the plate width, three variants of approximation were used: 12×4 for thick plates (12 finite elements along the radius, and four elements in the thickness direction), 24×2 for thin plates, and the intermediate variant 16×3. The number of equidistant nodes on the flat surface was 25, 49, and 33, respectively. To single out the thickness-symmetric vibrational modes, a boundary condition was introduced: the axial nodal displacement components were set equal to zero at the plane of symmetry $z = 0$ of the piezoelectric plate.

The results of the numerical calculations for the first radial mode were compared with the analytical solution [8] tested experimentally. Figure 2 presents the dependences of the resonance and antiresonance frequencies

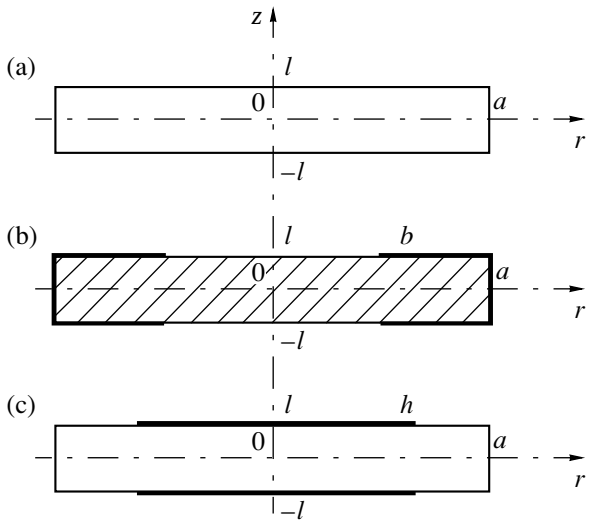

Fig. 1. Circular finite piezoelectric plate: (a) with complete electrodes; (b) with annular electrodes; (c) with circular electrodes.

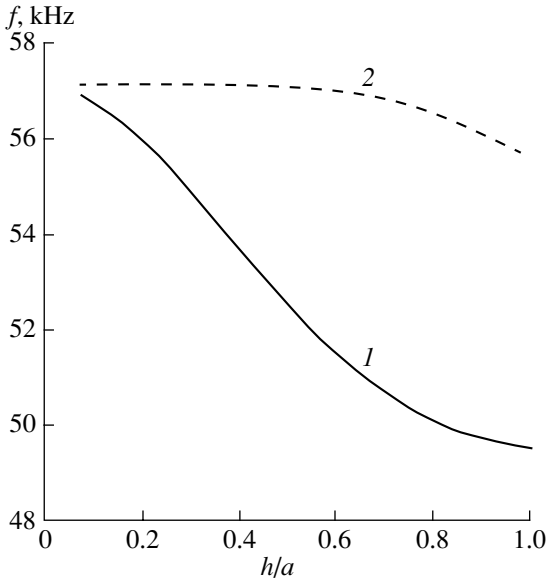

Fig. 2. Dependences of the (*1*) resonance and (*2*) antiresonance frequencies of the first mode of a TsTBS-3 piezoceramic plate on the radius of the circular electrodes.

of the first mode of radial vibrations on the size of circular electrodes. The radius of the piezoelectric plate is $a = 25$ mm, the thickness, which is ignored within the framework of the rough analytical model, is $2l = 1$mm, this value corresponding to the dimensionless ratio $l/a = 0.02$. The plate was made of TsTBS-3 piezoceramics whose parameters correspond to the reference data [18].

Qualitatively, the curves are similar to those obtained in [8] (for P1-60 piezoceramics, all parameters of which were not specified in the paper). It follows

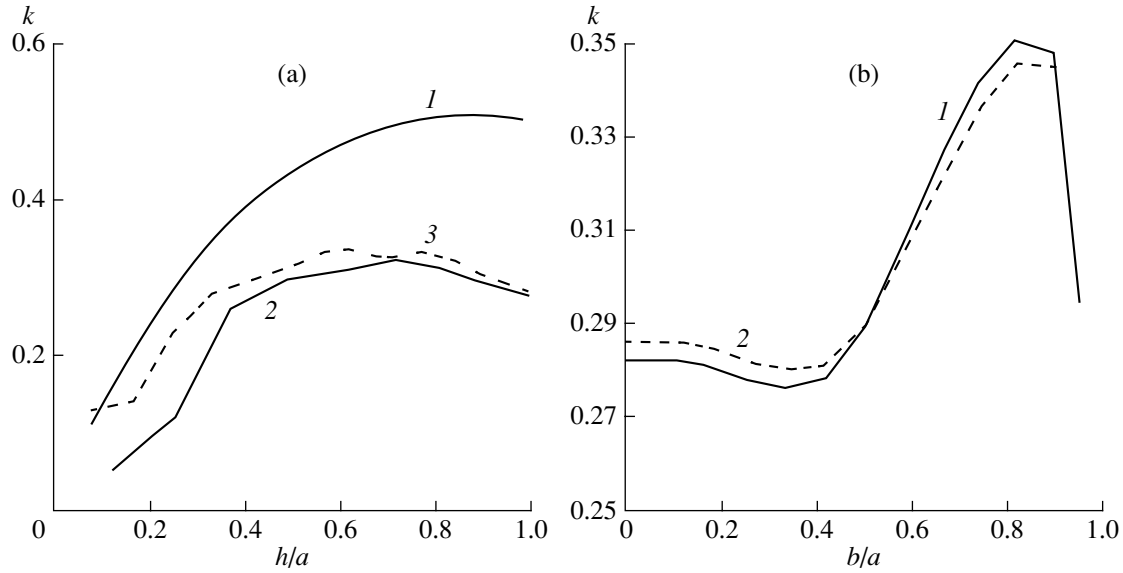

Fig. 3. Dependences of the dynamic electromechanical coupling coefficient of a TsTBS-3 piezoceramic plate on the radius of the partial electrodes: (a) (*1*) the first radial mode, $l/a = 0.02$; (*2*) the tenth mode, $l/a = 0.15$; (*3*) the thirteenth mode, $l/a = 0.115$; and (b) the fourth mode, $l/a =$ (*1*) 0.34 and (*2*) 0.36.

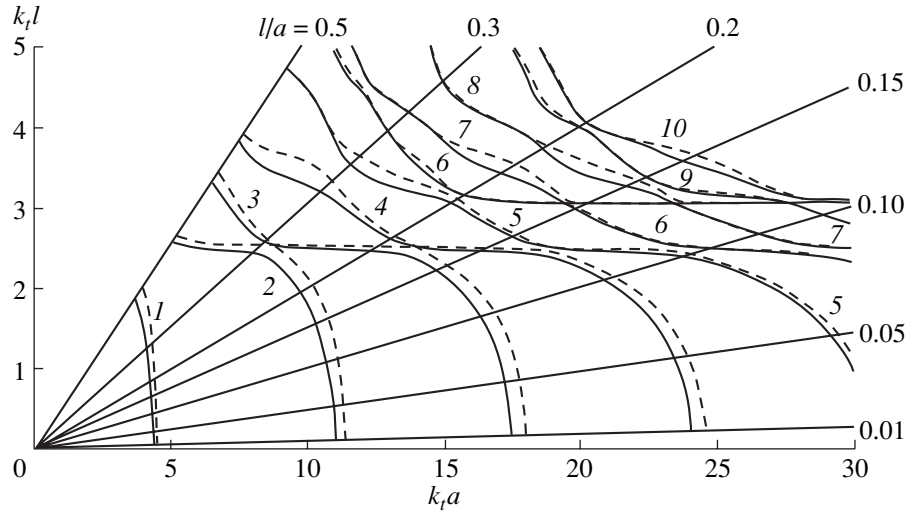

Fig. 4. Spectrum of the natural frequencies of a TsTBS-3 piezoceramic plate with annular electrodes, $b/a = 0.75$.

from Fig. 2 that the maximal difference between the resonance and antiresonance frequencies, which is proportional to the DCC, is reached at $h/a \approx 0.9$ (as in [8]) rather than in the complete-electrode case. This also validates our numerical results. Fig. 3a (curve *1*) demonstrates the dependence of the first-mode DCC on the size of the circular electrodes. The optimal (maximal) value of the DCC is reached at $h/a \approx 0.9$: $k_{max} = 0.51$, while for the complete electrodes, $k = 0.50$. Thus, at the first radial mode, the plate with the optimal partial electrodes operates somewhat more efficiently than the complete-electrode plate.

We made a great number of numerical computations for the natural frequency spectra and for the dependences of the DCC on the thickness of the piezoelectric plate in a wide range of the thickness values and the partial-electrode radii. One of the calculation variants is presented in Figs. 4 and 5. Figure 4 demonstrates the spectrum of natural frequencies in the resonance (the solid lines) and antiresonance (the dashed lines) regimes for a piezoelectric plate with annular electrodes at $l/a \in [0.01, 0.5]$ and $b/a = 0.75$. As for the case of the plate with complete electrodes [6, 7], the spectrum is represented in the coordinates $x = k_t a$ and $y = k_t l$; the mode numbers are indicated near the curves. Each ray issuing from the origin of coordinates corresponds to a certain value of the plate thickness l/a. The piezoactive regions, i.e., the regions where the difference

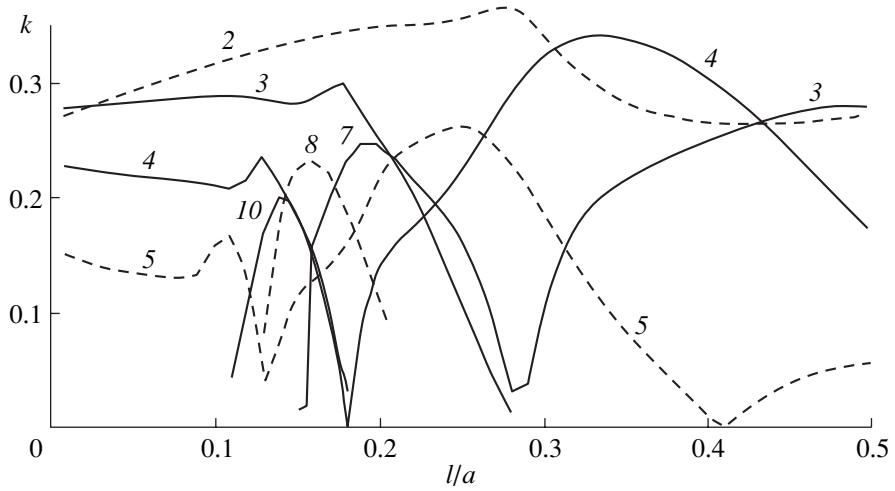

Fig. 5. Dependences of the dynamic electromechanical coupling coefficient of a TsTBS-3 piezoceramic plate with annular electrodes on the plate thickness, $b/a = 0.75$.

between the resonance and antiresonance frequencies is considerable and visible in the figure (which corresponds to a considerable value of the DCC), are not shaded in the computer-made figures, unlike the figures made earlier "by hand" in [6, 7]. Figure 5 demonstrates the dependences of the DCC on the piezoelectric plate thickness for the same variant; the mode numbers are indicated near the curves. The sixth and the ninth modes with a small value of the DCC are absent. The first mode has a large value of the DCC overstepping the limits of Fig. 5 and, therefore, is not presented in this figure. As the plate thickness increases, the DCC of the first mode grows almost linearly; for example, in the case of complete electrodes, the DCC increases from 0.504 to 0.581 for $l/a \in [0.01, 0.5]$.

Let us consider the change in the natural frequency spectra and the DCC of the piezoplates with annular electrodes compared to the complete-electrode case [6, 7]. The natural frequencies increase as the size of the electrodes is reduced. This is particularly clear for the first five radial modes for $l/a \in [0.01, 0.05]$. A pronounced increase is observed in the frequencies of the second, third, and fourth modes in the interval $l/a \in [0.01, 0.15]$ with a corresponding increase in the DCC of these modes for thin plates. The DCC of the fourth (quasi-thickness) mode increases at $l/a \approx 0.36$; the DCCs of the two other quasi-thickness modes decrease. The modes called in [6] the quasi-thickness ones are those whose axial components of the displacement u_z have cophased distributions at the face plane of the piezoelectric plate and dominate over the radial components u_r. It was also noted in [6] that the uniform (piston-like) distribution of u_z over the plate face, which corresponds to the one-dimensional theory, is observed for only the principal mode of a piezoelectric rod with $l/a > 1$ and is not observed for finite circular plates. That is why these modes were called the quasi-thickness ones. It was shown [6] that the quasi-thickness vibrations are formed by the fourth, seventh, tenth, thirteenth, and the subsequent modes at certain values of the plate thickness. Note also that the typical distributions of u_z presented for the complete-electrode piezoelectric plate in [6, 7] and in this paper are in good agreement with the experimental distributions reported in [2, 3], which validates the numerical results obtained here.

The distributions of u_z and u_r of the seventh and tenth mode over the face plane of the complete-electrode piezoelectric plate at the optimal (corresponding to the maximal DCC) values of the plate thickness are displayed in Fig. 6. In this figure, the displacement components are normalized to the value of u_z at the plate center. The abscissa axis represents the number of equidistant nodal points, where point 1 corresponds to the axis of symmetry of the plate ($r = 0$) and the last point (point 33 or 49, depending on the finite-element approximation of the piezoelectric plate) corresponds to $r = a$.

Let us consider the variant of increasing the DCC of the fourth mode, which has one minimum of u_z [6, 7], by disconnecting the electrode region corresponding to this minimum. This variant is not presented in Fig. 1. We disconnect the annular region that is centered at the point $n = 13$ (with 25 nodal points). We denote the step, i.e., the distance between adjacent nodes, by h_1. As the width of the disconnected region increases, the DCC grows monotonically (from the value $k = 0.286$ for the complete electrodes, $l/a = 0.36$) and reaches the maximal value $k = 0.348$ at the ring width $18h_1$. In this case, the electrodes occupy only a small central part with the radius $3h_1$ and a peripheral annular part with the width $3h_1$. As the plate thickness decreases from $l/a = 0.36$ to 0.34, the DCC grows slightly and reaches its maximal value $k = 0.353$, which is 0.86 of the static coupling coefficient k_t of this ceramics. Thus, by disconnecting a considerable part of the electrode near the minimum of u_z, we can raise the fourth-mode DCC by $\delta_4 = 23.4\%$.

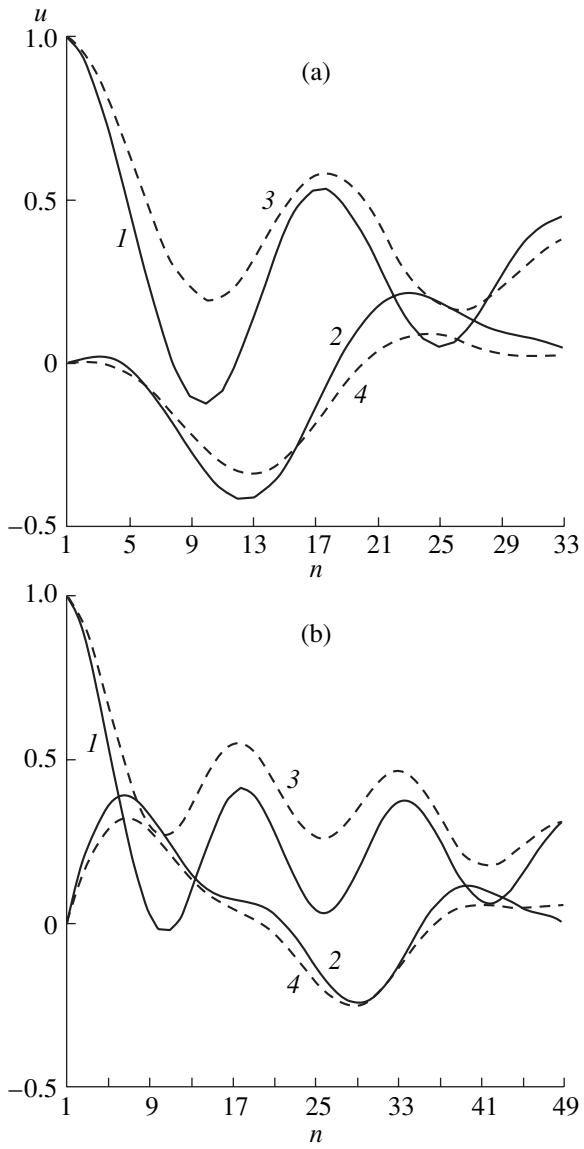

Fig. 6. Distributions of the (*1*, *3*) axial and (*2*, *4*) radial components of the displacement over the face of a TsTBS-3 piezoceramic plate of optimal thickness (*1*, *2*) with complete electrodes and (*3*, *4*) with optimal circular electrodes: (a) the seventh mode for (*1*, *2*) $l/a = 0.21$ and $k = 0.273$ and for (*3*, *4*) $l/a = 0.23$, $h/a = 0.63$, and $k = 0.292$; (b) the tenth mode for $l/a = 0.15$, $k =$ (*1*, *2*) 0.277 and (*3*, *4*) 0.323, and (*3*, *4*) $h/a = 0.72$.

The distributions of the displacement components in the case of such an optimal electrode differ only slightly from the distributions in the complete-electrode case [6, 7]. The main difference consists in a small increase in the minimal value of u_z. This effect will be more pronounced for higher quasi-thickness modes.

A similar result can be obtained with only annular peripheral electrodes (see Fig. 3b). In this case, at $b/a = 0.83$, the DCC reaches the values $k = 0.346$ at $l/a = 0.36$ and $k = 0.351$ at $l/a = 0.34$. Note that the DCC can be raised even higher by placing the annular electrode on the cylindrical surface close to the face plane of the piezoelectric plate. If the electrode occupies the upper half of the cylindrical surface (i.e., $z \in [l/2, l]$), the maximal DCC value $k = 0.379$ is reached. The same result is obtained in the total absence of electrodes at the plate face and in the case of annular peripheral electrodes of the width $2h_1$ with $l/a = 0.34$.

It is characteristic of the piezoplate with partial circular electrodes that the fourth-mode DCC drops with decreasing radius of the partial electrodes, whereas the DCC of two other quasi-thickness modes (seventh and tenth) rises. Let us consider the possibility for increasing the DCC of quasi-thickness modes by the utilization of partial circular electrodes.

The maximal DCC of the seventh mode of the complete-electrode piezoelectric plate is reached at the optimal thickness $l/a = 0.21$ and equals $k = 0.273$. Using the partial electrodes, one can slightly increase the DCC, so that it takes the maximal value $k = 0.288$ at the optimal electrode radius $h/a = 0.69$ for the same thickness of the plate. Changing the plate thickness to $l/a = 0.23$, one can obtain a somewhat higher value of the DCC: $k = 0.292$ at the optimal radius of the electrodes $h/a = 0.63$. Thus, the partial electrodes allow one to raise the seventh-mode DCC by only $\delta_7 = 7\%$.

The distributions of displacement components of the seventh mode are shown in Fig. 6a for the case of complete electrodes and optimal thickness and also for the optimal electrodes and optimal thickness. It is characteristic of the seventh and subsequent quasi-thickness modes that, in the case of partial optimal electrodes, the distributions of the displacement components, particularly, that of u_z, change considerably compared to the case of the complete-electrode piezoelectric plate. The optimal electrodes lead to an increase in the extremal values of u_z, particularly, the minimal ones; the amplitude of oscillations of u_z is reduced, and the antiphase region is absent in the minimum of u_z. This leads to the smoothing of the u_z distribution. Consequently, the average value of the function $u_z = u_z(r)$, which can be defined as $u_{z\mathrm{av}} = a^{-1}\int_0^a u_z(r)dr$, grows. The extremal absolute values of u_r are also reduced.

For the tenth mode, the optimal radius of partial electrodes is $h/a = 0.72$, the DCC reaching the value $k = 0.323$ (Fig. 3a, curve *2*) and increasing by $\delta_{10} = 16.6\%$. The tenth-mode distributions of the displacement components at the optimal plate thickness and complete electrodes and also at the optimal partial electrodes and optimal thickness are presented in Fig. 6b. As in the case of the seventh mode with the optimal electrodes, the amplitude of oscillations of u_z is reduced, and the average value increases.

The thirteenth quasi-thickness mode was also investigated. Its optimal piezoplate thickness is $l/a = 0.115$. The optimal electrode size also exists in this case (even two sizes, see Fig. 3a, curve *3*).The maximal value of

the DCC is $k = 0.336$ for the optimal electrode size $h/a = 0.63$. The distribution of the displacement components retain its behavior indicated above, and the DCC increases by $\delta_{13} = 18.7\%$.

Thus, the utilization of the optimal partial electrodes can raise the DCC of the quasi-thickness modes by the values varying from 7% for the seventh mode to 23% for the fourth mode. The distribution of the normal displacement component u_z changes: the amplitude of its oscillations decreases and the average value increases.

As was noted in [6], the main compositions of piezoceramics can be divided into two types, according to the type of the spectrum and the value of the DCC of quasi-thickness vibrations. The TsTBS-3 piezoceramics belongs to the first type determined by this classification system [6]. For this kind of ceramics, the maximal value of the DCC of quasi-thickness vibrations is $k \approx 0.7k_t$ (k_t is the static coupling coefficient of thickness vibrations) at the optimal value of the piezoelectric plate thickness. Taking the average DCC of quasi-thickness vibrations as $k \approx 0.32$ in the case of optimal partial electrodes, one can roughly assess the DCC in terms of k_t: $k \approx 0.78k_t \approx 0.8k_t$. Consequently, the TsTBS-3 piezoceramics (belonging to the first type) approaches in this index the second-type piezoceramics, which has $k \approx 0.8k_t$ [6].

Consider now the effect of the partial electrodes on the characteristics of piezoelectric plates made of the NBS-1 ceramics, which belongs to the second type. The DCC of the first radial mode slightly increases when the partial electrodes are used, as in the case of the TsTBS-3 ceramics. At $l/a = 0.12$ and the optimal electrode size $h/a \approx 0.9$, it reaches the maximal value $k = 0.341$, while in the case of complete electrodes, $k = 0.334$. The effect of partial electrodes on the characteristics of the quasi-thickness modes was studied for the optimal piezoelectric plate thickness. The partial electrodes proved to be unable to provide an increase in the DCC of any of the quasi-thickness modes.

It is evident that the process of energy transformation in the piezoelectric element is rather complex. It depends on the geometric shape of the element and the electrodes, on their size, and on the parameters of piezoceramics (its elastic, piezoelectric, and dielectric constants and its density). In every particular case, the full understanding of all features requires a detailed investigation of the distributions of the electric and elastic fields in the whole volume of the piezoelectric element and their conformity with the driving field. The practical conclusions are more easily made with the help of integral characteristics, which are necessary in the use of piezoelectric elements and can be tested experimentally. The integral characteristics are the value of the DCC and the distribution of the normal displacement component at the radiating surface, the latter being important for the analysis of the operation of an acoustically loaded piezoelectric element.

The analysis of the distributions of the displacement components of quasi-thickness modes in an NBS-1 piezoceramic plate (of the second type) at the optimal values of plate thickness and with complete electrodes shows [7] that they are different from the corresponding distributions obtained for the first-type TsTBS-3 piezoceramic plate. It is significant that the distributions obtained for the NBS-1 plate are closer to those for the TsTBS-3 plates with the optimal electrodes rather than with complete ones. In this case, the normal displacement component u_z has no negative regions near the minimum, and the average value of u_z is greater than that for the TsTBS-3 piezoceramic plate.

Thus, the two-type classification of piezoceramic compositions, which was proposed earlier, also proves to be useful in the analysis of the effect of partial electrodes on the characteristics of the quasi-thickness modes of piezoelectric plates. To verify this assumption, the characteristics of the quasi-thickness vibrations of piezoelectric plates made of other piezoceramic compositions were also investigated. They were the TsTSNV-1 (the first type) and the TBKS (the second type) piezoceramics. The above-mentioned differences in the distributions of the displacement components of the quasi-thickness modes of piezoelectric plates persist in both cases. For the TsTSNV-1 ceramics, the optimal partial electrodes can increase the DCC of the quasi-thickness modes: for example, the seventh-mode DCC increases by $\delta_7 = 10\%$. For the TBKS ceramics, the partial electrodes cannot increase the DCC of the quasi-thickness modes.

Consequently, for the piezoelectric plates made of the first-type piezoceramics (TsTBS-3, TsTSNV-1, or TsTS-19), their incomplete covering with electrodes can increase the DCC of the quasi-thickness modes up to $k \approx 0.8k_t$. For the piezoplates made of the second-type piezoceramics (NBS-1, TBKS, or TBK-3), the partial electrodes fail to increase the DCC of the aforementioned modes, the value of this coefficient being approximately the same in this case: $k \approx 0.8k_t$. In other words, complete electrodes are optimal for the quasi-thickness modes of piezoelectric plates made of the second-type piezoceramics.

REFERENCES

1. V. T. Grinchenko and V. V. Meleshko, *Harmonic Oscillations and Waves in Elastic Bodies* (Naukova Dumka, Kiev, 1981).
2. E. A. G. Shaw, J. Acoust. Soc. Am. **28**, 38 (1956).
3. *Physical Acoustics: Principles and Methods*, Ed. by W. P. Mason (Academic, New York, 1964; Mir, Moscow, 1966), Vol. 1, Part A.
4. R. Holland and E. P. Eer Nisse, *Design of Resonant Piezoelectric Devices* (MIT Press, Cambridge, 1969).
5. Y. Kagawa and T. Yamabuchi, IEEE Trans. Sonics Ultrason. **SU-23** (6), 379 (1976).
6. N. F. Ivina, Akust. Zh. **35**, 667 (1989) [Sov. Phys. Acoust. **35**, 385 (1989)].

7. S. M. Balabaev and N. F. Ivina, *Computer Simulation of Vibrations and Radiation of Finite Bodies: The Finite-Element and Boundary-Element Methods* (Dal'nauka, Vladivostok, 1996).
8. G. H. Schmidt, J. Eng. Math. **6** (2), 133 (1972).
9. Y. Kagawa, H. Arai, K. Yakuwa, *et al.*, J. Sound Vibr. **39**, 317 (1975).
10. Y. Kagawa and T. Yamabuchi, IEEE Trans. Sonics Ultrason. **SU-23** (4), 263 (1976).
11. R.-I. Yu. Kazhis and L. Yu. Mazheĭka, Nauchn. Tr. Vyssh. Uchebn. Zaved. Lit. SSR, Radioélektron. **19** (1), 25 (1983).
12. R.-I. Yu. Kazhis and L. Yu. Mazheĭka, Defektoskopiya, No. 6, 34 (1987).
13. J. Assaad, M. Ravez, and C. Bruneel, J. Acoust. Soc. Am. **100**, 3098 (1996).
14. J.-C. Debus, B. Debus, and J. Coutte, J. Acoust. Soc. Am. **103**, 3336 (1998).
15. D. Ekeom, B. Debus, and C. Granger, J. Acoust. Soc. Am. **104**, 2779 (1998).
16. S. M. Balabaev and N. F. Ivina, Prikl. Mekh. **25** (10), 37 (1989).
17. D. Boucher, M. Lagier, and C. Maerfeld, IEEE Trans. Sonics Ultrason. **SU-28** (5), 318 (1981).
18. *Piezoceramic Transducers*, Ed. by S. I. Pugachev (Sudostroenie, Leningrad, 1984).

Translated by A. Kruglov

Acoustical Physics, Vol. 47, No. 6, 2001, pp. 721–726. Translated from Akusticheskiĭ Zhurnal, Vol. 47, No. 6, 2001, pp. 816–822.

Interference of Opposing Longitudinal Acoustic Waves in an Isotropic Absorbing Plate and a Periodic Structure with Defects

A. A. Karabutov*, V. V. Kozhushko, I. M. Pelivanov*, and G. S. Mityurich****

** International Laser Center, Moscow State University, Vorob'evy gory, Moscow, 119899 Russia*
e-mail: ivan@sasha.phys.msu.su
*** Skorina State University, Gomel', ul. Sovetskaya 104, Gomel', 246699 Belarus*
e-mail: root@victor.belpak.gomel.by

Received July 17, 2000

Abstract—Interference of longitudinal acoustic waves propagating in opposite directions in a homogeneous isotropic absorbing plate and a periodic structure with a defect is considered theoretically. The periodic structure consists of alternating absorbing solid and transparent liquid layers. The defect is modeled by replacing a solid layer by a liquid layer of the same thickness. The dependences of the transmission spectrum of the energy flux on the amplitude ratio and phase difference of the interacting waves are studied. It is shown that, by varying the parameters of the opposite pressure wave, it is possible to change the transmission spectrum of the direct wave in a wide frequency range. An expression is obtained to determine the extremums of the wave amplitude transmitted through an absorbing plate depending on the amplitude ratio of the interacting waves. The results of studying a one-dimensional periodic structure demonstrate the possibility to considerably change the transmission spectrum of the pressure wave leaving the structure and also to eliminate the invariance of this spectrum under the interchange of the kth and $(n - k + 1)$th layers (where n is the total number of layers in the structure).

The effect of a transmission enhancement in thin metal films as a result of the interaction of electromagnetic waves propagating in opposite directions was studied in many papers. Later on, it was given the name of "tunnel" interference. Both the general laws of the interaction of opposing electromagnetic waves in absorbing crystalline and isotropic media and the possibilities to use the effect of tunnel interference in technology and various research problems were studied [1–4]. The most interesting results were the dependences of the intensity of a wave transmitted through an absorbing medium on the amplitude and phase of the opposite wave and on the coefficient of light absorption [2].

Drawing an analogy between electromagnetic and elastic waves, Efimov and Sementsov [5] demonstrated theoretically the possibility of increasing the transmittance of an absorbing elastic medium due to the interference of opposing longitudinal acoustic waves. This problem is undoubtedly important and interesting from the point of view of investigation of both absorbing media and multilayer structures, in which the interaction of opposing waves occurs as a result of multiple reflections of elastic waves from the boundaries [6]. In the cited paper [5], the dependence of the interference flux of waves propagating in opposite directions on the phase difference and layer thickness was studied.

We investigate the dependence of the transmission spectrum of a pressure wave transmitted through an absorbing medium on the amplitude and phase of a wave propagating in the opposite direction for two cases. In the first case, a homogeneous plane-parallel plate is considered, and in the second, a one-dimensional periodic structure consisting of alternating layers of a transparent liquid and an absorbing solid.

Let us consider the interference of longitudinal acoustic waves propagating in opposite directions in an isotropic absorbing plate. We assume that there are two ultrasonic sources in an immersion liquid with a plane-parallel plate between them. The plate plane is perpendicular to the line segment connecting the sources (Fig. 1). Two longitudinal monochromatic pressure waves, which have different amplitudes and a phase difference φ between them at the plate boundaries, propagate from the immersion liquid toward the plate normally to the plate surface. Mathematically, this can be expressed as follows:

$$\begin{aligned} p_f &= p_f \exp(i(\omega t - kx)), \\ p_b &= p_b \exp(i(\omega t + kx + \varphi)). \end{aligned} \tag{1}$$

Here, p_f and p_b are the amplitudes of the direct and opposite pressure waves, respectively; k is the wave number; and ω is the cyclic frequency.

Assuming that the waves under study have a plane wave front, we can ignore the formation of shear waves at the liquid–solid interface [7, 8]. Longitudinal acous-

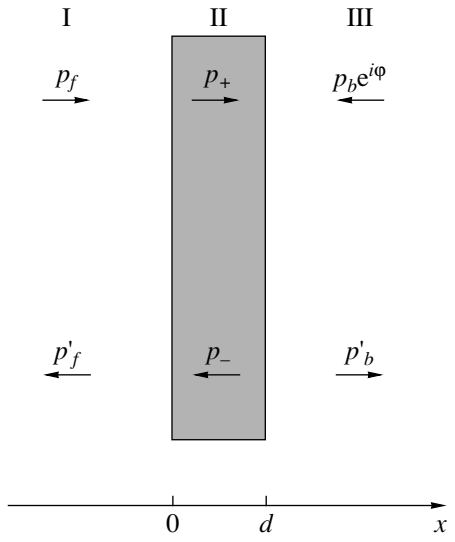

Fig. 1. Scheme of the interference interaction of longitudinal acoustic waves propagating in opposite directions in an isotropic absorbing plate.

tic waves are multiply reflected and interfere in the process of their propagation inside the plate. A result of such an interaction in the plate can be described by two waves, each of them being a superposition of single waves propagating in the same direction (see Fig. 1). To simplify the problem, we assume that the amplitudes of pressure waves are sufficiently small and nonlinear effects do not manifest themselves, which in its turn allows us to ignore the time dependence. The relation between the amplitude of a pressure wave and the particle velocity for a one-dimensional case with a dispersion-free medium is given by the expression [9]

$$\frac{\partial \nu(x,t)}{\partial t} = -\frac{1}{\rho}\frac{\partial p(x,t)}{\partial x}, \tag{2}$$

where ρ is the density of the medium and ν is the velocity of the medium particles.

From the boundary conditions implying equal pressures and particle velocities at the plate boundaries $x = 0$ and $x = d$, we obtain the following set of equations:

$$\begin{cases} p_f + p'_f = p_+ + p_-, \\ \dfrac{p_f}{\rho_0 c_0} - \dfrac{p'_f}{\rho_0 c_0} = \dfrac{p_+}{\rho c} - \dfrac{p_-}{\rho c}, \\ p_+ \exp(-ikd) + p_- \exp(ikd) = p_b \exp(i\varphi) + p'_b, \\ \dfrac{p_+}{\rho c}\exp(-ikd) - \dfrac{p_-}{\rho c}\exp(ikd) = -\dfrac{p_b \exp(i\varphi)}{\rho_0 c_0} + \dfrac{p'_b}{\rho_0 c_0}. \end{cases} \tag{3}$$

Here, ρ_0, ρ, c_0, and c are the densities and the velocities of sound propagation for the immersion liquid and the plate, respectively. The pressure amplitudes of all interacting waves are determined from the solution to the set of Eqs. (3). From the practical point of view, the most interesting parameters are the amplitudes of the pressure waves propagating from the plate into region I (p'_f) and into region III (p'_b), which can be represented in the form of a sum of waves transmitted through the plate and reflected from it [10].

The power flux density S of an acoustic wave can be represented as [9]

$$S = p\nu = \frac{|p|^2}{\rho c}. \tag{4}$$

It is easy to demonstrate that, in the case of a transparent plate, the difference between the energy fluxes carried by the waves toward the plate and away from it is equal to zero, which testifies to the conservation of the total flux and provides an opportunity to apply the obtained results in theoretical studies of absorbing media.

It is necessary to analyze the dependence of the energy carried by the wave p'_b into region III on the amplitude of the opposite wave p_b by fixing the total amount of energy supplied to the plate. Otherwise, it is irrelevant to discuss the energy gain resulting from the interaction of opposing waves [5]. For this purpose, we introduce the parameter a varying in the range from 0 to $\pi/4$ (the choice is determined by the problem geometry and by the absence of qualitatively new solutions in the range $\pi/4$–$\pi/2$) and represent the pressure amplitudes in the form $p_f = \cos a$ and $p_b = \sin a$. Then, we obtain a sequence of amplitudes of the pressure waves from the case of a unidirectional propagation ($a = 0$) to the case of opposing waves with equal amplitudes (at $a = \pi/4$).

We assume that, if the distances from the sources to the closest boundaries of the plate are different, a propagation path-length difference exists between the interacting waves, i.e., the phase difference in the studied frequency range is directly proportional to frequency. In the absence of the path-length difference, all waves of the selected spectral range approach the plate boundaries in phase. In this case, the transmission coefficient T_E for the energy flux (normalized to the total energy flux supplied to the plate by the waves of one frequency) that is carried by the wave p'_b into region III can be expressed as

$$T_E = \frac{16z^2 z_0^2 p_f^2 - 16 z z_0 (z^2 - z_0^2) p_f p_b \sin(2\pi\nu/\nu_0)\sin(\varphi) + 2(z^2 - z_0^2)^2 p_b^2 (1 - \cos(4\pi\nu/\nu_0))}{(z + z_0)^4 - 2(z + z_0)^2 (z_0 - z)^2 \cos(4\pi\nu/\nu_0) + (z_0 - z)^4}, \tag{5}$$

where $z = \rho c$ and $z_0 = \rho_0 c_0$ are the acoustic impedances of the plate and the immersion liquid, $\varphi = 2\pi\nu\Delta l/c_0$, Δl is the path-length difference, and $\nu_0 = c/d$ is the frequency at which the acoustic wavelength is equal to the plate thickness.

As one can see, the calculated transmission coefficient summarizes three fluxes, namely, the flux arriving from the source p_f in region I and transmitted through the plate, the flux resulting from the interaction of opposing waves, and the flux arriving from the source p_b and reflected by the plate. If the amplitude of the pressure wave generated by one of the opposite sources is equal to zero, Eq. (5) describes a reflected flux or a flux transmitted through the plate for the unidirectional case. The flux resulting from the interaction of opposing waves is described by the expression $16zz_0(z^2 - z_0^2)\sin(2\pi\nu/\nu_0)\sin(\varphi)p_f p_b$. The phase difference is of key importance for the determination of the value and direction of the opposite flux. An increase or decrease of the flux in region III is determined by the sign of this expression. If the phase difference between the interacting waves is a multiple of π (the absence of the phase difference is a particular case), the total flux to region III is equal to the sum of the fluxes transmitted through the plate and reflected from it.

The dependence of the energy flux carried by the wave p_b' through a transparent plate into region III on the frequency and on the ratio of the pressure amplitudes (the parameter a) in the case when a path-length difference occurs between the interacting waves is given in Fig. 2a. The parameters of the plate and the immersion liquid were taken to be those of plexiglas and water: $d = 1.6 \times 10^{-3}$ m, $\rho = 1.12 \times 10^3$ kg/m^3, $c = 2.65 \times 10^3$ m/s, $\rho_0 = 1 \times 10^3$ kg/m^3, $c_0 = 1.49 \times 10^3$ m/s, $\Delta l = 2 \times 10^{-3}$ m, and $\nu_0 = c/d$.

The peaks of the flux transmitted through the plate in the case of a unidirectional interaction occur when the plate thickness is equal to a whole number of half-waves. The transmission through a transparent plate at the corresponding frequencies ($\nu = \nu_0(m + 1)/2$, where m is a whole number) does not depend on the phase difference between the interacting opposing waves. We will demonstrate below that this is not true in the presence of absorption.

In the case of an absorbing plate, we represent the sound velocity in the medium in the form of a complex quantity with the imaginary part describing the absorption:

$$c = \frac{c}{(1 - i/2\pi Q)}, \tag{6}$$

where Q is the Q-factor relating the absorption to the acoustic wavelength (frequency). Absorption in plexiglas grows linearly with frequency in the studied frequency range 0.5–5 MHz: $Q = 1/\alpha\lambda \approx 30$ [11]. Absorption in water in the considered frequency range is insignificant.

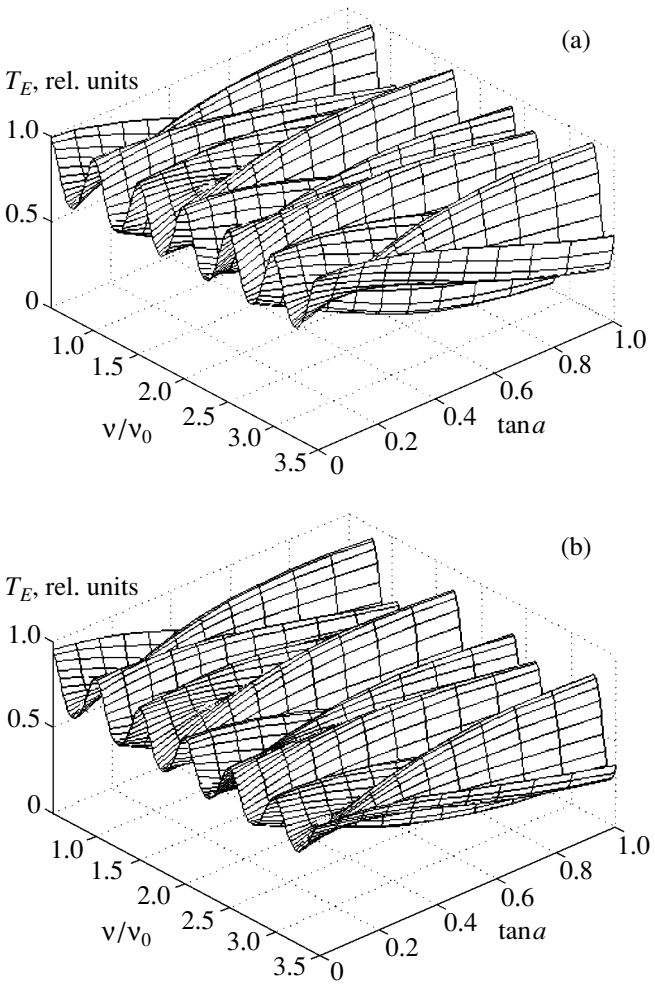

Fig. 2. Dependence of the transmission spectrum T_E of the energy flux carried by the pressure wave p_b' into region III on the amplitude ratio $\log a$ of opposing waves with the path-length difference $\Delta l = 2 \times 10^{-3}$ m: (a) a transparent plate and (b) an absorbing plate ($Q = 1/\alpha\lambda = 30$).

The results of the studies performed for an absorbing plate are presented in Fig. 2b. The inclusion of absorption in the medium leads a decrease in the transmission with increasing frequency. However, one can notice that the dependence $T_E(\nu)$ for an absorbing plate is not a monotonic, exponentially damped dependence. Taking into account only the first-order terms in the absorption coefficient, we can express the energy transmission coefficient as

$$\begin{aligned} T_E = [&16z^2 z_0^2 p_f^2 \exp(-2\nu/\nu_0 Q) + Int(\alpha, a) \\ &+ (z^2 - z_0^2)^2 p_b^2 (\exp(-4\nu/\nu_0 Q)) \\ &- 2\exp(-2\nu/\nu_0 Q)\cos(2\pi\nu/\nu_0) + 1)]/A, \end{aligned} \tag{7}$$

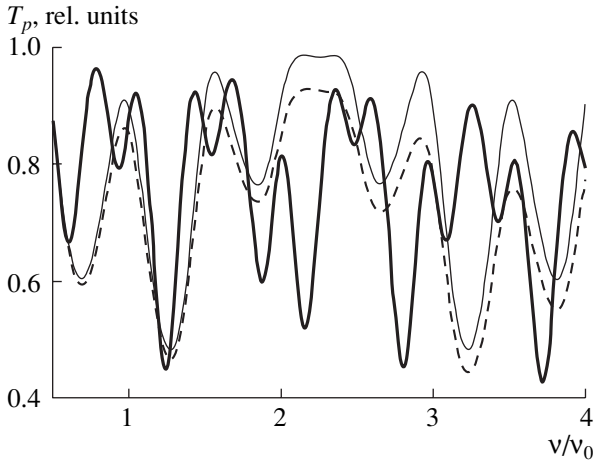

Fig. 3. Dependence of the transmission spectrum T_p of the pressure wave p_b' propagating into region III on the normalized frequency ν/ν_0 in the case of the interaction of opposing waves with different amplitudes ($a = \pi/7$) and with the path-length difference $\Delta l = 0.5 \times 10^{-3}$ m for a transparent plate (the thin line) and an absorbing plate (the dashed line) and 2×10^{-3} m for an absorbing plate (the thick line).

where

$$Int(\alpha, a) = 8zz_0(z^2 - z_0^2)(\exp(-\nu/\nu_0 Q) \times \cos(2\pi\nu/\nu_0 + \varphi) - \exp(-3\nu/\nu_0 Q) \times \cos(2\pi\nu/\nu_0 - \varphi))p_f p_b - \frac{8}{2\pi Q} zz_0(z_0^2 + z^2) \times (\exp(-\nu/\nu_0 Q)\sin(2\pi\nu/\nu_0 + \varphi) - \exp(-3\nu/\nu_0 Q)\sin(2\pi\nu/\nu_0 - \varphi))p_f p_b,$$

$$A = (z + z_0)^4 - 2(z_0^2 - z^2)^2 \exp(-2\nu/\nu_0 Q)\cos(2\pi\nu/\nu_0) + (z - z_0)^4 \exp(-4\nu/\nu_0 Q).$$

As one can see from Eq. (7), the absorption on the whole leads to a transmission decrease. The term proportional to the absorption coefficient is present in the expression describing the interferential interaction. However, it cannot considerably affect the transmission, because it is very small. The change in the transmission has a damping-oscillating character that is determined by the Q-factor Q and the relationships between the amplitudes and phases of the interacting waves.

If the path-length difference Δl of the interacting waves changes, the amplitude of the pressure wave propagating into region III also changes. The results obtained by studying the dependences of the wave amplitude transmitted through the plate on the path-length difference in a wide frequency range are presented in Fig. 3. The value of p_b' is determined by the ratio of the pressure amplitudes of the opposing waves and by their phase difference φ. In the general case of an arbitrary ratio of the opposing wave amplitudes, this value is limited by their sum and difference. An increase in the path-length difference between the interacting waves increases the phase difference $\varphi = \frac{2\pi\nu}{c}\Delta l$ and, consequently, changes the value and the direction of the flux given by Eqs. (5) and (7). In the ultrasonic transmission spectrum of the plate, an increase in the path-length difference between the interacting waves leads to more frequent changes of the flux direction with varying frequency. If the path-length difference between the interacting waves is absent and the amplitudes of opposing waves are equal in the whole frequency range, half of the total energy flux supplied to the plate will propagate into region III (this is a predictable result, which can be obtained from the symmetry of the considered problem).

It is interesting to study the dependence of ultrasonic transmission on the ratio of the amplitudes of opposing waves with fixed frequency and phase difference. Taking into account the absorption in the plate according to Eq. (6), the condition for the extremums of the amplitude of the transmitted pressure wave can be written in the form

$$\tan a = \frac{\exp(i2\pi\nu/\nu_0 + \nu/\nu_0 Q) - \exp(-i2\pi\nu/\nu_0 - \nu/\nu_0 Q)}{4}\left(\frac{z}{z_0}\frac{1 + i/2\pi Q}{1 + 1/4\pi^2 Q^2} - \frac{z_0}{z}\left(1 - \frac{i}{2\pi Q}\right)\right)\exp(i\varphi). \quad (8)$$

Let us compare it with the condition for the extremums in the case of a transparent plate, which can be obtained from Eq. (8) by passing to the limit $Q = \infty$:

$$\tan a = \frac{i\sin(2\pi\nu/\nu_0)}{2}\left(\frac{z}{z_0} - \frac{z_0}{z}\right)\exp(i\varphi). \quad (9)$$

One can see from Eq. (9) that, in the case of an arbitrary ratio of the wavelengths of the interacting waves and the thickness of the plate, the extremums manifest themselves at $\varphi = \frac{\pi}{2}(2m + 1)$, because $\tan a$ is real (here, m is a whole number). Moreover, if a whole number of half-wavelengths fits into the plate thickness, the phase difference does not affect the amplitude of the transmitted wave. In the case of an absorbing plate, all other conditions being the same, a phase shift appears in the indicated dependence in comparison with the case of a transparent plate. The shift value includes a constant component [the term in parenthesis in Eq. (8)]

and a component that depends on the wavelength (frequency) and is essential only for strong absorption. The amplitude of the wave transmitted through an absorbing plate is smaller than the amplitude of the wave transmitted through a transparent plate. However, it is possible to increase the transmission by changing the phase difference in certain regions (see Fig. 3). Thus, with the variation of the phase difference and the ratio of amplitudes of the interacting waves, the interaction of opposing waves provides an opportunity to change the transmission spectrum of an absorbing plate.

Now let us consider the interaction of waves propagating in opposite directions in one-dimensional periodic structures. In the case of unidirectional propagation of ultrasonic waves through a one-dimensional periodic structure, the transmission spectrum consists of transparency and opacity regions [12–15]. If a defect occurs in the structure (a layer disturbing the structure periodicity), a local maximum arises in the opacity region of the transmission spectrum [12, 16]. Experimental data on the transmission spectra in the case of unidirectional interaction agree well with the calculations [12]. On this basis, it was suggested to apply a nondestructive testing technique based on broadband acoustic spectroscopy [17] with a laser source of ultrasound [18]. In solving this problem, it is necessary to stress that the transmission spectra obtained for direct and inverse positions of a periodic structure with a defect are identical in the case of unidirectional propagation. As it will be demonstrated below, the interaction of opposing acoustic waves eliminates this ambiguity.

We assume that a multilayer structure consists of n isotropic layers with known physical constants and thicknesses. Longitudinal acoustic waves propagate toward the structure from opposite directions. The boundary conditions written for each boundary of the multilayer structure yield a set of equations analogous to Eqs. (3):

$$\begin{cases} P_f + P'_f = P_1^+ + P_1^-, \\ \dfrac{1}{c_0\rho_0}(P_f - P'_f) = \dfrac{1}{c_1\rho_1}(P_1^+ - P_1^-), \\ \dots \\ P_k^+ e^{-i\frac{\omega}{c_k}x_k} + P_k^- e^{i\frac{\omega}{c_k}x_k} = P_{k+1}^+ + P_{k+1}^-, \\ \dfrac{1}{c_k\rho_k}\left(P_k^+ e^{-i\frac{\omega}{c_k}x_k} - P_k^- e^{i\frac{\omega}{c_k}x_k}\right) = \dfrac{1}{c_{k+1}\rho_{k+1}}(P_{k+1}^+ - P_{k+1}^-), \\ \dots \\ P_n^+ e^{-i\frac{\omega}{c_n}x_n} + P_n^- e^{i\frac{\omega}{c_n}x_n} = P_b e^{i\varphi} + P'_b, \\ \dfrac{1}{c_n\rho_n}\left(P_n^+ e^{-i\frac{\omega}{c_n}x_n} - P_n^- e^{i\frac{\omega}{c_n}x_n}\right) = \dfrac{1}{c_0\rho_0}(-P_b e^{i\varphi} + P'_b), \end{cases} \tag{10}$$

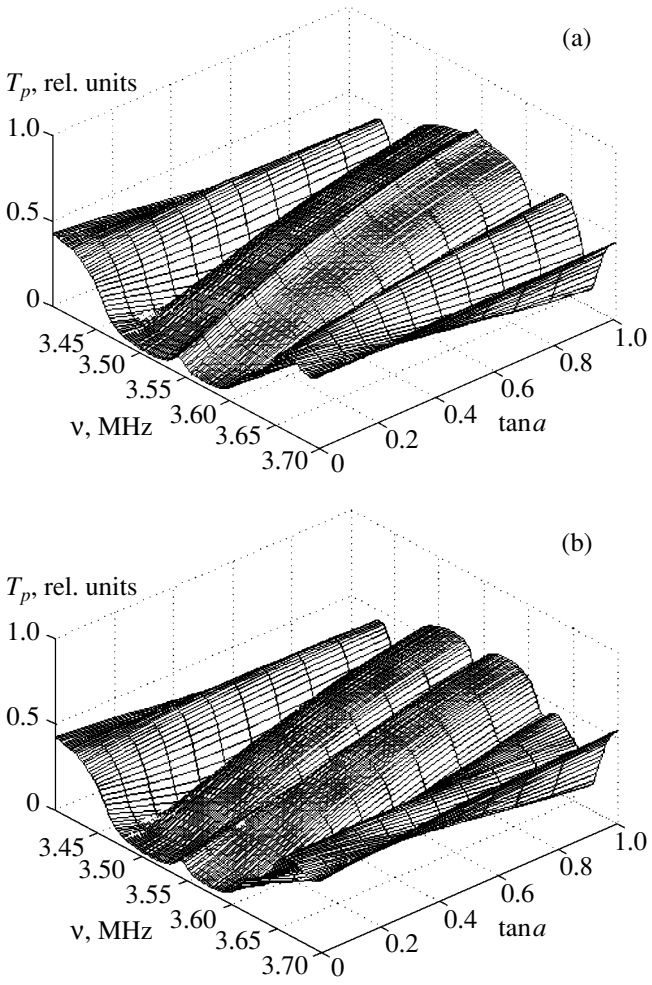

Fig. 4. Dependence of the spectrum of ultrasonic transmission T_p for a periodic structure consisting of ten plexiglas layers and nine water layers ($d = 1.6 \times 10^{-3}$ m, $c = 2.65 \times 10^3$ m/s, $d_0 = 1 \times 10^{-3}$ m, and $c_0 = 1.49 \times 10^3$ m/s) with a modeled defect; the path-length difference between the interacting waves is $\Delta l = 0.2 \times 10^{-3}$ m; the defect is (a) the *7*th layer and (b) the *13*th layer.

where x_k is the thickness of the kth layer; ρ_k and c_k are the density and the sound velocity in the layer located to the left of the boundary; ρ_{k+1} and c_{k+1} are those in the layer located to the right of it, respectively; P_k^+ and P_k^- are the amplitudes of pressure waves within the kth layer; k varies from 0 (the first boundary) to n (the last boundary); and ρ_0 and c_0 are the density and the sound velocity in the immersion liquid. Thus, we have a set of $2n + 2$ equations with the same number of unknowns. Solving this set, one can obtain the amplitudes of pressure waves. From the practical point of view, we are interested in the amplitudes of the waves propagating away from the structure. As in the case of a plate, we consider the transmission dependences with a fixed

total energy flux in the whole frequency range (we use the parameter a).

Here, we present the data obtained for the amplitude of a pressure wave (it is denoted as T_p in the figure). The periodic structure under study consisted of ten plexiglas layers ($d = 1.6 \times 10^{-3}$ m) and nine water layers ($d_0 = 1 \times 10^{-3}$ m). The modeled defect was a plexiglas layer replaced by a water layer of the same thickness. Absorption in plexiglas was taken into account in the same way as in the case of a plate, and ultrasonic absorption in water was ignored. The numerical analysis was performed with the help of the MATLAB software.

Figure 4 presents the dependences of the transmission spectra of periodic structures with defects (the seventh and thirteenth layers) for different ratios of the amplitudes of opposing waves with the path-length difference between them equal to 0.2 mm. It is important to note that, in the case of a unidirectional interaction ($a = 0$), the transmission spectra of the structures under consideration are identical and a local peak arises in the opacity region, which corresponds approximately to a frequency of 3.52 MHz in the plot. The interaction of opposing waves eliminates such an ambiguity: at $a \neq 0$, the ultrasonic transmission spectra of a periodic structure are different (the difference is most pronounced at the frequency close to the local maximum). An increase in the path-length difference between the interacting waves does not produce new results in comparison with a plane-parallel plate, but it changes the character of transmission in a broad frequency band, including the opacity region.

Thus, the considered problem of the interaction of waves propagating in opposite directions has an interference nature. We can consider the transmitted flux increase due to the changes in the parameters of the second source as an energy gain. The interaction of opposing waves provides an opportunity to model the flux transmitted through a plate in a broad frequency band. We obtained an expression for the extremums of the amplitude of the ultrasonic wave transmitted through an absorbing plate. The results of simulation for one-dimensional periodic structures demonstrated the difference in the ultrasonic transmission spectra of structures with defect layers symmetric with respect to the center (Fig. 4), these spectra being identical in the case of a single source. The results obtained can be useful for nondestructive testing. One can expect that similar dependences will occur in the case of the interaction of opposing electromagnetic waves.

REFERENCES

1. V. V. Sidorenkov and V. V. Tolmachev, Pis'ma Zh. Tekh. Fiz. **15** (21), 34 (1989) [Sov. Tech. Phys. Lett. **15**, 844 (1989)].
2. S. A. Afanas'ev, V. V. Efimov, and D. I. Sementsov, Opt. Spektrosk. **76** (3), 475 (1994) [Opt. Spectrosc. **76**, 425 (1994)].
3. D. Mugnai, Opt. Commun. **175** (4–6), 309 (2000).
4. G. S. Mityurich, A. N. Serdyukov, A. P. Zelenyi, and V. P. Zelenyi, J. Phys. (Paris) **4**, 769 (1994).
5. V. V. Efimov and D. I. Sementsov, Akust. Zh. **45**, 565 (1999) [Acoust. Phys. **45**, 504 (1999)].
6. G. Bal, J. B. Keller, G. Papanicolaou, and L. Ryzhik, Wave Motion **30** (4), 303 (1999).
7. D. A. Hutchins, R. J. Dewhurst, S. B. Pulmer, and C. B. Scruby, Appl. Phys. Lett. **38** (9), 677 (1981).
8. A. A. Karabutov, K. V. Kononets, and N. B. Podymova, Akust. Zh. **41**, 95 (1995) [Acoust. Phys. **41**, 81 (1995)].
9. L. M. Brekhovskikh and O. A. Godin, *Acoustics of Layered Media* (Nauka, Moscow, 1989; Springer, New York, 1990).
10. M. A. Isakovich, *General Acoustics* (Nauka, Moscow, 1973).
11. *Physical Quantities: A Handbook* (Énergoatomizdat, Moscow, 1991).
12. A. A. Karabutov, V. V. Kozhushko, I. M. Pelivanov, and N. B. Podymova, Akust. Zh. **46**, 510 (2000) [Acoust. Phys. **46**, 439 (2000)].
13. W. R. Scott and P. F. Gordon, J. Acoust. Soc. Am. **62**, 108 (1977).
14. M. S. Kushwacha, P. Halevi, L. Dobrsynski, and Djafari-Rouchani, Phys. Rev. Lett. **71** (13), 2022 (1993).
15. Tao Yu, Yan-Feng Chen, Yong-Yuan Zhu, *et al.*, Appl. Surf. Sci. **138–139**, 609 (1999).
16. R. James, S. M. Woodley, C. M. Dyer, and V. F. Humphrey, J. Acoust. Soc. Am. **97**, 2041 (1995).
17. A. A. Karabutov, M. P. Matrosov, N. B. Podymova, and V. A. Pyzh, Akust. Zh. **37**, 311 (1991) [Sov. Phys. Acoust. **37**, 157 (1991)].
18. V. É. Gusev and A. A. Karabutov, *Laser Photoacoustics* (Nauka, Moscow, 1991).

Translated by M. Lyamshev

Acoustical Physics, Vol. 47, No. 6, 2001, pp. 727–732. Translated from Akusticheskiĭ Zhurnal, Vol. 47, No. 6, 2001, pp. 823–829.

Multipath Maximums in the Correlation Function of a Wideband Noise Signal Produced by a Sea Object: Noise Immunity of Their Extraction

A. I. Mashoshin

Laboratory of Applied Acoustic Research, a/ya 10, Pushkin-4, St. Petersburg, 189620 Russia
e-mail: svi@t13755.spb.edu

Received February 16, 2000

Abstract—The noise immunity of the procedures used for extracting the local maximums of the autocorrelation and cross-correlation functions of a wideband noise signal produced by a sea object is studied. The autocorrelation and cross-correlation functions refer to the outputs of one or two spatial channels formed by a hydroacoustic array in the vertical plane. The limiting cases of low and high signal-to-noise ratios are considered. The noise immunity of extracting the maximums of the correlation function is compared with the noise immunity of the signal detection. © *2001 MAIK "Nauka/Interperiodica".*

Local maximums that occur in the correlation function (CF) of a wideband noise signal at the output of a sonar because of the multipath propagation in water carry the information on the coordinates of the source of the signal, and this fact is used in practice [1, 2]. The efficiency of using this information strongly depends on the noise immunity of the procedure used for extracting the aforementioned maximums (the noise immunity is understood as the possibility of extracting the maximums at a small signal-to-noise ratio (SNR) [3]).

The noise immunity of the CF maximum extraction procedures has been studied intensively (see, e.g., [4, 5]). Nevertheless, it is of interest to return to this issue and consider it from the viewpoint of the practical application of hydroacoustic devices under various operating conditions. This paper compares two CF maximum extraction algorithms and proposes convenient engineering formulas. The problem is solved for the case of a multipath hydroacoustic channel with constant (nonfluctuating) parameters.

Two algorithms for calculating the CF in order to localize its multipath maximums are used in practice. The first algorithm calculates the CF as the cross-correlation function (CCF) between the outputs of two spatial channels formed in the receiver. Horizontally, both channels look in the direction toward the noise source. Vertically, they are oriented in different directions toward the maximums of the spatial spectrum of the received signal. The second algorithm calculates the CF as the autocorrelation function (ACF) at the output of one of the spatial channels. This algorithm is used when the receiver has only one spatial channel in the vertical plane (e.g., when the sonar uses a horizontal linear array) or when the spatial spectrum of the signal has no more than one maximum in the vertical plane. Below, we consider these two algorithms separately.

The inverse fast Fourier transform (IFFT) applied to the real part of the cross spectrum of two spatial channel outputs

$$\tilde{K}(\tau) = \Phi^{-1}\{H(f)\tilde{S}_{12}(f)\} \quad (1)$$

is known to be the most efficient digital technique for calculating the CF [6]. Here, $\tilde{K}(\tau)$ is the accumulated CCF estimate; $\tilde{S}_{12}(f)$ is the accumulated estimate of the real part of the cross spectrum of the outputs of the first and second spatial channels:

$$\tilde{S}_{12}(f) = \overline{\mathrm{Re}\{\hat{G}_1(f)\hat{G}_2^*(f)\}}; \quad (2)$$

$\hat{G}_1(f)$ is the estimate of the complex spectrum at the output of the first spatial channel; $\hat{G}_2^*(f)$ is the complex conjugate of the estimate of the complex spectrum at the output of the second spatial channel; $H(f)$ is the weighting function (the frequency filter); $\Phi^{-1}\{*\}$ means the IFFT; and the function $\mathrm{Re}\{*\}$ equals the real part of its argument. The overbar symbol in Eq. (2) means the accumulation or, to be more precise, the time-averaging.

Note that, since the IFFT is linear, the averaging can be applied either to the real part of the cross spectrum or to the estimate of the CCF. However, the accumulation of the real part of the cross spectrum is more advantageous from the viewpoint of the calculation complexity.

The complex spectrum of a superposition of the multipath signal and noise at the output of the ith spatial channel can be represented as

$$G_i(f) = G_{co}(f)\sum_{m=1}^{L} A_{mi}(f)e^{-j2\pi f t_m} + G_{n_i}(f), \quad (3)$$

where $G_{co}(f)$ is the complex spectrum of the transmitted signal normalized by its amplitude spectrum (to put it differently, the complex spectrum of white noise with the unit amplitude spectrum); L is the number of paths the signal travels from the source to the receiving array; $A_{mi}(f)$ is the amplitude spectrum of the output of the ith spatial channel due to the signal arriving through the mth path; t_m is the time for the signal to travel the mth path from the source to the receiving array; and $G_{n_i}(f)$ is the complex spectrum of the noise at the output of the ith spatial channel.

By substituting Eq. (3) into Eq. (2), we obtain

$$\tilde{S}_{12}(f) = \sum_{m=1}^{L}\sum_{n=1}^{L} A_{m1}(f)A_{n2}(f)\cos(2\pi f\tau_{mn}) + S_{n_{12}}(f) + \Delta S_{12}(f), \tag{4}$$

where $\tau_{mn} = t_m - t_n$ is the time difference between the signals coming through the mth and nth paths; $S_{n_{12}}(f)$ is the real part of the cross spectrum of noise at the outputs of the first and second spatial channels; $\Delta S_{12}(f)$ is the error in the estimate of the real part of the cross spectrum of the superposition of the signal and noise, which has a zero expectation and variance determined as [7]

$$\sigma^2[\Delta S_{12}(f)] = \frac{S_1(f)S_2(f) + S_{12}^2(f)}{2\Delta f T_{\mathrm{CCF}}}; \tag{5}$$

$S_i(f)$ is the signal-plus-noise power spectrum at the output of the ith spatial channel:

$$S_i(f) = \sum_{m=1}^{L}\sum_{n=1}^{L} A_{mi}(f)A_{ni}(f)\cos(2\pi f\tau_{mn}) + S_{n_i}(f); \tag{6}$$

$S_{n_i}(f)$ is the noise power spectrum at the output of the ith spatial channel; Δf is the frequency resolution of the spectra $G_i(f)$, which is defined as [6]

$$\Delta f = \frac{1}{T_1}; \tag{7}$$

T_1 is the length of the realization subjected to the IFFT; and T_{CCF} is the CCF accumulation time.

For simplicity sake, we henceforth refer to the signal that came through the mth path as the mth signal.

It is known [8] that the noise immunity of procedures for extracting the local maximums of a spectrum (the CF, the indicative process) is completely determined by the so-called output (indicative) SNR, which in our problem is defined as

$$Q_{\mathrm{CCF}_{mn}} = \frac{M[\tilde{K}(\tau_{mn})] - M[\tilde{K}(\tau_{\Phi_{mn}})]}{\sigma[\tilde{K}(\tau_{\Phi_{mn}})]}, \tag{8}$$

where $Q_{\mathrm{CCF}_{mn}}$ is the output SNR for a local CCF maximum due to the correlation between the mth and nth signals; τ_{mn} is the abscissa of this maximum; $M[\tilde{K}(\tau_{mn})]$ is the expectation of the ordinate of this maximum; and $M[\tilde{K}(\tau_{\Phi_{mn}})]$ and $\sigma_2[\tilde{K}(\tau_{\Phi_{mn}})]$ are the expectation and variance of the background component of the CCF near the local maximum associated with correlation between the mth and nth signals.

Formula (8) assumes that

$$|\tau_{mn} - \tau_{\Phi_{mn}}| > \Delta\tau, \tag{9}$$

where $\Delta\tau$ is the signal correlation interval and, at the same time, the CCF resolution given, due to the symmetry of the frequency spectrum and CCF, by the formula similar to Eq. (7) [6]:

$$\Delta\tau = \frac{1}{f_{\mathrm{up}} - f_{\mathrm{low}}} \tag{10}$$

with f_{low} and f_{up} being the lower and the upper boundaries of the spectrum of the signal subjected to the IFFT.

Let us calculate the numerator and denominator in Eq. (8) separately. We begin with the numerator and designate it by X. For simplicity, we assume that the relative time differences of any two signal pairs, for example, τ_{mn} and τ_{ts}, differ by no more than $\Delta\tau$, i.e., the CF maximums due to the correlation between any two signals are separated.

By definition of the IFFT and in view of its property of being linear, we have

$$X = \int_{f_{\mathrm{low}}}^{f_{\mathrm{up}}} H(f)M[\tilde{S}_{12}(f)]\cos(2\pi f\tau_{mn})df - \int_{f_{\mathrm{low}}}^{f_{\mathrm{up}}} H(f)M[\tilde{S}_{12}(f)]\cos(2\pi f\tau_{\Phi_{mn}})df. \tag{11}$$

We substitute Eq. (4) into Eq. (11), replace the product of cosines with a sum of these, and collect similar terms. As a result, we obtain

$$X = \frac{1}{2}\int_{f_{\mathrm{low}}}^{f_{\mathrm{up}}} H(f)\sum_{t=1}^{L}\sum_{s=1}^{L} A_{t1}(f)A_{s2}(f) \times [\cos(2\pi f(\tau_{ts} - \tau_{mn})) + \cos(2\pi f(\tau_{ts} + \tau_{mn})) - \cos(2\pi f(\tau_{ts} - \tau_{\Phi_{mn}})) - \cos(2\pi f(\tau_{ts} + \tau_{\Phi_{mn}}))]df + \int_{f_{\mathrm{low}}}^{f_{\mathrm{up}}} H(f)S_{n_{12}}(f)[\cos(2\pi f\tau_{mn}) - \cos(2\pi f\tau_{\Phi_{mn}})]df. \tag{12}$$

By virtue of Eq. (9), all terms of this expression are integrals of the functions oscillating about zero and,

therefore, they tend to zero. Only two terms of the sum in the integrand of the first integral at $t = m$ and $s = n$ and at $t = n$ and $s = m$ are an exception. As a result, Eq. (12) takes the form

$$X = \int_{f_{\text{low}}}^{f_{\text{up}}} H(f)[A_{m1}(f)A_{n2}(f) + A_{m2}(f)A_{n1}(f)]df. \tag{13}$$

Since the estimates of the spectral components are mutually independent, the denominator in Eq. (8) can be written as

$$Y = \left[\Delta f \int_{f_{\text{low}}}^{f_{\text{up}}} H^2(f)\sigma^2[\tilde{S}_{12}(f)]\cos^2(2\pi f\tau_{\Phi_{mn}})df\right]^{\frac{1}{2}}. \tag{14}$$

Manipulations similar to those applied to the numerator yield

$$Y = \left[\frac{1}{4T_{\text{CCF}}}\int_{f_{\text{low}}}^{f_{\text{up}}} H^2(f)[[S_{s_1}(f) + S_{n_1}(f)] \times [S_{s_2}(f) + S_{n_2}(f)] + [S_{s_{12}}(f) + S_{n_{12}}(f)]^2]df\right]^{\frac{1}{2}}, \tag{15}$$

where $S_{s_i}(f) = \sum_{t=1}^{L} A_{ti}^2(f)$ is the sum of the power spectra of signals arriving through all L paths and observed at the output of the ith spatial channel (we call it the power spectrum of the signal) and $S_{s_{12}}(f) = \sum_{t=1}^{L} A_{t1}(f)A_{t2}(f)$ is the sum of the real parts of the cross spectra of signals arriving through L paths and observed at the outputs of the first and second spatial channels (we call it the signal cross spectrum).

With Eqs. (13) and (15), Eq. (8) yields

$$Q_{\text{CCF}_{mn}} = \sqrt{T_{\text{CCF}}}\frac{\int_{f_{\text{low}}}^{f_{\text{up}}} H(f)[A_{m1}(f)A_{n2}(f) + A_{m2}(f)A_{n1}(f)]df}{\left\{\int_{f_{\text{low}}}^{f_{\text{up}}} H^2(f)[[S_{s_1}(f) + S_{n_1}(f)][S_{s_2}(f) + S_{n_2}(f)] + [S_{s_{12}}(f) + S_{n_{12}}(f)]^2]df\right\}^{\frac{1}{2}}}. \tag{16}$$

Let us find the frequency response $H(f)$ of the filter that maximizes the $Q_{\text{CCF}_{mn}}$. Using the integral form of the Cauchy–Schwartz (Schwartz–Bunyakowsky) inequality [9], we obtain

$$\frac{\int_a^b H(f)C(f)df}{\sqrt{\int_a^b H^2(f)D^2(f)df}} \le \sqrt{\int_a^b \frac{C^2(f)}{D^2(f)}df}, \tag{17}$$

where $H(f)$, $C(f)$, and $D(f)$ are arbitrary functions.

The equality is attained in Eq. (17) when

$$H(f) = H_{\text{opt}}(f) = l\frac{C(f)}{D^2(f)}, \tag{18}$$

where l is an arbitrary nonzero constant.

With Eqs. (17) and (18), Eq. (16) yields

$$Q_{\text{CCFmax}_{mn}} = \sqrt{T_{\text{CCF}}} \times \left[\int_{f_{\text{low}}}^{f_{\text{up}}} \frac{[A_{m1}(f)A_{n2}(f) + A_{m2}(f)A_{n1}(f)]^2}{[S_{s_1}(f) + S_{n_1}(f)][S_{s_2}(f) + S_{n_2}(f)] + [S_{s_{12}}(f) + S_{n_{12}}(f)]^2}df\right]^{\frac{1}{2}}, \tag{19}$$

$$H_{\text{opt}_{mn}} = l\frac{A_{m1}(f)A_{n2}(f) + A_{m2}(f)A_{n1}(f)}{[S_{s_1}(f) + S_{n_1}(f)][S_{s_2}(f) + S_{n_2}(f)] + [S_{s_{12}}(f) + S_{n_{12}}(f)]^2}. \tag{20}$$

Expressions (16), (19), and (20) are obtained for the most general case of extracting the local maximums of the CCF. In practice, of primary interest is the noise immunity of the CCF maximum extraction at low SNRs $q_i(f)$, where $q_i(f)$ is understood as the signal-to-noise ratio at the output of the ith spatial channel:

$$q_i(f) = \frac{S_{s_i}(f)}{S_{n_i}(f)}. \quad (21)$$

At a low input SNR, the first terms in all three brackets in the denominators of expressions (16), (19), and (20) are less than the second terms. Taking into account that the spatial channels are oriented in the vertical plane so that the signal that came through one of the paths (e.g., the mth path) is better extracted at the output of the first spatial channel and the signal that came through another path (the nth path) is better extracted at the output of the second spatial channel, formulas (16), (19), and (20) can be represented in the form

$$Q_{\mathrm{CCF}_{mn}} = \sqrt{T_{\mathrm{CCF}}}\frac{\int_{f_{\mathrm{low}}}^{f_{\mathrm{up}}} H(f)A_{m1}(f)A_{n2}(f)df}{\left\{\int_{f_{\mathrm{low}}}^{f_{\mathrm{up}}} H^2(f)S_{n_1}(f)S_{n_2}(f)[1 + r_{n_{12}}^4(f)]df\right\}^{\frac{1}{2}}}, \quad (22)$$

$$Q_{\mathrm{CCFmax}_{mn}} = \left[T_{\mathrm{CCF}}\int_{f_{\mathrm{low}}}^{f_{\mathrm{up}}} \frac{[A_{m1}(f)A_{n2}(f)]^2}{S_{n_1}(f)S_{n_2}(f)[1 + r_{n_{12}}^4(f)]}df\right]^{\frac{1}{2}}, \quad (23)$$

$$H_{\mathrm{opt}_{mn}} = l\frac{A_{m1}(f)A_{n2}(f)}{S_{n_1}(f)S_{n_2}(f)[1 + r_{n_{12}}^4(f)]}, \quad (24)$$

where $r_{n_{12}}(f)$ is the normalized cross spectrum (the correlation coefficient at the frequency f) of noise at the outputs of the first and second spatial channels:

$$r_{n_{12}}(f) = \frac{S_{n_{12}}(f)}{\sqrt{S_{n_1}(f)S_{n_2}(f)}}.$$

The analysis of formula (23) gives two practical recommendations aimed at increasing the noise immunity of the extraction of the CCF maximums:

(i) The spatial channels should be pointed towards the strongest (in order to maximize the numerator) and, simultaneously, associated with the most distant sources (in order to decrease the noise correlation coefficient and, thereby, minimize the denominator) maximums of the signal spatial spectrum;

(ii) Since the integrand in Eq. (23) is nonnegative, the CCF should be calculated over the whole bandwidth of the receiver.

Under the assumption that the signal and noise spectra in Eq. (23) are frequency independent, we obtain the approximate formula for estimating the noise immunity of extracting the CCF maximums at low input SNRs:

$$Q_{\mathrm{CCFmax}_{mn}} \approx \left[(f_{\mathrm{up}} - f_{\mathrm{low}})T_{\mathrm{CCF}}\frac{A_{m1}^2}{S_{n_1}}\frac{A_{m2}^2}{S_{n_2}}\frac{1}{1 + r_{n_{12}}^4}\right]^{\frac{1}{2}}. \quad (25)$$

As follows from Eq. (25), the noise immunity of extracting the CCF maximums increases with increasing signal frequency band over which the CCF is calculated, CCF accumulation time, and SNR in each spatial channel and with decreasing noise correlation coefficient at the outputs of the two spatial channels.

Formula (24) shows that, if the spectra of both signals and the noise spectrum at the outputs of both spatial channels have similar shapes (which usually occurs in practice), the optimum filter given by Eq. (24) takes the form of the Eckart filter [8]:

$$H_{\mathrm{opt}} \approx l\frac{S_{s_1}(f)}{S_{n_1}^2(f)}. \quad (26)$$

In practice, it is convenient to calculate the numerator in Eq. (26) as the power spectrum of the signal estimated for the current hydroacoustic conditions and the expected distance to the source, and the denominator, as the squared noise power spectrum measured at the output of one of the spatial channels.

Let us compare the noise immunity of extracting the CCF maximums with the noise immunity of the signal detection. For this purpose, we assume that the signal is detected by the spatial channel, in which the signal power (and the SNR) is maximal. Then, according to [8], the noise immunity of detecting the signal can be calculated as

$$Q_{\mathrm{det}} = \left[T_{\mathrm{det}}\int_{f_{\mathrm{low}}}^{f_{\mathrm{up}}} \frac{S_{s_1}^2(f)}{S_{n_1}^2(f)}df\right]^{\frac{1}{2}}. \quad (27)$$

Under the assumptions used for deriving Eq. (26), Eq. (23) takes the form

$$Q_{\mathrm{CCFmax}_{mn}} \approx \left[T_{\mathrm{CCF}}\int_{f_{\mathrm{low}}}^{f_{\mathrm{up}}} \frac{w_{mn}A_{m1}^4(f)}{S_{n_1}^2(f)}df\right]^{\frac{1}{2}}, \quad (28)$$

where $w_{mn} = \frac{A_{n2}^2(f)}{A_{m1}^2(f)} \le 1$ is the power ratio between the nth and mth signals.

Using the same assumptions, we determine the ratio of expressions (28) and (27), which we will call

the relative noise immunity of extracting the CCF maximums:

$$\delta_{\mathrm{CCFmax}_{mn}} = \sqrt{\frac{T_{\mathrm{CCF}}}{T_{\mathrm{det}}} w_{mn} k_{m1}^2}, \quad (29)$$

where $k_{mi} = \dfrac{A_{mi}^2(f)}{A_{s_i}(f)} \le 1$ is the relative portion of power of the mth signal in the total signal power at the output of the ith spatial channel.

The analysis of Eq. (29) shows that the relative noise immunity of extracting the CCF maximums increases with increasing the ratio of the accumulation times for the CCF calculation and the signal detection, with decreasing difference in the amplitudes of the nth and mth signals at the output of the spatial channel ($w_{mn} \longrightarrow 1$), and with increasing the power contribution of each of these signals to the total power of the signal at the output of the spatial channel in which it is detected ($k_{m1} \longrightarrow 1$). In the most favorable situation of extracting the maximums of the CCF of the signal, in which both of the two spatial channels pointed at different directions receive signals of the same power (which can occur when the source is in the far-field region and the vertical dimension of the array is large in terms of the wavelength), Eq. (29) takes the form

$$\delta_{\mathrm{CCFmax}_{mn}} = \sqrt{\frac{T_{\mathrm{CCF}}}{T_{\mathrm{det}}}}.$$

Therefore, theoretically, the accumulation times can be chosen in this case to provide the noise immunity of extracting the CCF maximums at least as high as the noise immunity of the signal detection.

In practice, to bring the distance of the CCF maximum extraction closer to the signal detection distance, one should not only orient the spatial channels in the vertical plane as described above, but also increase the accumulation time while calculating the CCF (each doubling of the T_{CCF} increases the noise immunity of the CCF maximums extraction by 1.5 dB). One should keep in mind that, for the coherent CCF accumulation, a limit exists associated with a change in the abscissas of the extracted signals in time due the relative motion of the source and the receiver. This limit can be calculated as

$$T_{\mathrm{CCF}_{\max}} = \frac{\Delta\tau}{\dot{\tau}_{\max}}, \quad (30)$$

where $\dot{\tau}_{\max}$ is the maximal possible rate of change of the abscissas of the CCF maximums (a dimensionless quantity), which depends on the current hydroacoustic conditions, the source and receiver depths, the distance between them, and the relative radial speed of the source.

When, to achieve the required noise immunity of the CCF maximum extraction, it is necessary to increase the CCF accumulation time above $T_{\mathrm{CCF}_{\max}}$, this should be done using ranges (as in the known LOFAR and DEMON techniques).

It should be noted that, as the input SNR (21) in Eq. (19) increases, the output SNR for extracting the CCF maximums does not grow without limit (in contrast to the output SNR for the detection procedure), but rather tends to the limit

$$Q_{\mathrm{CCFmax}_{mn}} = \left[T_{\mathrm{CCF}} \int_{f_{\mathrm{low}}}^{f_{\mathrm{up}}} \frac{[A_{m1}(f) A_{n2}(f)]^2}{S_{s_1}(f) S_{s_2}(f)} df \right]^{\frac{1}{2}}, \quad (31)$$

the frequency response of the optimum frequency filter having the form

$$H_{\mathrm{opt}_{mn}} = l \frac{1}{S_{s_1}(f)}. \quad (32)$$

As follows from Eq. (31), the noise immunity of the CCF maximum extraction increases with increasing the portion of the power contributed to the total signal power at the output of each spatial channel by the signals that form the CCF maximum under consideration. If we assume that the spectra of the signals that travel different paths (and, hence, the total signals) have the same form, Eq. (31) yields the approximate formula for estimating the noise immunity of extracting the CCF maximums at high input SNRs:

$$Q_{\mathrm{CCFmax}_{mn}} = \sqrt{T_{\mathrm{CCF}}(f_{\mathrm{up}} - f_{\mathrm{low}}) k_{m1} k_{n2}}. \quad (33)$$

Formula (33) explains, in particular, that the local CCF maximums are difficult to extract when the hydrological conditions are such that the signal arrives at the receiving array through a large number of paths (e.g., in a totally illuminated shallow sea), because, in this case, all quantities k_{mi} can take very small values.

Let us consider the ACF. From the viewpoint of calculations, the ACF is a particular case of the CCF. Therefore, we can use the results obtained for the CCF. To this end, we drop indices associated with the spatial channel numbers in Eqs. (16), (19), and (20) and take into account that both the signal and the noise at the output of the same spatial channel are completely correlated. As a result, we obtain:

$$Q_{\mathrm{ACF}_{mn}} = \sqrt{2T_{\mathrm{CCF}}} \frac{\int_{f_{\mathrm{low}}}^{f_{\mathrm{up}}} H(f) A_m(f) A_n(f) df}{\left\{ \int_{f_{\mathrm{low}}}^{f_{\mathrm{up}}} H^2(f) [S_s(f) + S_n(f)]^2 df \right\}^{\frac{1}{2}}}, \quad (34)$$

$$Q_{\mathrm{ACFmax}_{mn}} = \left[2T_{\mathrm{ACF}} \int_{f_{\mathrm{low}}}^{f_{\mathrm{up}}} \frac{A_m^2(f) A_n^2(f)}{[S_s(f) + S_n(f)]^2} df \right]^{\frac{1}{2}}, \quad (35)$$

$$H_{\mathrm{opt}_{mn}} = l \frac{A_m(f) A_n(f)}{[S_s(f) + S_n(f)]^2}. \quad (36)$$

When the SNRs are small, the term $S_s(f)$ in the denominators of expressions (34)–(36) can be omitted.

When the SNRs are large, Eq. (35) can be reduced to

$$Q_{\mathrm{ACFmax}_{mn}} = \left[2T_{\mathrm{ACF}}\int_{f_{\mathrm{low}}}^{f_{\mathrm{up}}}\frac{A_m^2(f)A_n^2(f)}{S_s^2(f)}df\right]^{\frac{1}{2}}. \quad (37)$$

Under the assumptions used to derive Eq. (33), Eq. (37) can be reduced to

$$Q_{\mathrm{ACFmax}_{mn}} = \sqrt{2T_{\mathrm{ACF}}(f_{\mathrm{up}} - f_{\mathrm{low}})w_{mn}k_m^2}. \quad (38)$$

As applied to the ACF, Eq. (29) takes the form

$$\delta_{\mathrm{ACFmax}_{mn}} = \sqrt{\frac{2T_{\mathrm{ACF}}}{T_{\mathrm{det}}}w_{mn}k_m^2}. \quad (39)$$

As follows from Eq. (39), the most favorable situation for extracting the maximums in the ACF of the signal is when the total signal in the respective spatial channel is formed by two equal-power signals traveling along different paths (which can be observed when the source is in the far-field region of the array, as in the case of the CCF). Then, Eq. (39) takes the same form as for the cross-correlated reception (29) in the situation most favorable for extracting the maximums in the CCF of the signal:

$$\delta_{\mathrm{ACFmax}_{mn}} = \sqrt{\frac{T_{\mathrm{ACF}}}{T_{\mathrm{det}}}}.$$

Thus, the main factor that limits the noise immunity of extracting the multipath maximums of the CF is the signal-to-noise ratio in the frequency band within which the CF is calculated and the number of paths that form the signal field. To bring the distance, at which the maximums of the CF of the signal can be extracted, closer to the distance at which the signal can be detected, one should increase the CF accumulation time taking into account limitation (30) on the coherent accumulation time due to the relative motion of the source and the receiver.

REFERENCES

1. J. C. Hassab, J. Sound Vibr. **44**, 127 (1976).
2. V. I. Telyatnikov, Zarubezh. Radioélektron., No. 4, 66 (1978).
3. P. H. Moghaddam and H. Amindavar, in *Proceedings of the 1998 International Symposium on Underwater Technology, Tokyo, 1998* (IEEE, New York, 1998), p. 35.
4. L. M. Fink, *Theory of Discrete Message Transmission* (Sovetskoe Radio, Moscow, 1970).
5. K. I. Malyshev, in *The Third All-Union School–Seminar on Statistical Hydroacoustics: Abstracts of Papers* (Moscow, 1972), p. 109.
6. L. R. Rabiner and B. Gold, *Theory and Application of Digital Signal Processing* (Prentice Hall, Englewood Cliffs, N.J., 1975; Mir, Moscow, 1978).
7. Yu. I. Gribanov and V. L. Mal'kov, *Sample Estimates of Spectral Characteristics of Stationary Random Processes* (Énergiya, Moscow, 1978).
8. D. Middleton, *An Introduction to Statistical Communication Theory* (McGraw-Hill, New York, 1960; Sovetskoe Radio, Moscow, 1961), Vols. 1 and 2.
9. G. Korn and T. Korn, *Mathematical Handbook for Scientists and Engineers* (McGraw-Hill, New York, 1968, 2nd ed.; Nauka, Moscow, 1977, 4th ed.).

Translated by A. Khzmalyan

Acoustical Physics, Vol. 47, No. 6, 2001, pp. 733–738. Translated from Akusticheskiĭ Zhurnal, Vol. 47, No. 6, 2001, pp. 830–835.

Experimental Investigation of the Self-Action of Acoustic Waves in Systems with Dissipative Nonlinearity

V. E. Nazarov*, A. V. Radostin*, and Yu. A. Stepanyants**

** Institute of Applied Physics, Russian Academy of Sciences, ul. Ul'yanova 46, Nizhni Novgorod, 603600 Russia*
e-mail: nazarov@hydro.appl.sci-nnov.ru
*** Australian Nuclear Science and Technology Organization*
Received October 6, 2000

Abstract—The results of experimental investigation and analytical description of the self-action of acoustic waves in a glass tube filled with dry and water saturated river sand are presented. On the basis of the analysis of experimental results, phenomenological equations of state that describe such systems are derived and the values of their parameters are determined. © *2001 MAIK "Nauka/Interperiodica".*

Experimental investigations of nonlinear acoustic effects provide the basis for revealing the mechanisms of acoustic nonlinearity of various media and for developing nonlinear methods of diagnostics of their structure and state. A promising line of investigation for solving such problems is connected with the search for media and materials, as well as with the design of systems (e.g., resonators or sound ducts), in which nonlinear effects are most conspicuous, all other factors being the same. These properties are characteristic of microinhomogeneous media (in particular, some rocks [1, 2] and metals [3]) and also of systems designed on the basis of these media. Their acoustic nonlinearity often contains both elastic (reactive) and inelastic (dissipative) components, and the inelastic nonlinearity in a number of cases significantly exceeds the elastic component. For instance, in papers [4, 5] it was found that the propagation of acoustic waves in a glass tube filled with river sand is accompanied by the effect of self-clarification, which appears as a decrease in the attenuation constant of the wave with increasing wave amplitude. The experiments described in the cited papers were carried out with dry and fully water saturated sand. For an analytical description of the self-clarification at small and large amplitudes of acoustic waves, the equation of state involving dissipative nonlinearity in the form of a power function of the strain rate was used.

This paper presents the results of an extensive experimental investigation and analytical description of the effect of self-clarification in a similar system for various degrees of water saturation of sand. On the basis of the analysis of experimentally measured amplitude dependences, the equations of state describing such systems are proposed and the values of their parameters are determined.

The schematic diagram of the experimental setup is shown in Fig. 1. In the experiment, a glass tube *1* with an inner diameter of 9 mm, an outer diameter of 11 mm, and a length of 37 cm was used. At the beginning, the tube was filled with compressed dry sand, and the upper and lower ends of the tube were closed tightly with metal plugs *2* and sealed. The mean size of sand grains was about 2×10^{-2} cm. At the top and at the bottom of the tube, two openings about 2.5 mm in diameter were made in the tube wall, and flexible tubes *5* were pasted in each of these openings. A syringe connected with one of the flexible tubes was used to control the content of water in the sand. The degree of water saturation of sand ξ was determined as the ratio of the volume of water in the tube to its maximal possible value and was varied in the range from 100 to 44%. For fully water saturated sand, the volume content of water in the tube was 5.9 cm^3, while the calculated porosity of sand was about 31%. The lower plug was glued to an acoustic

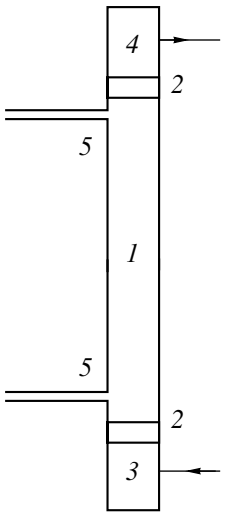

Fig. 1. Schematic diagram of the experimental setup.

1063-7710/01/4706-0733$21.00 © 2001 MAIK "Nauka/Interperiodica"

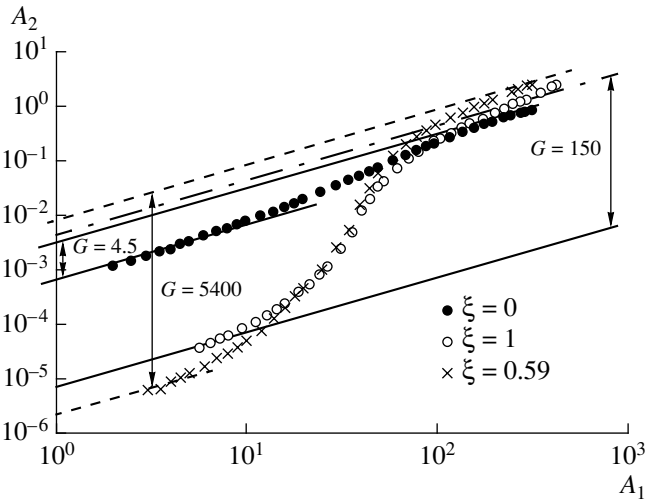

Fig. 2. Amplitude dependences for dry (ξ = 0), fully (ξ = 1), and partially (ξ = 0.59) water saturated sand.

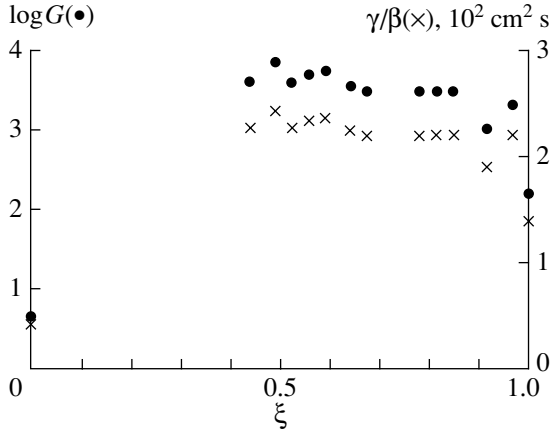

Fig. 3. Coefficient G and the ratio γ/β as functions of the relative water saturation of sand.

radiator *3* producing longitudinal waves. The radiator was fed from a power amplifier with high-frequency pulses characterized by the carrier frequency $f = 100$ kHz, the duration $\tau = 300$ μs, and the repetition frequency $F = 30$ Hz. The acoustic pulses transmitted through the tube were received by a piezoelectric accelerometer *4* glued to the upper plug. The amplitudes A_1 and A_2 of the radiated and received signals were measured by a two-channel oscilloscope. In our experiments, these amplitudes were proportional to the amplitudes of the displacements U_0 and $U(L)$ in the radiated and received acoustic pulses. A preliminary checking of the radiator–receiver system showed its linearity, i.e., $A_2 \sim A_1$. In the reference experiments with a glass rod and a tube without sand, no departure from this dependence was observed. The propagation velocity of an acoustic wave in such a system, when measured by the time delay of the received signal relative to the radiated one, was approximately 3.7×10^5 cm/s and depended only weakly on the water content in sand and on the pulse amplitude.

Figure 2 shows the dependence of the amplitude A_2 of the received signal on the amplitude A_1 of the radiated signal for a tube filled with dry (ξ = 0) and water saturated river sand. One can see that, with an increase in the amplitude of the radiated pulse, the amplitude of the received pulse increases as follows: for small and large amplitudes, a linear dependence of A_2 on A_1 is observed, and for medium amplitudes, A_2 grows faster than A_1. In a system with dry sand, the amplitude of the received pulse increases by a factor of 1.4×10^3 with the increase in amplitude of the radiated pulse by a factor of 3×10^2, i.e., the coefficient G characterizing the increase in the received signal relative to the radiated signal is about 4.5. This effect is called self-clarification. It results from the dissipative nonlinearity of the medium and appears in the fact that the attenuation constant of an acoustic wave decreases with an increase in its amplitude. Figure 2 also displays the experimental dependences of the amplitude A_2 of the received signal on the amplitude A_1 of the radiated signal for partially (ξ = 0.59) and fully (ξ = 1) water saturated sand. It is seen from this figure that, in the tube containing water saturated river sand, the self-clarification effect also exists, and the coefficient G changes (depending on the degree of water saturation of sand) in the range from 4.5 for the tube with dry sand to 7×10^3 for the tube with partially water saturated sand (ξ = 0.49). The dependence of the coefficient G on the degree of water saturation of sand ξ is shown in Fig. 3.

For the analytical description of the effect of self-clarification, we use the equation of state for a medium equivalent to the glass tube–river sand system [4, 5]:

$$\sigma(\varepsilon, \dot{\varepsilon}) = \sigma_1(\varepsilon) + \sigma_2(\dot{\varepsilon}), \qquad (1)$$

where σ is the longitudinal stress; $\sigma_1(\varepsilon)$ and $\sigma_2(\dot{\varepsilon})$ are the elastic and inelastic parts of the equation of state, respectively; $\varepsilon = U_x$ is the longitudinal strain; $\dot{\varepsilon}$ is the strain rate; and U is the longitudinal displacement.

We neglect the elastic nonlinearity of the system and assume that $\sigma_1(\varepsilon) = E\varepsilon$, where E is the elastic modulus. For describing the dissipative properties of the system, we take into account not only the usual linear viscous stress, but also the nonlinear stress. In hydrodynamics, the media exhibiting such properties are called non-Newtonian (or Bingham) ones [6, 7]. At first, we will use an exponential approximation of the nonlinear dependence $\sigma_2 = \sigma_2(\dot{\varepsilon})$, which is rather general and adequately describes the initial and terminal (i.e., corresponding to low and high strain rates) parts of the self-clarification process [4, 5]:

$$\sigma_2(\dot{\varepsilon}) = \rho(\alpha + g|\dot{\varepsilon}|^m)\dot{\varepsilon}, \qquad (2)$$

where ρ is the density and α, g, and m are the constant coefficients determining the linear and nonlinear vis-

cous stresses in the system. Depending on the coefficient g and the exponent m, the dissipative function behaves in essentially different ways: for $g > 0$, the effective viscosity of the medium increases with an increase in the deformation velocity for $m > 0$ and decreases for $m < 0$; for $g < 0$, the effective viscosity of the medium decreases for $m > 0$ and grows for $m < 0$. Note that, for $m < 0$, Eq. (2) is, generally speaking, inappropriate for describing the nonlinear viscous stress near the point $\dot{\varepsilon} \approx 0$, because $\sigma_2(\dot{\varepsilon} = 0) \longrightarrow \infty$. Consequently, for $m < 0$ and $|\dot{\varepsilon}| < d$ [d is a certain critical strain rate, beginning from which the viscous stress can be described by Eq. (2)], the nonlinear dissipative stress should be finite. As it will be seen from the following, when $m > -3$, Eq. (2) can be used for any $\dot{\varepsilon}$, because no singularities occur in the final expressions.

In the one-dimensional case, the equation of state (2), together with the equation of motion [11]

$$\rho U_{tt} = \sigma_x(\varepsilon, \dot{\varepsilon}), \tag{3}$$

and the boundary condition at the radiator

$$U(x = 0, t) = U_0 \sin \omega t, \tag{4}$$

describes the nonlinear propagation of longitudinal acoustic waves and, in particular, the self-clarification of the medium. Substituting Eqs. (1) and (2) into Eq. (3), we obtain the nonlinear wave equation for the displacements U:

$$U_{tt} - C_0^2 U_{xx} = \alpha U_{txx} + g[|U_{xt}|^m U_{xt}]_x, \tag{5}$$

where $C_0^2 = E/\rho$.

We assume that the nonlinearity of Eq. (5) is small and the equation can be solved by perturbation method. For this purpose, the condition

$$g U_0^m \omega^{2m-1}/C_0^{m+2} \ll 1 \tag{6}$$

should be satisfied. In this case, the solution to Eq. (5) can be found in the form of a harmonic wave at the fundamental frequency with slowly varying amplitude $U(x)$ and phase $\Phi(x)$:

$$U(x, t) = U(x)\sin[\omega t - kx + \Phi(x)], \quad \omega = C_0 k. \tag{7}$$

Substituting Eq. (7) into Eq. (5), expanding the nonlinear term on the right-hand side of Eq. (5) into Fourier series, and retaining the terms corresponding to the fundamental frequency, we obtain

$$U_x \cos\vartheta - U\Phi_x \sin\vartheta = -\delta U \cos\vartheta - \mu U^{m+1} \cos\vartheta, \tag{8}$$

where $\delta = \alpha\omega^2/2C_0^3$, $\mu = \dfrac{g\Gamma(m/2 + 3/2)\omega^{2(m+1)}}{\pi^{1/2}\Gamma(m/2 + 2)C_0^{m+3}}$, $\vartheta = \omega t - kx + \Phi(x)$, and $m > -3$.

The solution to this equation with the boundary condition (4) has the form [12]

$$U(x) = U_0 \exp(-\delta x)\{1 + aU_0^m[1 - \exp(-\delta x m)]\}^{-1/m}, \quad \Phi_x = 0, \tag{9}$$

where $a = \mu/\delta$.

By comparing Eq. (9) with the results of measurements (Fig. 2), it is possible, in principle, to determine the parameters of the system, namely, the coefficient g and the index m of dissipative nonlinearity. However, since the measurements were relative, it is possible to determine only the index m [4, 5]. Nevertheless, from the general form of the dependences $A_2 = A_2(A_1)$, it follows that, for low strain rates, we have $g < 0$ and $m > 0$, and for high strain rates, we have $g > 0$ and $m < 0$; i.e., at small wave amplitudes, the investigated system has the properties of a pseudoplastic medium, and at large amplitudes, it has the properties of a dilatant medium [6, 7].

For a small amplitude U_0^* of the wave produced by radiator, when the influence of nonlinearity is negligible, Eq. (9) can be reduced to

$$U^*(x) = U_0^* \exp(-\delta x). \tag{10}$$

Dividing Eq. (9) by Eq. (10) and introducing the designations $M = U(x)/U^*(x)$, $N = U_0/U_0^*$, and $b = aU_0^{*m}[1 - \exp(-m\delta x)] < 0$, we obtain

$$M/N = [1 + bN^m]^{-1/m}. \tag{11}$$

Taking the logarithm of this equation for $|bN^m| \ll 1$ two times, we derive the expression for determining the index m of dissipative nonlinearity in Eq. (2) at low strain rates:

$$\ln(\ln(M/N)) = \ln(-b/m) + m\ln N. \tag{12}$$

By using the results of measurements (Fig. 2), the dependences of $\ln(\ln(M/N))$ on $\ln N$ were constructed for the system with various degrees of water saturation of sand (Fig. 4). From this figure, by the slope of the dependence of $\ln(\ln(M/N))$ on $\ln N$, the index of dissipative nonlinearity m was determined as a function of the percentage of water in the sand ξ. The dependence of m on ξ is given in Fig. 5. From this figure, it follows that, for a tube with dry sand, $m = 1$, and, with the change of the water content in sand from 44 to 100% (fully water saturated sand), the index of dissipative nonlinearity changes from $m = 1$ to 2.

At large amplitudes U_0^* of the wave produced by the radiator, the influence of nonlinearity is also small, and from Eq. (9) we have

$$U^*(x) = U_0^* \exp(-\delta x). \tag{13}$$

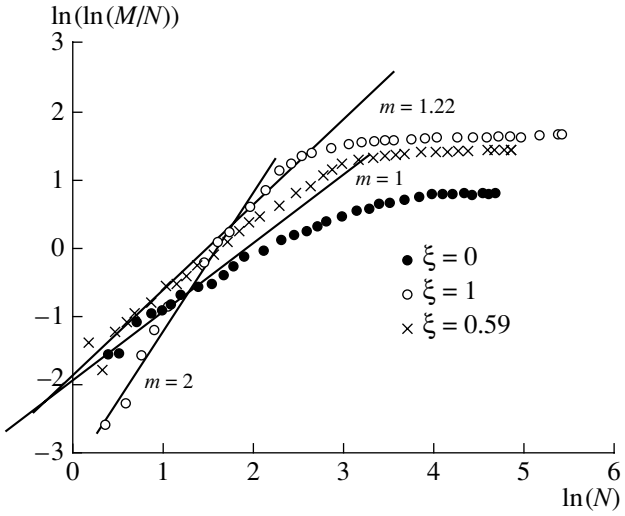

Fig. 4. Amplitude dependences for dry, partially, and fully water saturated sand for small amplitudes.

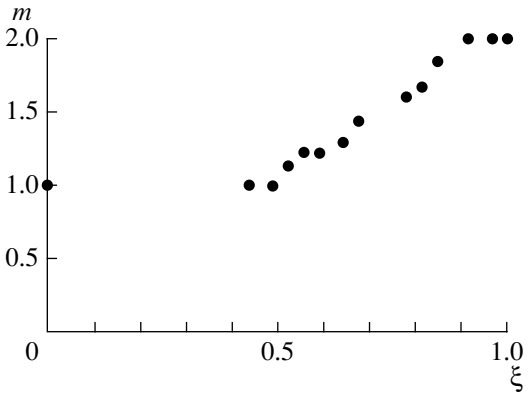

Fig. 5. Index of dissipative nonlinearity m as a function of the relative water saturation of sand.

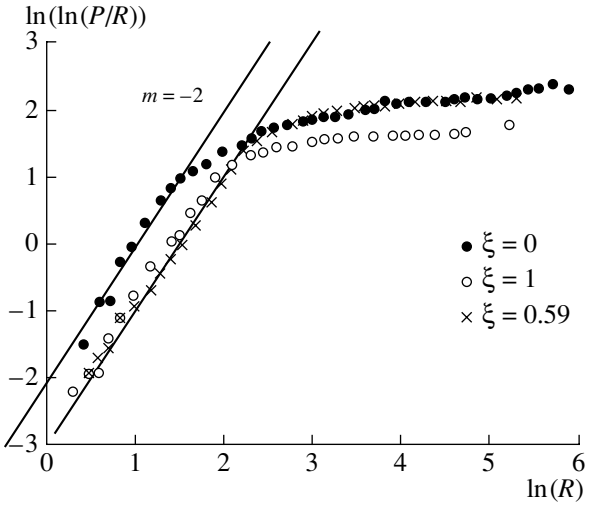

Fig. 6. Amplitude dependences for dry, partially, and fully water saturated sand for large amplitudes.

As before, we divide Eq. (13) by Eq. (9), introduce the designations $P = U^*(x)/U(x)$, $R = U_0^*/U_0$, and $b = aU_0^*[1 - \exp(-m\delta x)] < 0$, and derive (for $|bR^{-m}| \ll 1$)

$$\ln(\ln(P/R)) = \ln(b/m) - m\ln R. \tag{14}$$

For this case, using the results of measurements (Fig. 2), we also constructed the dependences of $\ln(\ln(P/R))$ on $\ln R$ for a tube with sand with various degrees of water saturation (Fig. 6). From this figure, it follows that, for high strain rates, $m \cong -2$ and does not depend on the water content in sand.

Thus, in choosing the dissipative component in the equation of the state of a system with dry and water saturated sand to describe the process of self-clarification in the whole range of amplitudes of acoustic waves, it is necessary to take into consideration the following requirements:

(i) at low and high strain rates, the system is linear and characterized by two different attenuation constants, the ratio of which determines the coefficient G of relative growth of amplitudes at the output and input of the system;

(ii) at low strain rates, the parameter of dissipative nonlinearity is $g < 0$ and the index m changes (depending on the water content) from $m = 1$ to $m = 2$; and

(iii) at high strain rates, the parameter of dissipative nonlinearity is $g > 0$ and the index m is $m = -2$ (regardless of the water content).

We now consider the equations of state describing the system under study. The most simple expression for the dissipative component complying with the aforementioned requirements corresponds to the system with fully water saturated sand. It can be written as

$$\sigma_2(\dot\varepsilon) = \alpha\rho\dot\varepsilon - \frac{\gamma|\dot\varepsilon|^2}{1+\beta|\dot\varepsilon|^2}\rho\dot\varepsilon, \tag{15}$$

where β and γ are positive coefficients. Substituting Eq. (15) into Eq. (3), we obtain, similarly to Eq. (8), the following equation for the wave amplitude $U(x)$:

$$\frac{dU}{dx} = -\frac{\alpha\omega^2}{2C_0^3}U \times\left[1 - \frac{\gamma}{\alpha\beta}\left(1 - \frac{2}{\beta(\omega kU)^2}\left(1 - \frac{1}{\sqrt{1+\beta(\omega kU)^2}}\right)\right)\right]. \tag{16}$$

Due to the complex nonlinearity of this equation, it is impossible to obtain its analytical solution. Therefore, we will consider the limiting cases of small and large amplitudes. For small amplitudes ($\beta\omega^2k^2U^2 \ll 1$), from Eq. (16) we derive the equation

$$\frac{dU}{dx} = -\frac{\alpha\omega^2}{2C_0^3}U[1 - a_1(kU)^2],$$

which has the solution

$$\frac{U^2(1-a_1k^2U_0^2)}{U_0^2(1-a_1k^2U^2)} = \exp\left\{-\frac{\alpha\omega^2}{C_0^2}x\right\}$$

or

$$U(x) = U_0\exp\left\{-\frac{\alpha\omega^2}{2C_0^3}x\right\} \times\left[1-a_1k^2U_0^2\left(1-\exp\left\{-\frac{\alpha\omega^2}{C_0^3}x\right\}\right)\right]^{-1/2}, \quad (17)$$

where $a_1 = 3\gamma\omega^2/4\alpha$.

It is readily seen that, for $a = -a_1$ and $m = 2$, Eqs. (9) and (17) coincide.

For large amplitudes ($\beta\omega^2k^2U^2 \gg 1$), from Eq. (17) we obtain

$$\frac{dU}{dx} = -\frac{\alpha\omega^2k}{2C_0^3}\left[1-\frac{\gamma}{\alpha\beta}+\frac{2\gamma}{\alpha(\beta\omega kU)^2}\right],$$

and this equation has the solution

$$\frac{U^2+\gamma/\nu}{U_0^2+\gamma/\nu} = \exp\left\{-\frac{\nu\alpha\omega^2}{C_0^3}x\right\}$$

or

$$U(x) = U_0\exp\left\{-\frac{\nu\alpha\omega^2}{2C_0^3}x\right\} \times\left[1-\frac{a_2}{\nu\varepsilon_0^2}\left(1-\exp\left\{\frac{\nu\alpha\omega^2}{C_0^3}x\right\}\right)\right], \quad (18)$$

where $a_2 = 2\gamma/\alpha\beta^2\omega^2$ and $\nu = 1 - \gamma/\alpha\beta$. From the comparison of Eqs. (9) and (18), it follows that, when $\delta = \nu\alpha\omega^2/2C_0^3$, $a = a_2/\nu$, and $m = -2$, they coincide and, consequently, the equation of state (15) satisfies the above requirements and can be used for describing the process of self-clarification in a tube with fully water saturated sand.

Now it is possible to determine the coefficient G equal to the ratio U_2/U_1, where U_2 and U_1 are the amplitudes of the displacements at the receiver, which are chosen on the linear portions of the curves given by Eqs. (18) and (17), respectively, for the same value of the amplitude U_0 at the radiator:

$$G = \exp\left\{\frac{\gamma\omega^2}{2\beta C_0^3}L\right\}. \quad (19)$$

From Eq. (19), it follows that the coefficient G is determined by the ratio of the parameters γ and β.

For the system with dry and partially water saturated sand, the dissipative component of the equation of state has a more complex form, as compared to Eq. (15). It can be represented by the expression

$$\sigma_2(\dot\varepsilon) = \alpha\rho\dot\varepsilon - \frac{\gamma|\dot\varepsilon|^m}{1+\beta|\dot\varepsilon|^m}\rho\dot\varepsilon\{H(\dot\varepsilon+\dot\varepsilon_{th})-H(\dot\varepsilon-\dot\varepsilon_{th})\} - \frac{\gamma}{\beta}\left(1-\frac{\dot\varepsilon_{th}^2}{|\dot\varepsilon|^2(1+\beta\dot\varepsilon_{th}^m)}\right)\rho\dot\varepsilon\{1-H(\dot\varepsilon+\dot\varepsilon_{th})+H(\dot\varepsilon+\dot\varepsilon_{th})\}, \quad (20)$$

where $H(\dot\varepsilon)$ is the Heaviside function, $\dot\varepsilon_{th}$ is a certain threshold value of $\dot\varepsilon$ at which a continuous transition from one nonlinearity [the second term in Eq. (20)] to the other (the third term) occurs. It can be easily shown that, for low and high strain rates, Eqs. (2) and (20) coincide qualitatively. Consequently, the solution to the equation of motion with this kind of nonlinearity in the limiting cases of small and large amplitudes will coincide with solution (9). In this case, in Eq. (9) it is necessary to assume that, at low strain rates, $a = \frac{\gamma\omega^m}{\alpha\pi^{1/2}}\frac{\Gamma(m/2+3/2)}{\Gamma(m/2+2)}$, and at high strain rates, $a = -\frac{3\gamma}{4\beta\delta}\frac{|\dot\varepsilon_{th}|^2}{(1+\beta\dot\varepsilon_{th}^m)}$, where $\delta = \left(\alpha-\frac{\gamma}{\beta}\right)\frac{\omega^2}{2C_0^3}$. Then, the coefficient G will be determined by Eq. (19) from which it is possible to extract the ratio of the parameters γ and β. Figure 3 shows the ratio γ/β as a function of water saturation of sand ξ. From this figure, it follows that the ratio γ/β varies most rapidly in the range $0 \le \xi \le 0.44$, and in the range $0.44 \le \xi \le 1$, the ratio $\gamma/\beta \approx$ const and the index m grows steadily from $m = 1$ to 2.

Thus, in this paper, we presented the results of the experimental study of the self-action of acoustic waves in a glass tube filled with dry and water saturated river sand: with increasing wave amplitude, the effect of self-clarification was observed in this system. On the basis of the amplitude relations obtained in the experiment, the phenomenological equations of state were proposed for these systems and the values of their parameters were determined. It was found that the parameters of dissipative nonlinearity of the system depend on the degree of water saturation of sand. This suggests that the effect of self-clarification can be used for the diagnostics of the state of porous gas and water saturated media.

In conclusion, we note that the choice of the dissipative nonlinearity in equations of state (2), (15), and (20) is not unambiguous in the sense that the coefficient determining the nonlinear viscosity of the system may depend not only on the strain rate but also on the strain. However, this will not affect the results of the analytical calculations of the index m of dissipative nonlinearity (because the amplitude dependences do not change in

this case) and will only lead to a renormalization of the constant coefficients g, γ, and β. To determine on which parameters (ε or $\dot{\varepsilon}$) the nonlinear viscosity of the system depends, it is necessary to carry out an experiment that will reveal the frequency dependence of the dissipative nonlinearity [3]. The results of this experiment will be presented in the following paper.

ACKNOWLEDGMENTS

This work was supported by the Russian Foundation for Basic Research (project nos. 01-05-64417 and 00-05-64252) and by the Interdepartmental Scientific-Engineering Center (project no. 1369).

REFERENCES

1. S. V. Zimenkov and V. E. Nazarov, Fiz. Zemli, No. 1, 13 (1991).
2. R. A. Guyer and P. A. Johnson, Phys. Today **52** (4), 30 (1999).
3. V. E. Nazarov, Fiz. Met. Metalloved. **88** (4), 82 (1999).
4. V. E. Nazarov and S. V. Zimenkov, Acoust. Lett. **16** (10), 218 (1993).
5. V. E. Nazarov, Akust. Zh. **41**, 349 (1995) [Acoust. Phys. **41**, 305 (1995)].
6. W. Wilkinson, *Non-Newtonian Fluids; Fluids Mechanics; Mixing and Heat Transfer* (Pergamon, New York, 1960; Mir, Moscow, 1964).
7. Z. P. Shul'man, *Lectures on Reophysics* (Nauka i Tekhnika, Minsk, 1976).
8. V. A. Pal'mov, Prikl. Mat. Mekh. **31** (4), 749 (1967).
9. V. N. Nikolaevskiĭ, Izv. Akad. Nauk SSSR, Mekh. Tverd. Tela, No. 4, 85 (1968).
10. V. A. Pal'mov, *Vibrations of Elastically-Plastic Bodies* (Nauka, Moscow, 1968).
11. L. D. Landau and E. M. Lifshits, *Course of Theoretical Physics*, Vol. 7: *Theory of Elasticity* (Nauka, Moscow, 1987; Pergamon, New York, 1986).
12. E. Kamke, *Gewöhnliche Differentialgleichungen* (Academie, Leipzig, 1959; Nauka, Moscow, 1976).

Translated by A. Svechnikov

Acoustical Physics, Vol. 47, No. 6, 2001, pp. 739–745. Translated from Akusticheskiĭ Zhurnal, Vol. 47, No. 6, 2001, pp. 836–842.

Shear Horizontal Acoustic Waves at the Boundary of Two Piezoelectric Crystals Separated by a Liquid Layer

P. A. Pyatakov

Andreev Acoustics Institute, Russian Academy of Sciences, ul. Shvernika 4, Moscow, 117036 Russia
e-mail: bvp@akin.ru

Received October 2, 2000

Abstract—Transverse acoustic waves that occur at the boundary of two piezoelectric halfspaces separated by a viscoelastic liquid layer are studied theoretically. Three variants of layered structures with different numbers of metallized interfaces are considered. It is demonstrated that two types of waves exist in each of these structures. The waves are localized near the boundaries and differ in both their structure and the dependences of the complex wave numbers on the frequency or the gap width. The properties of this family of shear horizontal waves are described. © *2001 MAIK "Nauka/Interperiodica".*

The so-called shear horizontal waves can exist at the boundaries of two piezoelectric halfspaces divided by a gap [1–3]. They are transverse acoustic waves with displacements in the plane of the boundary. The waves are piezoactive. Their energy is localized at the boundaries of the halfspaces and decreases exponentially with distance away from the gap on both sides of the latter towards the medium depth. Shear mechanical strains in the medium on both sides of the gap are related through only the electrostatic piezoelectric field accompanying the waves.

If the gap is filled with a liquid, the properties of the waves and their phase velocity, attenuation, and localization depth change depending on the properties of the liquid, its permittivity, viscosity, and elasticity. The variety of wave types increases. In this case, shear horizontal waves also exist when one or both surfaces are metallized. Metallization leads to the separation of the piezoelectric fields in the two halfspaces, but it does not destroy the mechanical coupling of oscillations in these halfspaces.

The waves of this type can be practically useful for the development of sensors for mechanical and electric properties of liquids [4]. Prototypes of such sensors are described in [5–8].

This paper presents a theoretical analysis of shear horizontal waves at the boundary of two piezoelectric halfspaces separated by a viscoelastic liquid layer.

We consider a layered structure consisting of two halfspaces filled with a medium with the same piezoelectric properties as class 6 crystals (Fig. 1). The crystallographic *Z* axis coincident with the hexagonal axis is directed perpendicularly to the figure plane and to the direction of wave propagation. At these conditions, the mechanical displacements *U* along the *Z* axis and the electrostatic field potential φ in the two media satisfy the wave equation and the Laplace equation, respectively. These equations are a consequence of the general equations of the theory of elasticity and electrostatics for media 1 and 2:

$$\rho\frac{\partial^2 U}{\partial t^2} = c_{44}(1+K^2)\Delta U, \qquad \Delta(\varepsilon_{11}\varphi - e_{15}U) = 0, \tag{1}$$

where $\Delta = \dfrac{\partial^2}{\partial x^2} + \dfrac{\partial^2}{\partial y^2}$ is the operator, $K^2 = \dfrac{e_{15}^2}{\varepsilon_{11}c_{44}}$ e_{15} is the piezoelectric constant, ε_{11} is the permittivity, and c_{44} is the elastic constant. Below, we will mark all quantities relating to media 1 and 2 with the corresponding indices 1 and 2 and omit the tensor indices for the material parameters (see Fig. 1). The mechanical displacements U_0 and the electric field potential φ_0 satisfy the wave equation and the Laplace equation, respectively,

$$\rho_0\frac{\partial^2 U_0}{\partial t^2} = c_0\Delta U_0, \qquad \Delta\varphi_0 = 0, \tag{2}$$

where ρ_0 is the liquid density, ε_0 is the permittivity of the liquid, and $c_0 = c_0' + ic_0''$ is the elastic constant of the viscoelastic liquid. In the particular case of a viscous liquid, we have $c_0 = i\omega\eta$, where ω is the cyclic frequency and η is the viscosity of the liquid. The conditions of continuity of mechanical displacement and

1063-7710/01/4706-0739$21.00

shear stress are satisfied at the boundaries of the halfspaces 1 and 2 and the liquid ($y = 0, h$):

$$U_{1,2} = U_0\big|_{x=0,-h},$$
$$c_{1,2}\frac{\partial}{\partial y}U_{1,2} + e_{1,2}\frac{\partial}{\partial y}\varphi_{1,2} = c_0\frac{\partial}{\partial y}U_0\big|_{y=0,-h}. \quad (3)$$

A metallized surface is characterized by a zero value of the electric potential:

$$\varphi_{1,2} = 0\big|_{y=0,h}. \quad (4)$$

The conditions for continuity of the potential and the normal component of the electric induction vector must be satisfied at an boundary without metallization:

$$\varphi_{1,2} = \varphi_0\big|_{y=0,-h},$$
$$\varepsilon_{1,2}\varphi_{1,2} + e_{1,2}U_{1,2} = \varepsilon_0\varphi_0\big|_{y=0,-h}. \quad (5)$$

We first consider a nonmetallized surface. The determination of the solutions satisfying Eqs. (1) and (2) with the boundary conditions given by Eqs. (3) and (5), which correspond to nonmetallized surfaces, is performed in a standard way (see [3] for example). Solutions to Eqs. (1) and (2) in the form

$$U_1 = A_1\exp(i\omega t - ikx - \kappa_1 y), \quad y \geq 0,$$
$$U_2 = A_2\exp(i\omega t - ikx - \kappa_1(y+h)), \quad y \leq -h,$$
$$\varphi_1 - \frac{e_1}{\varepsilon_1}U_1 = a_1\exp(i\omega t - ikx \mp |k|y), \quad y \geq 0, \quad (6)$$
$$\varphi_2 - \frac{e_2}{\varepsilon_2}U_2 = a_2\exp(i\omega t - ikx \mp |k|(y+h)), \quad y \leq -h,$$

and

$$U_0 = A_{01}\exp(i\omega t - ikx - \kappa_0 y) + A_{02}\exp(i\omega t - ikx + \kappa_0 y), \; 0 \geq y \geq -h,$$
$$\varphi_0 = a_{01}\exp(i\omega t - ikx - |k|y) + a_{02}\exp(i\omega t - ikx + |k|y), \quad 0 \geq y \geq -h \quad (7)$$

are substituted into the boundary conditions given by Eqs. (3) and (5). The following notations are introduced in Eqs. (6) and (7):

$$\kappa_i = \sqrt{k^2 - k_i^2}, \quad k_i = \omega/v_i, \quad i = 0, 1, 2,$$
$$v_0 = \sqrt{c_0/\rho_0}, \quad v_{1,2} = \sqrt{c_{1,2}/\rho_{1,2}(1 + K_{1,2}^2)},$$
$$|k| \equiv \sqrt{k^2}, \quad K_{1,2}^2 = e_{1,2}^2/(\varepsilon_{1,2}c_{1,2}).$$

Thus, we have a set of eight linear equations with eight unknowns. The conditions for the existence of a nontrivial solution to this set of equations, i.e., the zero value of the determinant of this set, yields a dispersion equation in the unknown wave number k:

$$d_1 d_2 - d_{12}d_{21} = 0, \quad (8)$$

where

$$d_{1,2} = (1 + K_{1,2}^2)\kappa_{1,2} - K_{1,2}^2|k|\left(1 + \frac{\varepsilon_{2,1}}{\varepsilon_0}\coth(|k|h)\right)\frac{1}{\Delta} + \frac{c_0}{c_{1,2}}\kappa_0\coth(|k|h), \quad (9)$$

$$\Delta = \left(1 + \frac{\varepsilon_1}{\varepsilon_0}\coth(|k|h)\right)\left(1 + \frac{\varepsilon_2}{\varepsilon_0}\coth(|k|h)\right) - \frac{\varepsilon_1\varepsilon_2}{\varepsilon_0^2}\frac{1}{\sinh^2(|k|h)}, \quad (10)$$

$$d_{12} = \left(\frac{c_0}{c_1}\frac{\kappa_0}{\sinh(|k|h)} - K_{12}^2\frac{|k|}{\sinh(|k|h)}\frac{1}{\Delta}\right),$$
$$d_{21} = \left(\frac{c_0}{c_2}\frac{\kappa_0}{\sinh(|k|h)} - K_{21}^2\frac{|k|}{\sinh(|k|h)}\frac{1}{\Delta}\right), \quad (11)$$
$$K_{12}^2 = \frac{e_1 e_2}{\varepsilon_1 c_1}, \quad K_{21}^2 = \frac{e_1 e_2}{\varepsilon_2 c_2}.$$

The coefficients in Eqs. (6) and (7) are as follows:

$$A_1 = A, \quad A_2 = \pm\alpha A, \quad \alpha = \sqrt{\frac{d_1 d_{21}}{d_2 d_{12}}},$$
$$a_1 = \left[-\frac{e_1}{\varepsilon_1}\left(1 + \frac{\varepsilon_2}{\varepsilon_0}\coth(|k|h)\right) \pm \frac{e_2}{\varepsilon_0}\frac{\alpha}{\sinh(|k|h)}\right]\frac{A}{\Delta}, \quad (12)$$
$$a_2 = \left[\mp\frac{e_2}{\varepsilon_2}\left(1 + \frac{\varepsilon_1}{\varepsilon_0}\coth(|k|h)\right) + \frac{e_1}{\varepsilon_0}\frac{1}{\sinh(|k|h)}\right]\frac{A}{\Delta},$$
$$A_{01} = \frac{A}{2\sinh(\kappa_0 h)}(e^{\kappa_0 h} \mp \alpha),$$
$$A_{02} = \frac{-A}{2\sinh(\kappa_0 h)}(e^{-\kappa_0 h} \mp \alpha),$$
$$a_{01} = \frac{A}{2\sinh(|k|h)}\left[e^{|k|h}a_1 - a_2 + \frac{e_1}{\varepsilon_1} \mp \frac{e_2}{\varepsilon_2}\alpha\right], \quad (13)$$
$$a_{02} = \frac{A}{2\sinh(|k|h)}\left[-e^{-|k|h}a_1 + a_2 - \frac{e_1}{\varepsilon_1} \pm \frac{e_2}{\varepsilon_2}\alpha\right],$$

where A is an arbitrary constant.

Two cases of mutual orientation of the crystallographic Z axes of the crystals are possible: (1) the axes have the same direction and (2) the directions of the axes are opposite. To change from the first case to the second, we have to change the sign of the piezoelectric constant in Eqs. (8)–(13): $e_2 \Rightarrow -e_2$.

When media 1 and 2 are identical, from Eqs. (9)–(13), we obtain $\alpha = 1$, $A_1 = \pm A_2$, and $a_1 = \pm a_2$. The distributions of mechanical and electric fields in halfspaces 1 and 2 are identical and can differ only in their sign. The plus sign corresponds to a symmetric wave (an s-wave), and the minus sign, to an antisymmetric wave (an a-wave). The distribution of mechanical displacements

Table

Parameter	$Bi_{12}GeO_{20}$	Water	90% solution	Glycerol
C [kg/(ms^2)]	2.7×10^{10}	$1.97 \times 10^5\, i$	$4.5 \times 10^7\, i$	$2.6 \times 10^8\, i$
ε	44	80	58	56
ρ, 10^3 [kg/m^3]	9.23	1	1.23	1.26

is shown schematically in Fig. 1. The dispersion equation (8) is reduced and takes on the form

$$(1 + K_1^2)\kappa_1 = K_1^2|k|\frac{\sinh(|k|h)}{\sinh(|k|h) + \frac{\varepsilon_1}{\varepsilon_0}\cosh(|k|h) \pm \frac{\varepsilon_1}{\varepsilon_0}\delta} + \frac{c_0}{c_1}\kappa_0\frac{(\pm 1 - \cosh(\kappa_0 h))}{\sinh(\kappa_0 h)}. \quad (14)$$

The constant is $\delta = 1$ when the Z axes of the crystals have the same direction and $\delta = -1$ when their directions are opposite. The first term on the right-hand side of the equation represents the piezoelectric effect and the second term corresponds to the contribution of the mechanical load caused by the liquid in the gap between the halfspaces.

Let us denote the right-hand side of Eq. (14) as $k_1 f(h, k)$. If the solution to Eq. (14) differs little from k_1, then, as one can see from Eq. (14), its is approximately equal to

$$k \approx k_1\left(1 + \frac{1}{2}\frac{f^2(h, k_1)}{(1 + K_1^2)^2}\right).$$

This expression gives good agreement with the exact values for the real part of the wave number, but it can give a rather large deviation for the imaginary part. The expression is inapplicable in the case of a small gap width, when the wave number is split in two values and can differ widely from k_1.

There are no exact analytical solutions to the transcendental equation (8). The results of computation for the frequency 30 MHz are given in Figs. 2 and 3. It was assumed during the computation that media 1 and 2 are bismuth germanate ($Bi_{12}GeO_{20}$) crystals characterized by the symmetry class 23, the cut (110), and the propagation direction $[1\bar{1}0]$. The liquid layer is glycerol, water, and a 90% solution of glycerol in water. The parameters of solids and liquids used for computation are given in the table.

As the plots show, the wave numbers of all shear horizontal waves are complex quantities, i.e., the waves are damped. As a rule, the real parts of the wave numbers are greater than the wave number of a bulk transverse wave $k_1 = 1.1088 \times 10^5$ m^{-1}. Therefore, the waves are of the surface type, and their mechanical displacements and electric fields are localized near the boundaries. In the case of a rather large thickness of the layer, the symmetric (s-waves) and antisymmetric (a-waves) waves are indistinguishable and their wave numbers almost coincide and correspond to transverse surface waves at the interface between a piezoelectric and a liquid. The behavior of the wave numbers as functions of the thickness of the liquid layer depends on both the wave type (s- or a-wave) and the mutual orientation of the crystallographic Z axes. Let us treat the cases (1) and (2) separately.

Case (1). The Z axes are co-directed (Figs. 2a and 2b). As the layer thickness decreases, antisymmetric waves slow down at first (Rek increases) and, at a very small thickness (about one micron at a frequency of 30 MHz), their phase velocity increases sharply (Rek decreases). As $h \longrightarrow 0$, a symmetric wave transforms to a bulk transverse wave propagating along the surface. It is interesting to note that, at small h, the phase velocities of s- and a-waves can be equal (Rek are equal in Fig. 2a). However, in this case, the imaginary parts of the wave numbers Imk stay unequal, and no complete degeneration of the waves takes place. Damping of s-waves at $h \longrightarrow 0$ tends to zero, while damping of a-waves increases sharply. Damping of shear horizontal waves is caused only by the viscosity of the liquid when the phase velocity of the waves is smaller than the phase velocity of a bulk transverse wave. If the latter condition is violated, as it is observed in the case of a-waves, additional damping occurs due to the energy radiation into a halfspace, and the wave becomes a leaky one.

Case (2). The Z axes have opposite directions (Figs. 3a and 3b). In this case, if the thickness of the liq-

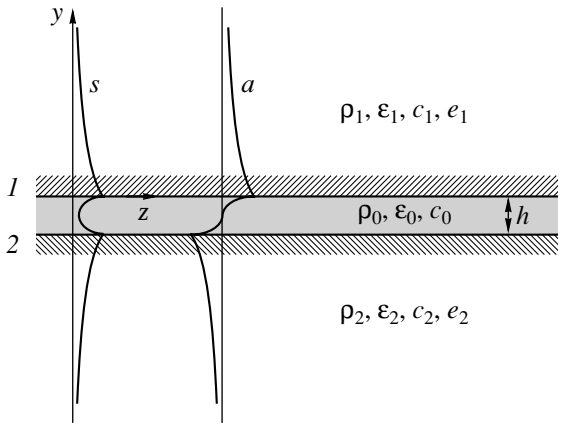

Fig. 1. Geometry of the problem.

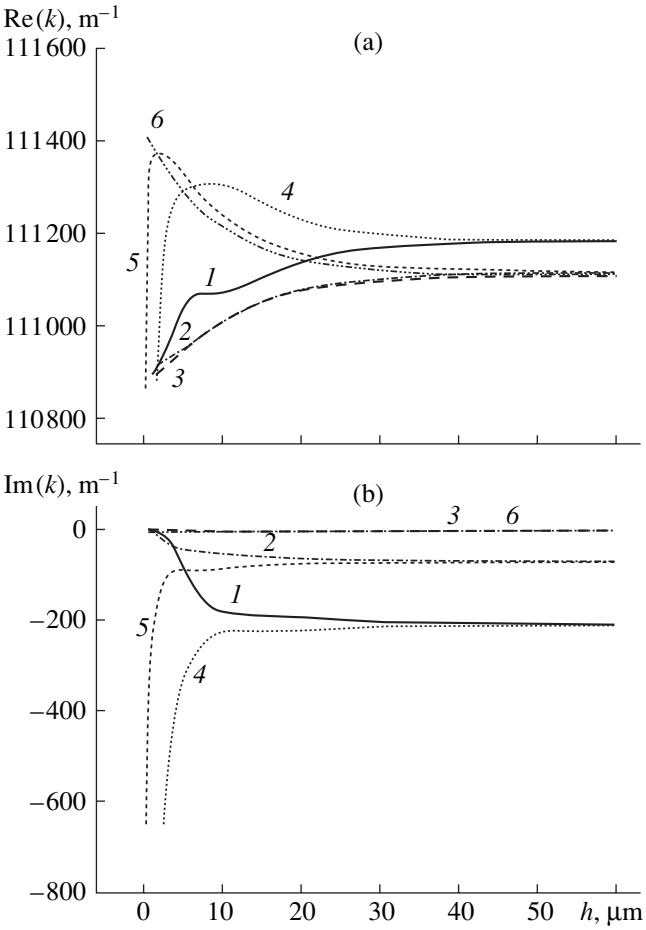

Fig. 2. Dependences of the (a) real and (b) imaginary parts of the wave number on the thickness of the liquid layer for (*1–3*) symmetric and (*4–6*) antisymmetric shear horizontal waves. The liquid is (*1*, *4*) glycerol, (*2*, *5*) a 90% solution of glycerol in water, and (*4*, *6*) water. Two nonmetallized halfspaces have identically directed *Z* axes.

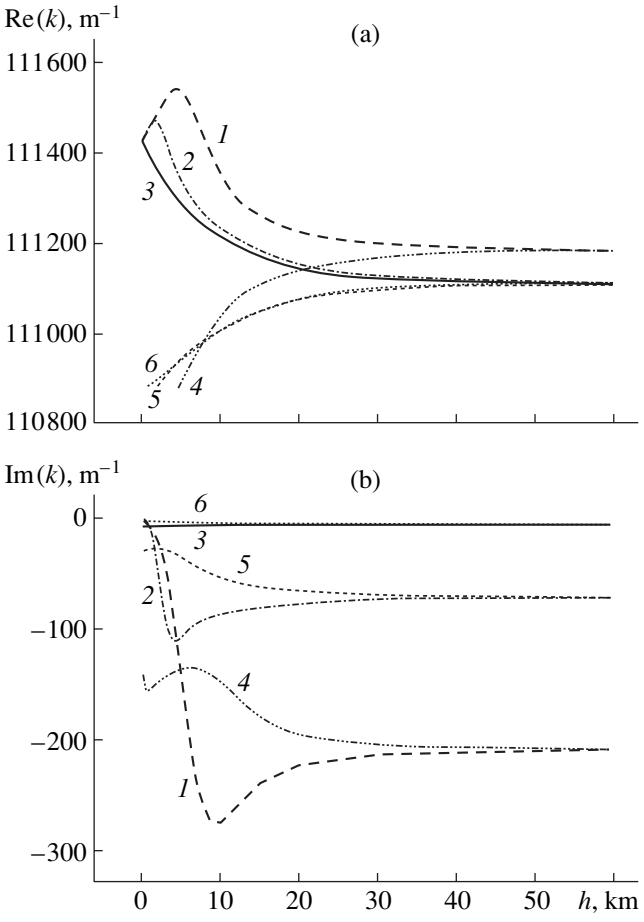

Fig. 3. Dependences of the (a) real and (b) imaginary parts of the wave number on the thickness of the liquid layer for (*1–3*) symmetric and (*4–6*) antisymmetric shear horizontal waves. The liquid is (*1*, *4*) glycerol, (*2*, *5*) a 90% solution of glycerol in water, and (*4*, *6*) water. Two nonmetallized halfspaces have opposite directions of their *Z* axes.

uid layer decreases, symmetric waves (s-waves) slow down and, in the limit $h \longrightarrow 0$, they transform to a surface wave at the interface of two crystals, which is described in [8]. As h decreases, antisymmetric waves degenerate into a bulk transverse wave propagating to the boundary, as in the first case. Damping of s-waves tends to zero as the layer thickness decreases.

If both surfaces of the solid are metallized, then, evidently, the electric coupling between the halfspaces vanishes. The dispersion equation becomes simplified to a certain extent:

$$d_1 d_2 - d^2 = 0, \tag{15}$$

where $d_{1,2} = (1 + K_{1,2}^2)\kappa_{1,2} - K_{1,2}^2|k| + \dfrac{c_0}{c_{1,2}}\kappa_0 \coth(\kappa_0 h)$

and $d = \dfrac{c_0}{\sqrt{c_1 c_2}} \dfrac{\kappa_0}{\sinh(\kappa_0 h)}$.

The wave structure is determined by Eqs. (6) and (7), where

$$\varphi_0 = 0,$$

$$A_1 = A, \quad A_2 = \pm\alpha A, \quad \alpha = \sqrt{\frac{d_1}{d_2}},$$

$$a_1 = -\frac{e_1}{\varepsilon_1}A, \quad a_2 = \mp\frac{e_2}{\varepsilon_2}\alpha A, \tag{16}$$

$$A_{01} = \frac{A}{2\sinh(\kappa_0 h)}(e^{\kappa_0 h} \mp \alpha),$$

$$A_{02} = \frac{-A}{2\sinh(\kappa_0 h)}(e^{-\kappa_0 h} \mp \alpha).$$

In the case of identical properties of media 1 and 2, $d_1 = d_2$ and the dispersion equation takes the form

$$(1 + K_1^2)\kappa_1 = K_1^2|k| - \frac{c_0}{c_1}\kappa_0 \frac{\cosh(\kappa_0 h) \mp 1}{\sinh(\kappa_0 h)}. \tag{17}$$

Denoting the right-hand side of Eq. (17) as $k_1 f_m(h, k)$, we determine an approximate solution to this equation:

$$k \approx k_1\left(1 + \frac{1}{2}\frac{f_m^2(h, k_1)}{(1 + K_1^2)^2}\right).$$

The numerical calculation of the roots of Eq. (17) for the parameters specified above yields the results presented in Figs. 4a and 4b.

All differences in the behavior of the wave numbers of shear horizontal waves in the two analyzed cases are caused by the different character of coupling. In the case of free boundaries, the two halfspaces are coupled both mechanically (possibly, viscoelastically as well) and electrically, which occurs due to the penetration of piezoelectric fields from one halfspace into another. The metallization breaks the electric coupling, and, when the gap width varies, the parameters of the shear horizontal waves are affected only by the mechanical properties of the liquid.

Let us indicate the major differences. A liquid with small viscosity, e.g., water, does not cause any noticeable splitting of the dispersion curves into s- and a-waves in the case of metallized surfaces (Figs. 4a and 4b), whereas in the first case, this splitting clearly manifests itself at the metal-free boundaries. The splitting into s- and a-waves in the case of free boundaries occurs for a thicker liquid layer, as compared to the case of metallized surfaces. This fact indicates "a longer-range" character of the electric coupling compared to that of viscous coupling.

Let only the surface of the second halfspace be metallized. The dispersion equation has the form of Eq. (15): $d_1 d_2 - d^2 = 0$, where

$$d_1 = (1 + K_1^2)\kappa_1 - K_1^2\frac{|k|}{1 + \frac{\varepsilon_1}{\varepsilon_0}\tanh(|k|h)} + \frac{c_0}{c_1}\kappa_0\coth(\kappa_0 h),$$

$$d_2 = (1 + K_2^2)\kappa_2 - K_2^2|k| + \frac{c_0}{c_2}\kappa_0\coth(\kappa_0 h), \qquad (18)$$

$$d = \frac{c_0}{\sqrt{c_1 c_2}}\frac{\kappa_0}{\sinh(\kappa_0 h)}.$$

The wave structure is determined by Eqs. (6) and (7) with the coefficients

$$A_1 = A, \quad A_2 = \pm\alpha A, \quad \alpha = \sqrt{\frac{d_1}{d_2}},$$
$$a_1 = -\frac{e_1}{\varepsilon_1}\frac{A}{1 + \frac{\varepsilon_1}{\varepsilon_0}\tanh(|k|h)}, \quad a_2 = \mp\frac{e_2}{\varepsilon_2}\alpha A, \qquad (19)$$
$$A_{01} = \frac{A}{2\sinh(\kappa_0 h)}(e^{\kappa_0 h} \mp \alpha),$$

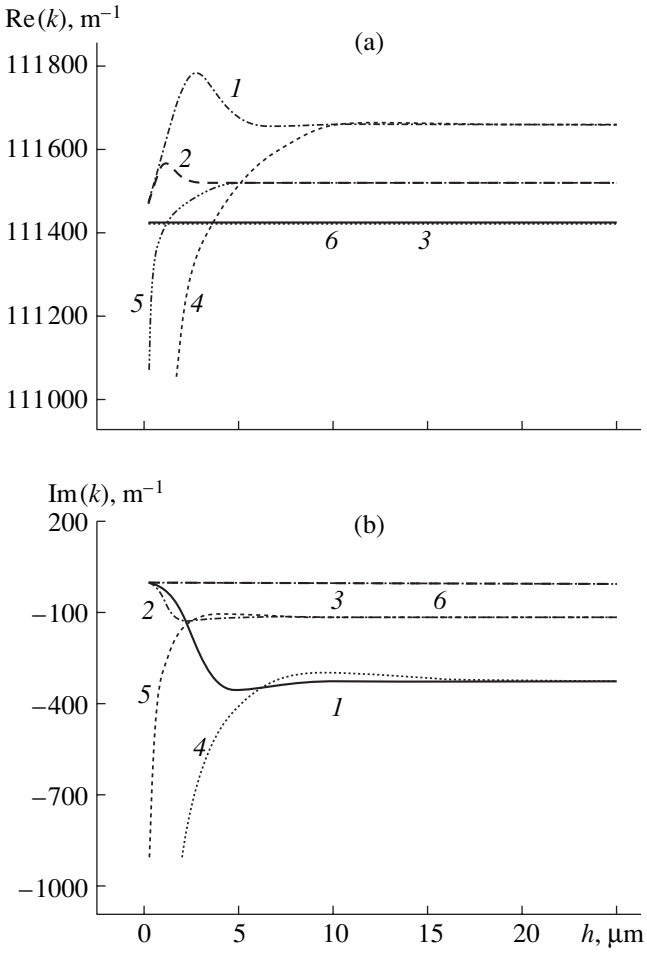

Fig. 4. Dependences of the (a) real and (b) imaginary parts of the wave number on the thickness of the liquid layer for (*1–3*) symmetric and (*4–6*) antisymmetric shear horizontal waves. The liquid is (*1*, *4*) glycerol, (*2*, *5*) a 90% solution of glycerol in water, and (*3*, *6*) water. Two metallized surfaces.

$$A_{02} = \frac{-A}{2\sinh(\kappa_0 h)}(e^{-\kappa_0 h} \mp \alpha),$$
$$a_{01} = e_1\frac{e^{|k|h}}{\varepsilon_0\cosh(|k|h) + \varepsilon_1\sinh(|k|h)}A, \qquad (20)$$
$$a_{02} = -e_1\frac{e^{-|k|h}}{\varepsilon_0\cosh(|k|h) + \varepsilon_1\sinh(|k|h)}A.$$

In the case of a single metallized surface, as well as in the case of two ones, there is no direct electric coupling between the halfspaces. However, in this case, the dielectric properties of the liquid still affect the wave numbers of shear horizontal waves. This follows from the dependence of d_1 on ε_0.

Shear horizontal waves in a layered structure with a single metallized surface have their own distinctive features. First of all, we should note that the structure itself

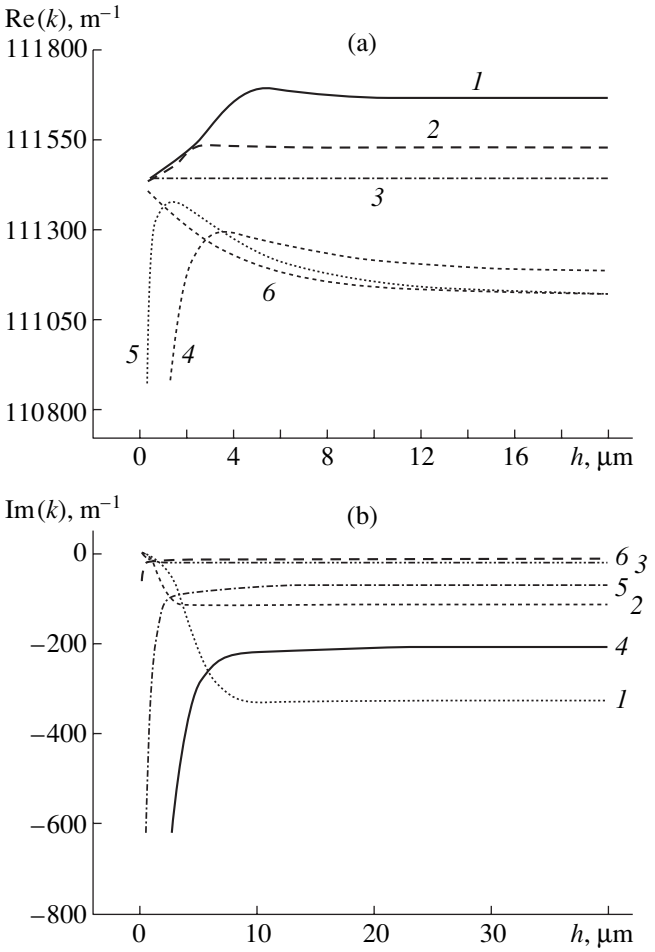

Fig. 5. Dependences of the (a) real and (b) imaginary parts of the wave number on the thickness of the liquid layer for (*1–3*) symmetric and (*4–6*) antisymmetric shear horizontal waves. The liquid is (*1, 4*) glycerol, (*2, 5*) a 90% solution of glycerol in water, and (*3, 6*) water. One metallized surface.

is nonsymmetric and the coefficient $\alpha \neq 1$ [see Eq. (19)] even when media 1 and 2 are identical. A consequence of this is the absence of strictly symmetric and antisymmetric waves in this structure. Although by analogy with the preceding cases, we assume that the upper sign in Eqs. (19) and (20) determines a "symmetric" wave and the lower sign, the "antisymmetric" one. The analysis of Eqs. (18) and the results of the numerical solution indicate the following particular features of the wave numbers as functions of the liquid layer thickness (Fig. 5). For large values of h, the wave numbers of "symmetric" and "antisymmetric" waves do not coincide and become closer in their values as h decreases. The difference between $\mathrm{Re}(k)$ for s- and a-waves reaches its minimum at the value of the gap width h_0, which is definite for each liquid, and increases sharply as the width h decreases further. The higher the value of the liquid viscosity, the greater is the width h_0. When $h \longrightarrow 0$, a "symmetric" shear horizontal wave transforms to a purely transverse surface wave, as in the case of two metallized surfaces, the latter wave being localized near the metallized surface.

Now let us consider the properties of shear horizontal waves that are caused by the piezoelectric effect. An important feature of piezoactive surface waves is the coefficient of electromechanical coupling $K_s^2 = 2\Delta v/v_f$, where $\Delta v = (v_f - v_m)$. This coefficient is equal to the double relative difference of phase velocities for the waves at the free (v_f) and metallized (v_m) surfaces. This parameter determines the efficiency of the wave excitation by the electrode transducers positioned at the surface. In contrast to surface waves, shear horizontal waves are localized in the region adjacent to the two surfaces. Hence, it is possible to associate two coefficients of electromechanical coupling with each shear horizontal wave: one coefficient corresponds to one metallized surface $K_{s1}^2 = \dfrac{v_f - v_m}{v_f}$ and the other corresponds to two surfaces, $K_{s2}^2 = \dfrac{v_f - v_{mm}}{v_f}$, where v_m and v_{mm} are the wave numbers of shear horizontal waves in structures with one and two metallized surfaces, respectively. We also introduce the coefficient of electromechanical coupling for a shear horizontal wave in a structure with a single metallized surface, $K_{s3}^2 = \dfrac{v_m - v_{mm}}{v_m}$. Each of these parameters depends on the wave type, the mechanical and dielectric properties of the liquid, and the thickness of the layer occupied by it. Figure 6 illustrates the dependences of K_{si}^2 on the thickness h of a glycerol layer for certain shear horizontal waves.

Numerical analysis and Fig. 6 demonstrate that the maximal coefficient of electromechanical coupling K_{s2}^2 corresponds to a symmetric wave in the case of identically oriented crystallographic axes in two halfspaces and to an antisymmetric wave in the case of their opposite orientations, the value of this maximal coefficient weakly depending on h. The coefficient K_{s1}^2, which corresponds to one metallized surface, exhibits similar properties only for a symmetric wave in a structure with identically directed axes. It is also necessary to note the dependences $K_{s3}^2(h)$. In the case of large values of the thickness h, the coefficient of electromechanical coupling is nonzero only for an "antisymmetric" wave. Noticeable values of K_{s3}^2 for a "symmetric" wave are observed only at a certain value of the liquid layer thickness.

Thus, we considered shear horizontal waves in a layered structure consisting of two piezoelectric halfspaces with a liquid layer between them. Expressions

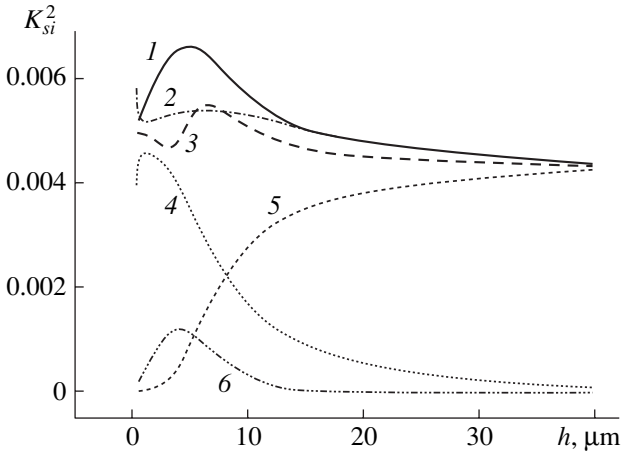

Fig. 6. Coefficients of electromechanical coupling: (*1*) K_{s2}^2, an s-wave, and identical directions of the axes; (*2*) K_{s2}^2, an a-wave, and opposite directions of the axes; (*3*) K_{s1}^2, an s-wave, and identical directions of the axes; (*4*) K_{s1}^2, an a-wave, and opposite directions of the axes; (*5*) K_{s1}^2, an s-wave, and opposite directions of the axes; and (*6*) K_{s3}^2, an s-wave, and any mutual orientation of the axes.

completely describing the structure of waves are derived, and the dependences of the complex wave numbers on the layer thickness and on the type of liquid are analyzed. It is demonstrated that these parameters depend either on the mechanical properties of liquids, as in the case of two metallized surfaces, or on their mechanical and dielectric properties. Two coefficients of electromechanical coupling, which correspond to the relative changes of phase velocities in the cases of metallization of one or two surfaces, are introduced and calculated for shear horizontal waves.

The knowledge of all these particular features of the propagation of shear horizontal waves can be useful for the development of a new technique for measuring the viscoelastic and dielectric properties of liquids.

ACKNOWLEDGMENTS

This work was supported by the Russian Foundation for Basic Research, project no. 00-02-16473.

REFERENCES

1. Yu. V. Gulyaev and V. P. Plesskiĭ, Akust. Zh. **23**, 716 (1977) [Sov. Phys. Acoust. **23**, 410 (1977)].
2. M. K. Balakirev and A. V. Gorchakov, Fiz. Tverd. Tela (Leningrad) **19** (2), 613 (1977) [Sov. Phys. Solid State **19**, 367 (1977)].
3. M. K. Balakirev, S. V. Bogdanov, A. V. Gorchakov, and A. É. Chakushin, Fiz. Tverd. Tela (Leningrad) **21** (8), 2508 (1979) [Sov. Phys. Solid State **21**, 1448 (1979)].
4. M. Inone, H. Moritake, K. Toda, and K. Yoshino, Jpn. J. Appl. Phys., Part 1 **39** (9B), 5632 (2000).
5. A. J. Rico and S. J. Martin, Appl. Phys. Lett. **50** (21), 1474 (1987).
6. J. Kondoh, K. Saito, S. Shiokawa, and H. Suzuki, Jpn. J. Appl. Phys., Part 1 **35** (5B), 3093 (1996).
7. V. I. Anisimkin and I. V. Anisimkin, Radiotekh. Élektron. (Moscow) **45** (7), 293 (2000).
8. C. Mayerfeld and P. Tornois, Appl. Phys. Lett. **19** (4), 117 (1971).

Translated by M. Lyamshev

Acoustical Physics, Vol. 47, No. 6, 2001, pp. 746–754. Translated from Akusticheskiĭ Zhurnal, Vol. 47, No. 6, 2001, pp. 843–852.

Precision of the Material Parameter Measurements in the Acoustic Low-Frequency Pipe

V. V. Tyutekin

Andreev Acoustics Institute, Russian Academy of Sciences, ul. Shvernika 4, Moscow, 117036 Russia

e-mail: tyutekin@akin.ru

Received January 25, 2001

Abstract—The effect of errors in the technique implementation on the precision of measurements using the Acoustic Low-Frequency Pipe system that is based on the principle of unidirectional sound reception is considered. Errors in determination of the complex reflection and transmission coefficients of sound for samples tested are calculated theoretically. A numerical analysis of these errors is performed using standard samples as examples. © *2001 MAIK "Nauka/Interperiodica".*

Development of low-frequency underwater echo-ranging techniques (see, e.g., [1, 2]) needed the development and implementation of adequate methods for measuring the acoustic parameters of materials and structures that are made of these materials and used in underwater acoustics. The structures used for sound-proofing and sound absorption, reflection, etc., belong to such objects. Their basic acoustic parameters are the complex values of impedances, reflection and transmission coefficients for sound, etc.

The measuring techniques used for this purpose earlier (e.g., a "pulsed pipe" [3] and some other methods [4]) provide the measurements starting from the frequency of several kilohertz. To lower the frequency range down to 50–100 Hz would require the elongation of a setup by several tens of times.

The measuring system called the Acoustic Low-Frequency Pipe (ALP) (some of its particular features are presented here) is described in detail in literature [5–9]. Its major property consists in the fact that, at a relatively small length of the pipe (it is equal approximately to 0.2λ at the lower frequency of the range), it provides an opportunity to measure the mentioned acoustic parameters in the traveling-wave mode. It should be noted that its modification intended for analogous measurements in air has been developed recently [10].

For clarity, we give here a brief description of both the method and the ALP system implementing it (Fig. 1). The measurements are conducted at different values of temperature and static pressure within (4) a thick-walled separable cylindrical pipe with a total length of 3.5 m that is filled with water. A sample under measurement is positioned in the middle of the pipe and fixed using a pendant at the upper flange plate of the lower half of the pipe. The sound field incident on the sample is excited by (6) a radiator fed from (7) a generator at fixed frequencies in the range 100–5000 Hz (divided in two sub-ranges, 100–1000 and 1000–5000 Hz) in a continuous radiation mode.

One of the characteristic features of the ALP is the utilization of the so-called unidirectional reception realizing the Huygens reception surface and widely used in one-dimensional systems of sound suppression. In the described system, the unidirectional reception of

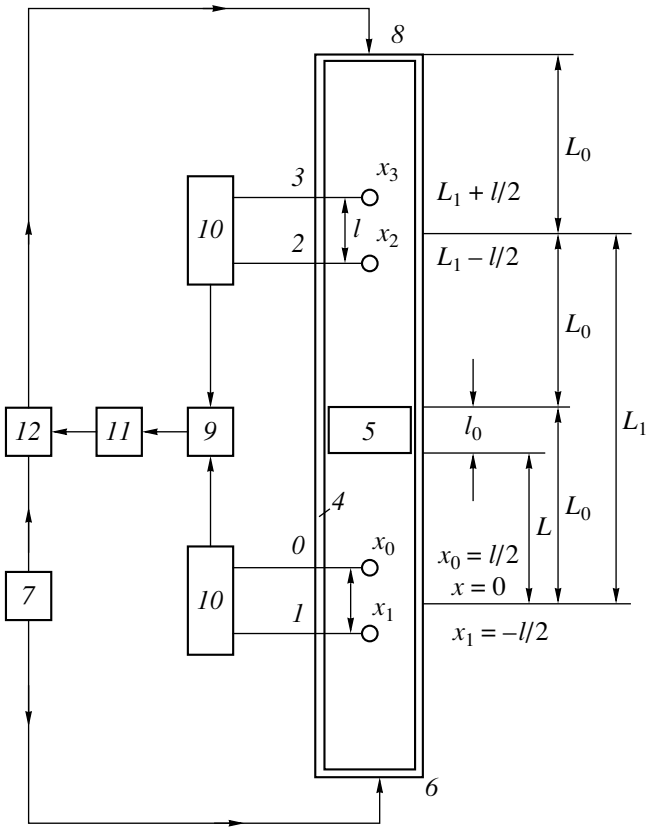

Fig. 1. Block diagram of the ALP measuring system.

1063-7710/01/4706-0746$21.00 © 2001 MAIK "Nauka/Interperiodica"

the fields incident on and reflected from a sample is performed by a receiving system consisting of two miniature hydrophones [(0) and (1)] and conducting alternately a unidirectional reception. In this case, the data from each of the hydrophones are subjected to combined processing with the introduction of a corresponding phase shift. This provides an opportunity to separately measure the complex amplitudes of an incident wave $\hat{a}_1$ and a wave reflected from the sample $\hat{a}_2$. Their ratio gives the value of the complex reflection coefficient $\hat{R} = \frac{\hat{a}_2}{\hat{a}_1}$.

The process of measurement is performed using an analog–digital technique. The radiation and reception are conducted by analog equipment (a generator, amplifiers, etc.). The signal processing, including the adjustment of a sound absorber, is performed by (9) a computer using specially designed codes. The mutual connection is realized using (10) an analog-to-digital converter and (11) a digital-to-analog converter.

The value of soundproofing is measured in the traveling wave mode, i.e., the wave transmitted through a sample is absorbed at the upper end of the pipe. An auxiliary radiator (8) exited coherently with the basic radiator is positioned there for this purpose. The parameters of the radiated sound field are selected with the help of (12) an amplitude-phase control unit in such a way that the field reflected from the surface of the auxiliary radiator is damped completely. Thus, the auxiliary radiator plays the role of an active sound absorber. The adjustment of the radiation and measurement of the sound field transmitted through a sample is performed by the second reception system consisting of two hydrophones [(2) and (3)]. This reception system is completely analogous to the first system [(0) and (1)] and separately measures the amplitudes of the transmitted $\hat{b}_1$ and reflected $\hat{b}_2$ waves. The quantity $D = \frac{\hat{b}_1}{a_1}$ gives the value of the soundproofing coefficient. The adjustment of the active sound absorber consists in the minimization of the quantity $\hat{R}_1 = \frac{\hat{b}_2}{\hat{b}_1} = \min$. Special computer codes provide an opportunity to perform the relative calibration of the hydrophone sensitivity, the measurements of the velocity and damping of sound in the pipe, etc.

At present, there is no detailed analysis of the effect of possible errors of the technique implementation on the precision of measurements of the complex coefficients of sound reflection and transmission in literature despite the fact that publications devoted to the ALP are fairly numerous and the ALP system is applied widely in the measurement practice. Such an analysis may help reveal the most significant errors and maximize the precision of measurements owing to the elimination or decrease of errors.

This paper treats the effect of the possible errors that are most essential in our point of view, first of all, errors in the hydrophone calibration. These errors lead to inconsistency between the sensitivities of the hydrophones, which form in pairs of unidirectional combined receivers.

Let us consider the problem of the effect of errors in hydrophone calibration on the precision of measurements; i.e., to what extent the measured complex coefficients of sound reflection and transmission differ from their corresponding "true" values. It will be possible to determine the value of permissible errors in calibration on the basis of the obtained results proceeding from the calculated and measured values for some standard samples.

Figure 1 demonstrates the block-scheme of the setup and the coordinate system used for further calculation. The coordinate origin corresponds to half of the distance between the hydrophones forming the lower reception system and positioned at the points with the coordinates $x_0 = \frac{l}{2}$ and $x_1 = -\frac{l}{2}$, where l is the distance between hydrophones 0 and 1. The lower surface of the sample has the coordinate $x = L = L_0 - l_0$, where L_0 is the distance to the pipe center and l_0 is the sample thickness.

The median plane of the upper reception system is located at $x = L_1$, where $L_1 = 2L_0$ is the distance between the median planes of the upper and lower systems. The hydrophones of the upper system with the numbers 2 and 3 have the coordinates $x_2 = L_1 - \frac{l}{2}$ and $x_3 = L_1 + \frac{l}{2}$. The distance from $x = L_1$ to the water surface is equal to L_0.

The pressure p_i in an incident plane wave of unit amplitude and the pressure p_r in a reflected wave can be written in the form

$$p_i = \exp(ikx), \quad p_r = \hat{r}\exp(-ikx). \tag{1}$$

Here, $k = \frac{\omega}{c_0}$ is the wave number, $\omega = 2\pi f$ is the circular frequency, c_0 is the sound velocity, and $\hat{r}$ is the complex coefficient of sound reflection from the sample. The latter quantity is reduced to the section $x = 0$ and is determined by the relation

$$\hat{r} = r\exp(i2kL), \tag{2}$$

where $r = r_0\exp(i\varphi)$ and r_0 and φ are the modulus and phase of the reflection coefficient.

The sound pressures p_i and p_r determined by Eq. (1) are received by each hydrophone and transformed by

them to corresponding voltages that can be calculated by the formulas

$$V_0 = p_i(l/2) + p_r(l/2) = \exp(ikl/2) + \hat{r}\exp(-ikl/2), \quad (3a)$$

$$V_1 = u[p_i(-l/2) + p_r(-l/2)] = \hat{u}[\exp(-ikl/2) + \hat{r}\exp(ikl/2)]. \quad (3b)$$

It is assumed in these formulas that hydrophone 0 is the reference one and its sensitivity is equal to unity. In this case, the sensitivity of hydrophone 1 is equal to $\hat{u} = u\exp(i\varphi_u)$. Further, according to the algorithm applied in the measuring technique for the formation of unidirectional reception, the following operation is used:

$$U_1 = V_1 + V_0\exp(i(kl + \pi)), \quad (4a)$$

$$U_2 = V_0 + V_1\exp(i(kl + \pi)). \quad (4b)$$

Here, U_1 is the voltage corresponding to the "incident wave" channel and U_2 is the same for the "reflected wave" channel. The factor $\exp(ikl)$ in Eqs. (4a) and (4b) describes the delay line introduced into the processing system.

Substituting Eqs. (3a) and (3b) into Eqs. (4a) and (4b) and performing the necessary transformations, we obtain

$$U_1 = -\exp(ikl/2) \times \langle i2\sin kl - (\hat{u} - 1)[\hat{r} + \exp(-ikl)]\rangle, \quad (5a)$$

$$U_2 = -\exp(ikl/2) \times \rangle i\hat{r}\,2\sin kl + (\hat{u} - 1)[1 + \hat{r}\exp(ikl)]\langle. \quad (5b)$$

Taking into account the that the quantity $i2\sin kl$ determines the sensitivity of a combined receiver and introducing the value of the offset ratio $\Delta\hat{u} = \dfrac{\hat{u} - 1}{i2\sin kl}$, we can write down a formula for the measured value of the reflection coefficient in the form

$$\hat{R} = \frac{U_2}{U_1} = \frac{\hat{r} + \Delta\hat{u}[1 + \hat{r}\exp(ikl)]}{1 - \Delta\hat{u}[\exp(-ikl) + \hat{r}]}. \quad (6)$$

Here, $\hat{R} = R\exp(i2kL)$, $R = R_0\exp(i\varphi_0)$, and R_0 and φ_0 are the modulus and phase of the measured reflection coefficient.

It follows from Eq. (6) that, at $\Delta\hat{u} = 0$, i.e., in the case of identical hydrophones, $\hat{R} = \hat{r}$, and, therefore, the measured reflection coefficient exactly coincides with the true one. In other cases, the relationship between these quantities is of a complex functional character. We can also note that, since we have $\Delta\hat{u} \sim (\sin kl)^{-1}$, we can expect larger discrepancies in the reflection coefficients at the boundaries of each frequency sub-range, as compared to their central parts.

Using Eq. (6), it is possible in principle to correct the calibration of the hydrophones. For example, if the theoretical and experimental values of the reflection coefficient for some standard sample are known, one can determine the value of the offset $\Delta\hat{u}$ from this formula:

$$\Delta\hat{u} = \frac{\hat{r} - \hat{R}}{1 + \hat{r}\exp(ikl) + \hat{R}\exp(-ikl) + \hat{r}\hat{R}}. \quad (7)$$

Then, on this basis, we can determine the true value of $\hat{u}$ and enter it into the program window of the calibration coefficients.

The formulas for the complex transmission coefficient are derived in the same way as for the complex reflection coefficient. The wave incident on the sample p_i is determined by Eq. (1). A transmitted wave can be represented in the form

$$p_d = \hat{d}\exp(ikx), \quad (8)$$

where $\hat{d}$ is the true transmission coefficient. In the case of the reflection coefficient of an electroacoustic absorber $\hat{\beta} = \beta\exp(i2kL)$, the wave reflected from it has the form

$$p_\beta = \hat{\beta}\hat{d}\exp(-ikx). \quad (9)$$

The sound pressures p_i and p_d determined by Eqs. (1) and (8) are received by hydrophones 2 and 3 and transformed by them to the corresponding voltages that can be calculated by the formulas

$$V_2 = \hat{u}_2[p_d(L_1 - l/2) + p_\beta(L_1 - l/2)] = \hat{u}_2\hat{d}\exp(ikL_1)[\exp(-ikl/2) + \hat{\beta}\exp(ikl/2)], \quad (10a)$$

$$V_3 = \hat{u}_3[p_d(L_1 + l/2) + p_\beta(L_1 + l/2)] = \hat{u}_3\hat{d}\exp(ikL_1)[\exp(ikl/2) + \hat{\beta}\exp(-ikl/2)]. \quad (10b)$$

Here, the quantities $\hat{u}_2$ and $\hat{u}_3$ are the sensitivities of hydrophones 2 and 3 relative to hydrophone 0. The voltage in the transmitted wave channel is calculated according to the formula analogous to Eq. (4a) and determined by the formula analogous to Eq. (5a):

$$U_3 = -\hat{u}_3\hat{d}\exp(ikl/2) \times \rangle i2\sin kl - (\hat{u}_d - 1)[\exp(-ikl) + \hat{\beta}]\langle, \quad (11)$$

where $\hat{u}_d = \dfrac{\hat{u}_2}{\hat{u}_3}$. The factor $\exp(ikL_1)$ is absent in Eq. (11), because it is involved on both sides of the formula. We obtain the measured value of the complex transmission coefficient from Eqs. (5a) and (11):

$$\hat{D} = \frac{U_3}{U_1} = \hat{d}\hat{u}_3\frac{1 - \Delta\hat{u}_d[\exp(-ikl) + \hat{\beta}]}{1 - \Delta\hat{u}[\exp(-ikl) + \hat{r}]}. \quad (12)$$

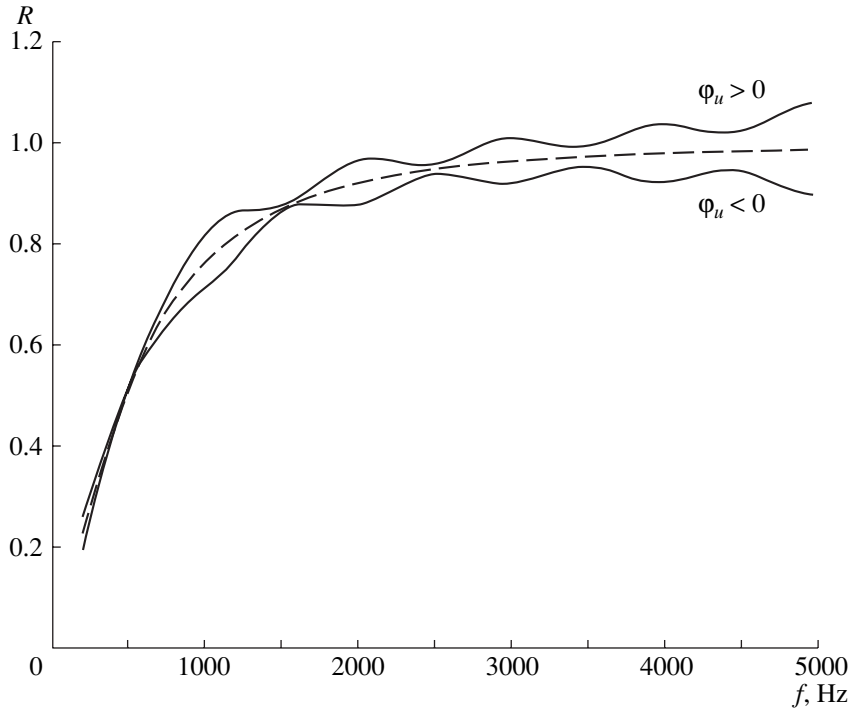

Fig. 2. Effect of the phase offset $\varphi_u = \pm 0.015$ on the modulus of the reflection coefficient for a standard sample.

Here, $\Delta\hat{u}_d = \dfrac{\hat{u}_d - 1}{i2\sin kl}$ is the offset ratio of the upper combined receiver. One can see from Eq. (12) that the condition $\hat{D} = \hat{d}$ is valid at $\Delta\hat{u}_d = \Delta\hat{u} = 0$ and $\hat{u}_3 = 1$.

Since Eq. (6) holds also for the upper receiving system (with the substitution of the quantity $\hat{u}_d$ for $\hat{u}$), it is possible to obtain the true coefficient of reflection from the electroacoustic absorber $\hat{\beta}$. Since the latter is adjusted according to the preset value of the modulus of β_0 measured in the process of adjustment, the quantity of interest $\hat{\beta}$ is determined by the formula

$$\hat{\beta} = \frac{\beta_0 - \Delta\hat{u}_d[1 + \beta_0\exp(-ikl)]}{1 + \Delta\hat{u}_d[\beta_0 + \exp(ikl)]}. \qquad (13)$$

It is possible to calculate the measurement error for any case only using the examples of specific measured samples with acoustic characteristics that can be determined theoretically. Metal (more often, steel) disks of different thickness, small compared to the wavelength, are used as such standard samples. The impedances of such disks can be assumed to be purely inertial. Below, we present the calculation of the complex reflection and transmission coefficients for such samples loaded on a water column (which imitates the upper half of the pipe) with an ideal sound absorber at the end [Eqs. (18)]. A standard steel sample with a thickness of 7 cm is selected for the calculation.

The results of calculations by Eqs. (6) and (18b), which are of illustrative character, are given in Figs. 2 and 3 for the modulus and phase of the reflection coefficient, respectively. The offset from a purely unidirectional case is given by the values $u = 1 \pm 0.05$ and $\varphi_u = \pm 0.015$ ($\approx \pm 1°$). The dashed lines represent the case $u = 0$ and $\varphi_u = 0$. Here, the values of R in the first case and φ_R in the second are not given, since the effect of the corresponding offsets on these values is very small. One can see from the figures that the offsets transform smooth (theoretical) curves into oscillating ones. It is essential to note that all observed frequency oscillations are almost periodic with the period $\Delta f \approx 1000$ Hz corresponding to the expression $\Delta(kL) = \pi$, where L is the distance from the center of the lower receiving system to the lower surface of the sample. We also note that the offset u mainly affects the value of the phase and the offset φ_u, the value of the modulus.

Similar results are obtained for the transmission coefficient.

Now, let us consider the effect of the efficiency of an active sound absorber. Another reason for possible errors in the measurement of the complex values of the reflection and transmission coefficients can be the insufficient efficiency of the active sound absorber ensuring the traveling wave mode in the ALP. With the usually set threshold value of the reflection coefficient $\beta_0 = 0.05$, the true efficiency of the absorber can be lower because of the departure of the upper receiving system from unidirectional reception. The true coefficient of reflection from the absorber $\hat{\beta}$ is given by Eq. (13).

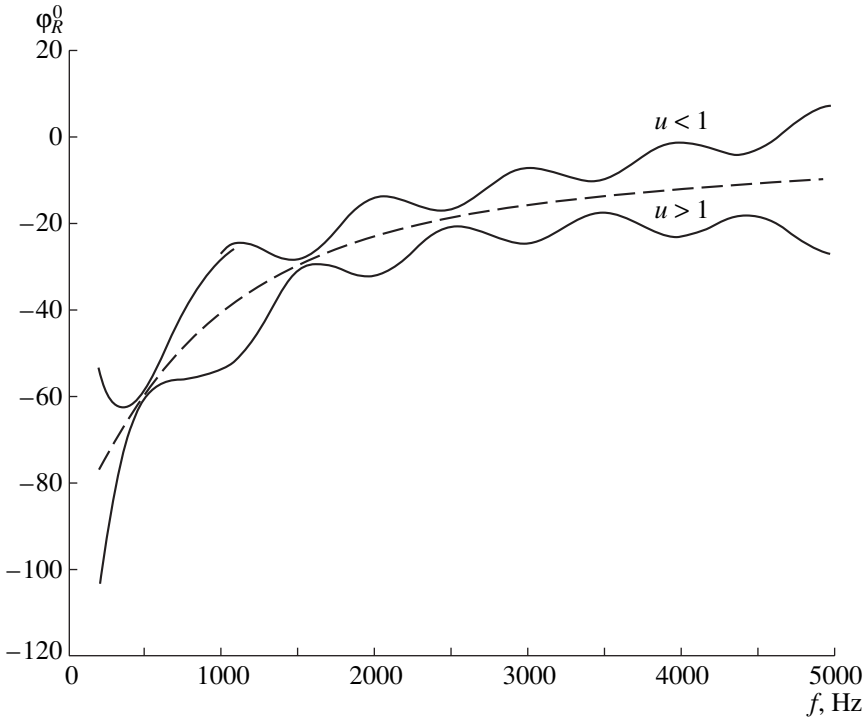

Fig. 3. Effect of the amplitude offset $u = 1 \pm 0.05$ on the phase of the reflection coefficient.

Let us use the standard samples described above to evaluate the effect of this factor and calculate the complex reflection and transmission coefficients of such samples loaded on a water column with a sound absorber characterized by the reflection coefficient $\hat{\beta}$ at the end. (At $\beta = 0$, the traveling wave mode is realized.)

The parameters of a standard sample are its density ρ and thickness l. We assume that the conditions of an ideal "lubrication" (see below) are satisfied at its cylindrical lateral surface.

The sound field in the region before the sample can be represented as follows:

the sound pressure

$$P_1 = \exp(ikx) + R\exp(-ikx); \tag{14a}$$

the particle velocity

$$V_1 = \frac{1}{\rho_0 c_0}(\exp(ikx) - R\exp(-ikx)), \tag{14b}$$

where $\hat{R}$ is the complex reflection coefficient of the sample.

For the sound field in the region behind the sample, we have, respectively,

$$P_2 = \hat{D}(\exp(ikx) + \hat{\beta}\exp(-ikx)), \tag{15a}$$

$$V_2 = \frac{\hat{D}}{\rho_0 c_0}(\exp(ikx) - \hat{\beta}\exp(-ikx)), \tag{15b}$$

where $\hat{D}$ is the complex transmission coefficient of the sample and $\hat{\beta} = \beta_0\exp(i2kL)$ is the reflection coefficient of the absorber, its value being reduced to the section $x = 0$.

To determine the unknown quantities $\hat{R}$ and $\hat{D}$, we jointly write the boundary conditions at the boundaries $x = 0$ and $x = l$:

$P_2(l) - P_1(0) = -i\omega\rho l V_1(0)$ is the condition at the boundaries of the mass load and $V_1(0) = V_2(l)$ is the condition of equality of particle velocities.

Substituting Eqs. (14) and (15) into these equalities, we obtain the following set of equations:

$$\alpha^+\hat{D}_1 - \hat{R}(1 + iX) = 1 - iX, \tag{16a}$$

$$\alpha^-\hat{D}_1 + \hat{R} = 1, \tag{16b}$$

where $\hat{D}_1 = \hat{D}\exp(ikl)$, $\alpha^\pm = 1 \pm \beta_0\exp(i2k(L - l))$, and $X = \dfrac{\omega\rho l}{\rho_0 c_0}$ is the dimensionless inertial impedance of the sample.

We obtain from Eqs. (16):

$$\hat{D}_1 = \frac{2}{\alpha^+ + \alpha^-(1 + iX)} = \frac{2}{2 + i\alpha^- X}, \tag{17a}$$

$$\hat{R} = 1 - \alpha^-\hat{D}_1. \tag{17b}$$

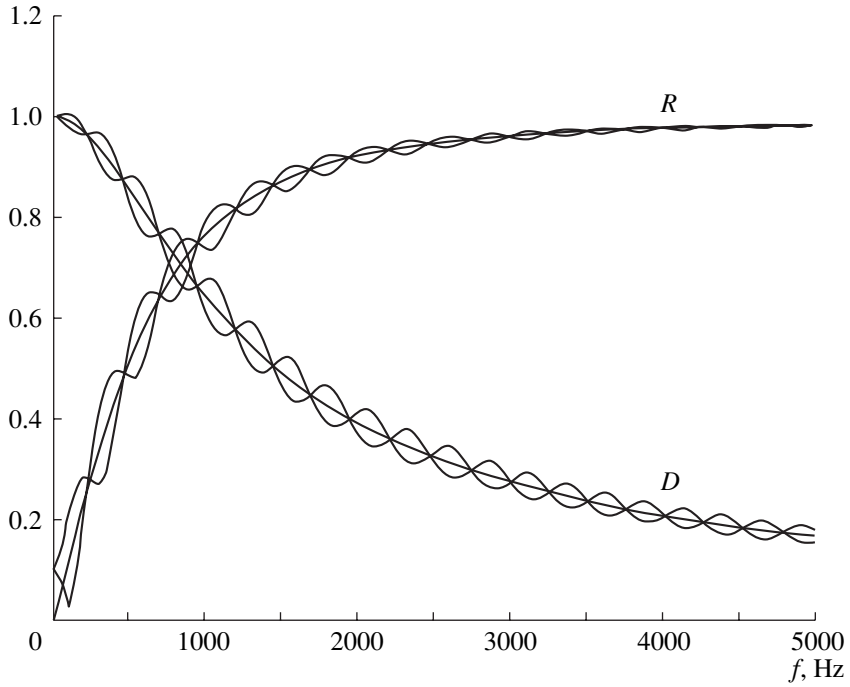

Fig. 4. Effect of the imperfection of the active absorber on the values of R and D; $\beta = \pm 0.1$.

For an ideal absorber $\beta_0 = 0$, we have $\alpha^- = 1$, and, therefore, we can write

$$\hat{D}_1 = \frac{2}{2 + iX}, \tag{18a}$$

$$\hat{R} = \frac{iX}{2 + iX}. \tag{18b}$$

The influence of the quantity β_0 on the characteristics of standard samples under measurement is illustrated in the figures described below. Figures 4 and 5 present the plots of the frequency dependences of R and D_1 and respective phases φ_R and φ_D for a standard steel sample with the thickness $l = 7$ cm for the values $\beta = 0$ and ± 0.1.

We can make the following conclusions by analyzing these figures.

(a) For $\beta \neq 0$, all curves exhibit an oscillating character. In this case, the period of oscillations is $\Delta f \cong 500$ Hz, which corresponds to the expression $\Delta(kL_1) = \pi$, where L_1 is the distance from the sample to the absorber surface.

(b) The change of the sign of β leads to a "swing" of the oscillation phase.

(c) When $|\beta|$ increases, the oscillation amplitude increases also.

(d) The maximal deviation is observed for both the modulus and the phase at small values of R (at low frequencies).

It is necessary to note that the application of an active sound absorber provides an opportunity to conduct measurements not only in the traveling wave mode, but also to form almost any complex load upon a sample in order to measure the complex reflection coefficient. Since $\hat{\beta} = \hat{\beta}_0 \exp(i2kL_1)$ is the absorber reflection coefficient reduced to the section $x = L_0$ (the upper surface of the sample), it is possible to determine the complex reflection coefficient of the absorber $\hat{\beta}_0$ that provides the preset value of the load impedance Z_0 according to the following formula:

$$\hat{\beta}_0 = \frac{Z_0 - 1}{Z_0 + 1} \exp(-i2kL_1).$$

One more source of measurement errors can be a cylindrical slot between the lateral surface of the sample and the pipe wall. The following evident physical factors should be mentioned:

(a) a possible viscous loss; and

(b) a sound "leakage" through the slot.

The first mechanism will be treated below as applied to the above-mentioned standard samples in the form of metal disks. The slot size h is usually small compared to the pipe radius a and the wavelength λ ($h/a \equiv 0.01$–0.02, $h/\lambda \leq 0.003$).

The equations of motion for a standard sample can be written in the form

$$-i\omega m V_0 = F_2 - F_1 + \sigma, \tag{19}$$

where V_0 is the particle velocity, $m = \rho l S$ is the sample mass, $F_1 = p_1 S$ and $F_2 = p_2 S$ are the summary forces produced by sound pressure and acting on the front and

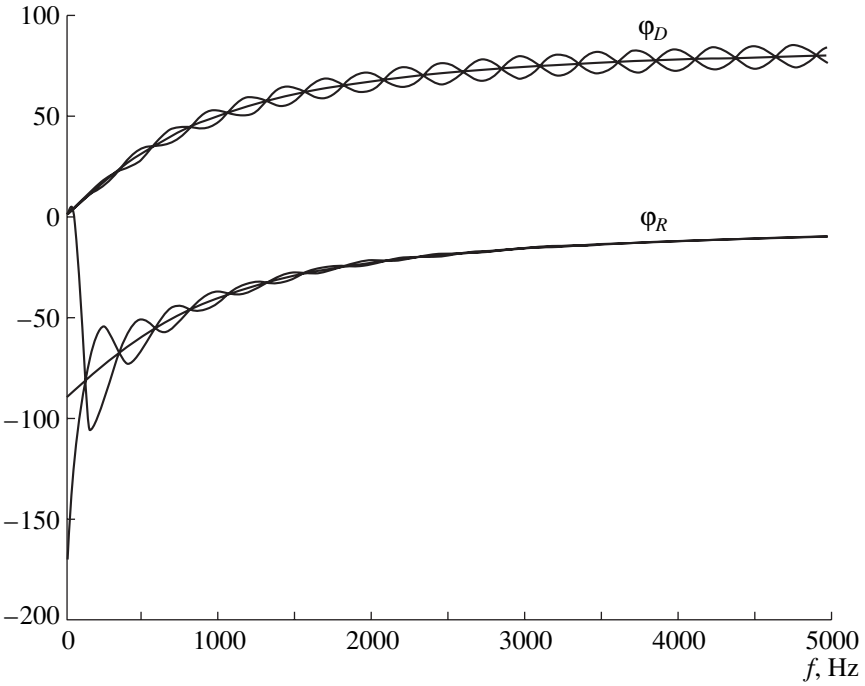

Fig. 5. Effect of the imperfection of the active absorber on the values of φ_R and φ_D; $\beta = \pm 0.1$.

rear surfaces of the sample $S = \pi a^2$, $\sigma = \sigma_0 S_1$ is the summary viscosity force acting on the lateral surface of the sample $S_1 = 2\pi a l$, and σ_0 is the viscous stress. Taking into account these notations, Eq. (19) can be represented in the form

$$-i\omega\rho l V_0 = p_2 - p_1 + \frac{2l}{a}\sigma_0. \tag{20}$$

To calculate the value of the viscous stress σ_0, we use the Navier–Stokes equation for an incompressible liquid [11]

$$\frac{\partial V}{\partial t} = \nu\frac{\partial^2 V}{\partial y^2}, \tag{21}$$

where V is the particle velocity in a viscous wave, ν is the viscosity coefficient of water, and y is the radial coordinate (since $h/a \ll 1$, the problem can be solved in the Cartesian coordinates). Since we have $V = V(y)\exp(-i\omega t)$, Eq. (21) transforms to the Helmholtz equation for viscous waves

$$\frac{d^2V(y)}{dy^2} + k_1^2 V(y) = 0, \tag{22}$$

where $k_1^2 = \dfrac{i\omega}{\nu}$ is the square of the wave number. A solution to Eq. (22) and the boundary conditions can be written down in the form

$$V(y) = A\cos k_1 y + B\sin k_1 y, \tag{23}$$

$$V(0) = V_0; \quad V(h) = 0. \tag{24}$$

Substituting Eq. (23) into Eqs. (24) we obtain the solution

$$V(y) = V_0\frac{\sin k_1(h-y)}{\sin k_1 h}.$$

The viscous stress is $\sigma = \eta\dfrac{dV}{dy}$, where $\eta = \nu\rho_0$ is the kinematic viscosity and ρ_0 is water density. Therefore, the desired quantity is

$$\sigma_0 = \sigma(0) = -k_1\eta V_0\cot k_1 h. \tag{25}$$

Substituting Eq. (25) into Eq. (20), we obtain

$$-i\omega\rho l V_0 = p_2 - p_1 - \frac{2k_1 l}{a}\eta V_0\cot k_1 h,$$

or

$$-i\omega l\left(\rho + i\frac{2k_1}{\omega a}\eta\cot k_1 h\right) = p_2 - p_1. \tag{26}$$

It follows from here that a standard sample can be described by a complex density

$$\bar{\rho} = \rho + i\frac{2k_1}{\omega a}\eta\cot k_1 h. \tag{27}$$

Since $k_1 h > 1$ and the quantity k_1 is complex, $|\cot k_1 h| \longrightarrow 1$, and the loss coefficient α ($\bar{\rho} = \rho(1 + i\alpha)$) can be written down in the form

$$|\alpha| = \left|\frac{2k_1}{\omega\rho a}\eta\right| = \frac{2\rho_0}{\rho|k_1 a|}. \tag{28}$$

At the lowest frequency of the ALP operation range ($f = 100$ Hz), we have $|k_1 a| \gg 1$, and we obtain $|\alpha| \approx 5 \times 10^{-5}$. At other frequencies, this value is even smaller.

Proceeding from the aforesaid, we can make a conclusion that the slot influence can be ignored from the point of view of viscous losses.

In the case of an exact calculation of the sound "leakage" through the slot with allowance for the presence of inhomogeneous waves, the problem can be reduced to an infinite system of algebraic equations [12], which can be solved using the reduction method. However, since the slot width is usually small compared to the pipe radius a and the wavelength λ (as indicated above), the problem of determining the value of R can be solved in the low-frequency approximation using the impedance technique.

Ignoring the viscosity, we can write down the specific dimensionless (in units of wave conductivity of water) conductivity of the slot in the form

$$g_0 = s, \tag{29}$$

where $s = 2h/a$ is the relative area occupied by the slot. In this case, the specific conductivity of a measured sample is expressed by the formula

$$g = (1 - s) g_{\text{sam}}, \tag{30}$$

where g_{sam} is the impedance of the measured sample.

The total dimensionless conductivity

$$G = s + (1 - s) g_{\text{sam}} \tag{31}$$

is connected with the measured reflection coefficient by the known formula

$$\hat{R} = \frac{1 - G}{1 + G}, \tag{32}$$

which leads [taking into account Eq. (31)] to the expression

$$\hat{R} = \frac{1 - g_{\text{sam}}}{a + g_{\text{sam}}}, \tag{33}$$

where the parameter is $a = \dfrac{1 + s}{1 - s}$.

It is possible to determine from Eq. (33) the value of g_{sam} and the true reflection coefficient $\hat{R}_0$ expressed through $\hat{R}$:

$$\hat{R}_0 = \frac{(1 + a)\hat{R}}{2 + (1 - a)\hat{R}}. \tag{34}$$

Figures 6 and 7 present the results of calculations for the values of R_0 and φ_{R0} for the same standard sample and the slot width $h = 0$, 0.1, and 0.2 cm ($s = 0$, 0.27, and 0.054, respectively).

The design of a pendant (mounting) for a sample in the pipe can affect considerably the precision of measurements. Together with other factors, it can produce a large systematic error. Since the sample is suspended in the pipe center so that its lower surface lies on a grid made of threads or wires that are fixed to the upper end of the lower half of the pipe, such a pendant, from the acoustic point of view, represents an elastic load connected in series with the sample under measurement in such a way that their impedances are added together:

$$Z = Z_0 + Z_{\text{pen}}. \tag{35}$$

Here, Z is the impedance of the sample + pendant system, Z_0 is the impedance of the sample under measurement, and Z_{pen} is the pendant impedance.

If we use at the beginning a standard sample of the same mass as a sample for measurements, the quantity Z_0 in this case is defined by the formula

$$Z_0 = iX + 1. \tag{36}$$

Here, X is the dimensionless impedance of a standard sample and the unit term corresponds to the wave resistance of water behind the sample (in the case of an "ideal" absorber). Measuring the complex reflection coefficient $\hat{R}_0$ of the mass + pendant system and taking

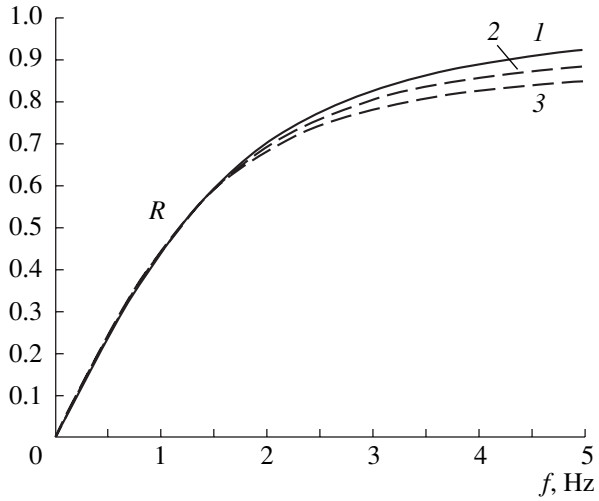

Fig. 6. Effect of the slot width h on the value of R; h = (*1*) 0; (*2*) 0.1; and (*3*) 0.2 cm.

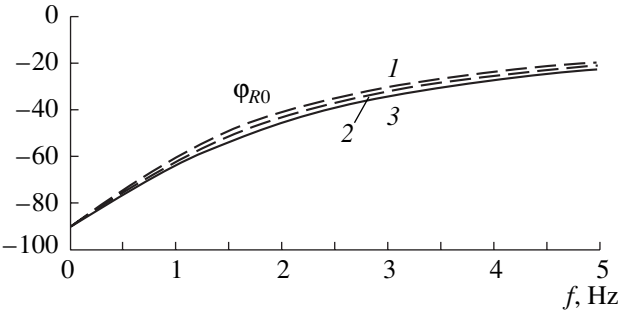

Fig. 7. Effect of the slot width h on the value of φ_{R0}; h = (*1*) 0; (*2*) 0.1; and (*3*) 0.2 cm.

into account Eqs. (35) and (36), we can determine the desired quantity Z_{pen}:

$$Z_{\text{pen}} = \frac{1 + \hat{R}_0}{1 + \hat{R}_0} - (1 + iX). \quad (37)$$

On the other hand, introducing the notation $\hat{R}_2$ for the coefficient of reflection from the sample of interest (with the same pendant), we obtain from Eqs. (35) and (37)

$$Z_0 = \frac{1 + \bar{R}_2}{1 - \bar{R}_2} - Z_{\text{pen}}. \quad (38)$$

Here, Z_0 is the true impedance of the sample under measurement that serves as the basis for the determination of the true complex reflection coefficient

$$\hat{R}_2 = \frac{Z_0 - 1}{Z_0 + 1}. \quad (39)$$

The calculation of the true complex transmission coefficient $\hat{D}_2$ is based on the condition of proportionality

$$\frac{\hat{D}_2}{\hat{D}_0} = \frac{u_2}{u_0} = \frac{1 - \hat{R}_2}{1 - \hat{R}_0}, \quad (40)$$

where u_2 and u_0 are the amplitudes of oscillations of the sample surface on the side of the incident wave. Thus, we have

$$\hat{D}_2 = \hat{D}_0 \frac{1 - \hat{R}_2}{1 - \hat{R}_0}, \quad (41)$$

where $\hat{D}_0$ is the complex transmission coefficient of the mass + pendant system.

It is necessary to note that the design of a sufficiently soft pendant that would not manifest itself within the frequency range of measurements is a very complex technological problem, especially in the case of heavy samples. Therefore, the technique described above seems to be the only method to eliminate the systematic error produced by the effect of the sample pendant. The practical realization of this technique can be computerized by introducing its algorithms into the operational software controlling the process of measurements.

The precision attained in reality in measuring the complex values of the reflection and transmission coefficients is as follows:

(a) ≈±2 dB in modulus within the low-frequency range and ≈±1 dB within the high-frequency range; and

(b) ≈±2°–3° in phase within the low-frequency range and ≈±1.5°–2° within the high-frequency range.

REFERENCES

1. Program of Forum Acusticum 1999, TU Berlin, 1999, Acust. Acta Acust. **85**, Suppl. 1, (1999).
2. *EC Proceedings of the Fifth European Conference on Underwater Acoustics, ECUA 2000* (2000), Vol 1.
3. N. S. Ageeva, Akust. Zh. **1**, 110 (1955) [Sov. Phys. Acoust. **1**, 117 (1955)].
4. R. Bobber, *Underwater Electroacoustic Measurements* (Naval Res. Lab., Washington, 1970; Mir, Moscow, 1974).
5. V. V. Tyutekin, A. E. Vovk, D. V. Stepanov, and S. P. Klimov, USSR Inventor's Certificate No. 480973 (10 May 1971).
6. V. V. Tyutekin, A. E. Vovk, and S. P. Klimov, USSR Inventor's Certificate No. 602988 (18 February 1974).
7. A. E. Vovk, S. P. Klimov, and V. V. Tyutekin, Izmer. Tekh., No. 7, 76 (1975).
8. A. E. Vovk, S. P. Klimov, and V. V. Tyutekin, in *IX All-Union Acoustical Conference* (Moscow, 1977), 0IVB-5, p. 53.
9. A. E. Vovk, S. P. Klimov, and V. V. Tyutekin, Izmer. Tekh., No. 12, 41 (1989).
10. A. Ya. Gorenberg, F. F. Kamenets, I. I. Sizov, *et al.*, in *Proceedings of X Session of the Russian Acoustical Society* (Moscow, 2000), Vol. 2.
11. L. D. Landau and E. M. Lifshitz, *Mechanics of Continuous Media* (Nauka, Moscow, 1965).
12. V. T. Grinchenko and I. V. Vovk, *Wave Problems of the Sound Scattering by Elastic Shells* (Naukova Dumka, Kiev, 1986).

Translated by M. Lyamshev

Acoustical Physics, Vol. 47, No. 6, 2001, pp. 755–757. Translated from Akusticheskiĭ Zhurnal, Vol. 47, No. 6, 2001, pp. 853–855.

SHORT COMMUNICATIONS

Experimental Study of Viscoelastic Properties of Liquids by Using Resonators

B. B. Badmaev, S. A. Bal'zhinov, and E. R. Ochirova

Buryat Scientific Center, Siberian Division, Russian Academy of Sciences, ul. Sakh'yanovoĭ 8, Ulan-Udé, 670047 Russia

e-mail: lmf@fpsrv.bsc.buryatia.ru

Received November 27, 2000

Earlier [1], the presence of shear elasticity in thin layers of liquids several microns thick was observed at a frequency of 74×10^3 Hz. This result attests that an unknown low-frequency viscoelastic relaxation process occurs in the liquids. The studies showed that the mechanical loss tangent was less than unity. This suggests that the relaxation frequency of this process was less than the frequency used in the experiment. Therefore, it is of interest to perform similar studies at lower frequencies. The investigation at a frequency of 74×10^3 Hz was carried out by the resonance method with the resonator in the form of an X-18.5°-cut rectangular piezoelectric quartz crystal whose dimensions were $34.7 \times 12 \times 5.5$ mm^3. The crystal cut was chosen so that one of the lateral faces performed pure tangential motion under the excitation of antisymmetric longitudinal vibrations. A thin layer of the liquid under study was spread between this face and an inertial cover plate near one end of the resonator. Since near the ends the tensile deformation is practically absent, the liquid is subjected to a purely shear stress.

The solution of the problem on the interaction between the resonator and the cover plate separated by a liquid interlayer with consideration for damping in the vibrating system yields the following expression for the complex shift of the resonance frequency Δf^* [2]:

$$\Delta f^* = \frac{Sk^*G^*}{4\pi^2 M f_0}\frac{1+\cos(2k^*H-\varphi^*)}{\sin(2k^*H-\varphi^*)}, \qquad (1)$$

where S is the area of the cover plate, $k^* = \beta - i\alpha$ is the complex wave number (β and α are the real and imaginary components), $G^* = G' + iG''$ is the complex shear modulus of liquid, H is the thickness of the liquid interlayer, φ^* is the complex phase shift at the wave reflection from the liquid–plate boundary, M is the mass of the piezoelectric crystal, and f_0 is its resonance frequency. Equation (1) is simplified to the utmost degree with the assumptions that, during the vibration of the resonator, the cover plate is practically at rest ($\varphi^* = 0$) due to the weak coupling through the liquid interlayer and that the interlayer thickness is much smaller than the wavelength in liquid ($H \ll \lambda$). Under these conditions, the real shear modulus G' and the mechanical loss tangent $\tan\theta$ are given by the following formulas

$$G' = 4\pi^2 M f_0 \Delta f' H/S, \qquad (2)$$

$$\tan\theta = G''/G' = \Delta f''/\Delta f', \qquad (3)$$

where $\Delta f'$ and $\Delta f''$ are the real and imaginary frequency shifts and S is the area of the cover plate. The influence of the asymmetry of the system that leads to a shift of the node of crystal vibration from its central position is considered in [3].

A reduction of the resonance frequency requires an increase in the resonator length. To perform investigations at a frequency of 10^4 Hz, we used a resonator in the form of a plate of polished glass, $240 \times 15 \times 1.2$ mm^3 in size. The experimental setup is shown schematically in Fig. 1. The glass plate was fixed at the center by two rubber pads, 3 mm wide and 1.5 mm thick. The theoretical analysis showed that, for a low rigidity of the pads, the asymmetry of the system can be neglected. Let μ_1 be the shear modulus of the pad, h_1 be its height, S_1 be the area of pressing, E be the tensile modulus of the res-

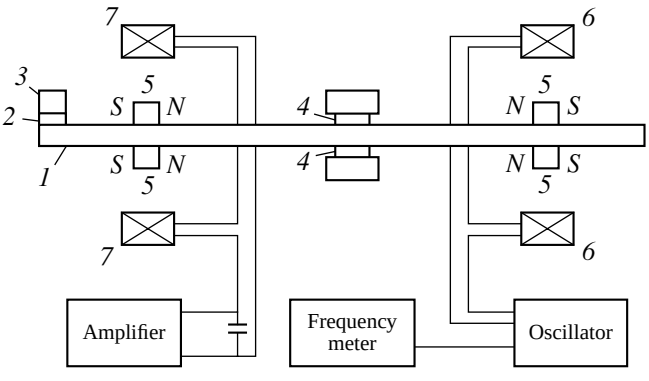

Fig. 1. Experimental setup for determining the viscoelastic properties of liquids by using resonators made of isotropic materials, at a frequency of 10 kHz: (*1*) resonator for longitudinal vibrations, (*2*) liquid layer, (*3*) cover plate, (*4*) rubber pads, (*5*) permanent magnets, (*6*) exciting coils, and (*7*) receiving coils.

1063-7710/01/4706-0755$21.00

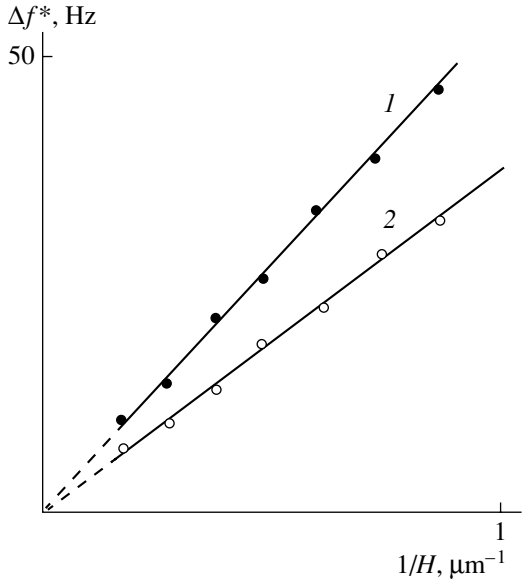

Fig. 2. Dependences of the (*1*) real and (*2*) imaginary shifts of the resonant frequency on the reciprocal of the thickness of the liquid interlayer for diethylene glycol.

onator, and L and S_r be the length and area of the resonator cross section, respectively. Then, the condition of a low rigidity of the pad can be written as

$$(\mu_1 L S_1)/(E h_1 S_p) \le 1. \quad (4)$$

Substituting into the dimensions of the resonator and the pads into Eq. (4), we obtain $\mu_1 < E/200$, which is always true for rubber.

The excitation and reception of vibrations were performed by the electromagnetic method. For this purpose, permanent ceramic magnets were glued to the large surfaces of the glass plate. The magnets were positioned symmetrically, on both sides of the plate center, at a distance of 90 mm from it (see Fig. 1). The polarities of the magnets on each side were coincident and directed along the resonator axis. The magnets were placed at some distance from the resonator ends to make the application of the liquid under study and the subsequent cleaning more convenient. Four fixed coils serving for the excitation and reception of vibrations were wound around dielectric cores $15 \times 3 \times 1.2$ mm^3 by a wire 0.12 mm in diameter. Each coil had 400 turns. At each end of the resonator, the coils were connected in series, so that their magnetic fields were opposite to each other. The resultant force acting on the magnets was directed along the resonator axis. This geometry of magnetic fields was chosen to reduce the noise induced in the receiving coils by the exciting coils and the external fields. The coils were fed from an RC-type oscillator (G3-107). An additional variable resistor was included in the oscillator circuit to provide a better accuracy in setting the frequency, namely, to within 10^{-3}%. The signal from the receiving coils was measured by a selective microvoltmeter. To increase the level of the input signal, a capacitor was connected in parallel with the receiving coils, which formed an oscillatory circuit tuned to the resonator frequency with a Q factor of about five.

The experimental setup had the following parameters: the frequency of the unloaded resonator was 9.84×10^3 Hz, the Q factor was 910, the level of noise induced in the receiving coils was 113 dB, and the level of the signal at the receiver input was 40 dB. Since the resonator is a thin plate, transverse vibrations of considerable amplitude can arise in it because of asymmetry that occurs in the system of excitation and gives rise to lateral forces, as well as the asymmetry of the load consisting of the liquid layer and the cover plate, which gives rise to a moment of force at the end of the plate. The transverse vibrations can distort the results of measurements by directly inducing an additional signal in the receiving coils and by the inverse action of the transverse vibrations of the liquid on the longitudinal vibrations of the resonator. To determine the level of the direct induced signal from transverse vibrations, the resonator was excited in a wide range of frequencies, from 63.5 to 20×10^3 Hz. Below the fundamental harmonic of longitudinal vibrations equal to 9.84×10^3 Hz, only transverse vibrations could be observed in the system. The greatest signal was observed at 65.7 Hz, but it was smaller than the value of the main signal at 9.8×10^3 Hz by 36 dB. At the frequencies above 700 Hz, the levels of signals did not exceed 56.4 dB and approached the noise level of the amplifier, which operated in this measurement in a wide-band mode. Thus, the error due to the direct induction was less than 1.5%. The study of the inverse effect of transverse vibrations on longitudinal ones was performed theoretically, by solving a set of simultaneous equations of motion for longitudinal and transverse vibrations coupled by the boundary conditions for the liquid layer. The calculations showed that, even in the most unfavorable case of coincident resonant frequencies of longitudinal and transverse vibrations, the error introduced in this case did not exceed 0.1%. The evaluation of the technique was performed with the use of petroleum jelly and castor oil, polymer liquids, and glycols. Figure 2 shows the dependences of the (*1*) real and (*2*) imaginary frequency shifts on the reciprocal of the thickness of the liquid interlayer for diethylene glycol. The dependences of the frequency shifts are linear, whence it follows that, according to Eqs. (2), at the frequency of shear vibrations 9.84×10^3 Hz, the liquid under study exhibits a shear elasticity. The calculations by Eqs. (2) and (3) yield the following values of the real shear modulus and the mechanical loss tangent: $G' = 0.15 \times 10^5$ Pa and $\tan\theta = 0.72$. For comparison, we present the corresponding parameters obtained at the frequency of shear vibrations 74×10^3 Hz [4]: $G' = 1.22 \times 10^5$ Pa and $\tan\theta = 0.31$. Similar dependences were observed for all tested liquids.

Comparing the results obtained at different frequencies, we can conclude that the real part of the shear modulus considerably decreases with decreasing frequency, and the mechanical loss tangent grows but remains less than unity. The mass of the resonator at the frequency 9.84×10^3 Hz was 12.85 g, and the area of the cover plate was 0.2 cm^2. The thickness of the liquid interlayer was measured by the interferometric method to within 0.01 μm.

In conclusion, it should be noted that the measurements of the viscoelastic properties of various liquids by other measuring techniques [5, 6] provided results that are in good agreement with our results.

ACKNOWLEDGMENTS

This work was supported by the Russian Foundation for Basic Research, project nos. 98-01-00503 and 98-01-00504.

REFERENCES

1. U. B. Bazaron, B. V. Deryagin, and A. V. Bulgadaev, Zh. Éksp. Teor. Fiz. **51**, 969 (1966) [Sov. Phys. JETP **24**, 645 (1967)].
2. U. B. Bazaron, B. V. Deryagin, K. T. Zandanova, and O. R. Budaev, Dokl. Akad. Nauk SSSR **215**, 309 (1974).
3. F. M. Kuni, U. B. Bazaron, Kh. D. Lamazhapova, and B. B. Badmaev, Kolloidn. Zh. **54** (2), 116 (1992).
4. B. B. Badmaev and B. B. Damdinov, Akust. Zh. **47**, 561 (2001)[Acoust. Phys. **47**, 487 (2001)].
5. H. See, A. M. Maher, J. Field, *et al.*, Rheol. Acta **38**, 443 (1999).
6. J. Ch. Hyoung, J. Stephen, and S. J. Myung, Polymer **40**, 2869 (1999).

Translated by A. Svechnikov

Acoustical Physics, Vol. 47, No. 6, 2001, pp. 758–759. Translated from Akusticheskiĭ Zhurnal, Vol. 47, No. 6, 2001, pp. 856–857.

SHORT COMMUNICATIONS

Effect of an Electric Load on the Duration of the Electric Pulse of a Piezoelectric Detector

S. I. Konovalov and A. G. Kuz'menko

St. Petersburg State Electrotechnical University, ul. Prof. Popova 5, St. Petersburg, 197376 Russia

e-mail: root@post.etu.spb.ru

Received July 25, 2000

The problem of the operation of piezoelectric transducers in pulsed modes remains topical. For example, Hole and Lewiner [1] considered the problem of the generation of a unipolar pressure pulse by selecting the form of the voltage pulse that excites the transducer with allowance for the matching elements between the transducer and the generator.

In our previous publications [2, 3], we considered the possibility of obtaining short pulses in the cases of transmission and reception with the help of quarter-wave layers. It was shown that the minimal pulse duration is not achieved at the maximal bandwidth but corresponds to an amplitude–frequency characteristic that is intermediate between single-peaked and double-peaked ones.

In this paper, we consider the possibility of reducing the pulse duration for signal reception by a piezoelectric plate that operates in the fundamental mode of thickness vibrations with an inductive–resistive electric load connected in parallel to it. An active resistance R is connected in series to an inductance L. The total resistance is characterized by the parameter $Q = \omega_0 L/R$, where ω_0 is the antiresonance frequency of the piezoelectric plate. The capacitance C of the piezoelectric plate in combination with the inductance L of the load forms an oscillatory circuit whose resonance frequency is characterized by the parameter $n = \omega_e/\omega_0$, where $\omega_e = 1/\sqrt{LC}$.

By choosing different values of the parameters n and Q, it is possible to obtain the amplitude–frequency characteristic of the piezoelectric detector in the form of a single-peaked or double-peaked curve. The acoustic load for the piezoelectric plate is water. For a damper, we use the model of a semibounded medium.

From the numerical calculations of the voltage pulse at the detector excited by a half-period of the particle velocity sinusoid with a frequency ω_0, it was found that the shortest pulse duration is obtained when the amplitude–frequency characteristic is intermediate between single-peaked and double-peaked ones. The optimal values of n and Q for TsTSNV-1 piezoelectric ceramics (a PZT ceramics) are presented in the table for different values of the acoustic impedance of the damper z_d. The relative bandwidth for the combinations presented in the table lies within 50–65%.

Figure 1 shows the voltage pulses across the receiving plate in the absence of mechanical damping ($z_d = 0$) for two cases:

(a) a two-peaked amplitude–frequency characteristic corresponding to the maximal bandwidth ($n = 1.1$ and $Q = 3.8$); and

(b) an amplitude–frequency characteristic that is intermediate between single-peaked and two-peaked ones ($n = 1.1$ and $Q = 1.5$).

The abscissa axis represents the number T of the half-periods of the fundamental frequency of the piezoelectric plate. The ordinate axis represents the voltages normalized to the maximal values. The pulse duration (as before) is assumed to be the time within which the amplitude decreases by a factor of ten relative to the maximal value (a decrease in level by 20 dB).

From Fig. 1, one can see that, in the case (a), the pulse duration is $T_p \approx 10$ whereas, in the case (b), $T_p \approx 5$, which is almost twice as small. In addition, in the second case,

Table

$z_d \times 10^{-6}$ Pa s/m	0	1.5	3	5	8	12
n	1.10	1.11	1.12	1.13	1.15	1.23
Q	1.5	1.5	1.5	1.5	1.5	1.5

1063-7710/01/4706-0758$21.00

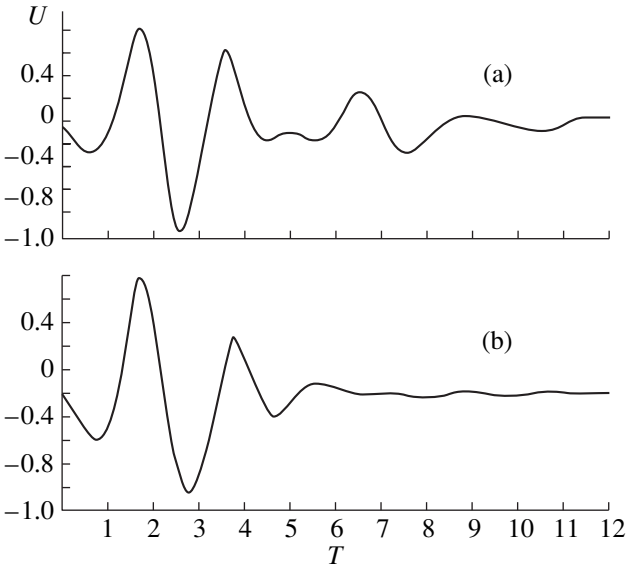

Fig. 1.

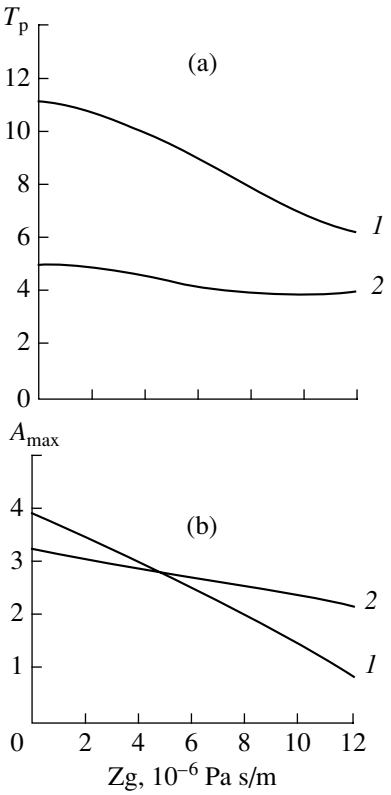

Fig. 2.

the curve is smoother, while, in the first case, it resembles a kind of beat.

Figure 2a presents the dependences of the pulse duration on z_d with the optimal electric load for (*1*) a double-peaked amplitude–frequency characteristic and (*2*) an intermediate one. It is obvious that curve *2* has an advantage over curve *1*, especially when the damping is weak or absent. The pulse duration is approximately two times shorter in this case.

Figure 2b shows the maximal pulse amplitudes expressed in arbitrary units as functions of z_d. Here, the curves are numbered as in Fig. 2a. One can see that, for small values of z_d, the amplitudes corresponding to curve *1* exceed the amplitudes corresponding to curve *2*. For greater values of z_d, the situation is reversed. One can notice that curves *2* shown in Figs. 2a and 2b are exhibit a weaker dependence on z_d, as compared to curves *1*.

Thus, the calculations performed by us confirm the criterion formulated earlier for matching layers: to obtain the shortest possible pulse, the parameters of the electric load should be chosen in such a way that the amplitude–frequency characteristic be intermediate between single-peaked and a double-peaked ones. In this case, the resonance frequency of the tuning frequency of the electric circuit somewhat exceeds the antiresonance frequency of the piezoelectric plate ($n \approx 1.1$–1.2), and the Q factor of the inductance is $Q \approx 1.5$, which is lower than in the case of the maximal bandwidth ($Q \approx 3$).

REFERENCES

1. S. Hole and J. Lewiner, J. Acoust. Soc. Am. **104**, 2790 (1998).
2. S. I. Konovalov and A. G. Kuz'menko, Akust. Zh. **44**, 119 (1998) [Acoust. Phys. **44**, 100 (1998)].
3. S. I. Konovalov and A. G. Kuz'menko, Akust. Zh. **45**, 568 (1999) [Acoust. Phys. **45**, 507 (1999)].

Translated by E. Golyamina

Acoustical Physics, Vol. 47, No. 6, 2001, pp. 760–761. Translated from Akusticheskiĭ Zhurnal, Vol. 47, No. 6, 2001, pp. 858–859.

CHRONICLE

Andreĭ Viktorovich Gaponov-Grekhov (On His 75th Birthday)

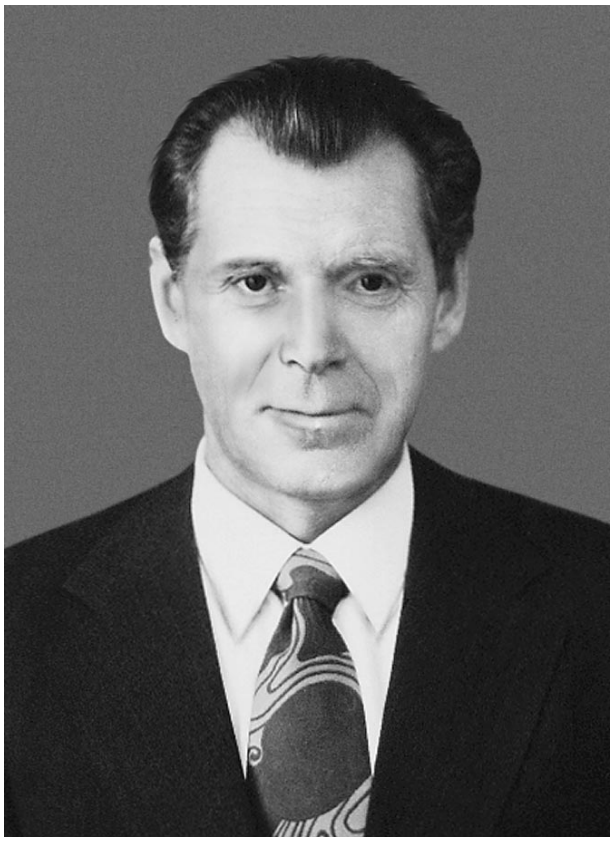

In June 2001, the outstanding scientist Academician Andreĭ Viktorovich Gaponov-Grekhov turned 75-years-old.

Gaponov-Grekhov is a former student and successor of Academician A.A. Andronov, the founder of the Gor'ki–Nizhni Novgorod scientific school in radiophysics, which has gained worldwide recognition among the scientific community. Today, Gaponov-Grekhov is the leader of this school. His former students and his students' students carry out basic and applied research in different fields of modern physics. It is difficult to list here all the scientific results that were obtained by Gaponov-Grekhov and that determined for years the development of the physics of nonlinear oscillation and wave processes. They include outstanding achievements in electrodynamics, microwave electronics, theory of oscillations of distributed systems, and the dynamics of waves in nonlinear media. The style of Gaponov-Grekhov's work in research can be illustrated by the history of the development of a new class of high-power generators and amplifiers operating in the centimetric, millimetric, and submillimetric wave bands, i.e., the cyclotron-resonance masers. Gaponov-Grekhov's versatile talent provided for the simultaneous and harmonic development of the theory, the experiments, and the design of these instruments, which proved to have record characteristics in terms of power and efficiency. This work resulted in the mass production of new instruments for technological purposes and for experiments on heating a fusion plasma by microwave radiation.

In parallel with the studies in electrodynamics and microwave electronics, Gaponov-Grekhov and his students started research in the dynamics of waves in nonlinear media and in the theory of oscillations of distributed systems, which later formed one of the key directions of research in modern physics. The general physical concepts of nonlinear wave processes and the mathematically justified asymptotic and rigorous methods of nonlinear wave dynamics, which were proposed by Gaponov-Grekhov, played an especially important role. They served as a basis for the subsequent studies of the dynamic chaos and self-organization in complex dynamic systems.

The contribution made by Gaponov-Grekhov to the development of underwater acoustics is less well known. In fact, the participation of outstanding scientists in solving the problems of shipbuilding and seamanship has become a tradition in Russia. The variety of these problems and phenomena causing them, as well as the urgency of their solution within limited times and the *a priori* absence of trivial ways for such a solution, has always been challenging and, therefore, attractive for prominent scientists. Academician A.N. Krylov, for example, combined basic research with applied studies in shipbuilding. Later on, the problems of shipbuilding became the object of intensive studies carried out by one of the founders of the nuclear-powered fleet Academician A.P. Aleksandrov. He called the attention of Gaponov-Grekhov to the burning problems of shipbuilding and, specifically, to the problem of "acoustic safety" and the related problems. Gaponov-Grekhov actively participated in the work of the Scientific Council on the Complex Problem of Hydrophysics, which was headed by Aleksandrov at that time. Starting from 1991, Gaponov-Grekhov has been the permanent chairman of this Council. The Council united prominent scientists and engineers,

1063-7710/01/4706-0760$21.00 © 2001 MAIK "Nauka/Interperiodica"

navy specialists, and industrial managers, and it was intended to provide scientific support to the development of nuclear-powered submarines. With time, acoustical problems have become one of the main issues considered by the Council. Gaponov-Grekhov's broad education in physics and his ability to approach different phenomena in a general manner allowed him to achieve fundamental understanding of the problems of ship acoustics.

On Gaponov-Grekhov's initiative and with his active participation, intensive studies of low-frequency sound propagation in the ocean were carried out, and the possibility of remote sensing of the underwater medium on long-range (up to 1000 km) propagation paths was proved experimentally. Under Gaponov-Grekhov's supervision, scientific and technological foundations were laid for the design of low-frequency coherent acoustic radiators, which were necessary for the experimental studies of low-frequency coherent acoustic phenomena in the ocean. Today, these radiators developed at the Institute of Applied Physics of the Russian Academy of Sciences are unsurpassed. They were used in the joint Russian–American studies of low-frequency transarctic propagation, which in fact were a pilot experiment on the acoustic monitoring of the global temperature variations in the ocean and, hence, on the acoustic monitoring the climate of the Earth.

Gaponov-Grekhov paid much attention to the problems of ship noise control. He has put forward the idea of "acoustic design" in shipbuilding. Usually, the problem of noise suppression was addressed when a vessel was already designed and it was necessary to reduce the noise of a practically completed vessel. However, the design was often chosen in such a way that noise reduction was fundamentally impossible. To avoid such situations, acoustic design should be introduced in the general project. Gaponov-Grekhov supervised a number of projects in which this principle was successfully implemented.

However, perhaps the most important result of Gaponov-Grekhov's activity in acoustics is the formation of an acoustic scientific school in Nizhni Novgorod, which has become one of the branches of the Nizhni Novgorod radiophysics and which has made substantial contributions to different fields of acoustics, such as low-frequency ocean acoustics, nonlinear acoustics, coherent seismoacoustics, vibration acoustics, and medical acoustics.

As a rule, the role of prominent scientists in the development of science is not confined to the results obtained by them personally or by their students. Gaponov-Grekhov belongs to the type of scientist who devotes much time and energy to organization activities. He is the permanent director of the Institute of Applied Physics of the Russian Academy of Sciences. This institute was founded more than quarter of a century ago, and, under Gaponov-Grekhov's supervision, the Institute of Applied Physics has become one of the large leading institutes of the Russian Academy of Sciences. The work of this institute follows the style developed by Gaponov-Grekhov in combining fundamental and applied studies. The institute occupies firm positions in hydrophysics and hydroacoustics, plasma physics, high-power electronics, quantum radiophysics and nonlinear optics, and physics of millimetric and submillimetric waves. At the present time, which is rather difficult for science, the Institute of Applied Physics grows, acquires new young scientists, and launches new projects in the new fields of the ever-young physics.

Gaponov-Grekhov's services for Russian science and industry were honored many times with state awards and prizes. The recognition of these services by professionals resulted in awarding Gaponov-Grekhov the Large Gold Medal of the Russian Academy of Sciences in 2000 for outstanding contribution to the development of the physics of oscillation and wave processes.

We congratulate Andreĭ Viktorovich Gaponov-Grekhov and wish him health and further success in all fields of his widely varied activities.

Translated by E. Golyamina

Acoustical Physics, Vol. 47, No. 6, 2001, pp. 762–763. Translated from Akusticheskiĭ Zhurnal, Vol. 47, No. 6, 2001, pp. 860–861.

CHRONICLE

Samuil Akivovich Rybak (On His 70th Birthday)

August 14, 2001, marked the 70th birthday of Samuil Akivovich Rybak, one of the most prominent Russian acousticians, head of a sector of the Theoretical department of the Andreev Acoustics Institute; Professor of the Moscow Institute of Physics and Technology; Doctor of physics and mathematics; member of the Russian, American, and European acoustical societies, and laureate of the Russian Federation State Award.

Rybak began his career in science as a third-year student of the Kiev Polytechnical Institute by studying the behavior of the electrical resistance of alloys near the point of the second-order phase transition under the supervision of Professor A.A. Smirnov. Simultaneously, Rybak also carried out other investigations, and, by the day of his graduation in 1953, he already had several scientific publications. These first publications demonstrated Rybak's solid background in physics and mathematics, which proved to be of a great benefit to him in his following work. In the 1950s, Rybak worked at the Laboratory of Special Alloys of the Academy of Sciences of the Ukrainian Soviet Socialist Republic. There, in cooperation with M.A. Krivoglaz, he studied the scattering of light near the critical point, and the results of these studies are cited in literature to this day.

In the following years, the scientific activity of Rybak has been related to acoustics. In 1960, he became a postgraduate student at the Acoustics Institute. Earlier, in Kiev, he took part in solving some problems of noise and vibration control in airplanes (at that time, he worked at the Antonov Design Office as head of the laboratory). Working at the Acoustics Institute, he substantially contributed to solving the problems of noise control on ships. In this connection, with the aim to solve the problem of vibration damping for structural noise, Rybak performed original theoretical studies of wave propagation in laminated plates. As a result of a thorough physical analysis, Rybak correctly formulated the equations for the vibrations of plates consisting of alternating metal and viscoelastic layers. The ideas developed by Rybak at that time served as a basis for a new direction in the studies of layered structures and made it possible to develop reliable methods for predicting the efficiency of the use of such structures in practice. In 1963, Rybak successfully defended his candidate dissertation, which was entitled "Vibrations of Inhomogeneous Plates."

After completing his postgraduate courses, Rybak became involved in the development of new space-rocket systems at the Korolev Design Office (now, RKK Énergiya). He worked on the problems related to the analysis of the dynamic stability of fuel systems of liquid-propellant rocket engines. Later, the results of this work were described in the monograph *Dynamics of the Fuel Systems of Liquid-Propellant Rocket Engines* (1975).

The following studies performed by Rybak were concerned with the statistical characteristics of waves in randomly inhomogeneous structures. Working in this important field of acoustics, he developed the theory of multiple scattering of waves in elastic structures in which waves of different types are excited. It should be noted that the development and the application of the methods of the theory of wave scattering in acoustics runs through the whole fifty-year-long scientific activity of Rybak. He considered this subject in one of his early publications, and its thorough investigation can be found in Rybak's doctoral dissertation (1973).

Rybak was the first to notice that taking into account loss is a necessary condition of applicability of the energy transport equation in the case of the wave prop-

1063-7710/01/4706-0762$21.00 © 2001 MAIK "Nauka/Interperiodica"

agation through inhomogeneous structures. Rybak developed a method for determining the distribution of the wave energy in inhomogeneous structures and derived the expressions for the stationary energy spectra of different types of waves. The ideas put forward in his doctoral dissertation gave an impetus to the development of the new direction of research concerned with wave propagation in inhomogeneous structures. These ideas are close to those developed by the well-known American acousticians, Prof. G. Maidanik and R. Lyon. Later on, they formed the basis for the methods related to the statistical energy analysis (SEA) in various complex structures that are widely used in practice.

In the following years, Rybak, together with his colleagues and students, studied different aspects of the dynamic and statistical nonlinear interaction of waves. In a number of publications (together with K.A. Naugol'nykh), he determined the character of the turbulent spectra of waves in dispersive media, he also studied the problem of the attenuation and amplification of waves in a noise field due to a nonlinear resonance interaction and considered the conditions of the excitation of surface capillary-gravity waves by sound. He investigated nonlinear waves in media with random parameters and the nonlinear fields and wave structures that occur in stratified liquids because of shear instability. Here, it is appropriate to mention the investigations concerned with wave instabilities in a moving liquid and in elastic structures in contact with it. Rybak analyzed the role of waves with negative energy in the development of instabilities at the linear and nonlinear stages of this development. He revealed the dipole mechanism of sound generation in the boundary layer due to the fluctuations of the tangential stresses at the wall and estimated the intensity and directivity of the resulting emission. In recent years, the results concerning the fundamental role of viscosity in the energy distribution in elastic structures with random parameters were further developed by other acousticians in application to the new problem of the so-called fuzzy structures. In studying nonlinear waves in multiphase media, Rybak also obtained quite important results. For example, for nonlinear media with a strong (resonance) dispersion, he determined the structure of stationary solitary and periodic waves and analyzed the relation between their form and the acoustic and dissipative parameters of media. The results of these studies find their application in the problems of monitoring multiphase, e.g., bubbly, media. Today, the aforementioned phenomena are the subject of the graduate projects carried out by a number of students of the Moscow State Institute of Physics and Technology.

Rybak is the author of more than 160 scientific publications. His versatile and deep knowledge made it possible to explain some fairly complex and poorly understood physical phenomena of mechanical, acoustic, and hydrodynamic natures and to solve new topical practical problems. Rybak's personal achievements and the achievements of his scientific school in the aforementioned directions of research in physical acoustics gained worldwide recognition. In 1997, Rybak received the Russian Federation State Award for his studies of nonlinear wave processes in inhomogeneous multiphase media.

Rybak's contribution to the education of a new generation of scientists is fairly large. He supervised the work of 20 young scientists who successfully defended candidate and doctoral dissertations. Currently, these scientists are working successfully in Russia and in other countries. The former students of Rybak have become skilled researchers, not only in acoustics but also in other fields of physics. Today, Rybak delivers lectures to the graduate and postgraduate students of the Moscow State Institute of Physics and Technology and the Acoustics Institute. He conducts a regular seminar on the topical problems of physical acoustics at the Acoustics Institute, and many physicists from Moscow and other Russian cities participate in the work of this seminar. Rybak is the leader of a scientific school, which includes both scientists from the Acoustics Institute and students from the Moscow State Institute of Physics and Technology. Since 1993, Rybak has taken part in the activities of the Russian Foundation for Basic Research.

Rybak is one of the leading Russian acousticians known not only among Russian scientists, but also among the international scientific community. He celebrates his 70th birthday in the prime of his creative life, he continues his scientific and tutorial activities and develops new ideas and plans. The friends, colleagues, and students of Samuil Akivovich Rybak congratulate him on his birthday and wish him health, many happy days, and further success in his creative work.

Translated by E. Golyamina

Acoustical Physics, Vol. 47, No. 6, 2001, pp. 764–766. Translated from Akusticheskiĭ Zhurnal, Vol. 47, No. 6, 2001, pp. 862–864.

INFORMATION

International Symposium on Hydroacoustics

The Third International Symposium on Hydroacoustics was held May 28–31, 2001 in Jurata, a summer resort town near the city of Gdansk (Poland). It was organized by the Polish Naval Academy (Gdynia), the Technical University of Gdansk, and the Technical University of Koszalin with the support from the International Commission on Acoustics, the European Acoustics Association, the Polish Acoustical Society, the Committee on Acoustics of the Polish Academy of Sciences, and other institutions. Professor E. Kozaczka and Professor A. Stepnowski were the Symposium cochairmen. The Chairperson of the Organizing Committee was Dr. G. Grelowska.

The symposium program included both invited and contributed papers and a poster session. All reports were distributed in nine sections and covered the following fields of underwater acoustics: Acoustics in Fisheries, Instrumentation and Measurements, Sea Floor Characterization, Signal and Data Processing, Sonar Systems, Sound Propagation in the Sea, and Transducers and Antennas. Cultural events were also organized.

To clarify the topics discussed at the Symposium, we briefly describe the invited and some contributed papers in the sequence determined by the symposium program.

T.H. Neighbors (USA) and L. Bjorno (Denmark) presented a paper "Anomalous Low Frequency Sea Surface Reverberation." It was noted that the results of many experimental studies of sound scattering by the sea surface agree well with the theory of sound scattering by an uneven surface within the frequency range from several kilohertz to approximately 60 kHz. However, at frequencies below several kilohertz, the sound backscattering by the sea surface, which was observed in the experiments conducted by Chapman and Harris, Chapman and Scott, Brown and Saenger, and Ogden and Erskine during the period from the 1960s to 1990s in deep seas, was considerably higher than that which follows from the theory of sound scattering by an uneven surface. The authors indicate an opportunity to develop alternative theories taking into account the sound scattering by not only an uneven surface, but also by the bubble clouds generated by breaking sea surface waves. It was found that the difference between the results of measurements and the predictions of the theory of sound scattering by an uneven surface depends on the angle of incidence of a sound wave, the wind speed, and the presence of "white plumes" on a rough sea surface. A calculation of the sound scattering by an uneven surface (a two-dimensional case) in the presence of bubble clouds in the subsurface layer was performed at the Danish Technical University (Lyngby, Denmark). It follows from this theory that, in the case of grazing angles of incidence of a sound wave on the sea surface, the scattering from the bubble clouds must increase. This result agrees well with the experimental data. Models of bubble clouds in the form of cylinders with ellipsoidal cross sections and the bubble concentration 10^{-6}, as well as spherical clouds with the bubble concentrations 10^{-2}–10^{-4} and symmetric and nonsymmetric bubble formations (plumes) with the concentrations 10^{-2}–10^{-6}, were considered. The authors expect that the three-dimensional theory of sound scattering by the sea surface with allowance for the formation of subsurface bubble clouds will provide an opportunity to explain in more detail the experimental data on the low-frequency sound backscattering by the sea surface.

The problem of sound backscattering by the surface and bottom of the ocean was also discussed in the paper by L.M. Lyamshev (Russia) and A. Stepnowski (Poland) "Fractal Laws of Sound Backscattering by the Sea Surface and Bottom." It was noted that dynamic chaos and fractals occupy an important place among the outstanding discoveries of the 20th century. They are closely connected with each other. Dynamic chaos is represented by chaotic oscillations similar to stochastic oscillations that arise in deterministic nonlinear dynamic systems. Chaotic oscillations have a dynamic property, i.e., a fractal structure. In other words, chaotic oscillations (phenomena) occur in nonlinear dynamic systems described by regular laws and are not a "formless" chaos but a chaos with a hidden order, i.e., with a fractal structure. Fractals are self-similar objects with fractional dimension. They have a property of scaling. The structural (correlation) functions and their spectra characterizing fractal objects are described by power laws with fractional indices. The concept of fractals and dynamic chaos in many cases provides an opportunity to more adequately describe the processes taking place in nature, since nature is a nonlinear dynamic structure in a certain sense. It was noted in the paper that frequency–angular dependences of the sound backscattering by the sea surface, which were observed in many experiments, are described by power laws with fractional indices. This is characteristic of wave scattering by a fractal surface. The authors of many theoretical papers devoted to the wave scattering from a fractal uneven surface demonstrated that a frequency–angular dependence of the intensity of wave scattering obeys a fractal law. The paper provides information on the papers attesting to the fact that a real sea surface has

1063-7710/01/4706-0764$21.00

fractal properties. Other papers were also cited, where it was determined in many experiments that the uneven surface of the ocean bottom and the volume inhomogeneities in the bottom sediments are also characterized by fractal laws. It was shown in some recent experiments that the observed sound scattering by the ocean bottom in these cases is governed by power laws with fractional indices. It was stressed in the paper that the fractal laws of sound scattering by the sea surface and bottom (bottom sediments) "work" in limited frequency ranges, when the "fractal" scales characterizing the surface and bottom of the sea are comparable to the sound wavelength.

A paper by D. Brecht and B. Fedders (Germany) "Detection of Objects Buried in the Sea Floor with a 3D Sediment Sonar" was devoted to the important problem of searching for mines and objects lying on the sea floor and immersed in the bottom sediments, which were left from World War II. It was shown that it is possible to detect a buried object with the help of a sonar system that was specially designed by the authors and has a planar array and a special data processing unit that forms a three-dimensional image of a certain volume of the sediment layer. In particular, the sonar utilizes autofocusing of the sounding signal and the principle of synthetic aperture. It has a classification system that provides an opportunity to perform acoustic identification of objects shaped as spheres, cylinders, and similar objects in the bottom sediments. The sonar operates at a frequency of 20 kHz. Its resolution is $3^\circ \times 3^\circ \times 10$ cm (in distance). It can be installed on a ship and is intended for operation at small depths.

A paper "High Intensity Ultrasound Waves from a Strongly Focused Circular Source" was delivered at the section on Nonlinear Acoustics by T. Kamakura and M. Akiyama (Japan). The authors conducted calculations and an experiment with focused ultrasound of high intensity in the conditions when the technique based on the Khokhlov–Zabolotskaya–Kuznetsov (KZK) equation is inapplicable to the calculation of the field of finite-amplitude waves. The spheroidal beam equation (SBE) was used for the calculation. According to the authors' opinion, this equation can be applied to the calculations of acoustic fields for the values exceeding the limiting values for the KZK equation. The data of the experiments conducted at a frequency of 1.6 MHz by using a transducer with a circular cross section 73 mm in diameter and with a focal distance of 75 mm in water were presented. The experiments were conducted in a pulsed mode. Pulses forming trains of three periods of a signal at a frequency of 1.6 MHz were used. This provided an opportunity to observe in detail the nonlinear distortions arising in the process of the pulse propagation. It was demonstrated that the experimental data agree well with the results of calculations on the basis of the SBE model.

A paper by N. N. Didenkulov, N. V. Mart'yanov, D. A. Selivanovskiĭ, and N. V. Pronchatov-Rubtsov (Russia) "Bubble Diagnostics with the Nonlinear Acoustic Scattering Method" noted that a high nonlinear response of a bubble in water to acoustic excitation opens an opportunity for remote observation of bubbles in the sea. A description of a series of nonlinear acoustic methods and their applications for the observation of bubbles in the sea, including their distribution in size and concentration, was presented. A description of a device (a bubble counter) for the observation of bubbles in the subsurface layer of the sea from a moving ship was given. Experiments on the determination of the size and concentration of bubbles were described. The data obtained in these experiments were discussed.

A description of a SeaBat 8110 System multibeam sonar was given in the paper by T. Avnstrom (Denmark) "Advances in Practical Multibeam Sonar and Data Processing Technology." The block-scheme of the device and a detailed description of its operation were presented. The processor unit, the monitor, the special recorder, and the computer software incorporating the commands corresponding to the modes of the sonar operation were described. It is necessary to note that sonars of the type presented in the paper are well known in the market of these devices, and the report dealt not just with scientific problems, but also with advertising.

N. Gorska (Poland) and D. Chu (United States) presented a paper "On Sound Extinction by Biological Targets." Sound damping in a medium with biological scatterers and, namely, in the sea, due to the sound scattering by fish shoals or zooplankton (the deep-scattering layers) is important for understanding the conditions of sound scattering. Fish shoals and clouds of zooplankton can affect the sound damping considerably. In many cases, it is necessary to take this damping into account in the process of acoustic measurements. Theoretical methods for the evaluation of this damping were discussed. The calculated values of damping were compared with experimental data.

Several contributed papers should be noted. G. Grelowsky, A. Grelowska, and E. Kozaczka (Poland) presented extensive data characterizing hydrology and conditions of sound propagation in various regions of the Baltic Sea for different seasons in their paper "Short- and Long-Term Predictions of the Conditions for the Sound Propagation in the Baltic Sea." The complexity of the "acoustic climatic conditions" was indicated. It was noted that, in many cases, long-term forecasts for sound propagation are possible, although it is a difficult problem. Many factors affect the conditions of sound propagation in the sea. The general mechanism of the formation of seasonal changes in the "acoustic climate" in the sea is basically well known. However, the diversity of random factors affecting these changes is very wide. Long-term forecasts are connected mainly with meteorological conditions, while short-term forecasts, with local hydrological factors.

A. Elminowicz (Poland) presented a poster "Multibeam Side-Scan Sonar." Detailed descriptions of a multibeam side-scan sonar and the principles of its operation were given. It was noted that existing single-beam side-scan sonars with the directivity pattern up to 1° are almost useless for detecting small objects on the sea floor from a moving ship. Sonars with a very high angular resolution of 0.1°–0.2° operate in the conditions of the near wave field and need a low towing speed. The multibeam side-scan sonar presented by the author is free of these disadvantages.

Another paper devoted to a sonar description was the paper "Stationary Sonar for Shallow Water" by A. Elminowicz, E. Gorosinska, and A. Kotlowski (Poland). A description of an active sonar permanently installed aboard a ship (and not towed) and capable of operating in the conditions of a shallow sea at depths starting from 8–10 m was given. The device is intended for the detection of small objects on the sea floor, at distances along the route up to several hundreds of meters. Special attention was given to the utilization of the methods of suppressing the surface and bottom reverberation in the sonar in order to secure its effective operation.

The Symposium was well organized. The participants were very active. Almost all papers provoked questions and animated discussions. The papers were printed in a yearbook published by the Polish Naval Academy in Gdynia and Technical University of Gdansk: Hydroacoustics, Annual Journal, Vol. 4, 2001.

L. M. Lyamshev

Translated by M. Lyamshev